Towards an improved understanding of the Antarctic coastal zone and its contribution to future global sea level

Kenichi Matsuoka[1], Geir Moholdt[1], Jennifer F. Arthur[1], Julien A. Bodart[2], Xiangbin Cui[3], Fausto Ferraccioli[4], René Forsberg[5], Vikram Goel[6], Tom A. Jordan[7], Felicity S. McCormack[8], Ruth Mottram[9], Hamish D. Pritchard[7], Calvin Shackleton[1], Kirsty Tinto[10], Fredrik Boberg[9], Marie G. P. Cavitte[11], Reinhard Drews[12], Pierre Dutrieux[7], Jörg Ebbing[13], Olaf Eisen[14,15], Hannes Eisermann[14], Alex S. Gardner[16], Chad A. Greene[16], Nicholas Holschuh[17], Stewart S. R. Jamieson[18], Byeong-Hoon Kim[19], Naomi Krauzig[20], Bernd Kulessa[21], Carlton Leuschen[22], Jilu Li[22], Lu Li[23, 24, 25,], Jonas Liebsch[1, 13], Joseph A. MacGregor[26], Emma MacKie[27], Anirudha Mahagaonkar[1,6], Joséphine Maton[1], Mathieu Morlighem[28], Francisco Navarro[29], Peter Neff[30], Inès N. Otosaka[31], Frank Pattyn[32], Antonia Ruppel[33], Rebecca J. Sanderson[34], Hélène Seroussi[28], Andrew Shepherd[31], Matthew R. Siegfried[35], Thomas Slater[31], Arjen P. Stroeven[36], Michael Studinger[26], Thomas Teisberg[37], Ryan A. Venturelli[35], Paul J. Winberry[38], Chen Zhao[39], Lu An[40], Jonathan L. Bamber[41], Robin E. Bell[10], Robert G. Bingham[42], Johanna Brehmer-Moltmann[1], Graeme Eagles[14], Jamin Greenbaum[43], Jorn Gronset[44], Won Sang Lee[18], Emmanuel Le Meur[45], Lenneke M. Jong[46], Katrin Lindbäck[47], Sven Lidström[1], Mareen Lösing[23,24], Masahiro Minowa[48], Mayuri Pandey[49], Yogesh Ray[6], Mirko Scheinert[50], Dustin M. Schroeder[37], Thorsten Seehaus[51], Kaian Shahateet[45], Daniel Steinhage[14], Xueyuan Tang[3], Drew Taylor[52], Hannah Verboncoeur[35], Junjun Yang[53], Duncan A. Young[54]

1. Norwegian Polar Institute, Norway
2. University of Bern, Switzerland
3. Polar Research Institute of China, Chila
4. Institute of Oceanography and Applied Geophysics, Italy
5. Technical University of Denmark, Denmark
6. National Center for Polar and Ocean Research, India
7. British Antarctic Survey, UK
8. Monash University, Australia
9. Danish Meteorological Institute, Denmark
10. Larmont-Doherty Earth Observatory, Columbia University, USA
11. UCLouvain, Belgium
12. University of Tubingen, Germany
13. Kiel University, Germany
14. Alfred Wegener Institute Helmholtz Centre for Polar and Marine Research, Germany
15. Faculty of Geosciences, University of Bremen, Bremen, Germany
16. Jet Propulsion Laboratory, USA
17. Amherst College, USA
18. Durham University, UK
19. Korea Polar Research Institute, Korea
20. Università Politecnica delle Marche, Italy
21. Swansea University, UK
22. University of Kansas, USA

23. School of Earth Sciences, The University of Western Australia, Perth, WA, Australia
24. Australian Centre of Excellence for Antarctic Science, The University of Western Australia, Perth, WA, Australia
25. Mineral Resources, CSIRO, Kensington, WA, Australia
26. NASA Goddard, USA
27. Univ. Florida, USA
28. Dartmouth College, USA
29. Universidad Politécnica de Madrid, Spain
30. Univ. Minesota, USA
31. Northumbria University, UK
32. University of Libre de Bruxelles, Belgium
33. Bundesanstalt für Geowissenschaften und Rohstoffe, Germany
34. Newcastle University, UK
35. Colorado School of Mine, USA
36. Stockholm University, Sweden
37. Stanford University, USA
38. Western Washington University, USA
39. University of Tasmania, Australia
40. Tongji University, China
41. University of Bristol, UK
42. University of Edinburgh, UK
43. Scripps Institute of Oceanography, UC Sandiego, USA
44. Skytraders PTY LTD, Australia
45. University of Grenoble Alpes, France
46. Australian Antarctic Division, Australia
47. Mid Sweden University, Sweden
48. Hokkaido University, Japan
49. Banaras Hindu University, India
50. Technical Univ. Dresden, Germany
51. Friedrich-Alexander University, Germany
52. University of Alabama, USA
53. MNR Key Laboratory of Airborne Geophysics and Remote Sensing Geology, China Aero Geophysical Survey and Remote Sensing Center for Natural Resources, China Geological Survey, China
54. Institute of Geophysics, University of Texas, USA

Abstract

Understanding the coastal zone of the Antarctic Ice Sheet, where it interacts with the Southern Ocean and warmer air masses, is crucial for predicting Antarctica's influence on the global climate and sea level. This region has multiple tipping mechanisms that could trigger large, rapid, and potentially irreversible changes in the Antarctic Ice Sheet, the Southern Ocean and their global connections in the coming centuries. The Antarctic Ice Sheet remains the largest source of uncertainty in future sea-level projections. Bed topography beneath the ice shelves and the coastal ice sheet is not yet well documented, but is a major source of this uncertainty. This review assesses current knowledge of the coastal zone and highlights methods to investigate it, including aerogeophysical surveys, ground- and ship-based measurements, satellite observations, and computer modeling. An ensemble analysis of published bed topography datasets identifies significant data gaps and their regional distribution, framed in the context of current ice-sheet behavior and potential instability. We propose scientific priorities and guidelines for future aerogeophysical surveys, advocating for a comprehensive, coordinated international effort to build a next-generation dataset of Antarctic bed properties. Such an initiative would significantly advance understanding of the role of coastal processes in ice-sheet dynamics, reducing uncertainties in sea-level rise projections and enhancing predictions of future ocean and climate changes.

Key points

- Antarctic sea-level contribution is largely controlled by coastal ice-sheet processes, emphasizing the need for detailed observations in this region.
- Data gaps in the ice sheet’s coastal zone are identified through comprehensive analysis of existing datasets from various sources.
- Priorities and guidelines are proposed to address these gaps via international, multidisciplinary collaboration and coordinated efforts.

Plain language summary

The Antarctic Ice Sheet is shrinking and is expected to continue losing ice in the coming centuries as the world warms. This directly impacts global sea levels, but significant uncertainties remain about how much sea level will rise, which ice-sheet regions will contribute the most, what mechanisms will drive the changes, and how quickly they will occur. Understanding the interactions between the atmosphere, ocean, ice, and the solid Earth is key to answering these questions. In this paper, an international group of scientists reviews current knowledge of the Antarctic Ice Sheet's coastal zone, where these interactions are most dynamic. We analyze existing datasets to identify gaps in our understanding and propose strategies for future surveys to fill these gaps, helping to improve estimates of the current Antarctic ice discharge and overall mass balance, as well as predictions of future sea-level rise.

Table of Contents

1. Introduction

Averaged over the past century, the global mean sea level has risen at a speed of 1.73 mm yr^{-1}, accelerating to 3.69 mm yr^{-1} in the past decade (Palmer et al., 2021; WCRP Global Sea Level Budget Group, 2018). Numerical models project further acceleration, reaching 5.2 mm yr^{-1} by 2100 for a low greenhouse gas emission scenario (shared socio-economic pathway, SSP1-2.6) and 12.1 mm yr^{-1} for a high-emission scenario (SSP5-8.5) (Fox-Kemper et al., 2021). As such, the Intergovernmental Panel on Climate Change (IPCC) provides median estimates of the total sea-level rise to 0.44 m by 2100 and 0.68 m by 2150 for SSIP1-2.6, and to 0.77 m by 2100 and 1.32 m by 2150 for SSP5-8.5 (Table 9.9 in Fox-Kemper et al., 2021). High-end estimates exceed these estimates significantly to 0.9 m in 2100 and 2.5 m in 2300 for SSP1-2.6 and 1.6 m in 2100 and 10.4 m in 2300 for SSP5-8.5 (Van De Wal et al., 2022). The resulting inundation of land may severely affect many of the 230 million people who currently live in coastal lands less than 1 m above the current sea level (Kopp et al., 2017).

According to the recent sixth assessment report of the IPCC (IPCC AR6; Table 9.8 in Fox-Kemper et al., 2021), the Antarctic Ice Sheet (AIS) will contribute 26% (SSP1-2.6) and 16% (SSP5-8.5) of the sea-level rise predicted for the coming century, which is comparable to the individual contributions of ocean thermal expansion, and melting from the Greenland Ice Sheet and mountain glaciers. Nevertheless, 51–52% of the total uncertainty (based on the ensemble median) in sea-level rise comes from the AIS, which is far more than that from other sources. Moreover, the uncertainty estimates consider only physical processes with medium or higher confidence. Medium confidence indicates that the process is supported by several lines of evidence and moderate agreement among studies, although some uncertainties remain. These processes include surface mass balance (Section 2.4.2), oceanic melt under ice shelves (Section 2.7.2) and Marine Ice Sheet Instability (MISI, Section 2.8.4). However, their representation in models remains limited, primarily due to uncertainties such as incomplete mapping of bed topography. The AIS may introduce even larger levels of uncertainty to future sea levels when considering less-understood processes that could lead to large, rapid, and possibly irreversible changes in the ice sheet (Section 2.8.4). Therefore, it is crucial to precisely monitor the mass balance of the AIS and to improve our knowledge of the interconnected systems of the cryosphere, atmosphere, ocean, and solid Earth in Antarctica. Uncertainties in estimating ice discharge and consequently AIS's net mass balance and contributions to the global sea-level rise are largely rooted in our limited knowledge on bed topography in the coastal zones (Intergovernmental Panel On Climate Change (IPCC), 2022). Mass loss from the AIS will alter global ocean and atmospheric circulation, which could affect ecosystems elsewhere so that the impact of the Antarctic mass loss is not just a matter of sea-level rise (e.g., Li et al., 2023).

This article examines the coastal zone of the AIS, where this vast ice mass meets and interacts with the Southern Ocean and warmer air masses (Figure 1). The complex inter-connected system in the Antarctic coastal zone largely controls mass loss from Antarctica and will significantly affect ongoing and future sea-level rise in the coming centuries. We first review the physical systems in the Antarctic coastal zone (Section 2) and the methods available to investigate them (Section 3). Then we present new ensemble analyses of existing data (Section 4). In Section 4, we show that bed topography data in the Antarctic coastal zone remain very sparse and contribute largely to the uncertainty of the ice-discharge flux, and existing models project highly variable grounding-line locations by 2100. A case study is also presented to estimate the data density required to develop a bed topography map to a targeted uncertainty. Based on these analyses, we define a new flux gate – a cross-sectional boundary across which ice flow flux is measured by integrating ice velocity and thickness – to carry out new bed topography surveys and estimate ice-discharge flux. Finally, we identify outstanding science priorities in the coastal zones and propose completely-circum-Antarctic surveys at least along three rings around Antarctica (Section 5 and illustrated in Figure 13). The first, the primary ring, follows the new flux gate, in the vicinity of the simplified current grounding line. Its goal is to deliver a precise estimate of the current ice-discharge flux, thereby improving the accuracy of Antarctic contributions to sea-level rise. The second, the seaward ring, is over the ice shelves, also over ice rises and rumples, key components to the stability of the ice shelves. This ring will document present-day ice-shelf mass balance and map seabed topography beneath the shelves. The third, the landward ring, is landward within about 50 km from the current grounding line. Its purpose is to reveal bed topography in the vicinity of the future grounding line, which is critical for modeling present-day ice dynamics and projecting future changes. The RINGS concept emphasizes the pan-Antarctic coverage but only three RINGS are inadequate to address these scientific questions in full. Dense surveys at various regions in Antarctica need to be well coordinated so that no data gaps are left after these campaigns.

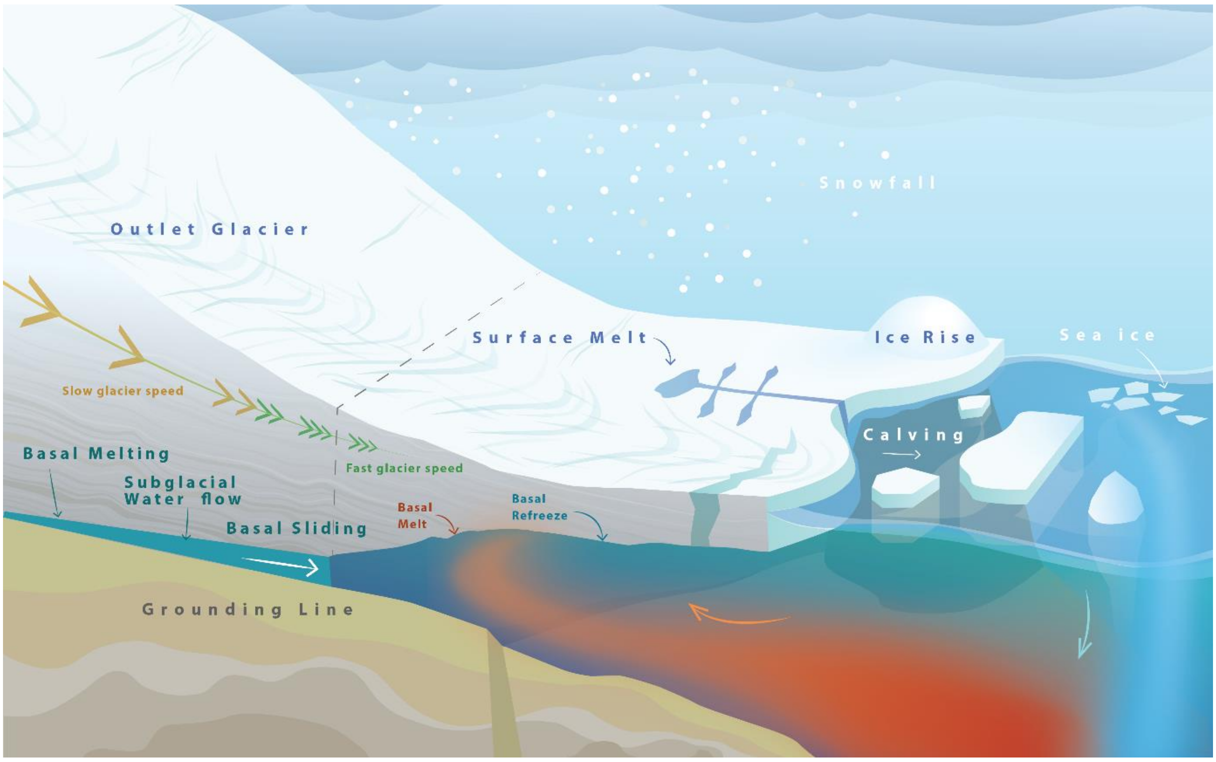

Figure 1: Schematic showing key elements and processes of the physical processes in the coastal zones of Antarctica. The Antarctic Ice Sheet (AIS) includes fast-flowing outlet glaciers that often have significant basal sliding associated with basal meltwater supplied from inland and local basal melt. Warm seawater can access the vicinity of the grounding line where the grounded AIS reaches floatation. In several places in Antarctica, surface melt causes meltwater runoff and even drained directly into the ocean at the calving front. Sub-ice-shelf oceanic melt and calving are the main mechanisms for ice-shelf mass loss. Ice shelves and locally-grounded ice rises give buttressing to stabilize the grounding line position and ice-discharge flux. Iceberg and sea-ice distributions vary largely both in space and time. All of these processes compensate the mass input to the AIS as snowfall and their balance determines the net mass balance of the ice sheet. Subglacial geology is an important factor to determine fundamental characteristics of the ice flow. Figure 13 serves as a companion to illustrate how these physical processes can be studied in practice.

All abbreviations used in this article are listed in Appendix Table A1. Numerous location names are mentioned in this article, and the Composite Gazetteer of Antarctica (CGA), developed and maintained by the Scientific Committee on Antarctic Research (SCAR)'s Standing Committee on Antarctica Geographic Information (SCAGI), is a valuable resource for identifying these locations. The CGA is accessible online at https://data.aad.gov.au/aadc/gaz/scar/ (or directly via the name-based query page at https://data.aad.gov.au/aadc/gaz/scar/search.cfm) and is also included in the standalone GIS data package Quantarctica, which covers Antarctica, the Southern Ocean, and sub-Antarctic islands (Matsuoka et al., 2021). Quantarctica can be downloaded from https://www.npolar.no/quantarctica/ and requires QGIS as its base software environment (https://qgis.org/).

2. Physical processes in the coastal zones of Antarctica

Ice, ocean, atmosphere, and solid Earth meet in the coastal regions of Antarctica, where their interactions produce complex, interconnected behavior of the AIS, Southern Ocean, and ultimately elsewhere in the planet through global circulations of the oceans and atmosphere. Here we review this complex system with an emphasis on the stability of coastal regions, defined as the persistence of their physical state over time, including (but not limited to) grounding line positions, ocean stratification, and atmospheric conditions.

2.1 Ice-sheet mass balance

The rate of change in ice-sheet mass, the ice sheet mass balance, is the difference between gains and losses of all water, solid and liquid, on the ice sheet. A wide variety of processes can alter the ice-sheet mass. Mass inputs (i.e., positive contributions) include snowfall, rainfall, and freeze-on under the base of the AIS. Mass outputs (i.e., negative contributions) include ice-flow discharge into the oceans across the grounding line, melting from the ice-sheet base, and runoff of meltwater from the surface as well as sublimation and erosion from the ice-sheet surface. If the mass transfers associated with all these processes do not sum to zero, then the ice sheet is in a state of imbalance. The net mass balance of an ice sheet is an essential climate variable because it is (i) a key indicator of the ice-sheet stability; (ii) a direct measure of the ice sheet contribution to global sea-level change; and (iii) a critical boundary condition for models that predict ice-sheet evolution (Dirscherl et al., 2020; Edwards et al., 2021; Shepherd & Nowicki, 2017). Because of (ii), we define the ice-sheet mass balance excluding ice shelves here. Mass balance of the ice shelves can be defined including ice discharge from the AIS as an input and calving as an output, whereas ice-ocean interactions at the base of the ice shelves can be either input or output terms (Section 2.7.2). Mass balance of the ice shelves largely controls the location of the grounding line and ice discharge through the grounding line (Section 2.8.2). Overall, knowledge of Antarctic ice-sheet and ice-shelf mass balance is therefore of considerable importance to society.

However, the AIS lies in a remote, extensive, and inhospitable region, making it difficult to determine its mass balance using in situ measurements alone. To overcome this, a range of satellite-based techniques have been developed over recent decades to quantify fluctuations in ice-sheet mass (Bamber et al., 2018; Shepherd et al., 2012). A significant ice-sheet imbalance has been observed throughout the satellite era, and the processes that control this mass loss are also identified using satellite measurements including the acceleration of ice streams and glaciers (e.g., Gardner et al., 2018; Rignot et al., 2004) and to a lesser extent fluctuations in the rate of surface melting (e.g., Bell et al., 2018; Orr et al., 2023a).

2.1.1 Methods for measuring or inferring ice-sheet mass balance

Ice-sheet mass balance is determined using measurements of mass input and output terms individually (termed the input-output method or budget method; Rignot & Thomas, 2002; Rignot et al., 2008), elevation changes (Wingham et al., 1998), and changes in gravitational attraction (Velicogna & Wahr, 2006). Except for ice thicknesses, these variables are derived from spaceborne sensors. The methods tend to agree on average when applied to continental-scale ice masses, but in the variable environments found in the coastal zone, one method can work significantly better than the others in a given region (Otosaka et al., 2023).

The input-output method compares net estimates of the ice-sheet surface mass balance (SMB; Section 2.4.2) with estimates of ice-flow discharge computed from measurements of the ice speed and thickness at the ice-sheet margin (Section 2.2). This method relies on sparse ice thickness data (Matsuoka et al., 2022) and SMB estimates which are often derived using regional climate models (RCM, e.g., Agosta et al., 2019; Mottram et al., 2021; van Wessem et al., 2018). This method can be used back to 1979 when satellite measurements of flow speed started (Rignot et al., 2019).

The ice-sheet volume-change method is based on measurements of the surface elevation change as determined from satellite altimetry using either radar (ERS-1/2, ENVISat, CryoSat-2) or laser (ICESat, ICESat-2) sensors (e.g., Davis et al., 2005; Nilsson et al., 2022; Pritchard et al., 2009; Schröder et al., 2019; Wingham et al., 1998), which date back to the 1980s. The record can be extended back to 1978 using Seasat satellite, although the accuracy is lower and geographical coverage is limited for areas north of 72°S. The altimetry method provides the highest spatial (<10^2 km^2) and temporal (<monthly) sampling (Section 3.7.1), but the absolute accuracy is dependent on the assumptions of underlying mechanisms responsible for the surface elevation changes (e.g., Shepherd et al., 2019; Smith et al., 2020; Sørensen et al., 2011). Altimeters measure the integrated elevation change arising from SMB processes and ice dynamics processes, but also those resulting from firn processes and from the solid Earth visco-elastic response, which are not associated with an ice-mass change. For example, if the mechanism involves surface processes, specifically the amount of snowfall, then one must assume a firn density (~300–500 kg m^{-3}) to account for firn air content and convert elevation changes to the mass changes (e.g., Huss, 2013). The near-surface firn densities come either from a simple model that partitions the ice sheet into areas of ablation and accumulation, or by modeling with a spatially and time-dependent firn density (e.g., Gardner et al., 2022; Hansen et al., 2021; Helsen et al., 2008; Ligtenberg et al., 2011; Medley et al., 2022). However, there are only sparse in-situ measurements that can be used for calibration and validation of these model results. The mechanism of the elevation changes can also come from ice dynamics, specifically thinning or thickening of the solid ice column. The solid ice density (917 kg m^{-3}) is used for this elevation-to-mass conversion. As both mechanisms can contribute to the observed total elevation changes, some uncertainty arises from estimating the fractional contributions from each (e.g., Hansen et al., 2021).

The gravimetric method is based on satellite measurements of regional changes in Earth's gravitational field due to ice-sheet mass changes (e.g., Luthcke et al., 2006; Velicogna et al., 2020; Velicogna & Wahr, 2006). Such measurements began in 2002. The technique provides high temporal (monthly) sampling and moderate (10^5 km^2) spatial resolution, but is limited by the accuracy of the model-based corrections for glacial isostatic adjustment (GIA, Section 2.6.1) and mass trends occurring elsewhere in the climate system. GIA is a combined effect of the solid Earth viscoelastic response to the redistribution of past ice masses since the last deglaciation and the solid Earth elastic response to contemporary mass loading (Whitehouse, 2018). Gravitational signals caused by GIA are of the same order of magnitude as the signals of ice mass change (Caron & Ivins, 2020), so that understanding and accounting for the GIA effect is a critical component of the gravimetric method. In addition to this, signal leakage from near- and far-field processes such as ocean mass variability and land hydrology need to be considered (Velicogna & Wahr, 2013).

These three methods have different spatial and temporal resolutions, and distinct sensitivities for various conditions. Therefore, it is crucial to reconcile these results to have the best possible estimate. Also, the input-output method gives most explicit estimates on the roles of SMB and ice dynamics responsible for observed net mass balance in individual drainage basins.

2.1.2 Contemporary mass balance

Measurements have shown that ice losses from Antarctica have increased from 1979–2017 (Rignot et al., 2019). This loss is driven by accelerated ice discharge in West Antarctica (Mouginot et al., 2014), where glaciers of the Amundsen Sea basin experienced grounding-line retreat (Joughin, 2003; Rignot et al., 2014) accompanied by speed-up and dynamic thinning up to several hundreds of kilometres inland from the grounding line (Konrad et al., 2017). These rapid changes highlight the vulnerability of the region around the Amundsen Sea (Joughin et al., 2014), a region prone to marine ice sheet instability (MISI; Section 2.8.4) as it is grounded well below sea level and parts of its bed deepen inland (Schoof, 2007). Glaciers in the neighboring Bellingshausen Sea basin and in the Getz region are also in dynamical imbalance (Christie et al., 2016; Gardner et al., 2018; Selley et al., 2021). Showing the opposite trend, the Kamb Ice Stream and neighboring ice streams along the Siple Coast have a positive mass balance primarily due to slowdown of the ice streams with persistent SMB (Joughin & Tulaczyk, 2002; Retzlaff & Bentley, 1993). On the Antarctic Peninsula, glaciers accelerated and thinned after the disintegration of the Larsen A and Prince-Gustav ice shelves in 1995 and Larsen B Ice Shelf in 2002 (Berthier et al., 2012; Rignot et al., 2004; Rott et al., 2014, 2018; Seehaus et al., 2015) with a rate of mass loss rising from 7 ± 11 Gt yr^{-1} in 1992–1996 to 20 ± 11 Gt yr^{-1} in 2002–2006 (Otosaka et al., 2023). The mass loss rate, however, has declined in the following 20 years since the abrupt acceleration that followed the disintegration of the ice shelves, although flow speed of these tributary glaciers is still 26% faster than before the ice-shelf collapses (Rott et al., 2018; Seehaus et al., 2018). Finally, East Antarctica has largely remained in a state of mass balance over the satellite record, with two exceptions. One is Wilkes Land where Totten Glacier’s grounding line retreated by 1–3 km between 1996 and 2013 (Li et al., 2015), associated with ice dynamic thinning (Khazendar et al., 2013; Shepherd et al., 2019). The other is Denman Glacier, which has accelerated by 17% since the 1970s following grounding line retreat largely originated from ice tongue thinning and unpinning (Miles et al., 2021; Rignot et al., 2019).

The acceleration in Antarctica’s net ice losses has been identified from all three mass balance records of altimetry, gravimetry, and the input-output method (The IMBIE team, 2018). When compared over common spatial and temporal domains (Figure 2), estimates from all three techniques are in close agreement over both West Antarctica and the Antarctic Peninsula with a standard deviation in their estimated rates of mass change of less than 20 Gt yr^{-1} (Otosaka et al., 2023). The largest disagreement between the three techniques occurs in East Antarctica between 2002 and 2019. Here the gravimetry method records a mass gain of 52 ± 24 Gt yr^{-1} whereas the input-output method instead records a mass loss of the same magnitude (-53 ± 23 Gt yr^{-1}, (Otosaka et al., 2023)). As 360-Gt mass loss is equivalent to 1-mm increase of sea level, this mass loss corresponds to 2.5 mm sea level rise in the 17 years. The East Antarctic Ice Sheet (EAIS) covers two thirds of the Antarctic continent but counts fewer in-situ measurements than the rest of the continent, making it difficult to evaluate satellite products or models of SMB (Section 2.4.2) and GIA (Section 2.6.1).

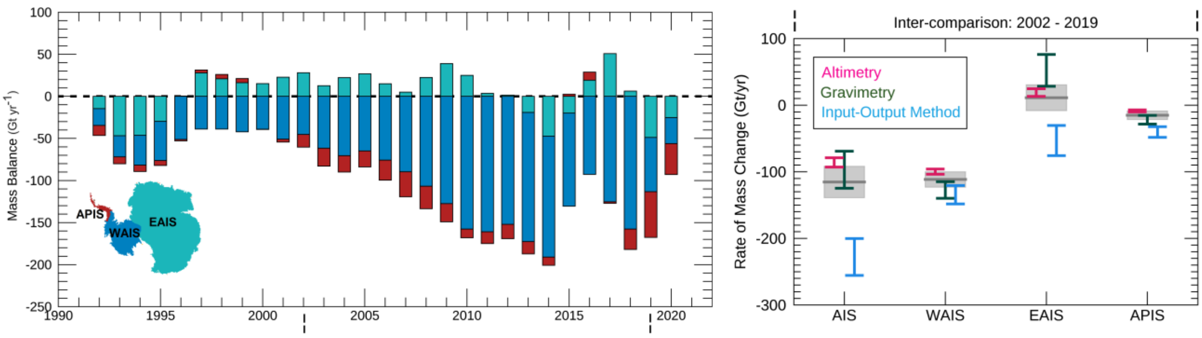

Figure 2: Recent mass balance of the AIS in three regions of the West Antarctic Ice Sheet (WAIS), East Antarctic Ice Sheet (EAIS), and Antarctic Peninsula (AP) compiled by Ice Sheet Mass Balance Inter-Comparison Exercise (IMBIE, Otosaka et al., 2023). (a) Annual mass balance from 1992 to 2020. (b) Inter-comparison of the rate of mass change between

2002 and 2019 derived with the altimetry, gravity, and input-output methods. Gray line and box show IMBIE's reconciled value and uncertainty.

To better understand differences between ice-sheet mass-balance estimates, and reduce uncertainties in Antarctica's mass balance, it is essential to have comprehensive and consistently high-resolution ice-thickness measurements around the coastal region of Antarctica, as well as high-resolution firn stratigraphy observations elsewhere in Antarctica (Section 5). The former is needed to reduce uncertainties in ice-flow discharge calculations. The latter is needed to investigate the impact of uncertainties of modeled SMB and GIA on ice-sheet mass balance (e.g., Seroussi et al., 2011; Van de Wal et al., 2023). Continued efforts towards understanding differences between the techniques will help reduce uncertainties in Antarctica's contribution to global mean sea level. Satellite missions are currently being planned to continue these efforts (Section 3.7) but ensuring the continuity of the satellite record over the polar regions is critical to predict how climate change will affect Antarctica's future. Such work also requires a community effort to collect airborne observations around Antarctica that can be used to test existing satellite measurements and thus help to improve current estimates of ice-sheet mass balance. Airborne surveys provide observational constraints on parameters that cannot be measured from space to date yet are essential for accurately measuring ice discharge and for simulating Antarctica's future in a warmer climate. Measuring ice thicknesses in the zone near the grounding line all around Antarctica and measuring SMB elsewhere in Antarctica will thus reduce uncertainties in ice-discharge measurements and help reconcile the altimetry, gravimetry, and input-output method estimates of Antarctica's mass balance.

2.1.3 Future mass balance

Projections of Antarctica's contribution to sea-level rise this century and beyond are needed to inform appropriate policy to mitigate the effects of climate change (Fox-Kemper et al., 2021). In addition, observations of ice-sheet mass balance and conditions at the ice-sheet margins, such as bed topography, oceanic properties, and ice-shelf melt rates, are needed to reduce uncertainties and improve model representations of the complex interactions in the coastal zone. As the data here are sparse both spatially (e.g., Dutrieux et al., 2014; Stanton et al., 2013) and temporally (Barker et al., 2020; Dutrieux et al., 2014; Morlighem et al., 2020), it is essential to develop model parameterizations of key processes (Jourdain et al., 2020; Levermann et al., 2020; Nowicki et al., 2020; Seroussi et al., 2020).

For example, consider the projections from the IPCC assessment reports. The median range of the latest IPCC AR6 projections of AIS mass change track recent satellite observations (Fox-Kemper et al., 2021; Otosaka et al., 2023), whereas the observations were in the high-end range of the projection in the previous AR5 (Church et al., 2013; Intergovernmental Panel on Climate Change, 2014; Slater et al., 2020). This is in part due to significant progress in several areas: (1) having a better understanding of the ice-shelf and grounding-line evolution (Cornford et al., 2020; Durand et al., 2009; Levermann et al., 2020; Seroussi et al., 2020), (2) improved RCMs (Agosta et al., 2019; Mottram et al., 2021; van Wessem et al., 2018), (3) better uncertainty quantification (Edwards et al., 2021; Levermann et al., 2020), and (4) the use of observations to calibrate Antarctica's ice dynamic response (Edwards et al., 2021; Nias et al., 2019; Ritz et al., 2015; Wernecke et al., 2020). If ice losses from the AIS were to continue on this median range trajectory from AR6, they would raise global sea levels to between 103 and 115 mm by 2100 (Figure 3). However, AR6 shows that uncertainties in modeling Antarctica's response to global climate change contribute disproportionately more to the uncertainties in projections of global sea level rise. For the year 2100, the ensemble median Antarctic contribution to global mean sea level across five emission scenarios is about 109 mm, with a wide uncertainty range: the 10th percentile is about 13 mm and the 90th percentile about 369 mm (Figure 3). This spread is driven primarily by uncertainties in modelling Antarctica's response to climate change, rather than by differences among emission scenarios. Current models show no consistent scenario dependence as they must balance competing processes in the ocean and atmosphere (Barthel et al., 2020; Edwards et al., 2021; Golledge et al., 2019). Therefore, continued progress in modeling is required, particularly by improving our understanding in (1) ice–ocean interactions, including coupled ice–ocean models (Pattyn et al., 2017; Seroussi et al., 2017); (2) observational and model descriptions of ice-shelf basal melting (Jourdain et al., 2020; R. Reese et al., 2020) and potential ice-shelf disintegration (Gilbert & Kittel, 2021; Trusel et al., 2015); (3) marine ice-sheet instability (Cornford et al., 2020; Robel et al., 2019; Sun et al., 2020); and (4) marine ice-cliff instability (Clerc et al., 2019; DeConto & Pollard, 2016; Edwards et al., 2019), all of which are discussed further in Sections 2.7 and 2.8. These efforts would greatly benefit from new measurements of subglacial topography and of the ice-shelf cavity geometry via increased knowledge of the seabed topography at the ice-sheet margins.

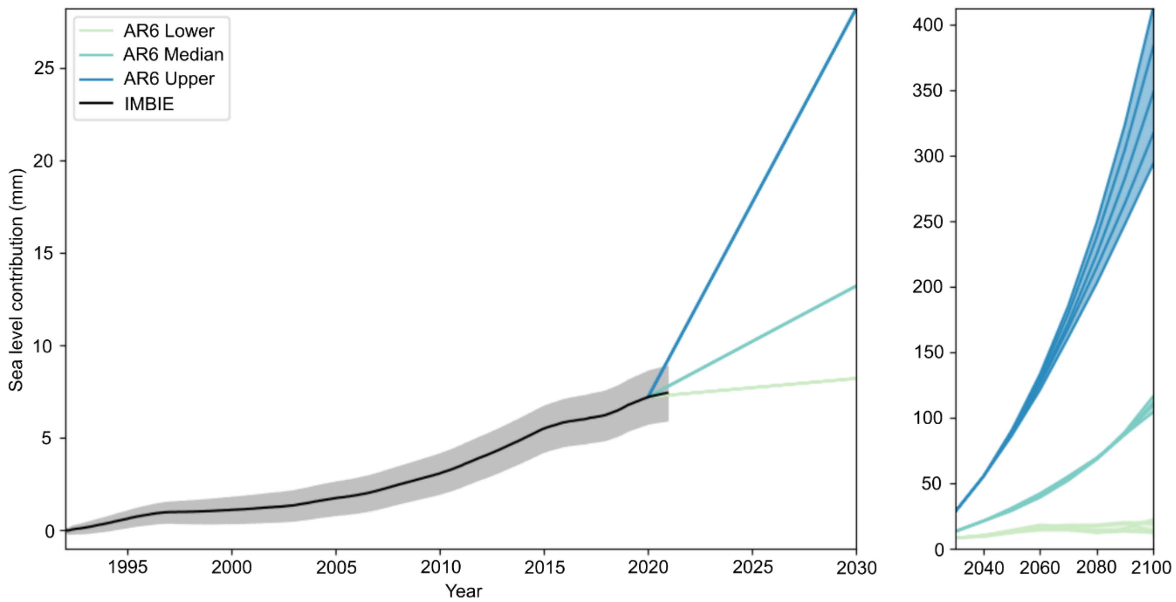

Figure 3: Comparison of observed Antarctic contributions to the sea level from 1993 to 2022 compiled by IMBIE (Otosaka et al., 2023) and modeled future Antarctic contributions compiled by the IPCC AR6 from 2020 to 2100 (Fox-Kemper et al., 2021). For observed data, the solid curve and gray stripes show reconciled mean and standard deviation. For projections, shown are 10th percentile (309–428 mm by 2100), median (103–115 mm), and 90th percentile (8–17 mm) of the projected Antarctic contributions for five emission scenarios: low, intermediate, and high SSP scenarios (SSP1-1.9, SSP1-2.6, SSP2-4.5, SSP3-7.0 and SSP5-8.5). Despite the difference between the emission scenarios, the 10th percentile, median and 90th percentile from all emission scenarios display three distinct clusters for each. This demonstrates that the primary source of projection uncertainty stems from the variability in the modeled physical systems of the AIS and our limited knowledge of the AIS, rather than from uncertainties related to emissions.

2.2 Ice-flow discharge

Amongst ice-loss processes, ice-flow discharge across the margin of the AIS is by far the largest. Changes in ice discharge are driven by changes in the stress balance near the grounding line, where the ice sheet lifts off its bed to float on the ocean. A slow change in discharge typically results from changes in the driving stress caused by changes in ice thickness and surface slope. More rapid changes in discharge can be attributed to changes in ice-shelf buttressing, changes in basal friction, or grounding-line migration. These processes are discussed further in Section 2.8.

Current estimates of ice discharge are derived by combining satellite-measured ice surface velocity with measured or modelled ice thickness across pre-defined flux gates near the grounding line. The flux gates are defined as a cross-sectional boundary across which ice flow flux is measured by integrating ice velocity and thickness. Surface velocity is now continuously monitored using repeat-pass satellite imagery from around Antarctica, taking about a year for each complete data coverage (e.g., Gardner et al., 2018; Mouginot et al., 2017). Usually, the surface velocity is assumed to equal the depth-averaged velocity, because most fast-flowing glaciers have weak basal shear stress due to either sliding or till deformation. Gardner et al. (2018) argue that this introduces a small positive bias in discharge estimates, and other studies neglect it entirely when evaluating relative differences of discharge time series (e.g., Miles et al., 2022). Also some recent studies show that crystal anisotropy of the ice sheet may yield a deviation from this assumption (McCormack, Warner, et al., 2022; Rathmann & Lilien, 2022). For the ice-thickness values, due to the often sparse and highly variable measurements near the grounding line (Section 4.3), Gardner et al. (2018) used measured ice-thickness profiles even though they may be located distant from the grounding line, whereas Rignot et al. (2019) interpolated ice thickness closer to the grounding line from gridded ice-thickness products. For the former method, they corrected for the impact of SMB and ice-dynamical thickness changes between the flux gate and the grounding line. This approach has less uncertainty in ice thickness, yet requires additional correction data from RCMs (SMB) and satellite altimetry (thickness changes), which have their own inherent uncertainties (Verjans et al., 2021).

Based on these methods, Gardner et al. (2018) estimated a total ice discharge from Antarctica in 2015 (excluding ice rises and islands) of 1929 Gt yr^{-1}, whereas Rignot et al. (2019) obtained 2229 Gt yr^{-1} for the period 2009 to 2017, and 2307 Gt yr^{-1} for year 2015. The large difference of 300 Gt yr^{-1} (or 378 Gt yr^{-1} for the year 2015) or about 15% (18% for 2015) of the total discharge, cannot be explained by differences in the satellite-derived surface velocity datasets because both approaches rely on similar input data in this regard. The discrepancy therefore is more likely linked to the methods, particularly pertaining to the derived ice thickness near the grounding line. To help understand the discrepancy, we examine the year 2015 discharge values by region, using the 27 drainage basins defined by Zwally et al. (2002). The results in Figure 4 show that the discharge estimates of Rignot et al. (2019) are consistently higher than those of Gardner et al. (2018), with no clear spatial pattern. The consistency suggests a systematic difference related to the choice of flux gates and input ice thickness data. For instance, one main difference between the methods is that Rignot et al. (2019) rely extensively on hydrostatically inferred ice thickness from satellite altimetry or digital elevation models (DEMs) over ice shelves (~39% of the grounding line). In addition, Rignot et al. (2019) use modeled SMB as a proxy for discharge in drainage basins with poor or missing data for ice thickness and surface velocity (~34 % of grounding line). In contrast, Gardner et al. (2018) use actual ice-thickness measurements for 95% of their flux gates which is a clear improvement to Depoorter et al. (2013) who at that time managed 69%. However, it requires additional corrections for SMB and ice-dynamical thickness changes between a given flux gate and the grounding line (302 and 16 Gt yr^{-1}, respectively). Thus, ultimately the 300 Gt yr^{-1} difference arises from a severe lack of ice-thickness measurements along the grounding line. This motivates an internationally collaborated effort to provide the missing bed topography data in the vicinity of the grounding line (Section 5.1). Miles et al (2022) analyzed discharge from individual drainage basins and concluded that discharge from glaciers within some regions can change similarly, whereas in other locations neighboring catchments can behave very differently. This emphasizes the need to determine topography at the catchment scale if we are to understand ice-flow discharge.

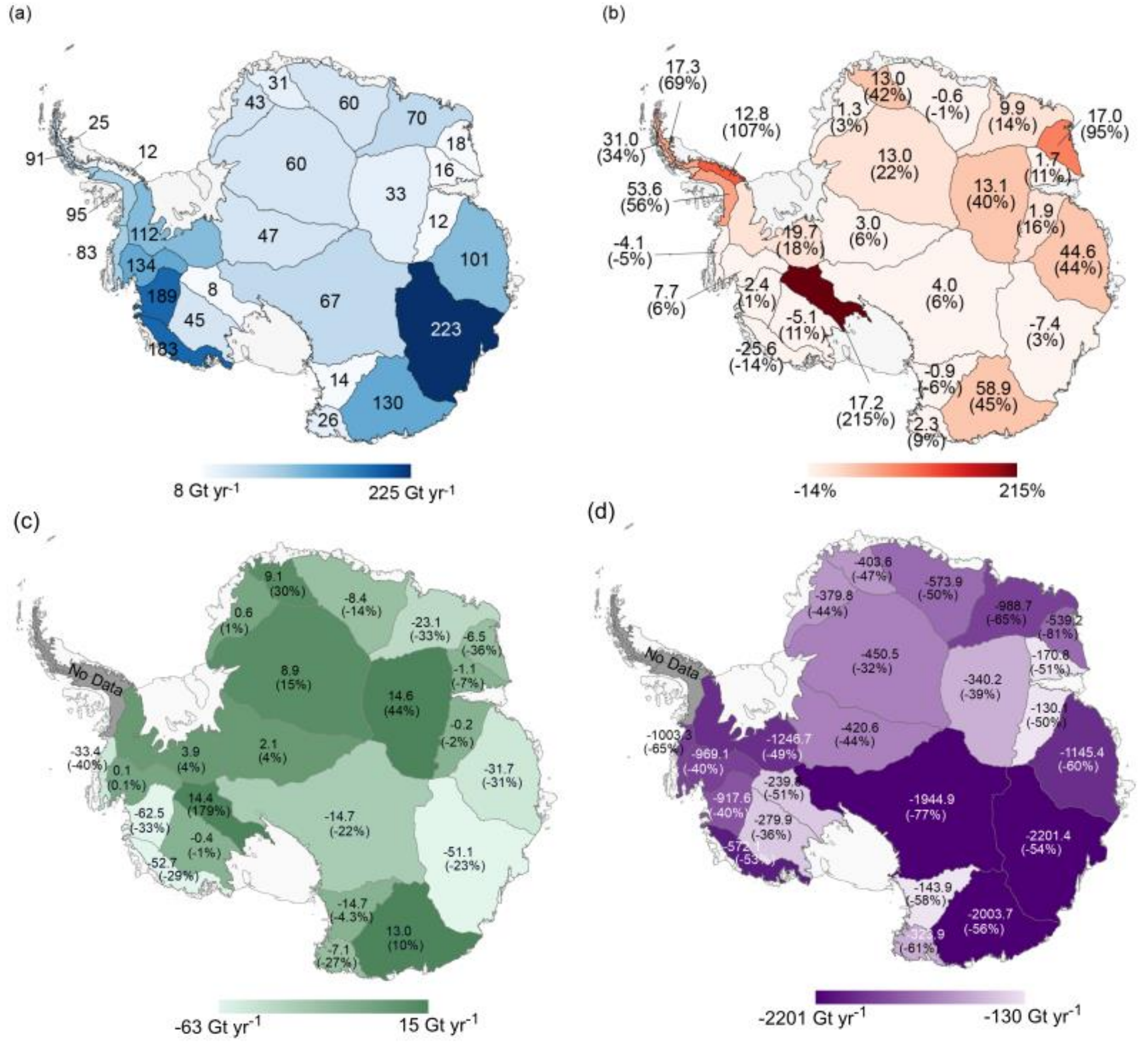

Figure 4: Comparison of recent ice-discharge estimates for 27 drainage basins of the AIS. (a) Estimates for the year 2015 based on surface velocities from Landsat-8 across flux gates set close to available radar-data locations (Gardner et al., 2018). (b) Differences between Gardner et al. (2018) and Rignot et al. (2019) as excesses beyond the estimates by Gardner et al. (2018), both in values and fractions in percentage relative to Gardner et al. (2018). Rignot et al. (2018) provide time series of ice discharge based on measured surface velocity and estimated ice thickness at the grounding line, and year 2015 is reported as Supplementary Information for 68 basins which are here consolidated into the 27 basins defined by Zwally et al. (2002) and used by Gardner et al. (2018), although their boundaries do not exactly match. (c) Same as (b) but showing the differences between

Gardner et al. (2018) and Miles et al. (2022) for the year 2015. (d) Differences between Rignot et al. (2019) and Miles et al. (2022) as excesses beyond the estimates by Rignot et al. (2019), both in values and fractions in percentage relative to Rignot et al. (2019) for the 18-year period between 1999 and 2017, the period that both studies cover. The values are converted to the unit of Gt yr^{-1} for comparison.

2.3 Subglacial water discharge

In addition to ice-flow discharge, surface and basal meltwater runoff can also contribute to the total mass balance of the ice sheets. Unlike the Greenland Ice Sheet, surface meltwater runoff in Antarctica is small (Section 2.4.3). However, the AIS experiences basal melt due to several factors, specifically, the high overburden pressure causing the melt-point reduction, geothermal heat flow, frictional heating at the ice–solid Earth interface, and internal heating from ice deformation. In all, the base of the AIS melts around 63 ± 4 Gt yr^{-1} (Gardner et al., 2018; Van Liefferinge & Pattyn, 2013). However, it remains unknown how much basal meltwater is discharged to the ocean and there is evidence of meltwater accretion at the base of the AIS (Bell et al., 2011).

Subglacial water is routed either through distributed or organized networks from the interior towards the coast. In organized networks, subglacial water is routed along subglacial conduits (Dow et al., 2022). At the grounding line, these localized injections of fresh water can lead to significantly enhanced and localized basal melting that forms ice-shelf channels further seawards (Drews et al., 2017; Le Brocq et al., 2013; Zhou et al., 2025). This has been observed on a pan-Antarctic scale (Alley et al., 2016). Other settings are better described as estuaries (Horgan et al., 2013), meaning a more diffuse zone where ocean water and subglacial meltwater mix across a wider spatial range. This concept challenges the traditional definition of the grounding line, and suggests that ocean-induced melting may also have a more spatially diffuse character, with implications for grounding-line migration. Mechanisms of how ocean-water can access locations upstream of the grounding line are still being discussed, and potential candidates are flexural bulging (Walker et al., 2013) or elastic peeling (Warburton et al., 2020). Radar surveys landward of the grounding line will provide critical information about the spatial distribution of subglacial water, providing a way forward in order to understand relevant processes around grounding-line migration (Section 5.1).

Independent of the specific form of subglacial water flow, subglacial discharge into ice-shelf cavities modifies ocean-induced melting through buoyant plume dynamics (Gourmelen et al., 2017, 2025; Nakayama, Cai, et al., 2021; Wei et al., 2020; Xu et al., 2013). For the Greenland Ice Sheet, observations and ice-sheet modelling show that basal meltwater discharge from the grounded ice sheet contributes almost 10% to the ice-sheet net mass loss (Karlsson et al., 2021). For Antarctica, subglacial melt is modeled (Van Liefferinge & Pattyn, 2013), but neither observational evidence nor estimates of subglacial water discharge to the ocean are available (Ashmore & Bingham, 2014).

Direct observation of freshwater melt from the base of the ice sheet is challenging, but Jackson & Straneo (2016) analyzed salt budgets of seawater sampled with mooring in a fjord in Greenland to differentiate between meltwater sources, specifically those originating from subglacial melt or ocean-driven ice-shelf melt. Similar observations around Antarctica will aid in determining the volume and variability of subglacial discharge into ice-shelf cavities from the ice-sheet base. Another approach is to track changes in water levels of subglacial lakes using satellite altimetry or imagery. For instance, Smith et al., (2017) observed sudden and simultaneous drops in water level in subglacial lakes of the Thwaites Glacier in West

Antarctica, resulting in the release of approximately 5 Gt of additional freshwater into the ocean. Continuous observation of water levels in subglacial lakes can provide valuable insights to the anomalous variations in subglacial discharge. Further constraints on the evolution and variability in the subglacial hydrology system and impact on ice-shelf melting will be essential for estimating and projecting mass loss (Lepp et al., 2022, Wilson et al., 2025).

2.4 Atmospheric processes

2.4.1 Antarctic climate

The AIS is geographically isolated from other continents by the Southern Ocean, but the Antarctic climate is strongly coupled with climate systems in the mid and low latitudes (e.g., Dalaiden et al., 2022; Orr et al., 2023a). One significant manifestation of these latitudinal teleconnections is our growing appreciation of the influence of north-south migrations of southern-hemisphere westerly winds, which are commonly investigated by a proxy termed the Southern annular mode (SAM). SAM is classified as being in a positive phase when the westerlies are closer to Antarctica, and in a negative phase when they have moved north (Marshall, 2003) and these oscillations have been linked to oscillations in the ice-dynamic behaviour of coastal West Antarctica (Christie et al., 2023; Ding et al., 2011; Turner, Orr, et al., 2017). In addition, Pacific–South American patterns (PSA) are climate modes in the mid-to-high southern latitudes that affect the El Niño–Southern Oscillation (ENSO), particularly in the southeast Pacific and southwest Atlantic (Irving & Simmonds, 2016). Recent statistical analysis found that variations in SAM and PSA can explain much of the spatial patterns in SMB at annual-to-decadal timescales in Antarctic climate (Fogt & Marshall, 2020). For example, SAM is strongly related to the position of the Amundsen Sea Low (Christie et al., 2023; Turner et al., 2013) and affects the Antarctic Circumpolar Current, which in turn affects sea-ice growth (Crosta et al., 2021) as well as the ocean circulation within ice-shelf cavities (Verfaillie et al., 2022).

Kim et al. (2020) and Hansen et al. (2021) found SAM to correlate strongly with SMB, but in opposite ways in different basins of the ice sheet. For instance, a positive SAM correlates with an increase in SMB in the Weddell and Bellingshausen basins, while a negative SAM is linked to an increase in SMB in the Ross and Amundsen Sea basins, creating a distinct bipolar pattern over Antarctica. A recent study by Orr et al. (2023a) shows that the same variability applies to surface melt over ice shelves. For instance, in East Antarctica, surface melt on ice shelves is associated with a negative SAM and an increase in coastal easterlies. In West Antarctica, surface melt on ice shelves tends to occur with the central Pacific El Niño pattern and a strong anticyclone over the high-latitude South Pacific. Christie et al. (2023) have further shown that the pace, magnitude and extent of ice destabilization around Antarctica, as indicated by variations in grounding-line retreat, vary by location, with the Amundsen Sea coastline most sensitive to interdecadal variations in SAM. These analyses imply that it is essential to understand the wider regional- and hemispheric-scale circulation patterns when interpreting climate model outputs. A similar requirement also holds when interpreting in situ data such as firn cores or SMB stake measurements that, unless stretching over several decades of observation, may be influenced by decadal or multidecadal scale variability.

Synthesis of shallow ice/firn core data over the AIS show an overall increase in SMB over the ice sheet during the last 200 years (Medley & Thomas, 2019). The trend differs by basin yet overall, it correlates strongly with SAM. Moreover, the amount of increase in SMB exceeds the range of its annual variability, suggesting that climate change is already measurable in terms of SMB in Antarctica (Medley et al., 2018). After accounting for SAM variability, the same argument applies to similar analyses of the temperature time series in Antarctica, though the strength and trend of the temperature signal vary strongly on a regional basis, partly also due to confounding effects of ozone depletion (Jones et al., 2019; Steig et al., 2009). The increase in SMB has likely mitigated the sea-level rise contribution of the ice sheet by around 1 mm per decade between 1901 and 2000, and up to 2.5 mm per decade since 1979 (Medley & Thomas, 2019), though a brief synthesis emphasizes the problems posed by synoptic variability and inadequate field data in assessing longer-term trend (Gorte et al., 2020).

The recent increase in SMB appears to be due to stronger synoptic-scale events rather than changes in large-scale atmospheric circulation. For example, Dalaiden et al. (2020) argue that an increase in global temperatures, by producing an increase in specific humidity, leads to higher poleward moisture transport (e.g., Seager et al., 2010). These studies, which are based on reanalysis data (assimilation of field and satellite observations using climate models; Section 3.8.3), also found that different processes controlled the multidecadal versus the interannual SMB variabilities. However, it is difficult to extract long-term records from observational data that include both long-term effects and the short-term high-magnitude events such as atmospheric rivers that carry warm and moist air inwards over the deep inland of the AIS (Lenaerts et al., 2013). Another example is that some atmospheric rivers have delivered the annual-mean snowfall in a single event lasting only a few days or weeks (Turner et al., 2019). As a result, SMB averaged over a few years may be easily biased by a few short-term events. Hence, measurements over only a few years can easily be misinterpreted (Gorodetskaya et al., 2014), underscoring the need for paleoclimate evidence of WAIS variability (Fudge et al., 2016; Sproson et al., 2022). An important example is the anomalously high snowfall in Dronning Maud Land that produced almost ten years of accumulation over a single year starting in 2009 (Boening et al., 2012; Gorodetskaya et al., 2013). This example alone demonstrates the importance of maintaining long-term monitoring of atmospheric processes to understand climate variability in Antarctica.

The impact of atmospheric rivers may be modulated with SAM. Wille et al. (2021) found that atmospheric rivers reach deeper inland, most likely when blocking conditions in the Southern Ocean amplify the circumpolar jet. However, different regions in West Antarctica have a different association between atmospheric rivers and SAM: on the Antarctic Peninsula, more atmospheric rivers occur during a positive SAM, whereas the Bellingshausen Sea coastline has more atmospheric rivers during a negative SAM.

Atmospheric rivers have two effects on the Antarctic mass balance. One, they carry moisture and thus can at least locally increase SMB. For example, recent modelling focused on the Amundsen Sea Embayment and Marie Byrd Land has shown that while atmospheric rivers are infrequent (occurring 3% of the time) they account for 11% of precipitation in the form of extreme snowfall events (Maclennan et al., 2023). On the other hand, they promote melt via both sensible heat flux and long-wave-driven fluxes from low moist clouds (e.g., Li et al., 2023). In extreme cases, this can result in meltwater runoff, locally decreasing SMB. The episodic warming associated not only with atmospheric rivers but also Foehn wind events (dry winds descending from high elevations and warming rapidly due to adiabatic processes) over ice shelves can increase surface melt intensity and extent, potentially weakening ice shelves leading to their collapse and subsequent speed up of glaciers feeding into the ice shelves (Rignot et al., 2004; Scambos, 2004). Warm air and strong winds also weakens and breaks up sea ice, yielding a lack of buttressing and exposure to large ocean swells preceding major ice-shelf calving and collapses on the northern Antarctic Peninsula (Wille et al., 2019, 2022). In addition, Wille et al. (2019) find 40% of the meltwater generated across the Ross Ice Shelf and up to 100% of the meltwater in Marie Byrd Land to be associated with atmospheric rivers. One prominent example that illustrates this dual nature of atmospheric rivers is the East Antarctic event of March 2022 where a record-warm temperature occurred at Dome Concordia. At the same time, the MAR regional climate model suggested that the single event had deposited 69 Gt of snow and rain in the interior of the continent (the fourth wettest day in the model record), but the associated weather conditions also led to the break up and loss of the Conger Ice Shelf (Colomb et al., 2022). This dual nature of atmospheric rivers makes it difficult to predict the likely net impact of any future changes in frequency or intensity of atmospheric rivers on overall Antarctic mass balance.

In assessing the Antarctic contribution to sea-level rise, determining the large internal climate variability is a significant challenge. While RCMs can represent local and regional scale processes well, when used for hindcasting and projection they rely on global climate models for their boundary forcing. Compared to the previous CMIP5 models, the CMIP6 generation of general circulation models (GCMs) has better spatial representations of both the atmosphere (Bracegirdle et al., 2020) and the Southern Ocean (Heuzé, 2021). However, there are still substantial biases present in the way models characterize the internal variability around the continent. Gorte et al. (2020) concluded that there was little to no improvement from CMIP5 to CMIP6 in terms of forcing realistic SMB at the present day, implying that downscaling with RCMs is still necessary to produce realistic snowfall patterns across Antarctica. Thus, although improved model resolution and physical parameterizations will help, the importance of long timescales of direct observations (e.g., by firn cores and shallow sounding ice-penetrating radar (IPR) as well as in situ observations; see Section 3.6.3) must be emphasized to understand how this internal variability is represented in SMB records.

2.4.2 Surface mass balance

Surface mass balance (SMB) generally decreases from the coastal regions to the inland, though strong orthographic effects make SMB in the coastal regions highly variable (Figure 5). Such features have been observed with satellites and in-situ methods such as IPR, ice cores and stakes (e.g., Arthern et al., 2006; Eisen et al., 2008). However, given the large size of Antarctica, the currently available number of in situ observations of SMB is too few, and only a small subset of these cover a sufficiently long time series. For example, the collection of observed SMB values in Wang et al. (2021) includes 3579 individual multi-year-averaged observations from stakes, snow pits, ice cores, and ultrasonic sounder measurements, of which 687 are annually resolved from 675 sites (Figure 5c). Wang et al. (2021) also included the dataset with shallow-sounding IPR measurements (often using ground-penetrating radar) that covers an area of 22,025 km^2, which amounts to less than 0.15% of the AIS. In addition, automatic weather stations (AWS) operate continuously at many locations (Figure 5c; Wang et al., 2023), giving another opportunity to estimate SMB as well as providing data on other atmospheric conditions and ice-air interactions. Nevertheless, together with the short coverage of a few years for many of the observations available in SMB and AWS datasets, the current data density leaves large parts of the AIS underrepresented (Favier et al., 2013) and many important areas not covered at all by SMB observations.

Given the paucity of observational data, researchers have used RCMs, forced with a climate reanalysis, to estimate SMB over the AIS (e.g., Agosta et al., 2019; Beaumet et al., 2021; Mottram et al., 2021; van Wessem et al., 2018). For example, Mottram et al. (2021) compiled results of five RCMs to determine the ensemble mean and standard deviation of SMB for the period 1987–2015 over a common ice mask (including ice shelves). The models are COSMO-CLM (Souverijns et al., 2019), HIRHAM5 (Eerola, 2013), MetUM (Walters et al., 2017), MAR v.3.10 (Agosta et al., 2019), and RACMO2.3p2 (van Wessem et al., 2018). The results are plotted in Figure 5. When integrated, the ensemble mean and standard deviation SMB over the ice mask are 2329 ± 684 Gt yr^{-1}, which is dominated by accumulation of snowfall (Lenaerts et al., 2019).

The coastal regions are particularly complex but important for understanding SMB. This is because these narrow coastal regions receive 46% of the total SMB and constitute 60% of its standard deviation, although the ice shelves and grounded ice sheet within 50 km of the grounding line occupy just 23% of the entire ice sheet and ice shelves by area. An additional complexity is that surface melt and runoff estimates are available only for two of the five models mentioned above, partly due to the historical assumption that melt is negligible and mostly refreezes. However, Hansen et al. (2021) find a value of runoff between 100 and 200 Gt yr^{-1} over the grounded ice sheet. Although this is small compared to the total SMB over the AIS, the surface meltwater can nevertheless possibly influence the local ice dynamics if it reaches to the base of the ice sheet (Section 2.4.3).

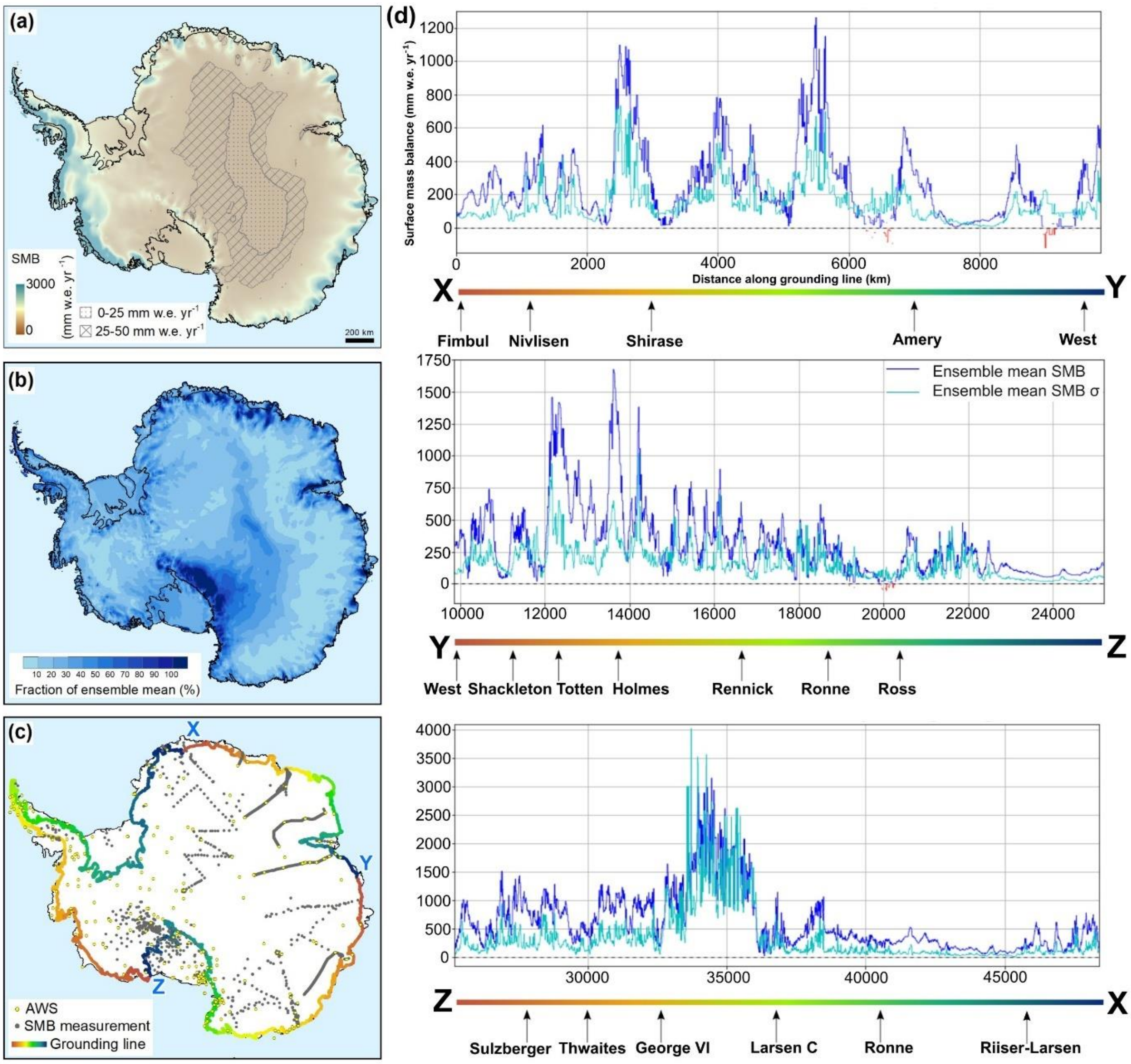

Figure 5: Modelled annual SMB averaged between 1987 and 2015, together with locations of SMB observations and AWS. (a) Ensemble mean of five model results (see Section 2.4.2

for all model names). (b) Ensemble standard deviation of these modeled SMB. These models have variable model-cell sizes (12.5–50 km) so all model results were interpolated to 12.5 km model cells (Mottram et al., 2021). (c) Locations of existing SMB data (grey dots) collected with snow stakes and firn/ice cores (Wang et al., 2021). Location of AWS are shown with yellow dots (Wang et al., 2023). The color code along the grounding line gives a location reference for panels (d). (d) Ensemble mean (blue or red when negative) and standard deviation (green) of SMB at the grounding line. Note that the three panels are not scaled. The ends of these three profiles are shown with the letter X, Y and Z and color bars indicate locations between these XYZ-labeled locations. Major ice shelves are labeled.

While atmospheric circulation drives weather systems that affect SMB at the mesoscale, the height and shape of the ice sheet determines the spatial SMB distribution on the regional-to-local scale. For instance, most of Antarctica's snowfall occurs because the steep coastal topography and sloping ice-sheet margins trigger orographic precipitation. The high SMB values along the East Antarctic coastal zone correlate with local elevated features (Figure 5a). At these locations, SMB can be nearly an order of magnitude larger than their adjacent regions over the lateral scales of several tens of kilometers or less (Figure 5d). The interior and especially the high plateau is, by contrast, famously arid. In addition, cold and thus dense inland air mass flows down to the coast causing strong katabatic winds that can exceed 100 km hr^{-1}. These winds play an important role for large-scale redistribution of snow even deep inland where wind is much weaker compared to the coastal zone (Van Liefferinge et al., 2021) as well as promote sublimation from the surface (Dattler et al., 2019). Strong sublimation and low snow accumulation are also driving factors in the formation of blue ice areas that cover roughly 1% of the continent (Bintanja, 1999).

The comparison study of modeled SMB (Mottram et al., 2021) shows large ensemble standard deviation (Figure 5b), which demonstrates that even when models are forced by the same climate reanalysis they tend to show a spread of around 15–20% in estimates of mean annual SMB (~300–400 Gt yr^{-1}). The study of Mottram et al., (2021) found no convincing trend of model-estimated ensemble SMB over the last 40 years, with no single model replicating observed SMB best in all regions. It is well known within the climate community that the mean of an ensemble of models often performs better than any single model (Christiansen, 2020).

The largest spread in SMB estimates between models occurs over the ice shelves (Mottram et al., 2021), which is also where the largest SMB changes are projected to occur in the future (Gilbert & Kittel, 2021). This spread is also true between models that include nudging schemes to bring the modelled weather closer to that of the driving reanalysis. It suggests that the internal physical schemes and parameterizations within individual models account for the differences. For instance, some studies suggest a crucial role of cloud parameterization (Beaumet et al., 2021; Kittel et al., 2022) as clouds can drive melting via long-wave emissivity towards the surface. In addition, van Wessem et al. (2023) show that snowfall is also important for ice shelf melt as high snowfall acts as a shield to melting in warmer and wetter regions of Antarctica.

Other factors that account for differences in SMB estimates include model resolution and domain size, as well as associated simplification in surface topography and omission of some atmospheric and surface processes. These processes include blowing snow redistribution and sublimation that can be represented with varying levels of complexity in climate models. Sublimation from blowing snow may account for ice loss of

393 ± 196 Gt yr^{-1} based on a dataset developed with the CALIPSO satellite data of snow sublimation and transport during 2006–2016 (Palm et al., 2017). This magnitude equals about ~15% of annual mean total SMB in Antarctica according to the analysis of RCMs (Mottram et al., 2021). Post-depositional wind erosion and drift also complicate the interpretation of in situ observations of SMB and weather (Genthon et al., 2011).

In summary, accurate modeling of SMB and adequate observation for model evaluation are crucial for accurate estimates of net mass balance of the AIS (Section 2.1). High resolution is certainly important for SMB estimates in some regions, particularly in coastal regions with steep slopes and where processes such as Foehn winds need to be resolved to accurately capture melt events. The SMB near the grounding line also affects estimates of ice discharge (Sections 2.2 and 4.5.3).

To learn more about SMB, Lenaerts et al. (2019) and Mottram et al. (2021) are recent review papers in this field.

2.4.3 Surface meltwater and its runoff

Although early versions of RCMs used for Antarctica largely ignored melt and runoff, close examination of satellite data and aerial photographs have revealed widespread surface melt. The melt is most extensive on the ice shelves, yet also occurs on the ice sheet itself (Figure 6; e.g., Arthur et al., 2022; Johnson et al., 2022; Kingslake et al., 2017; Stokes et al., 2019). For example, the collapse of the Larsen B Ice Shelf in 2002 was partly attributed to the effects of surface meltwater ponding (e.g., Scambos, 2004), while the development of surface rivers and estuaries have the potential to minimize the impact of melt (Bell et al., 2017) or to introduce new calving mechanisms (Boghosian et al., 2021). This finding motivated new studies to observe and model these processes, resulting in a number of *in situ* and satellite datasets of surface meltwater (e.g., Jakobs et al., 2020; Trusel et al., 2013). In addition, the air content of the firn layer is a key characteristic controlling its meltwater retention capacity. The ability of firn to soak up meltwater directly influences the amount of excess surface meltwater on Antarctic ice shelf surfaces, determining their risk of meltwater-driven hydrofracturing and collapse (Kuipers Munneke et al., 2014; Lai et al., 2020). As a result, modelling firn and snowpack processes has been a priority for SMB studies in Antarctica (Verjans et al., 2021). Properties of the ice/snow surface also affect radiative properties of the clouds (Hofer et al., 2021; Orr et al., 2023b). The melt events often associated with Foehn winds over ice shelves on the Antarctic Peninsula (e.g., Datta et al., 2022; Turton et al., 2020). For example, a significant surface melt event over the Ross Ice Shelf in January 2016 was attributed to Foehn winds in this region (Zou et al., 2021a, 2021b).

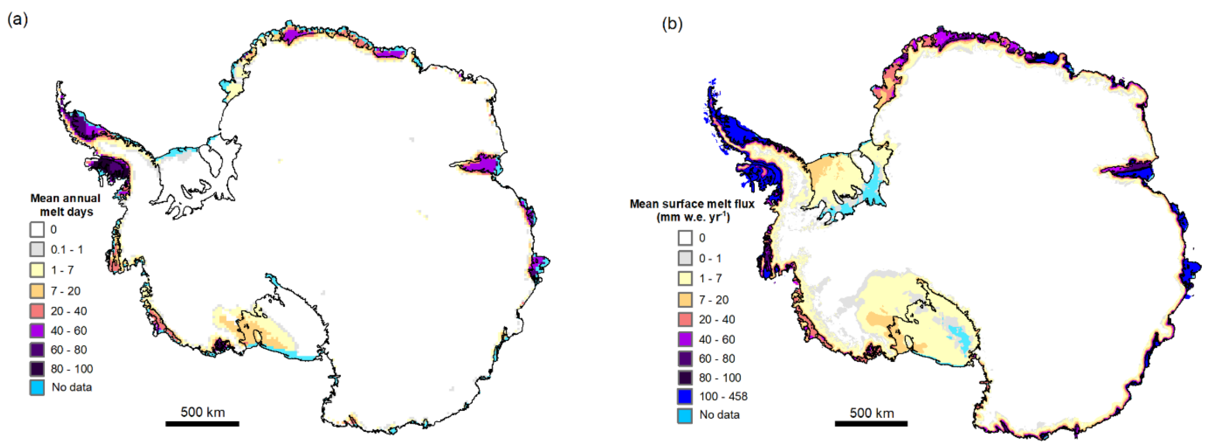

Figure 6: Mean annual melt days derived from satellite data between 1979 and 2020. (a) Derived from passive microwave observations (Johnson et al., 2022). (b) Derived from microwave scatterometer (Trusel et al., 2013).

Future warming will likely cause more frequent melt events with high melt intensities, but climate models have difficulty predicting surface runoff. Zou et al. (2021a, 2021b) show that high-resolution models and realistic surface schemes that represent the surface energy budget over snow and ice surfaces are key to accurate modelling of surface melt over large ice shelves. Also, the initialization of snowpack models to allow for refreezing is crucial to evaluate inland extents and the intensity of meltwater runoff in the coastal regions (Hansen et al., 2021). Finally, Gilbert & Kittel (2021) show that different GCMs capture the very large internal variability in the Southern Ocean differently, resulting in different boundary conditions and forcings for the RCMs. These differences lead to variable model outcomes on the lifetime and strength of surface melt and subsequent meltwater runoff in the coastal regions.

2.5 Bed topography

Bed topography strongly influences glacier and ice-sheet response to climate change (Section 2.6.4). The first comprehensive map of the bed topography of the AIS was released in 1983 (Drewry, 1983), followed by the first digital map in 2001 as part of the Bedmap project (Lythe et al., 2001). Since then, more IPR measurements and better interpolation techniques have improved the representation of bed topography underneath the ice which is particularly important for understanding fast-flowing glaciers near the coast, In this section. we summarize continental topographic features. Methods for mapping bed topography are discussed in Section 3.6.1.

The Transantarctic Mountains extend across the entire continent, from the eastern side of the Ronne Ice Shelf, in the Weddell Sea, to the western side of the Ross Ice Shelf and along the coast of the Ross Sea to Victoria Land and Oates Land (Figure 7a). This mountain range divides ancient thick cratonic lithosphere of East Antarctica from thinned crust of the West Antarctic Rift System (Section 2.6.1); the high relief of today's Transantarctic Mountains as a topographic feature cause the subdivision of the WAIS from the EAIS. The highest peaks of the Transantarctic Mountains are more than 4,500 m above sea level (a.s.l.), and yet a few fast and narrow ice streams pierce through this mountain range from the EAIS to feed the Ross Ice Shelf. These fast ice streams have been slowly eroding the bedrock, making deep incisions between mountain peaks. The waxing and waning of Byrd Glacier, for example, led to the formation of a valley that is about 3,000 m below sea level, flanked by summits that are almost 3,000 m a.s.l. There are similarly deep incisions over the entire western side of the Ross Ice Shelf that are carved by the fast-flowing Scott, Amundsen, Beardmore, Nimrod, and Skelton glaciers. The isostatic response to the incision of these deep troughs has been partly responsible for the uplift of the mountain peaks to their modern height (Fitzgerald, 1992).

The EAIS covers about two thirds of the entire continent and holds about 85% of the entire AIS volume (Morlighem et al., 2021). Wilkes Land, George V Land, and a few more locations host large ice-discharge basins with their beds below sea level, making them marine ice sheets. When their bed slopes deepen towards the interior of the continent, the marine ice sheets may be subject to MISI, a well-known ice-sheet instability resulting in a rapid retreat of the grounding line (Section 2.8.4). For example, the Wilkes Subglacial Basin—the largest marine-based ice drainage basin in East Antarctica—has the potential to generate self-sustained discharge equivalent to 3-4 m of global sea-level rise once retreat is initiated. This retreat could be triggered by the initial loss of a comparatively small ice volume at the margin of the Wilkes Land, equivalent to less than 80 mm of global sea-level rise (Mengel & Levermann, 2014). The EAIS has two notable mountain ranges. In the center of the EAIS and under the ice at Dome A, which is at least 1–2 km thick, lies the Gamburtsev Subglacial Mountains which have an alpine topography carved by ancient glaciers with several peaks over 2,500 m a.s.l. (Ferraccioli et al., 2011; Rose et al., 2013). The second mountain range is located in the coastal area of Dronning Maud Land. Here, the glaciers gradually rise to more than 1,000 m a.s.l. and reach a steep escarpment with peak elevations of 3,400 m a.s.l. some 150–200 km inland followed by the ice-covered Antarctic plateau. Finally, the bed topography of Princess

Figure 7: Overview of the AIS. (a) Contemporary bed topography (Morlighem et al., 2020; Dorschel et al., 2022). (b) Ice-surface flow speed (Gardner et al., 2022). (c) Modelled paleo bed topography when the AIS was initiated first time around 34 Million years ago (Ma) (Hochmuth et al., 2020; Paxman et al., 2019). To compare paleo and contemporary bed topography, plate rotation is removed. Such motion is approximately grid eastward in the past 34Ma. The contemporary grounding line is outlined for geographical reference. (d) Subglacial sedimentary basin distribution likelihood (Li et al., 2022a) with major fault systems (Aitken et al., 2014; Tankersley et al., 2022; Cox et al., 2023). (e) Gravity anomaly (Scheinert et al., 2016). (f) Magnetic anomaly (Golynsky et al., 2018). White blanks represent large data gaps that cannot be interpolated from airborne surveys and satellite data.

Elizabeth Land as well as between the Recovery and Support Force glaciers were referred to as “poles of ignorance” in the Bedmap2 compilation (Fretwell et al., 2013) due to their lack of direct IPR measurements. These regions have since been surveyed by several international airborne surveys, giving no longer flat features in these locations in the most recent Bedmap3 compilaiton (Pritchard et al., 2025). Additionally, new insights on the shape of Antarctica’s bed in sparsely surveyed regions are now emerging from inverting subglacial topography from high-resolution surface DEM and velocity datasets (Ockenden et al., 2025).

In contrast, the bed below the WAIS is primarily below sea level due to the isostatic load of the WAIS (Section 2.6.1). This loading, along with deposition of eroded sediments from the interior offshore, helps to generate very long reverse-sloping beds whereby the topography beneath the center of WAIS is deeper than at the coast. The consequence of this is that the Amundsen Sea Embayment is considered particularly sensitive to MISI, and it is also the fastest changing region of the entire ice sheet. Several glaciers have already been thinning and accelerating, leading to fast grounding-line retreat (e.g., Rignot et al., 2014). This predisposition for unstable retreat is exacerbated by the intrusion of warm circumpolar deep water (CDW) that is brought to the grounding line by the glacial troughs that cut across the continental shelf (Hochmuth et al., 2020; Livingstone et al., 2013; Paxman et al., 2019). This CDW is thinning the floating ice shelves of the Amundsen Sea basin (Section 2.7.1), leading to a reduction in ice-shelf buttressing (Section 2.8.4). The grounding line of Thwaites Glacier, for example, is retreating nearly 1 km per year at some locations and the underlying bed ridges may not be sufficient enough to slow down this retreat (Milillo et al., 2019; Wild et al., 2022).

The Antarctic Peninsula is one of the most mountainous regions in the AIS, with peaks reaching 2,800 m a.s.l. As the Peninsula extends north of the Antarctic circle, its climate is considerably warmer than the rest of the continent. As a result, several extensive floating ice shelves have collapsed over the past decades, including the Larsen A Ice Shelf in 1995 and more recently the Larsen B Ice Shelf in 2002. The latter ice shelf had been present over the entire Holocene and, in just over 2 months, starting in February 2002, 3,250 km^2 of its surface area collapsed (Scambos, 2004; Domack et al., 2005). The Larsen C Ice Shelf is the fourth largest ice shelf in Antarctica and thus has been closely monitored recently, particularly since the large calving event of July 2017 (Hogg & Gudmundsson, 2017; Jansen et al., 2015; Turton et al., 2020).

The AIS is surrounded by a continental shelf that is generally shallow compared to the Abyssal basin, with typical depths around 500 m but ranging from less than 100 m to nearly 1000 m in places (Figure 7a).This shelf extends between 50 and 500 km off the coast except along a few locations in Dronning Maud Land and Wilkes Land (Figure 7a). In such locations, a few incisions, probably originating from paleo ice-streams and tectonics, exist all around the ice sheet and provide pathways for CDW to reach some ice shelves and thus greatly contribute to their melting (Section 2.7.2). Offshore bed topography is measured using multi-beam sonar and airborne gravity surveys (Section 3.6.2). Onshore bed topography is today measured using IPR (Section 3.1.1). Seabed topography under ice shelves is retrieved only from sparse surface-based seismic data and inversion of airborne gravity data. However, to assess the stability of the interconnected systems of the ice sheet, ice shelves, and warm water pathways, it is crucial to obtain a better description of the seabed topography under floating ice shelves (Section 2.7.2). The current coverage of bed topography and bathymetry data are analyzed in Sections 4.3 and 4.4.

2.6 Geology and tectonics

Bed topography under the AIS is a primary controlling factor of the ice flow, and in turn the ice flow modifies the bed over geological timescales. Their interactions ultimately determine the sensitivity of the ice sheet to climate change. Below the ice, the distribution of water, sediment, and geothermal heat flow (GHF) controls how the AIS flows on timescales ranging from hours to millions of years (Blankenship et al., 2001; Noble et al., 2020; Reading et al., 2022; Studinger et al., 2001). However, comprehensive observations over this vast inaccessible region are difficult, and thus we have largely relied on interpretations of geophysical data to understand the sub-ice geology and the exposed coastal lithologies.

2.6.1 Evolution of the Antarctic continent

The isolated continent and Southern Ocean arose out of the formation and break up of Gondwana. The final stage of Gondwana assembly is marked as the Precambrian Australo-Antarctica Craton amalgamated with Indo-Antarctica 600–500 Ma (Mulder et al., 2019). During and after amalgamation, several significant exhumation events, including Pan-African and Ross Orogenies (Fitzgerald & Goodge, 2022) and Pangea rifting (Maritati et al., 2020), caused widespread denudation and cooling to shape the landscape (Maritati et al., 2020). The break-up of Gondwana since the Late Jurassic caused localized denudation and reactivation of rift structures (Maritati et al., 2020). The West Antarctic Rift System is the main cause for uplift, denudation, and exhumation of the Transantarctic Mountains. Both East and West Antarctica have a network of rift structures: East Antarctic Rift System transecting the Gamburtsev Subglacial Mountains (Ferraccioli et al., 2011), and Weddell Sea Rift System and West Antarctic Rift System (Jordan et al., 2020). Compared to West Antarctica, East Antarctica has been tectonically stable over this period.

As a result of the continuous fragmentation of Gondwana and the opening of the Southern Ocean (Boger, 2011), tectonically driven subsidence and opening of the Tasman Gateway and Drake Passage (Eagles & Jokat, 2014; Scher et al., 2015) established the conditions for onset of the Antarctic Circumpolar Current, causing or contributing to a dramatic cooling ~34 Ma (Sauermilch et al., 2021). Around this time, the atmospheric carbon dioxide level decreased (e.g., Zachos et al., 2001). Eventually, with the exact timing probably modulated by insolation changes related to multi-period orbital cyclicity (DeConto & Pollard, 2003), the ice sheets formed. Since then, repeated advancing and retreating of the ice sheets have driven erosion beneath and around the fluctuating ice body, deposited sediments, and carved topography in some areas—particularly those that now host the main outlet glaciers (Figure 7; Hochmuth et al., 2020; Jamieson et al., 2010, 2014; Paxman et al., 2019).

In addition, changes to the ice sheet and nearby seawater depth alters the loading to the bedrock, causing deformation and isostatic rebound over a viscous mantle, which in turn alters bed slopes and seawater depths along the margin of the ice sheet (Whitehouse et al., 2012, 2019), and ultimately affects the ice-sheet system (Pollard et al., 2017). All of these processes describing the response of the solid Earth, the gravitational field, and the oceans to the growth and decay of the global ice sheets are collectively called Glacial Isostatic Adjustment (GIA) (e.g., Le Meur & Huybrechts, 1996; Whitehouse, 2018). GIA can be split into instantaneous components (elastic deformation, changes in the rotational state of the Earth, and changes to the gravitational potential) and time-dependent components (viscoelastic mantle deformation and its associated rotational and gravitational perturbations) that operate over a wide range of time scales (Kachuck et al., 2020). GIA has a stabilizing effect on the evolution of the AIS by reducing the grounding-line migration that may happen following thinning (Section 2.8.4; Gomez et al., 2010). The timescale and strength of this feedback depend on ice-load history and the non-uniform viscosity of the Earth's mantle (van Calcar et al., 2022). In particular, the mantle generally has a high viscosity beneath East Antarctica, and a low viscosity beneath West Antarctica (e.g., van der Wal et al., 2015; Hazzard et al., 2013; Li et al., 2025), although absolute viscosity values are poorly constrained, and significant regional deviations from the east/west contrast are to be expected (Ivins et al., 2023).

Our understanding of thermomechanical structures and mantle viscosity has improved with advances in modeling capabilities (Hazzard et al., 2023; Li et al., 2025); however, the resolved viscosity remains largely limited not only by the resolution of the input seismic model, but also by its accuracy and the inherent non-uniqueness of seismic inversions. . Recent results of simulations over the last glacial cycle (the last 130 ka or so) show that changing the viscosity by an order of magnitude can move the grounding-line position up to 500 km and change the ice thickness by about 1.5 km (van Calcar et al., 2022). Moreover, an analysis indicates that, in regions of Antarctica with a low mantle viscosity, the contribution of GIA to modern records of sea-level change and solid Earth deformation may be more sensitive to ice loading during the late Holocene than across the last deglaciation (Gomez et al., 2018; Simms et al., 2018). Furthermore, interhemispheric interactions come into play. A recent modeling study has shown that the AIS dynamics are amplified by Northern Hemisphere sea-level forcing (Gomez et al., 2020). In particular, a large or a rapid Northern Hemisphere sea-level forcing results in enhanced grounding-line advance and associated mass gain of the AIS during glaciation, and in grounding-line retreat and mass loss during deglaciation. These results underline and quantify the importance of including local GIA feedback effects in ice-sheet models when simulating the AIS evolution over the last glacial cycle.

Over million-year timescales, another process shaping the landscape is deep mantle convection, with upward mantle flow expected to cause surface uplift and downward flow subsidence (Braun, 2010). This surface response to mantle flow is commonly referred to as dynamic topography. Global convection models have returned considerable variation in the length scales and amplitudes of supported topography in their lithospheres as a result. Global observational studies suggest this topography may occur over wavelengths of hundreds to thousands of kilometers and produce topographic amplitude variations of 500–800 m (Davies et al., 2019). In Antarctica, the large-scale undulation and its relative change influence paleo sea-level reconstructions and ice-sheet stability through time (Austermann & Forte, 2019). Thus, it is essential to account for landscape evolution when using paleo records to evaluate past climate dynamics (Fox et al., 2024). In the Wilkes Subglacial Basin, a GIA model predicts that in the mid-Pliocene the bedrock was lower than it is today due to such surface uplift, which has significantly increased the stability of the ice sheet since 3 Ma (Austermann et al., 2015). The paleo topography reconstruction shows that Antarctic Peninsula rose tectonically by up to 1.5 km due to dynamic topography, which has dramatically shaped glaciation patterns (Fox et al., 2024).

2.6.2 Geothermal heat flow

Geothermal heat flow (GHF) through the Earth's surface comes both from primordial heat in the mantle and from radiogenic heat production in mantle and crustal rocks (Reading et al., 2022), and is a driving mechanism of thawed bed in the inland AIS where frictional heat provides a small contribution (Pattyn, 2010). Crustal radiogenic heat production might locally contribute up to 70% of GHF, though it depends on the geochemical composition (Burton-Johnson et al., 2017). GHF at the base of the ice sheet strongly influences the ice-sheet temperature and thus stiffness (Burton-Johnson et al., 2020). For example, where the ice-sheet base is at its pressure-melting point, the GHF could increase the basal melt by up to ~0.3–0.4 mm yr^{-1} $(mW\ m^{-2})^{-1}$ (Seroussi et al., 2017; Shen et al., 2020). Many fast-flowing glaciers are in deep subglacial valleys where GHF is locally enhanced (Van de Veen et al., 2007), which can lead to enhanced sliding and ice-flux discharge (Section 2.8.4) and subglacial water discharge (Section 2.3). The magnitude and spatial variation of GHF is thus important to know for estimating the subglacial meltwater production and characterizing the regional ice-flow configuration (McCormack et al., 2022; Pittard et al., 2016).

As few direct measurements with large uncertainties of GHF exist for Antarctica (e.g., Burton-Johnson et al., 2020), geophysical models have been used to derive a spatial map of heat flow. One way of calculating GHF from geophysical data uses magnetic data to calculate the depth to the Curie point isotherm (e.g., Martos et al., 2017). Knowing this Curie depth enables calculation of the geothermal gradient between it and the surface, and from it the surface heat flow. Another method to estimating the geothermal gradient uses upper mantle seismic shear wave velocities (e.g., An et al., 2015), which are expected to vary with temperature of the upper mantle. The models significantly disagree in the details yet consistently predict higher GHF in West Antarctica and lower GHF in East Antarctica. In addition, within East Antarctica, most (but not all) models predict that, compared to the interior, GHF is elevated at the outlets of basins where crust is thinner and where topography is more deeply incised although it is likely still lower than most of West Antarctica (Burton-Johnson et al., 2020). The model disagreements can be understood in terms of their use of different constraints and assumptions (Burton-Johnson et al., 2020; Reading et al., 2022), which capture different processes (Lösing et al., 2020).

As a result, recent approaches use multiple geophysical and geological datasets and combine them either with statistical approaches like multivariate analysis (Stål et al., 2021) or machine learning (Lösing & Ebbing, 2021). These models are able to reproduce GHF inputs such as lithospheric component, the majority of neotectonic zones, and the large-scale impact of volcanoes on the Antarctic continent, but are unable to capture a number of local contributions to GHF such as the details of the crustal heat production and thermal refraction that arise from local subglacial topography and geological variation (Reading et al., 2022). Nevertheless, the statistical models provide an accurate uncertainty estimate, that can be exploited both on the regional scale by linking GHF models and satellite-based ice-temperature models (e.g., Macelloni et al., 2019) and on the local scale by adding information from airborne datasets through direct estimates (e.g., Dziadek et al., 2021) or through geophysical joint inversion (e.g., Lösing, 2022, Lösing et al., 2025). At an even finer scale, topographic correction can be applied to correct thermal refraction due to subglacial topographic relief (Colgan et al., 2021). However, nonuniformity in thermal conductivity due to geological variations should be included as it controls heat transfer from bedrock to ice (Willcocks et al., 2021). Such methods become important when refining GHF in coastal areas due to the expected large changes in the geothermal gradient that accompany crustal thickness and composition variations that mark the onshore to offshore transition.

Radiogenic heat production varies markedly amongst outcrops in Antarctica, with the 25th to 75th percentile of heat production ranging from 0.6 to 2.4 μW m^{-3} (Sanchez et al., 2021). Continental-wide heat production has been estimated using geological and geophysical data (Stål et al., 2020; Li and Aitken, 2024; Hazzard and Richards, 2024). However, challenges remain as there is a general lack of geological information beneath the AIS, and there is also a lack of empirical information on continental-wide heat production (Stål et al., 2024). These two factors create a major challenge how we scale from small samples to large volumes of crust. In addition, hydrothermal circulation influenced by fault systems or groundwater systems can locally increase GHF (Gooch et al., 2016; Jordan et al., 2018; Tankersley et al., 2022). Thus, high-resolution geophysical studies that focus on subglacial geology and potential pathways for hydrothermal circulation are essential to constrain GHF.

To learn more about GHF, Burton-Johnson et al. (2020) and Reading et al. (2022) are recent review papers in this field.

2.6.3 Sediments

Subglacial sediment (unconsolidated material) transported and deposited by ice and subglacial water can influence subsequent ice flow. Beneath ice sheets, sediment can build up as grounding-zone wedges and moraines that may serve as pinning points to stabilize ice-sheet retreat (Alley et al., 2007; Batchelor & Dowdeswell, 2015). In a subglacial environment, loose sediment often forms a deformable till layer (Evans et al., 2006), reducing basal friction and thus contributing to sliding faster and forming an ice stream (Alley et al., 1986). Conversely, places without such till layers tend to have higher friction with slower ice flow (Weertman, 1957). Over a period of decades to centuries or even shorter periods in the case of fast flow, the resulting sediment erosion can change the basal conditions (Smith et al., 2007, 2012). Hence, to maintain ice-sheet streaming, a continuous supply of subglacial sediment is needed. These sediments can sourced via two ways: marine deposition during the interglacial cycle or subglacial erosion (Evans et al., 2006). Importantly, subglacial erosion often acts on bedrock, and relatively weak bedrock lithologies—such as many sedimentary rock types—are more susceptible to erosion (Krabbendam & Glasser, 2011). Unlike loose sediment, sedimentary rock is consolidated and requires mechanical erosion to break down, but once eroded, it provides long-term sediment supplies to maintain fast basal sliding (Anandakrishnan et al., 1998; Bell et al., 1998).

Other than facilitating basal sliding, sediment also influences the ice-sheet geometry (Schannwell et al., 2020) and how the ice-sheet system responds to external forcing. In areas with a till-rich environment, as an ice-sheet flow modelling study of the Thwaites Glacier showed (Parizek et al., 2013), ice-sheet flow follows a plastic flow law in which stress changes at the ice-sheet margin drive interior acceleration, increasing the supply of ice from the interior to compensate for marginal ice loss and stabilizing the grounding line. In turn, areas with limited till show a local response to external forcing with a viscous flow law, driving coastal thinning and more rapid grounding line retreat. However, in the long term, interior thinning with a plastic bed leads to faster grounding line retreat once floatation off the current grounding line begins (Koellner et al., 2019).

When a sedimentary basin (formed by consolidated sedimentary rock) is permeable, it provides a subglacial groundwater system (Gustafson et al., 2022) that is an important component of the water budget for the subglacial hydrology system (Christoffersen et al., 2014). This is distinct from loose sediment layers, which mainly store porewater locally; sedimentary basins represent large-scale geological structures controlling groundwater flow. Permeable sedimentary basins discharge and recharge groundwater during ice-sheet changes (Gooch et al., 2016; Lemieux et al., 2008; Person et al., 2012). Recent observations show that their response is rapid, even to small ice-sheet changes (Liljedahl et al., 2021). In particular, ice-sheet expansion causes groundwater recharge, which is associated with reducing basal temperature (Gooch et al., 2016). Ice-sheet retreat is associated with dynamic thinning, where the groundwater discharge rate is coupled with the ice-sheet retreat rate (Li et al., 2022b). For a slow-retreating ice sheet, groundwater contributes a small amount of the water budget, whereas a fast-retreating glacier could lead to a groundwater discharge that is a significant portion of the subglacial water budget (Li et al., 2022b; Robel et al., 2023). Over longer timescales, groundwater dynamics within sedimentary basins are largely controlled by basin geometry, with groundwater exfiltrating where the basin becomes shallower and re-infiltrating where it becomes deeper (Cairns et al., 2025). The discharge of groundwater facilitates basal sliding and also provides additional feedback to weaken the till layer, which would entrain ocean heat near the ice-ocean interface, thus increasing oceanic melting and potentially reducing ice-shelf stability (Gooch et al., 2016; Le Brocq et al., 2013). This positive feedback suggests that the presence of sedimentary basins makes the boundary conditions for the inland ice sheet highly variable and dynamic.

Mapping sediment distribution is challenging due to its high spatial variation, including thin layering (Muto et al., 2019) and our limited measurement resolution. However, in post-glacial regions, the subglacial sediment distribution is highly correlated with regional geology (Gowan et al., 2019). For example, thick and widespread coverage of glacial sediments tends to occur in pre-existing sedimentary basins (Gowan et al., 2019). This correlation exists because sedimentary basins (bedrock structures) provide accommodation space for sediment accumulation, whereas crystalline bedrock areas typically have thinner sediment cover. Thus, an understanding of subglacial sedimentary basin distribution is a prerequisite to understanding sediment distribution and potential areas of groundwater discharge. In addition, the variation of subglacial morphology is highly correlated with sediment distribution (Muto et al., 2019) and thus can be used to map sediment on a catchment scale (MacKie et al., 2021). Thus, high-resolution geophysical studies are required to capture this morphological information and better constrain sediment distribution and boundaries to crystalline rocks (e.g., Smith et al., 2013). Towards this goal, Li et al. (2022) created a high-resolution subglacial geology classification for Antarctica by applying a supervised machine-learning method to geophysical data, revealing a likelihood map for sedimentary basins beneath the ice (Figure 7d). They then used this map to discuss the hydrological system. However, this approach may introduce circular reasoning because bedrock density used to define a priori cluster for the joint inversion also influences the classification. Lösing et al. (2022) demonstrated an approach where cluster analysis is directly coupled with a physical Earth model, jointly inverting gravity and magnetic data to image the 3D crustal structure. Their results indicate that magnetic data are generally less sensitive to bed topography, but more sensitive to lateral near-surface changes related to geology. Building on this, integrating such joint inversion techniques with supervised geological classification may offer a useful pathway to constrain bedrock density variations and enhance coupling to geological information. Achieving this will require well-coordinated regional airborne surveys, complemented by geological investigations at outcrops and seismic surveys, to develop robust geological models under the ice sheet.

To learn more about sediments, Aitken et al. (2023) is a recent review paper in this field.

2.6.4 Geological and topographic impacts on ice flow

The vulnerability of the AIS to a warming climate is also related to geological heterogeneity of the Antarctic Continent. This heterogeneity is the product of a complex combination of tectonic processes, erosion, deposition, and associated isostatic adjustment (Paxman et al., 2019, 2020). Tectonic processes initialize the pre-glacial landscape, including by forming mountain ranges (Ferraccioli et al., 2011), rift and transtensional sedimentary basins (Jordan et al., 2013), broader sag basins (Aitken et al., 2014), and volcanos (Blankenship et al., 1993). These pre-glacial landscapes are then modified by surface processes such as fluvial incision and weathering creating a weaker substrate for growing ice to expand over and erode (Jamieson et al., 2010, 2014). Since glaciation began, long-term erosion has concentrated within rift systems and sedimentary basins, reflecting the strong contrast in crust rheology and erodibility between sediment and crystalline basement.

Selective erosion due to fluvial or glacial action mainly occurs in narrow rift basins, with associated isostatic-flexure adjustment, generating cold-based plateau and warm-based over-deepening (Egholm et al., 2017; Paxman et al., 2017; Thomson et al., 2013). The narrow, channelized ice flow along with topographic over-deepening can produce MISI-susceptible conditions (Section 2.8.4). For example, CDW can reach the ice-sheet margin and cause dynamic ice thinning where an over-deepened extension connects to the continental shelf (Bingham et al., 2012). Areal scouring produces areas with broad, subsided basins with a steep, reversed bed slopes (Paxman et al., 2019, 2020). In addition, the thermal subsidence after extension produced lowered bed elevations in the West Antarctica Rift System (Paxman et al., 2019; Wilson & Luyendyk, 2009). Such topographic changes increase the vulnerability of the AIS to MISI. The broader tectonic-controlled structure could also influence ice-shelf stability. For example, the tectonic boundary beneath the Ross Ice Shelf controls the long-term asymmetry of sedimentation and seabed topography, which influences the sub-ice-shelf ocean circulation (Tankersley et al., 2022; Tinto et al., 2019). In addition to their topographic control, geological differences also have a strong influence on ice-sheet bed conditions, including tectonic regimes, fault patterns, sediment distribution, variable subglacial hydrological systems (GHF and groundwater), and basal thermal state (Noble et al., 2020; Schannwell et al., 2020).

2.7 Ocean and sea ice

The AIS drains into the surrounding ocean, often terminating in floating ice shelves that provide stability through buttressing (Section 2.8.1). Reductions of buttressing have been attributed to ocean-driven basal melting and calving (e.g., Adusumilli et al., 2020; Liu et al., 2015; Rignot et al., 2013, 2019). Consequently, to determine how oceanic heat transport affects basal melting of ice shelves, we need to understand ocean circulation and ice-ocean interactions (Jacobs et al., 2011).

2.7.1 Circulation regimes of the Southern Ocean

The strongest source of oceanic thermal forcing is the warm modified CDW, which is typically ~0.5–1.5°C in the Amundsen and Bellingshausen Seas and located below ∼300 m depth. The CDW originates from the Antarctic circumpolar current (ACC) at intermediate depths in the offshore region (Orsi et al., 1995). The ACC flows clockwise around Antarctica due to strong westerly winds that dominate at ~50°S (Figure 8a). This current is traditionally identified based on three primary oceanic fronts: the sub-Antarctic, the polar, and the southern ACC fronts (Orsi et al., 1995; Sokolov & Rintoul, 2009). These fronts contribute significantly to the isolation of the Southern Ocean (Falco & Zambianchi, 2011; Trani et al., 2014). Further south, the continental slope inhibits southward transport of the CDW that is driven by geostrophic mean flows, supporting instead a sharp fourth front, the Antarctic slope front (ASF), which coincides with the westward-flowing Antarctic slope current (ASC) at the surface along most of the continental shelf break (Jacobs, 1991; Whitworth et al., 1985). Moreover, the subpolar Weddell and Ross Gyres affect the circulation between the ACC and ASC (e.g., Park & Gambéroni, 1995), and are wide enough to isolate cold shelf water from warm CDW (Marshall & Speer, 2012; Pellichero et al., 2018; Thompson et al., 2018). As it interacts with the geometry of the continental shelf break, the ASC's structure and variability have important influences on both the way that water circulates on the continental shelf, and the exchange of heat and mass beneath the ice shelves (Schmidtko et al., 2014). Along significant portions of the EAIS, the circum-poleward deep water has moved southward shifting warmer water towards the Antarctic coastal zone (Herraiz-Borreguero & Naveira Garabato, 2022; Yamazaki et al., 2021).

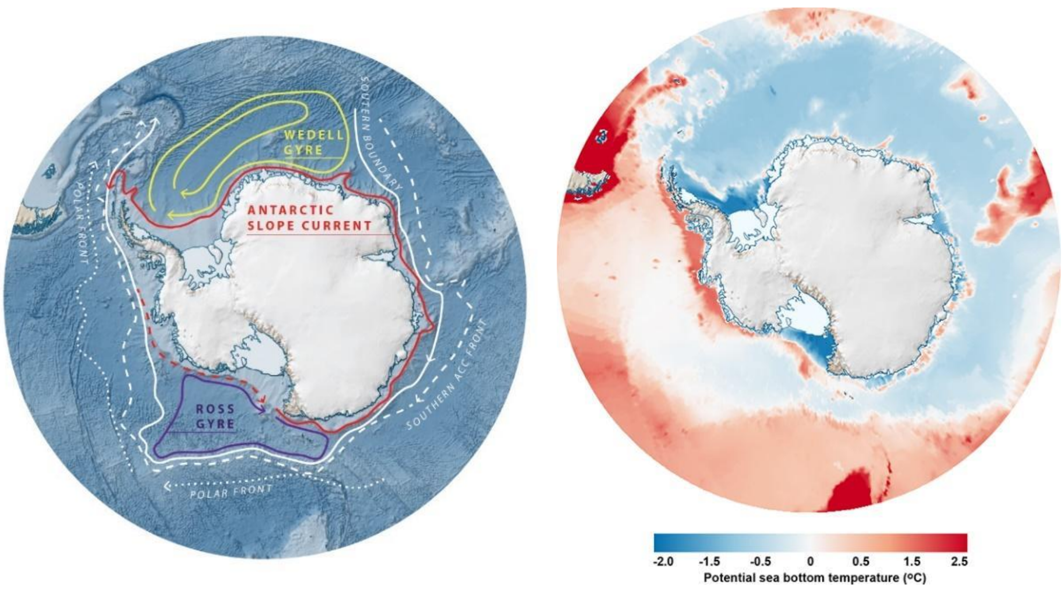

Figure 8: Southern Ocean circulation regimes and bottom temperature. (a) Circulation regime of the Antarctic margins. The Antarctic Slope Current (ASC, red) is depicted as a near-circumpolar, anticyclonic (westward) feature appearing at the shelf break in East Antarctica and the Weddell Sea. Uncertainty regarding the initiation of the ASC is indicated by the dashed line in the Bellingshausen and Amundsen Seas, as well as the western Ross Sea. Along the West Antarctic Peninsula, a slope current flows eastward, along with the southern boundary of the Antarctic Circumpolar Current (ACC). Interactions with the Weddell (yellow) and Ross (purple) Gyres (based on Armitage et al. (2018)), as well as the southern fronts of the ACC (white; based on Orsi et al. (1995)) are

highlighted by their proximity to the ASC in various locations around the Antarctic margins, (e.g., east of the Cosmonauts Sea). Also shown are sub-Antarctic Front and Polar Front. This figure is adapted from Thompson et al. (2018). (b) Ocean bottom temperatures around Antarctica based on the WOCE global hydrographic climatology (Noble et al., 2020). Note the existence of two primary regimes: a warmer sector in west Antarctica (the western Peninsula, Bellingshausen Sea and Amundsen Seas, between 60^{o}W and 120^{o}W) and a colder sector around the rest of the continent. Continental Shelf edge is well visualized with the location of Antarctic slope current in panel (a). The basemap of these panels is made with Quantarctica (Matsuoka et al., 2021).

In areas where the ACC veers south and approaches the continental shelf break, warm CDW can efficiently transfer heat on the shelf and further reach into the ice-shelf cavities (e.g., Dutrieux, De Rydt, et al., 2014; Jacobs et al., 1996; Jenkins et al., 2018; Nakayama et al., 2013). However, a combination of continental slope and shelf geometry, the magnitude of the ASF, and the associated westward ASC inhibits heat transport around a large portion of the continent (Thompson et al., 2018), which can only be broken in key locations by processes such as eddy transport, tidal currents, overturning circulation, and changes in the position and strength of the westerly winds (Budillon et al., 2011; Castagno et al., 2017; Stewart & Thompson, 2015). In regions where the ASF is weak (e.g., Amundsen Sea and West Antarctic Peninsula), this inhibition is less effective and thus heat can more easily access the continental shelf. This contrast is evident in the bi-modal distribution of the ocean temperature at the shelf seabed (Figure 8b) that enables the Antarctic ice shelves to be categorized as either cold-water or warm-water ice shelves (e.g., Adusumilli et al., 2020). Correspondingly, the warm-water ice shelves in the Amundsen and Bellingshausen Sea are expected to melt faster due to the heat exchange with CDW (e.g., Dutrieux et al., 2014; Nakayama et al., 2018; Orsi et al., 1995; Pritchard et al., 2012; Rignot et al., 2013).

Several studies show, however, that other marine-based portions of the AIS are also highly vulnerable to ocean-driven melt (e.g., Rignot et al., 2013; Rintoul, 2018). Satellite measurements and numerical simulations revealed that several parts of the EAIS have lost significant mass at the ice-shelf base (Depoorter et al., 2013; Li et al., 2015; Rignot et al., 2013; Rintoul, 2018). One such rapidly melting ice shelf in the EAIS is the Totten Ice Shelf. This ice shelf has the second largest basal melt rate in Antarctica (after that in the Amundsen Sea) and abuts the Totten Glacier that holds an ice volume equivalent of more than 3.9 m of global sea-level rise (Li et al., 2015). Conjointly, recent oceanographic observations found ice-shelf-cavity intrusion of a relatively warm modified CDW (Figure 9) in front of and under the Totten Ice Shelf through narrow submarine canyons (Aitken et al., 2016; Greenbaum et al., 2015; Greene et al., 2017; Rintoul et al., 2016; Silvano et al., 2017).

Our current understanding of what drives southward ocean heat fluxes along this crucial ASF gateway and the associated oceanic melting of the ice shelves is based on a few scattered observations and numerical models. Local wind-driven processes and their tropical-to-subtropical origins have long been seen as the main modulator of these fluxes (Dutrieux et al., 2014; Holland et al., 2019; Naughten et al., 2022; Thoma et al., 2008). However, the relationship between the wind and the climate system here is now considered less clear (Holland et al., 2022); for example, recent modelling suggests that the connection between the wind and ocean heat fluxes may also need additional study (Silvano et al., 2022).

Regions where large and rapid changes are ongoing (e.g., the Amundsen Sea) are relatively well-studied observationally. In other locations where the ice appears to be currently more stable, multi-decadal freshening trends have been observed in continental shelf seas (e.g., Jacobs et al., 2022). Yet most of the ocean around Antarctic ice shelves has minimal observations. Moreover, the ocean and the atmosphere vary strongly on seasonal (Webber et al., 2017) to decadal (Jenkins et al., 2018) timescales, dwarfing any long-term (and eventual anthropogenic) trends. Hence, long-term *in situ* observations of the ocean and the ice's response are needed to decipher the complex and varied dynamical connections linking atmosphere, ocean, and ice for accurate quantitative predictions of future changes.

2.7.2 Ocean circulation under ice shelves

Iceberg calving and ocean-driven basal melting are the main ways ice shelves lose buttressing and increase their discharge into the ocean (Adusumilli et al., 2020; Rignot et al., 2019; Sun et al., 2020). In turn, ice-shelf melting is driven by ice-ocean interactions that involve a broad range of spatio–temporal scales (Rosevear et al., 2021), from microscale ice–ocean boundary layer processes (Vreugdenhil & Taylor, 2019) to large-scale ocean circulation (e.g. Jenkins et al., 2018). Crucial factors are the properties of the water masses that intrude into the ice-shelf cavity due to distinct oceanographic processes (Jacobs et al., 1992). Based on these processes, ice-shelf melting can be linked to three main density-driven circulation modes (Figure 9; Adusumilli et al., 2020; Jenkins et al., 2016).

The first and most common mode (Mode 1 in Figure 9) comes from the inflow of cold and dense high-salinity shelf water (HSSW). The HSSW is produced in coastal polynyas where a combination of strong katabatic winds and a physical barrier that blocks inflow of sea ice leads to strong air–sea interactions, seawater freezing and export, associated brine rejection and the densification of the water column (e.g., Aulicino et al., 2018; Sansiviero et al., 2017; Yoon et al., 2020). As sea ice is continuously produced and advected away by the wind in a coastal polynya area, the dense HSSW submerges and enters into the sub-shelf cavity with a water temperature at the surface freezing point. As the freezing point decreases with pressure, heat becomes available to melt ice at the ice-shelf base depth. The resulting melt mainly occurs in the deepest part of the large cavities where it initiates thermohaline convection where the dense shelf water evolves into colder than freezing but relatively fresh and therefore buoyant ice-shelf water (Bergamasco et al., 2002). Rising plumes of this buoyant water mass flow out of the cavity along the ice-shelf base, which then sustains an overturning circulation within the sub-ice-shelf cavity. In addition, these buoyant plumes can lead to refreezing downstream, creating a layer of marine ice on the ice-shelf base that protects it from fracturing and melting (Kulessa et al., 2014). This circulation mode may promote both melting and refreezing processes beneath major parts of the Filchner-Ronne, Ross, and Amery ice shelves (e.g., Silvano et al., 2016).

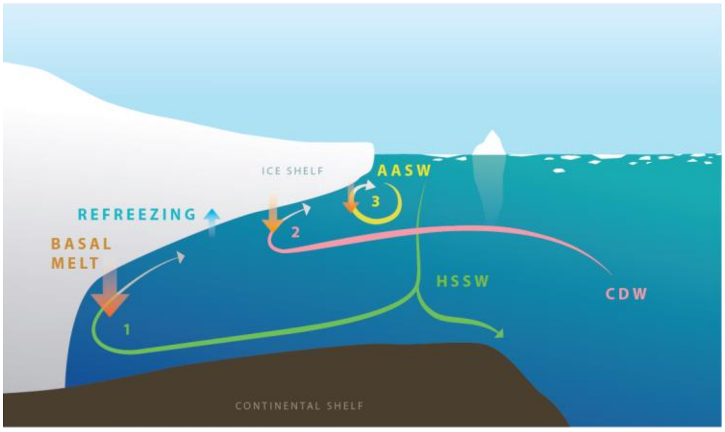

Figure 9: Schematic diagram of the ocean circulation above the Antarctic continental shelf and the corresponding three modes of ice-shelf basal melting. Numbers and colors refer to the respective melting modes discussed in the text and each water mass is indicated by its abbreviation. Mode 1 is driven by cold HSSW, Mode 2 by warm mCDW/CDW and Mode 3 by seasonally warmed AASW. The outflow from the cavity is a mixture of glacial meltwater with HSSW, mCDW, and AASW, which is called ice shelf water (not shown). This diagram is adapted from Jacobs et al. (1992).

The second mode (Mode 2 in Figure 9) occurs when warm CDW or mCDW flows into the ice-shelf cavity at an intermediate or seabed depth. This water mass is significantly warmer (up to ~3K) than the freezing point at the ice-shelf base (Jacobs et al., 1996; Minowa et al., 2021), and thus causes rapid basal melting and subsequent loss of large volumes of basal ice (e.g., Cook et al., 2016; Jenkins et al., 2018). This mode has been shown to be largely responsible for the accelerated melt rates of ice shelves in the Amundsen and Bellingshausen Seas (Jacobs et al., 2011; Jenkins et al., 2016; Jourdain et al., 2017). The net melt rate of this mode ranges between two extremes. The high-melting case occurs when warm water fills most of the sub-ice cavity and causes significant melting (Potter & Paren, 1985). This occurs today in the Amundsen and Bellingshausen Seas (e.g., Biddle et al., 2017; Jacobs et al., 2011), where relatively warm (~1°C – 1.5°C) and salty (34.5 – 34.7) mCDW flows southward across the ASF and, because HSSW is not there, fills the bottom layer of the continental shelf (Jenkins et al., 2016; Silvano et al., 2016). The low-melting case occurs when mCDW flows southward in the Weddell and Ross Sea. Here, large anticyclonic gyres of relatively cold water (Weddell Gyre and Ross Gyre, respectively) isolate the continental margin from the warm waters of the ACC (e.g., Bebieva & Speer, 2021; Orsi & Wiederwohl, 2009) and the ice-shelf cavities are filled with the colder, regionally produced HSSW instead.

The third circulation mode (Mode 3 in Figure 9) is driven by seasonally-warmed Antarctic surface water (AASW), a much lighter water that intrudes under the shelf during austral summer, causing basal melting near its front (e.g., Hattermann et al., 2012; Stewart et al., 2019). Although the warm AASW can be transported in various ways (e.g., tides, eddies, Ekman transport, and ocean currents; Silvano et al., 2016), it mostly interacts with relatively shallow glacial bases and walls within 100 km distance of the ice fronts into the cavity due to tidal pumping and the seasonally warmer waters of the coastal current (Jacobs et al., 1985, p. 19). Occasionally however, when the grounding line is relatively shallow, the basal melt rates driven by warm AASW can reach the grounding line. This circulation mode has been observed at the Ross and McMurdo ice shelves (Arzeno et al., 2014; Stern et al., 2013), the Ronne-Filchner Ice Shelf (Joughin, 2003), and the Fimbul Ice Shelf (Hattermann et al., 2012). Along the front of the Ross ice shelf AASW has been persistently thinning the ice shelf front for over 80 years (Das et al., 2020; Tinto et al., 2019).

While these modes and the relevant processes are widely accepted, their contribution to the local melting rates vary greatly around Antarctica (Adusumilli et al., 2020). Each mode is influenced by several external processes, regional atmospheric and oceanic conditions, as well as by the sea-ice distribution (e.g., Bett et al., 2020; Rintoul, 2018; Turner et al., 2017). A broad range of in-situ survey technologies (Sections 3.1.6 and 3.5.3), satellite sensors (Section 3.7), and numerical models (Section 3.8) all contribute to our understanding of this complex system. Nevertheless, most of our observational understanding to date is based on shipborne surveys in front of a few ice shelves (e.g., Dutrieux et al., 2014; Jacobs et al., 2013; Jacobs et al., 2022; Jenkins et al., 2018; Jenkins & Jacobs, 2008; Rintoul et al., 2016), on observations under the ice obtained through boreholes (e.g., Vaňková & Nicholls, 2022), and on autonomous underwater vehicles (see Barker et al., 2020 for an overview). More comprehensive circum-Antarctic surveys of ocean properties and associated ice melt, as well as improved bathymetric data, are crucial for better understanding of the complexities involved in heat and mass exchanges at the ice-ocean interface and calving front. Such knowledge is needed to parameterize ocean processes for Earth system models to ultimately increase the reliability of our climate and sea-level predictions.

2.7.3 Sea ice and its impacts on ice-shelf instability

Antarctic sea ice strongly influences air-sea heat exchange, local surface albedo, and the upper ocean freshwater budget (e.g., Budillon et al., 2000; Fusco et al., 2018; Newman et al., 2022; Pellichero et al., 2018). The sea ice extent around Antarctica exhibits substantial spatio–temporal variability, with an asymmetric seasonal cycle that occurs over large interannual variability (Eayrs et al., 2019, 2021; Parkinson, 2019; Roach et al., 2022). Seasonally, its extent ranges between about 3 and 19 million km^2 (Handcock & Raphael, 2020). Thus, its winter extent exceeds 14 million km^2 of the AIS and Antarctic ice shelves. The seasonal variability is characterized by a slow growth period followed by a fast melt period due to strong atmospheric forcings and oceanic feedbacks (Goosse & Zunz, 2014; Holland, 2014).

With only limited *in-situ* measurements, large-scale spatio–temporal variations of sea ice rely upon satellite observations (Fogt et al., 2022; Parkinson & Cavalieri, 2012; Tamura et al., 2008). The satellite measurements have shown that the winter sea-ice extent has slowly increased since 1979 to a record maximum during 2012–2014, then rapidly decreased to historically low values in 2016 that have continued to date (Eayrs et al., 2021; Meehl et al., 2019; Polar Research Board et al., 2017). This recent decline led to a record minimum of more than 2 million km^2 below the long-term mean (Eayrs et al., 2021), which is equivalent to 30 years of sea-ice loss in the Arctic (Parkinson, 2019). This trend continued to another record minimum in February 2022 (Turner et al., 2022; Wang et al., 2022).

Concerning the main driver of the recent sea-ice reduction, several studies suggest the atmosphere (Holland & Kwok, 2012; Schemm, 2018; Silvano et al., 2018, 2020; Wang et al., 2019), whereas others argue for a substantial oceanic influence (Kusahara et al., 2018; Meehl et al., 2019). For instance, Eayrs et al. (2021) suggest that the decline was strongly influenced by the interaction of a decades-long ocean warming trend with an early spring southward advection of atmospheric heat. However, currently no consensus exists on the primary mechanisms controlling these changes, and relevant comprehensive reviews have pointed out the complexity of the ocean-ice-atmosphere system in the Southern Hemisphere (e.g., Hobbs et al., 2016; Jones et al., 2016). Moreover, the computation of the sea-ice thickness, particularly the prediction of its interannual variability, remain a significant challenge (Aulicino et al., 2014; Fogt et al., 2022; Morioka et al., 2022; Turner & Comiso, 2017). Contemporary models have been unable to reproduce the observed changes accurately (e.g., Roach et al., 2020; Rosenblum & Eisenman, 2017; Turner et al., 2013), leading to a low confidence in projections of future trends in Antarctic sea-ice coverage.

For forecasting, a further complication is variability due to polynya activity (Beadling et al., 2020; Hobbs et al., 2016; Holland et al., 2019). Coastal polynyas, persistent ice-free areas primarily maintained by strong katabatic winds, can be major sources of sea ice production and dense water formation as well as high heat exchanges over the open ocean throughout the austral winter (Aulicino et al., 2018; Fusco et al., 2009; Ohshima et al., 2016; Talley, 2011; Yoon et al., 2020). More specifically, as sea ice is continuously produced and transported offshore, strong polynya activity impacts the ocean heat flux to the AIS and promotes the formation of HSSW through intense heat loss and brine release. As described in Section 2.7.2, this HSSW formation in active polynya areas is directly linked to the first mode of ice-shelf basal melting, whereas the dense water produced in strong polynyas (e.g., in the Ross Sea, Weddell Sea, Prydz Bay region) fills the bottom layer and limits the access of CDW to the ice-shelf cavities (Arzeno et al., 2014; Herraiz-Borreguero et al., 2015; Silvano et al., 2018).

In a warmer climate, an increase of glacial meltwater to the shelf waters could reduce or even prevent HSSW formation, despite the strong air-sea forcing and buoyancy loss in polynya areas (Silvano et al., 2018). A significant reduction of dense water formation could trigger a transition from a cold ice shelf with low rates of ice-shelf basal melt, to a warm regime with year-round stratification and high rates of melt (Silvano et al., 2018). Relevant freshening of bottom water, associated with the inflow of fresh water from the Antarctic Peninsula and Amundsen Sea, has already been observed in the Weddell and Ross Sea, respectively (Budillon et al., 2011; Castagno et al., 2019; Fusco et al., 2009; Jullion et al., 2013). These changes are very important because HSSW is a precursor of the dense Antarctic bottom water (Orsi & Wiederwohl, 2009) that drives the global thermohaline circulation, ventilates the abyssal ocean, and stores heat and carbon for centuries (e.g., (Castagno et al., 2019; de Lavergne et al., 2017; Lumpkin & Speer, 2007; Orsi et al., 1999; Orsi & Wiederwohl, 2009; Silvano et al., 2020).

In addition, meltwater-induced changes in stratification could enable the spreading of warm water across the continental shelf towards ice-shelf cavities (Naughten et al., 2021; Silvano et al., 2018), leading to increased ice-shelf basal melt, and thus reduced buttressing of the AIS. Therefore, to make accurate projections, it is crucial to understand how changes in the ocean–sea ice interactions are influencing basal melt of the ice shelves. Recent studies implied that sea ice may also influence ice-shelf stability and glacial ice discharge, for example by protecting ice-shelf frontal zones from destructive ocean swells (Massom et al., 2018; Van Achter et al., 2022). Landfast sea ice could also mechanically bond to, and thus exert a buttressing force on floating glacier tongues and ice-shelf fronts. This is especially the case when landfast sea ice persists year round (called multi-year landfast ice), which provides stability to Stancomb-Wills Glacier Tongue in the Brunt Ice Shelf (Khazendar et al., 2009) and Totten Glacier Tongue (Greene et al., 2018; Wearing et al., 2020). The removal of landfast sea ice and subsequent loss of buttressing can cause ice-shelf breakup, particularly for ice shelves that were already structurally weak. For example, rapid landfast sea ice breakout was shown to have triggered synchronous break-up of four outlet glaciers in Porpoise Bay (Miles et al., 2017) and the Voyeykov Ice Shelf (Arthur et al., 2021), both in Wilkes Land, East Antarctica. Modeling studies also show that multiyear landfast sea ice cemented with a heavily-crevassed, unconfined Thwaites Glacier Tongue provides buttressing to the ice sheet, and the removal of this protective sea ice buffer could potentially trigger increased ice flux (Reese et al., 2018; Rott et al., 2020).

The combination of new observations, advances in theory, and improvements in modelling promises to lead to a much better understanding of this complicated system. As pointed out by Eayrs et al. (2021), programs like SOCCOM (Riser et al., 2018) and Deep Argo (Zilberman, 2017) should shed light on the dynamic oceanographic processes that drive sea-ice evolution (Section 3.5.3). Moreover, orbits of ICESat-2 (Markus et al., 2017) and CryoSat2 (Wingham et al., 2006) satellites were recently modified to increase their overlap. It allows to substantially refine the algorithms used to estimate Antarctic sea-ice thickness, which plays a crucial role in studying sea-ice formation and melting.

Reviews by Hobbs et al. (2016), Turner & Comiso (2017), and Newman et al. (2019) highlight crucial research directions and developing techniques that have the potential to increase the confidence in projections of future trends in Antarctic sea-ice coverage.

2.8 Ice-flow processes

Ice flow is a key feature of the AIS, being critical in completing the cycle of mass balance from the inland regions, where ice accumulates through snowfall (Section 2.4.2), to the coast where ice is lost through flow discharge (Section 2.2) and runoff of surface meltwater (Section 2.4.3) and subglacial meltwater (Section 2.3). From inland to the coast, the flow speed of ice at the surface increases by five orders of magnitude: from about a centimeter per year at inland domes and ridges to kilometers per year at the margins and on the larger ice shelves (Rignot et al., 2011b). The ice flows fastest in ice streams and outlet glaciers, and accounts for most of Antarctica's ice and sediment discharges across the grounding line (Bamber et al., 2000). Here, we examine ice-flow processes and relevant mechanisms of instability.

2.8.1 Coastal buttressing

Glaciers across Antarctica, and particularly in the WAIS, have been accelerating, with concurrent increases in ice discharge, grounding line retreats, and mass losses (Gardner et al., 2018; Rignot et al., 2019; Shen et al., 2018). A key factor underlying these trends is the loss of buttressing as ocean warming drives ice-shelf thinning and calving. In general, buttressing describes the resistive stresses that ice shelves impose on the upstream ice (Thomas et al., 2004) through interactions with bed topography over ice rises and rumples (Matsuoka et al., 2015).

Almost three quarters of Antarctica's coastline is fringed by floating ice shelves. As these ice shelves thin and calve, their contact with topography is reduced or lost and buttressing stresses decrease. In response, the upstream ice accelerates almost instantaneously, leading to dynamic ice-thinning, grounding-line retreat, increased ice discharge into the oceans, and sea-level rise (Gudmundsson et al., 2019; Pritchard et al., 2012; Reese et al., 2018; Smith et al., 2020). This sequence of events was observed during the breakup of the Larsen B Ice Shelf in 2002, followed by widespread acceleration of its tributary glaciers (Wang et al., 2022). For example, Flask Glacier's surface speeds were 55% greater in 2012 than in 1997 (Khazendar et al., 2015). Outlet glaciers in the Amundsen and Bellingshausen Sea basins have been observed to be thinning, with consequent upstream ice acceleration due to excess ice shelf melt by CDW (Holland et al., 2019; Konrad et al., 2017; Milillo et al., 2019; Shepherd et al., 2019). Similar trends of mass loss linked to CDW intrusions have also been observed in glaciers in Wilkes Land, East Antarctica (Greene et al., 2017; Nakayama et al., 2021; Silvano et al., 2019). The viability of ~60% of Antarctic ice shelves could be compromised under a high-emission scenario by 2300 (Burgard et al., 2025).

2.8.2 Grounding zone dynamics

The dynamics at and near the grounding line are critical in the processes of ice flow, glacier retreat, and ice-mass loss from grounded regions into the ocean (Durand et al., 2009; Fabien Gillet-Chaulet & Durand, 2010; Konrad et al., 2018; Rignot et al., 2011b; Vieli & Payne, 2005). For example, the stress configuration in ice changes rapidly as it transitions from grounded to floating ice, causing a characteristic surface topography reflecting transient stress configurations (Figure 10; Fricker & Padman, 2006). The location of the grounding line is essential in calculations of ice discharge, and the rate of grounding-line migration is a key indicator of the state of the ice sheet and its stability.

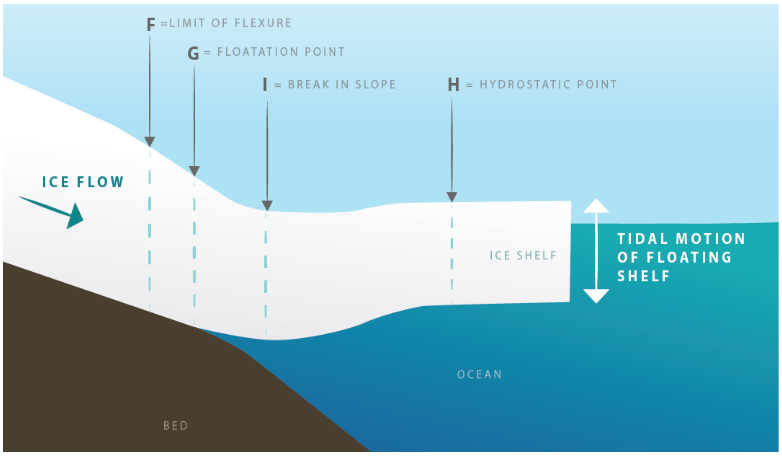

Figure 10: Elements of the grounding zone. The point F marks the limit of flexure (hinge line), G the point at which the ice begins to float (i.e., grounding line), I the break in ice

surface slope, and H the point where ice is freely afloat. This figure is adapted from Fricker et al. (2002).

The grounding line is defined as the location where the ice transitions from grounded to floating, i.e., the (landward) limit of ice floatation (point G in Figure 10). However, this exact location fluctuates on a range of timescales from hours due to the tides (Walker et al., 2013; Wild et al., 2025), seasons (Boxall et al., 2022), or even longer timescales depending on modes of climate variability (Snow et al., 2017). For example, the grounding line position varies with the tides, so it largely fluctuates over timescales of hours to months (Padman et al., 2018; Thomas, 2007). Given this variability, it is helpful to define a grounding zone (Fricker & Padman, 2006) as the region defined from the landward limit of ice flexure (point F in Figure 10) to the inflexion point (point I in Figure 10), the latter point being the break in ice surface slope where the surface is below the hydrostatic level. The width of the grounding zone and the position of the grounding line (point G) within this zone varies considerably in Antarctica (Dawson et al., 2020), depending on the local ice-sheet thickness, the bedrock slope, SMB, and the basal conditions including basal shear stress and subglacial hydrology. Different satellite techniques are used to detect these points and to characterize the grounding zone (Section 4.1). For example, Konrad et al. (2018) mapped grounding-line retreat from 2010 to 2016, finding that almost a quarter of West Antarctica's grounding lines are retreating faster than their retreating rates at the last glacial maximum. The record-high grounding line retreating rate is estimated at 55–610 m d^{-1} across a virtually-flat ice-sheet bed based on spacing between corrugation ridges on deglaciated regions of the Norwegian Sea, northwest offshore of Norway (Batchelor et al., 2023). Similar corrugation ridges are observed both offshore of the eastern Antarctic Peninsula (Dowdeswell et al., 2020) and in the Amundsen Sea Embayment (Graham et al., 2013, 2022).

Beyond geomorphic indicators such as corrugation ridges, the broader marine geological imprint of past ice shelves offers additional constraints on grounding-zone evolution. Paleo-derived evidence shows that reductions in ice-shelf extent in the past frequently promoted grounding-line retreat and enhanced ice discharge, analogous to modern observations. Yet reconstructing these past configurations remains difficult due to uncertainties in sedimentary interpretation and dating resolution. Advances in identifying diagnostic sub-ice-shelf deposits, landforms, and chronological markers have improved our ability to reconstruct past grounding-line stillstands, pinning-point behavior, and retreat trajectories (Smith et al., 2019). These findings indicate that some sectors of the Antarctic margin may have undergone millennial-scale thinning and preconditioning that influences their present-day instability.

2.8.3 The subglacial environment

As ice is an efficient insulator, it is estimated that approximately 55% of the ice at the base of the AIS lies at or near the pressure-melting point (Pattyn, 2010), producing about 63 Gt yr^{-1} of meltwater across the continent (Van Liefferinge & Pattyn, 2013). Characterizing the subglacial environment with this meltwater is essential for understanding ice flow and mass loss. In particular, estimating ice discharge and mass loss relies on what processes and properties control ice flow, and how they vary spatially and temporally, particularly in the faster-flowing regions of Antarctica (Figure 7b). Ice flows by deformation of ice itself and by basal sliding. The latter term is understood here with its broader meaning, encompassing both sliding of the glacier over its bed, whether hard or deformable, and the deformation of subglacial sediments. The magnitude of basal sliding depends on the amount of liquid meltwater at the ice-bed interface and within the deformable till (Clarke, 2005; Kamb, 2001).

Sliding is assumed to be the dominant mechanism of ice flow in fast-flowing regions of the ice sheet (surface flow speed > 50 m yr^{-1}) where there is active subglacial hydrology (Bell, 2008; Rignot et al., 2011b; Ehrenfeucht et al.,2025). The rate of basal sliding depends on a number of subglacial properties, including the subglacial roughness (Hoffman et al., 2022; Kyrke-Smith et al., 2018), the substrate material properties (Koellner et al., 2019), and the presence or absence of subglacial water (Weertman, 1957).

Because acceleration in the ice sheet system is small, driving stresses must be balanced by resistive stresses throughout the ice sheet system. At the base of a glacier, these stresses are partitioned between "form drag" (resistance to flow associated with the macro-scale morphology of the substrate) and "skin drag" (resistance to flow associated with the material strength of the interface between ice and its substrate). As a result, knowledge of substrate roughness at a variety of scales is important for understanding and modeling glacier sliding (Hoffman et al., 2022; Weertman, 1957). Errors in our knowledge of the subglacial topography propagate into our estimates of subglacial material strength, and can lead to erroneous projections of sliding as the stress state of the glacier changes.

In the interior of a hydrological catchment, meltwater typically flows through a distributed "sheet-like" system (Weertman, 1957), often characterized by linked cavities (multiple connecting lake-like or accumulation features), as inferred in the Thwaites Glacier catchment (Schroeder et al., 2013) and the Aurora Subglacial Basin (Dow et al., 2020; Wright et al., 2012). Routing of subglacial water changes with changes in the ice geometry (Young et al., 2016). As the drainage system changes, channelized efficient hydrological systems form, particularly near the grounding line, typically within a few tens of kilometers or less (Hewitt, 2013; Sommers et al., 2018; Werder et al., 2013). Furthermore, over 600 subglacial lakes have been detected in Antarctica from radio-echo sounding and satellite measurements (Livingstone et al., 2022; Siegert et al., 2016). For example, surface elevation changes have been detected using satellite altimetry, indicating the draining and filling of "active" subglacial lakes (Fricker et al., 2016; Stearns et al., 2008; Wingham et al., 2006), although surface elevation changes alone are not sufficient in determining their water volume changes (Siegert et al., 2016).

Subglacial hydrology plays a key role in ice dynamics (Dow et al., 2020; Dow, 2023). However, there are many unknowns that increase uncertainty associated with the amount of basal meltwater produced, and the variability in the subglacial hydrology system. For example, Smith-Johnsen et al. (2020) found that GHF influences the extent and efficiency of the subglacial hydrology system in the Northeast Greenland Ice Stream, although the estimated GHF is argued geologically unfeasible (Bons et al., 2021) and in any case similar analyses have not yet been done for the AIS. Furthermore, modelling analysis shows that fine scale (< 20 km) variability in GHF can increase the basal meltwater production compared with a smoother GHF field (McCormack et al., 2022). Ehrenfeucht et al. (2025) produced the first subglacial hydrology model for Antarctica, showing the widespread presence of subglacial melt, particularly in marine basins. Recent evidence suggests that subglacial hydrology could increase ice loss from Antarctica under climate change (Kazmierczak et al., 2024; Pelle et al., 2023, 2024; Zhao et al., 2025). These highlight the importance of better characterizing the subglacial environment across the AIS.

Airborne and satellite remote sensing can provide insight into bed properties, including the substrate and presence of sediments (Aitken et al., 2016; Chu et al., 2021; Li et al., 2022a; Schlegel et al., 2022; Schroeder et al., 2014), as well as subglacial hydrology (Fricker et al., 2007, 2010, 2016; Schroeder et al., 2013; Siegert et al., 2016; Smith et al., 2009; Stearns et al., 2008; Wingham et al., 2006), and GHF (Burton-Johnson et al., 2020;

Damiani et al., 2014; Golynsky et al., 2018; Lowe et al., 2022; Martos et al., 2017). Modelling sensitivity studies have been used to determine high-priority regions for measurements of the subglacial environment. For example, McCormack et al. (2022) determined the minimum basal heating required to bring the ice base to the pressure-melting point in the Aurora Subglacial Basin, East Antarctica, and hence determined areas where measurements of basal heat sources will be of most use in constraining basal meltwater production estimates. Such modelling sensitivity studies could help guide field surveys, including determining priority targets for measurement.

Calculations of mass balance that rely on estimates of the discharge across the grounding line typically assume that the main mechanism of ice flow is sliding. This assumption allows one to approximate the depth-averaged ice velocity with the satellite-measured surface velocity. This assumption may not hold in a region that has a channelized subglacial hydrology system, where basal lubrication has been lost or where basal roughness or substrate strength is otherwise high. For example, in the ~100 km upstream of the Thwaites Glacier grounding line, radar evidence points to a channelized subglacial hydrological network (Schroeder et al., 2013) in a non- sedimentary region without deformable till, known as a “strong bed” (Joughin et al., 2009). In this region, modelling suggests that bed-parallel vertical shear deformation may locally contribute up to 40% of the overall surface flow, depending on the flow law used, indicating that the assumption of the depth-averaged velocity being equal to the surface velocity is not valid (McCormack et al., 2022). More broadly, ice deformation may play a more substantial role in ice flow and dynamics than what is typically assumed for estimates of ice discharge (Millstein et al., 2022; Minchew et al., 2018; Ranganathan et al., 2021; Zeitz et al., 2020), and yet is relatively poorly understood. This influence of ice deformation has important implications for projections of Antarctic mass loss and warrants further study.

2.8.4 Mechanisms for instability

Establishing the stability of the AIS is a critical question (Noble et al., 2020), with a history dating back to the early 1970s (e.g., Mercer, 1978). The ice-sheet instability is mostly influenced by the ice and bed properties in the vicinity of the grounding zone (Schoof, 2007; Thomas & Bentley, 1978; Weertman, 1974). Several mechanisms for ice-sheet instability have been proposed (Figure 11), the most well-known of which is MISI.

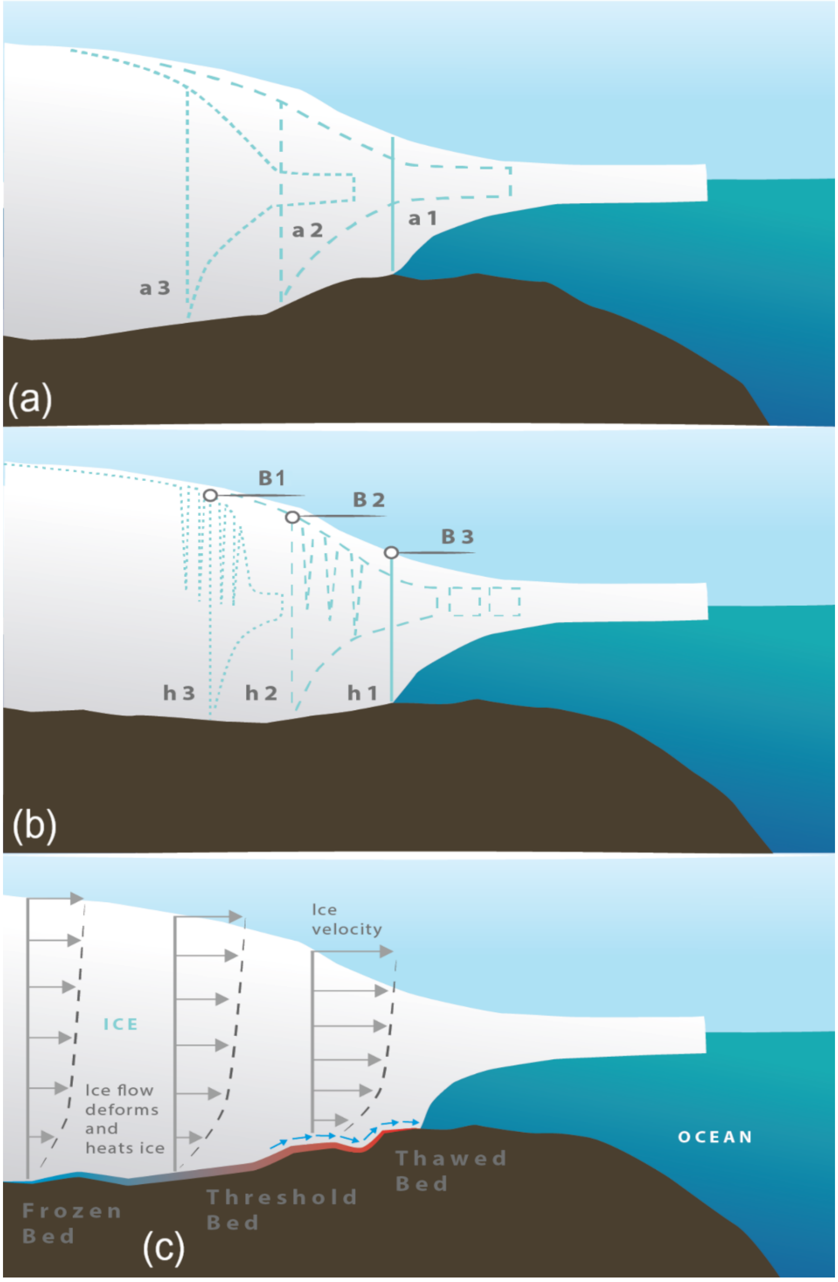

Figure 11: Three mechanisms of ice-sheet instability. The solid strokes in the all panels outline the ice-sheet geometry today and the dashed strokes in panels (a) and (b) outline the ice sheet geometry in the future. (a) Marine Ice Sheet Instability (MISI) that can occur when the grounding line locates on the retrograde (inland lowering) slope of the bed under the sea level. As the grounding line retreat, ice thickness increases so that the cross-sectional area *a* of flux to the ocean increases: a3 > a2 > a1. (b) The proposed Marine Ice Cliff Instability (MICI) that can occur regardless of the bed slope directions when the ice-sheet terminus is a very tall cliff which cannot be stabilized. As the terminus retreats, height *h* of the ice-sheet terminus above the sea level becomes larger (h3 > h2 > h1), resulting in more readily calving and reduced buttressing *B*: B3 < B2 < B1. (c) Thermo-frictional feedback to melt the base of the ice sheet as flow speed increases towards the grounding line.

MISI is a positive feedback process that may occur when a grounding line retreats on a retrograde bed slope (sloping downwards into the interior of the catchment) of a marine ice sheet (i.e., an ice sheet whose bed lies below sea level). At the landward location of the initial grounding line, the ice below the sea level is thicker and thus becomes buoyant resulting in the initial grounding-line retreat. Once the grounding line retreats, the ice thickness at a new grounding line increases and thus ice-discharge flux increases. On a prograde bed slope, enhanced discharge from grounding line retreat can be offset by reduced glacier thinning, yielding smaller ice-discharge flux that stabilizes the grounding-line retreat. But on a retrograde bed slope, thinning causes further ungrounding, which causes acceleration and thinning and further ungrounding.

Glaciers with a retrograde bed slope include the Thwaites and Pine Island glaciers in the Amundsen Bay, WAIS, and major EAIS outlet glaciers such as the Totten and Denman glaciers (Rintoul et al., 2016; Thompson et al., 2023). A number of ice-sheet modeling studies have examined their potential for undergoing irreversible retreat. For example, Joughin et al. (2014) suggests that the accelerating grounding line retreat and discharge from Thwaites Glacier may indicate that this glacier is experiencing MISI. However, a more recent study indicates that under the preset-day ice geometry, Thwaites Glacier grounding line is not currently undergoing irreversible retreat (Urruty et al., 2022), although under long-term, sustained present-day climate forcings it is possible to find ice-sheet-model parameter combinations that could lead to irreversible collapse of the Amundsen Sea Embayment (Reese et al., 2022). Evidence points to a similarly unstable retreat occurring at the Pine Island Glacier (Favier et al., 2014), and that, under 1.2°C warming, retreat of the Pine Island Glacier could lead to the collapse of the WAIS (Rosier et al., 2021).

Recent extensions to the MISI theory demonstrate that local ice and bed properties alone are not sufficient in establishing the conditions for grounding-line stability. For example, grounding-line retreat depends not only on the bed slope, but also the bed curvature (Sergienko & Wingham, 2022) and the presence of locally elevated topography (Figure 12a; e.g., Castleman et al., 2022; McCormack et al., 2021; Schlegel et al., 2018). Grounding-zone wedges—sedimentary buildups formed during grounding-line stillstands—can provide pinning points that locally stabilize grounding-line position and modulate retreat trajectories. Also, isostatic uplift in response to ice-mass unloading (GIA; Section 2.6.1) can temporarily or permanently halt grounding-line retreat (Figure 12b; Kachuck et al., 2020; Suganuma et al., 2022; Hoarier et al., 2025). For instance, a theoretical study using elastic Earth models showed that gravity and deformation-induced sea-level changes local to the grounding line contribute to stabilizing ice sheets grounded on retrograde bed slopes over several hundred years (Gomez et al., 2010). In a simulation at continental scale, Larour et al. (2019) showed how these instantaneous solid Earth responses to load redistribution can stabilize grounding lines after 250 years, with noticeable effects after 350 years. Stabilizing effects also hold when considering viscoelastic mantle models and time scales up to several millennia (e.g., Gomez et al., 2015). Regarding viscous effects, earlier studies suggested that on short timescales (< ~500 years) viscous effects may be ignored when the ice sheet model is forced from steady state (Gomez et al., 2012). However, a recent analysis suggests that an effective equilibrium between Pine Island Glacier's retreat and the response of a weak viscoelastic mantle can reduce the loss of ice mass by almost 30% over just a 150-year period (Kachuck et al., 2020).

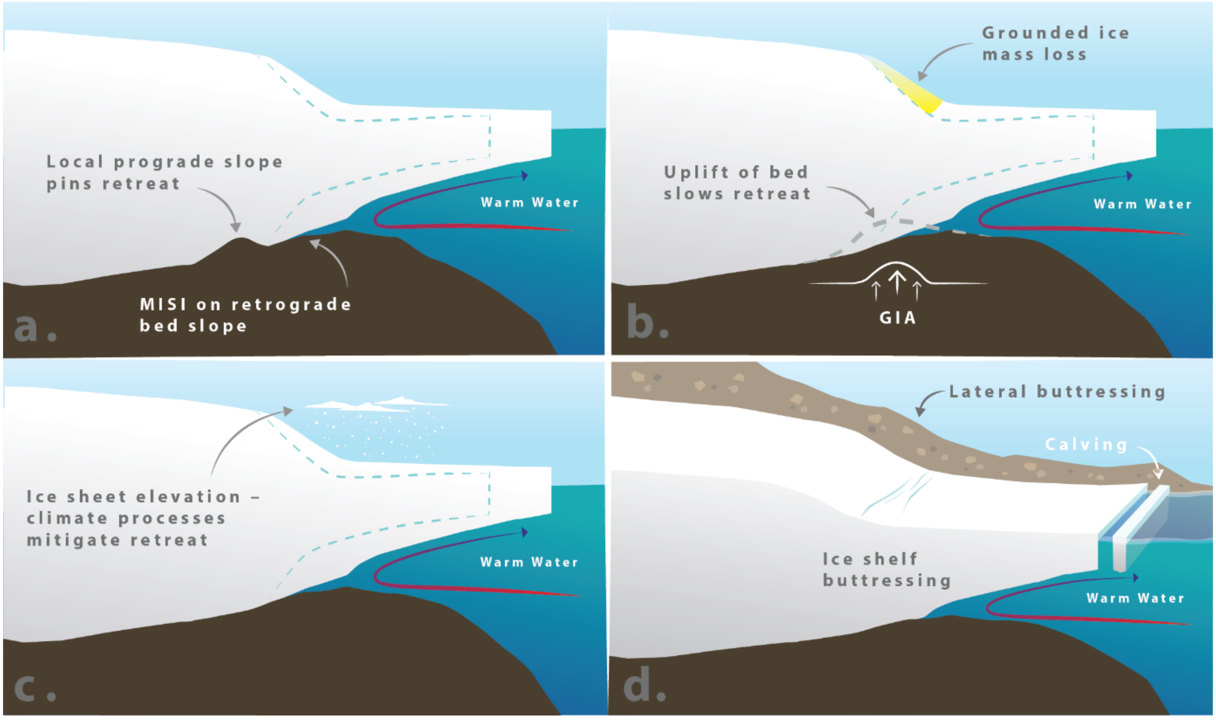

Figure 12: Hypothesized mechanisms that impact the stability of a marine-ice-sheet grounding line on a retrograde bed slope (i.e., MISI-prone grounding line) under the influence of a warming ocean. In each panel, the solid strokes outline the ice-sheet geometry today and the dashed strokes outline the ice sheet geometry in the future. (a) Retreat onto significant topography can temporarily or permanently prevent MISI, depending on changes in climate forcing. (b) Solid-earth uplift in response to ice mass unloading (i.e., GIA) can slow (or even prevent) grounding line retreat. (c) Ice-atmosphere interactions, including the dependence of SMB and surface melt on the ice surface elevation and temperature can stabilize the grounding line on a retrograde bed. (d) Where a marine ice sheet is in an embayment, a grounding line lying on a retrograde bed may be stable or unstable, depending on lateral buttressing and boundary conditions, including calving.

A recent study has highlighted the importance of ice-climate feedbacks, demonstrating that no general stability conditions hold when the effects of ice surface temperature and elevation on SMB are taken into consideration (Figure 12c) (Sergienko, 2022). When a marine ice sheet has a confining boundary such as the embayment in Figure 12d, the lateral buttressing may stabilize the grounding line despite the retrograde slope (Haseloff & Sergienko, 2018). Because of the lateral confinement, this last situation is not a valid application of MISI theory; nevertheless, given the irregularities of an actual coastline, a given ice sheet may have sections that are partly confined and thus subject to some degree of lateral buttressing. From these examples, we argue that the stability of individual systems can only be determined on a case-by-case basis, varying with the ice dynamic processes, regional topographic controls, bed topography, as well as the climate and solid-Earth feedbacks.

The marine ice cliff instability (MICI; Figure 11b) was proposed as an instability mechanism for rapid glacier retreat and consequent sea-level rise (DeConto & Pollard, 2016; Pollard et al., 2015). MICI was motivated by records from the Pliocene warm periods that show a global-mean sea level 10–20 m higher than today's despite similar global mean temperatures. MICI is hypothesized to be driven by a combination of ocean-driven ice-shelf melt and accompanied atmospheric warming as temperatures rise, leading to ice surface melting, hydrofracture, and eventual ice-shelf collapse. If the ice freeboard is greater than ~90 m a.s.l. (i.e., ice shelf thicker than about 900 m), the ice exceeds its yield stress and cliff collapse could occur, leading to accelerated grounding-line retreat as long as the ice thickens into the interior even in the absence of a retrograde bed slope (Needell & Holschuh, 2023). By including MICI, some models estimate higher rates of mass loss and sea-level rise (Bars et al., 2017; Fox-Kemper et al., 2021). However, as with other threshold behaviors for the ice sheets, MICI is sensitive to parameters that are poorly known, and including the mechanism in projections therefore substantially increases their uncertainties. For example, modelling suggests that MICI may be sensitive to the parameterization of ice-ocean processes (Edwards et al., 2019; Golledge et al., 2019). Furthermore, modelling by Clerc et al. (2019) indicates that the strength of ice is an important controlling property in MICI, and under the Pliocene conditions, cliff heights > 540 m are required to induce instability. So far, MICI is not widely supported, and no direct observational evidence supports MICI, although there may be some evidence of cliff failure in paleo records (Wise et al., 2017). A recent study using three ice sheet models (Morlighem et al. 2024) shows that the WAIS is not vulnerable to MICI under climate forcing scenarios to 2100, highlighting the need to better understand processes underlying cliff failure.

A final type of potential grounding-line instability is based on internal ice thermo-frictional feedbacks (Figure 11c; Brinkerhoff & Johnson, 2015; Payne & Dongelmans, 1997; Schoof & Mantelli, 2021). The mechanism applies to regions where the ice base is close to the pressure-melting point. In such a region, internal ice thermo-frictional feedbacks could generate spontaneous thaw as a result of both the temperature dependence of sliding (Fowler, 1986; Mantelli et al., 2019; Mantelli & Schoof, 2019) and deformational flow (Budd & Jacka, 1989; Payne, 1999). Self-reinforcing feedbacks could then lead to the formation of ice streams that would accelerate ice loss and sea-level rise. Recent modelling of the dependence of rapid ice flow on basal temperature shows that only a few degrees of warming at the ice bed–such as that generated by viscous and dissipative heating–could induce thaw in slow-flowing regions of the EAIS, leading to large-scale mass loss (Dawson et al., 2022). However, as with MICI, this mechanism is not yet supported by observations.

Considering all three mechanisms, their potential application for predicting instability and rapid sea-level rise highlights the need for detailed bed topography across the grounding zone, including adjacent seabed, as well as improved estimates of basal and englacial temperatures and hydrology, particularly beneath the fast-flowing ice.

3. Surveying the coastal zone of Antarctica

The coastal zone of Antarctica were surveyed only near established research stations at the beginning of the modern scientific era of Antarctic research. Survey coverage expanded with over-snow traverses both inland and along the coast (e.g., Robin, 1953). Pioneering airborne surveys began during the 1970s, easing the way to survey the vast AIS (Drewry, 2023). Here we review instruments, platforms, and logistics suitable for such airborne surveys (Figure 13). Airborne surveys often need complementary ground-based and vessel-based surveys, and are also combined with satellite data to make a more complete, synthesized dataset. Such a dataset can then be used to constrain or test numerical models of ice, solid Earth, ocean, and regional atmosphere. Connecting these multi-disciplinary approaches seamlessly and efficiently requires well-established processing pipelines to generate large-volume datasets in standard data formats that can then be widely and openly shared and archived in perpetuity through an efficient data management system. Here, we review these items and identify remaining challenges for future surveys in the coastal zone of Antarctica.

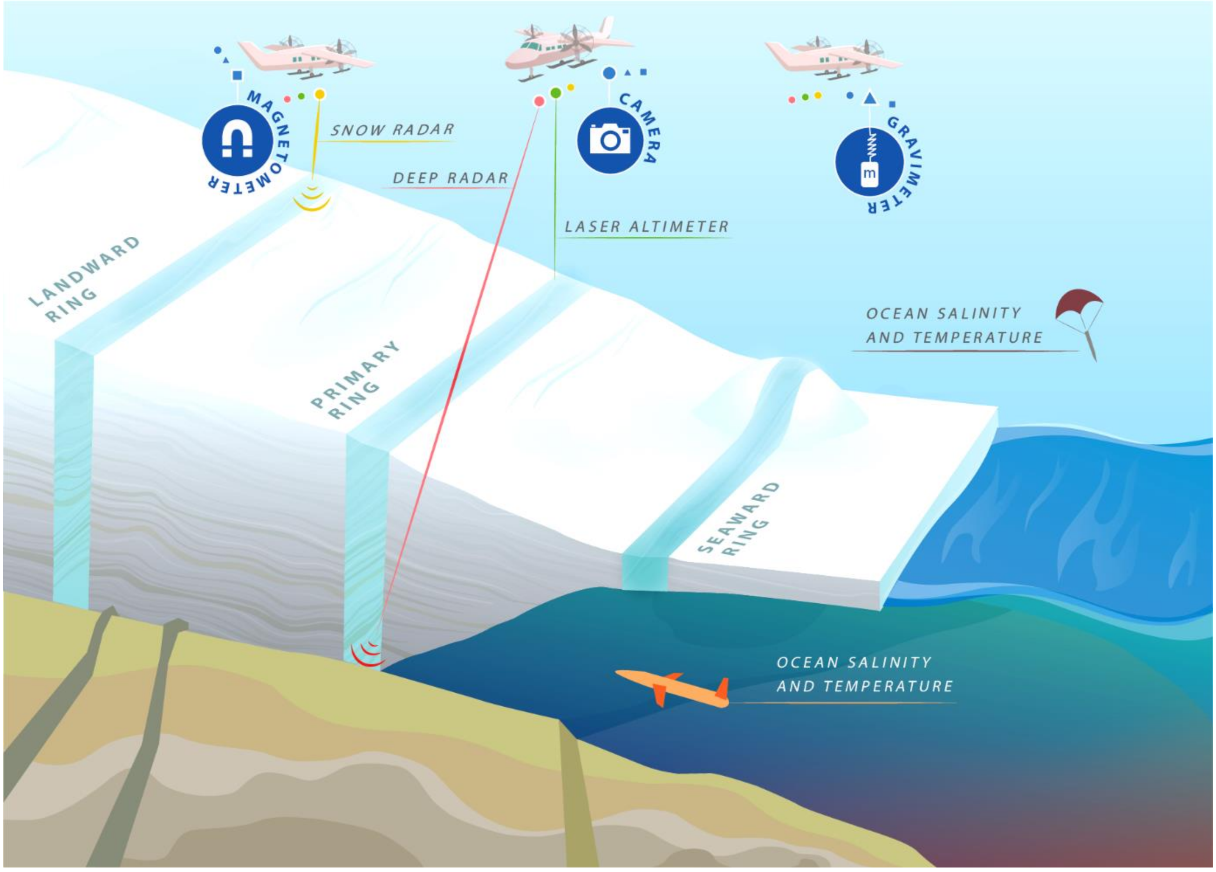

Figure 13: Schematic of airborne surveys targeting the coastal zone of Antarctica, including ice-sheet terminus, the vicinity of the grounding zone, ice shelves, and open or sea-ice-covered ocean. Three profile locations in the coastal zone are here called landward ring, primary ring and seaward ring, to reflect the need of circum-Antarctic surveys (Section 5). All instruments are valuable for surveys at three rings locations; three airplanes illustrate different applications and priorities of these instruments.

3.1 Airborne instruments

3.1.1 Deep-sounding ice-penetrating radar

Ice-penetrating radar (IPR) is the most widely deployed instrument to measure an ice sheet's thickness, investigate its basal properties, and unravel its internal stratigraphy (Figure 14; e.g., Bingham & Siegert, 2007; Drewry, 1983; MacGregor et al., 2021; Schroeder et al., 2020; Bingham et al., 2025; Franke et al., 2025). IPR has provided much of the data for our understanding of the topography beneath the AIS (e.g., Fretwell et al., 2013; Morlighem et al., 2020; Pritchard et al., 2025) as well as the AIS's subglacial hydrology (e.g., Christianson et al., 2016; Schroeder et al., 2013), subglacial roughness (Eisen et al., 2020), internal structure and rheology (e.g., Cavitte et al., 2016; Koutnik et al., 2016; Matsuoka et al., 2003; Young et al., 2021), and the complex interactions between these features (e.g., Bell et al., 2011; Hills et al., 2022; Schroeder et al., 2014; Wolovick et al., 2014; Franke et al., 2024). IPR is critical to understanding the boundary conditions and processes that govern the flow of the AIS toward its coastal outlets.

Terrestrial IPR measurements vary in several aspects, including by platform type (ground-based or airborne, 10 km h^{-1} to > 300 km h^{-1} platform speed), by center frequency (~1 to > 500 MHz) and bandwidth, and by system design (e.g., pulsed, chirp pulse, and continuous waveform). All involve the downward transmission of a repeatable radio-frequency signal into the subsurface and then the subsequent detection and interpretation of typically fainter reflections from dielectric contrasts within and beneath the ice (Figures 14 and 15b). In contrast to their use in warmer and wetter terrestrial environments elsewhere, IPR here can usually probe the full depth of the multi-kilometer-thick AIS because of the relative transparency of dry ice to radio waves (e.g., MacGregor et al., 2007; Matsuoka et al., 2012). However, the returned signal can be weak when the bed is rougher or steeply sloped (e.g., deeply incised trough), and in regions with rugged terrain when the bed echo is nearly indistinguishable from other overlapping echoes.

Figure 14 shows various radargrams collected across outlet glaciers. Figure 14a is a case that the echo from the ice-sheet surface and bed are well recorded, and the glacier (represented with high flow speed) is located in a lowland with elevated beds at both lateral sides. When a glacier lies in a valley with steep lateral walls, bed echo from the walls can be intermittent (Holt et al., 2006). Figure 14b shows an example of such a case where the bed is not detected continuously but a data interpolation method can estimate bed topography there (Sections 3.6.1 and 4.2). Where a glacier has an active subglacial or englacial hydrological system, radar echoes sometimes also appear from those features (Figure 14c). Subglacial water usually appears as a strong reflector, but water trapped within basal ice reduces radar bed-echo strength at active subglacial lakes, complicating their detection (Hills et al., 2024). In the coastal zone of Antarctica, particularly on the more northerly Antarctic Peninsula, IPR sounding of bed topography there may be challenging due to seasonal surface meltwater networks and valley sidewalls. Another common problem–even far inland–is surface clutter from extensive surface crevassing (Peters, 2005). Modern multi-channel systems with array of antennas are especially useful for this purpose (Gogineni et al., 2014), and may also use phase differences in the arrival of bed echoes in a cross-track array to determine the direction of arrival for incoming waves, allowing for the discrimination of clutter from nadir reflections (e.g., Li et al., 2013). Such radars can perform three-dimensional mapping of bed topography from both ground-based platform (Paden et al., 2010) and more recently from airborne platform (Holschuh et al., 2020). Another solution to reduce surface clutters is to deploy a lower-frequency IPR with a longer wavelength that is less sensitive to water and crevasses but this may make signal interpretation harder in rugged terrain (e.g., Mouginot et al., 2014).

Radar data collected across fast-flowing glaciers often do not record englacial reflectors. However, ice stratigraphy in slowly moving ice out of fast-flowing glaciers can often be visualized at least the top half to one third of the ice thickness depending on the performance of the IPR and coherence of radar reflectors. Because these englacial reflectors are in most cases isochrones, their shapes are affected by SMB (e.g., Waddington et al., 2007), ice deformation (e.g., Kingslake et al., 2016), and if they are very close to the bed, subglacial processes including both locally-enhanced melting (e.g., Jordan et al., 2018) and accretion (e.g., Bell et al., 2011). Figure 15b shows ice stratigraphy of an ice rise, Martin Peninsula in West Antarctica. In the vicinity of the topographic crest where the ice surface is much flatter than the flank, non-linear ice rheology makes the ice highly rigid, resulting in upward arches of isochrones if the crest position has been stable over several millennia (Raymond, 1983). These upward arches indicate older ice at a given depth near the divide and dome, compared to the flank sites. The shape of these arches are often used to evaluate evolution of the ice rise and deep ice-coring site (e.g., Martin et al., 2014).

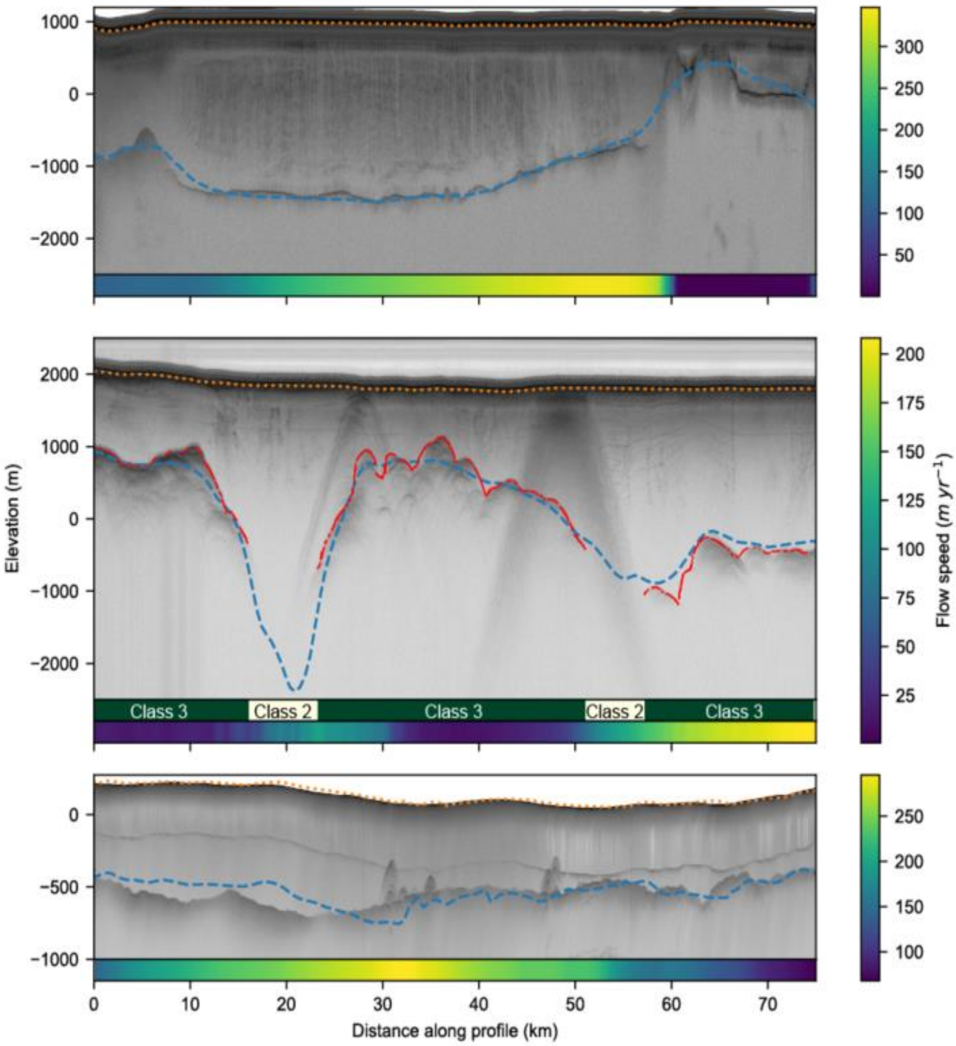

Figure 14: Across-ice-flow topography of fast-flowing outlet glaciers detected with airborne deep-sounding IPR. All profiles are 80-km long, and panels (a) and (b) have the same vertical exaggeration. Radar echoes from the surface (orange) and bed are used to determine ice thickness. Then it is combined with airplane's location data collected with GNSS and lidar to determine the ice-sheet surface to derive surface and bed elevations. Blue dotted curves near the bed echo show interpolated Bedmachine topography (version 3, Morlighem et al., 2020). The color stripe at the bottom of each panel shows ice flow speed; the scale of the color stripe is different for all panels. (a) Bed is well visualized beneath more than 2-km-thick ice (Recovery Glacier, Corr et al., 2021). (b) Very steep valley walls are hardly imaged using radar because of small back scattering (Denman Glacier, CReSIS, 2024). Also, the bottom of the valley is under thick, fast-flowing glacier; surface crevasses cause large scattering loss and warm and thick ice body causes large power attenuation, both of which may result in very weak echo from the bed. In this panel, the picked bed echo for ice-thickness extraction is shown with red; we categorize the location where the bed is continuously detected as class 3, whereas the bed that is not detected over 0.5 km or longer is classified as class 2 (the binary color stripe above the flow speed). (c) Bed is flatter and ice is thinner, favorable conditions for bed detection using IPR, but spontaneous hyperbola-shape echoes from subglacial water conduits

appear as well. Also a continuous echo in the middle of the ice sheet represents a double-bounced echo; two trips between the airplane and the ice sheet (Ragnhild Glacier, Drews et al., 2017).

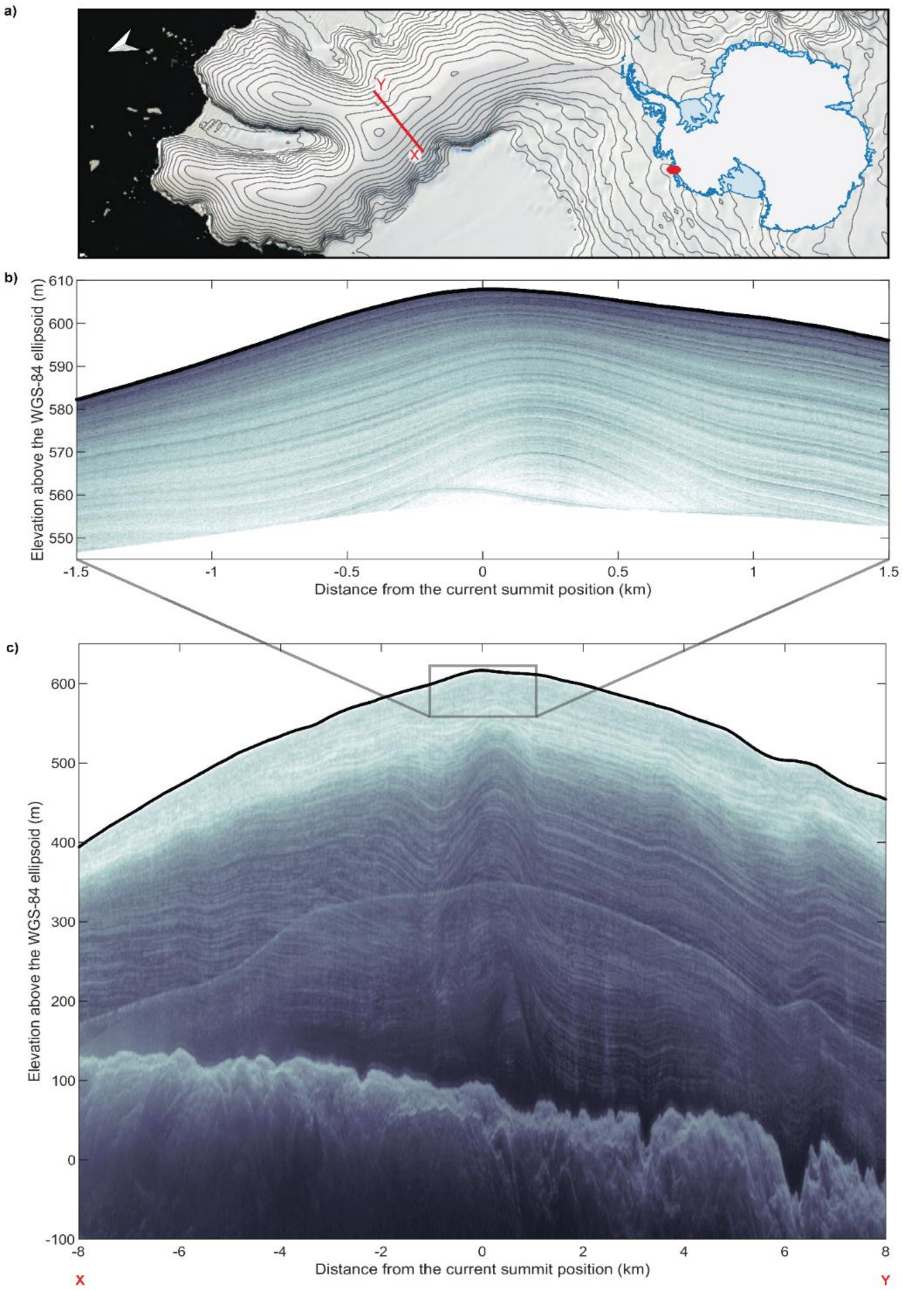

Figure 15: Radargrams over Martin Peninsula in the Amundsen Embayment, West Antarctica, collected by NASA Operation Ice Bridge across the local topographic ridge. (a) Surface topography (40 m contour intervals using REMA (Reference Elevation Model of Antarctica) DEM; Howat et al., 2019). Background is Landsat 8 satellite images. (b) Radargram of the near surface detected with a microwave IPR (snow radar in Table 1). The radar images the firn stratigraphy in the top ~60 m and the data were shifted according to the surface topography. These englacial reflectors represent isochrones and can be used to determine spatial pattern of SMB (Section 3.6.3). NASA OIB flight frame

ID: 20141111_02_331. (c) Radargram of the deep-sounding IPR (MCoRDS in Table 1). Double-bounced echo appears. The standard NASA OIB processing does not reveal the Raymond Arches characterizing the stable ridge position over a few millennia (section 3.6.3), mainly because the slope of the englacial reflectors associated with the arches are too steep (up to ~ ±4^{o}) for the standard synthetic aperture angle of 18^{o}. To visualize steeper englacial reflectors near the crest, the full aperture angle of 115^{o} was used in synthetic aperture radar processing using the CReSIS Toolbox (CReSIS, 2024). This angle corresponds to an along-track resolution of 0.25 m. NASA OIB flight frame ID: flight 20141111_08-010.

Several airborne IPR systems have been used to survey the AIS (Table 1) and remain available for future surveys. Historically, each IPR was developed by an individual research institution or National Antarctic Program for a specific platform and then deployed over the course of several-week to month-long campaigns, spanning years to decades. However, as IPR systems have improved, at least two IPRs (MCoRDS and MARFA in Table 1) have become sufficiently standardized to be used by multiple nations on different aircraft. These improvements have also made it easier to compare or integrate datasets acquired using nearly identical IPRs across Antarctica.

Table 1: Airborne IPRs suitable for surveying the coastal zone in Antarctica. Except for the snow radar targeting the shallowest 100 m, all the other radar systems are for deep sounding.

IPR system name	Frequency range (MHz)	Maximum depth (m)	Operated or adaptable (*) Platform(s)	Key reference
Multi-channel Coherent Radar Depth Sounder (MCoRDS)	180 – 210 (P-3), 150 – 600 (BT-67)	> 4000	P-3 *, BT-67 *, DHC-6, multiple UASs	Arnold et al. (2019), Hale et al. (2016), Rodriguez-Morales et al. (2013)
Multifrequency Airborne Radar-sounder for Full-phase Assessment (MARFA)	52.5 – 67.5	>3000	BT-67 *, DHC-6 *, AS-350*[b]	Young et al. (2016)
High Capacity Airborne Radar Sounder (HiCARS)	52.5 – 67.5	> 4000	DHC-6*, AS-350*	Young et al. (2016)
IcePod Deep ICE Radar (DICE)	158– 218	> 4000	LC-130H	Tinto et al. (2019)
IcePod Shallow Ice Radar (SIR)	1700-2300	~350	HC-130H	Tinto et al. (2019)
RLK-130	122.5 – 137.5	> 3000	Antonov Aircraft An-2	Popov (2020)

Polarimetric radar Airborne Science Instrument (PASIN)	145 – 155	>4000	DHC-6 *	Jeofry et al. (2018)
Snow Radar	2,000 – 18,000	<100	P-3 *, BT-67*, DHC-6	Rodríguez-Morales et al. (2014)
Airborne SAR/Interferometric Radar Altimeter System (ASIRAS)	13,000 – 14,000	< 20	BT-67, TO, DO-228, P-3	Kowalewski et al. (2021)
Arizona Radio Echo Sounder (ARES)[a]	1.25 – 3.75, 2.5 – 7.5	>1500	DHC-3 *, DHC-6	MacGregor et al. (2021)
Platform for Experimental Radio Echo Geophysics in Remote Ice Navigation and Exploration (PEREGRINE)[a]	350–450	<500?	X-UAV Talon *	Teisberg et al. (2022)

[a] ARES and PEREGRINE have not yet been deployed to Antarctica but are considered candidate IPRs for such surveys.

[b] Helicopter rather than fixed-wing aircraft.

In general, airborne IPR data are best obtained 1) by flying at a low, fixed altitude above ground level (< 500 m if possible) to stabilize and minimize the geometric spreading loss of the transmitted wavefront as well as to reduce surface clutter, 2) by flying at slower survey speeds (< 100 m s^{-1} or 360 km h^{-1} if possible) to increase effective receiver averaging and suppress incoherent noise, 3) by flying with minimal aircraft maneuvers to reduce off-nadir fading of specular reflections especially internal reflections (Figure 15; Sections 3.5.1 and 3.6.3), and 4) by flying at an altitude with which multiples between the airplane and the ice-sheet surface do not distract from interpretations of primary reflections (Figures 14c and 15c). However, even with sub-optimal flight characteristics, a combination of faster and more stable electronic subsystems, improved geolocation and pointing data, and post-processing techniques permit high-quality IPR data acquisition. Because of its fundamental value for understanding glacier and ice-sheet processes, progressive miniaturization of electronic subsystems, and the typically low-interference environment of glaciated regions, IPR is now regularly integrated into small- to medium-size uncrewed aerial systems (UAS; Section 3.4).

3.1.2 Shallow-sounding ice-penetrating radar

Shallow IPR is distinguished from more traditional, deep-sounding IPR by the generally higher center frequencies needed (~500 MHz to ~20 GHz) to resolve firn stratigraphy (Figure 15b). This shallow stratigraphy (<100 m depth) is challenging to resolve with the lower-frequency IPRs designed to detect the bed under thick polar ice sheets due to their substantial surface clutter, which masks reflections from within firn. Several studies have used ground-penetrating radar on the ground (e.g., Eisen et al., 2008) and shallow airborne IPR to derive SMB from firn stratigraphy (e.g., Dattler et al., 2019; Le Meur et al., 2018; Medley et al., 2013) and repeated the measurements to derive firn compaction rates (Medley et al., 2015).

Also, some deep-sounding IPR can resolve firn stratigraphy when system parameters are optimized for it (Koch et al., 2024). However, the recent increase in surface melting may transform the warmer parts of the AIS surface into seasonally complex hydrologic networks that more closely resemble the ablation zone of the Greenland Ice Sheet (Kingslake et al., 2017). Meltwater infiltration can disturb the firn stratigraphy, thus hampering SMB reconstructions from the IPR data. Such infiltration can also generate widespread anomalous near-surface ice-lens features that can be detected with shallow IPR (e.g., Culberg et al., 2021, 2022; MacFerrin et al., 2019).

Shallow IPRs have similar survey design requirements as deep IPRs and have been used for sounding firn stratigraphy in both the ice-sheet interior and the annually deposited snow layers in high-accumulation coastal zone. However, interpretating these data is difficult in the percolation and ablation zones (Section 2.4.3) where the simple assumption of detecting annual layering breaks down (Section 3.6.3).

3.1.3 Laser altimetry and digital optical imagery

Airborne laser altimetry, or lidar, has long been recognized as a powerful tool for monitoring changes in ice-surface elevation and thus is used to determine the mass balance of ice sheets, ice caps, and glaciers (e.g., Abdalati et al., 2002; Krabill et al., 2002 and references therein).To help analyze the lidar, surveys often include high-resolution, high-accuracy optical imagery. The imagery is also helpful for classifying surface features (e.g., Studinger et al., 2022).

To compile accurate bed elevation maps from the IPR ice-thickness data, we need reliable ice-surface elevations. Airborne lidar provides much more accurate ice-surface elevations than that from IPR, and thus should improve the accuracy of bed elevation measurements. The increased accuracy of bed elevations will reduce cross-over errors and improve accuracy of gridded products. In addition to improving the accuracy and internal consistency of the radar-derived bed elevations, lidar also establishes a surface elevation baseline. Such a baseline serves as a reference to determine future ice-surface elevation changes and therefore geodetic mass balance of the ice sheet (Section 2.1.1). Although polar-orbiting spaceborne lidars can provide data, their coverage has gaps near the coastal areas of Antarctica. Airborne lidar surveys can fill this gap and develop historical changes of the ice thickness in the coastal zone in principle. However, it requires not only lidar data but very accurate airplane positions at the centimeter precision both in the vertical and horizontal directions, which is not always possible. Additional optical imagery can provide a low-cost auxiliary dataset that helps us to interpret lidar and other data. See MacGregor et al. (2021) for a list of optical cameras and their specifications that have been used to map ice sheets.

Three lidar systems have been used extensively at low elevations in polar regions (Table 2), together with deep-sounding IPRs. NASA’s ATM (airborne topographic mapper) consists of two conically scanning laser altimeters that independently measure the surface elevation along the path of the aircraft at 15° and 2.5° off-nadir. The most recent version of the ATM system uses co-located 532 and 1,064 nm lidars. The other two systems are the Riegl VQ-580 II and the Riegl Q240i, both of which are commercially available line scanners using near-infrared lasers, with the former Riegl being the newer and more capable system.

Table 2: Select examples of airborne lidars used over polar ice sheets. PRF stands for Pulse Repetition Frequency, and FOV stands for Field Of View. For more details, see MacGregor et al. (2021).

Name	Operator	Wavelength (nm)	PRF (kHz)	Scan type	Scanner FOV	Waveform recording
ATM	NASA	532 and 1,064	10	conical	5°, 30°, and 45°	yes
Riegl VQ-580 II	Univ. Alaska, Fairbanks	1,064	100#	linear	75°	no
Riegl Q240i	Technical univ. Denmark (DTU-Space)	904	10	linear	60° and 90°	no

this is a nominal value. The PRF for Riegl VQ-580II is adjustable.

Key lidar parameters relevant for mapping detailed surface topography in Antarctic coastal zone include wavelengths, scan geometry, waveform recording, flight elevation, and flight speed. Existing lidars mainly use near-infrared (905 or 1064 nm) or green (532 nm) wavelengths. The green may have some subsurface penetration and subsurface volume scattering that could result in an elevation bias (e.g., Cooper et al., 2021; Fair et al., 2024; Smith et al., 2025; Studinger et al., 2024). If so, subsurface penetration would be an issue for repeat ice thickness measurements. Nevertheless, both near-infrared and green lidars are suitable for coastal surveys.

The lidars should illuminate the area on the ice surface that is imaged on the bed by the IPR. Most IPRs are along-track, nadir-looking, but given the size of the radar footprint at the bed being several hundred meters wide (e.g., Peters, 2005), a lidar swath on the ice surface is desirable. If the method includes tomographic radar processing, resulting in across-track radar coverage of up to several kilometers from the nadir point (e.g., Holschuh et al., 2020; Paden et al., 2010). To complement this wide radar swath, lidars with large scan angles (i.e., 90°) across the track are required to capture matching surface elevation data.

Swath lidars have been used with either a conical scan geometry or a linear, unidirectional scan geometry. The advantage of conical scanners is the near constant angle of incidence, which results in a nearly constant return signal strength. The large variation in return signal strength of line-scanning airborne lidars between nadir and the edge of the scan can affect the calculated range in a way that depends on the waveform tracking algorithm. This variable influence, known as range walk, needs to be carefully calibrated to produce an accurate range, and therefore elevation, measurement (e.g., Studinger et al., 2022). The advantage of a linear scan geometry is a more regular scan pattern and point density compared to conical scanners. Modern line and conical scanners both meet the requirements necessary for coastal surveys.

Most high-end commercial and custom-build lidars such as NASA's ATM, record both transmit and return waveforms for further analysis. Waveform analysis enables estimates of water depths of supraglacial lakes and streams (Studinger et al., 2022) and extraction of higher-order geophysical moments, such as centroid, skewness, and kurtosis for data interpretation (e.g., Yi et al., 2015). However, the merits of these applications must be balanced against the increased cost and associated larger data volume and complexity.

For optical imagery, commercially available digital single-lens reflex cameras and shutterless cameras with interchangeable lenses provide cost-effective alternatives to specialized, high-end photogrammetry cameras used in the past (e.g., MacGregor et al., 2021). Options range from low-cost, time-tagged images to high-resolution, geolocated, and orthorectified imagery, which requires substantially more processing effort. Pixel resolutions for these cameras are typically smaller than the lidar footprint size on the ground, making them well suited to support lidar interpretation and footprint-scale surface classification.

Both lidars and optical cameras require a cloud-free line of sight between the survey aircraft and the surface. Lower flight elevations (~500 m above ground level) improve the likelihood of successful data collection compared to high-altitude altimeters, an important consideration in the Antarctic coastal zone where cloud cover is frequent. Modern lidars with high pulse-repetition frequencies allow operation at flight speeds compatible with radar data collection during combined missions.

Currently no civilian operational drone-borne-lidar system appears capable of large-scale data collection over Antarctica in combination with IPR and other sensors. UAS operations are constrained by absence of de-icing capabilities for low-level, coastal flights and by limited real-time satellite communication in high-latitude environments (Section 3.4).

3.1.4 Gravimeters

Gravity measurements are an important part of the airborne surveys in the coastal zone of Antarctica, allowing estimates of the depth and geometry of the bed of deep outlet glaciers where IPR data are missing or disturbed by crevasse fields, englacial and subglacial water network, and strong off-nadir reflections from steep valley flanks (Figure 14). Over ice shelves, airborne gravity is even a primary tool for estimating sub-shelf ocean depths (Section 3.6.2). Due to the need for heavy filtering to suppress the effects of aircraft accelerations and vibration, airborne gravity data currently have a low spatial resolution (typically around 5 km); nevertheless, they can still provide an important quality check on bed depth and geometry of major subglacial valley networks for IPR data. Also, together with aeromagnetic imaging gravity can yield insights into subglacial geology, and in particular the distribution and shape of sedimentary basins that can aid and steer fast glacial flow (Section 2.6.3).

Traditional spring gravimeters mounted on a stabilized airborne platform such as the LaCoste and Romberg AirSea instruments were modified marine or static gravimeters not originally designed or engineered for reduced sensitivity to air turbulence and aircraft motions, resulting in relatively low-resolution (3-4 mGal) data that still cover large areas of Antarctica (Brozena, 1992; LaCoste et al., 1982; Nettleton et al., 1960; Scheinert et al., 2016; Verdun et al., 2002). Most airborne operators in Antarctica have thus changed to optimized re-engineered LaCoste-Romberg systems (e.g., Riedel et al., 2012; Tinto et al., 2019), accelerometer-stabilized systems such as SGL AirGrav (e.g., Argyle et al., 2000; Millan et al., 2017), or GT-1A and GT-2A inertial gravimeter systems (e.g., Eagles et al., 2018; Eisermann et al., 2020; Studinger et al., 2008). Some have started to use novel temperature-stabilized strapdown IMU systems such as iMAR (e.g., Jensen et al., 2019; Jordan & Becker, 2018; Simav et al., 2020). The AirGrav and GT systems reliably deliver data at sub-mGal accuracy under a range of flight conditions, but are large, heavy, and require long installation and stabilization periods. Strapdown systems are much lighter and smaller and capable of reaching 1 mGal (10^{-5} m s^{-2}) accuracy under benign survey conditions. In a well-constrained regional gravity inversion benefiting from independent seismic point measurements over an ice shelf (Section 3.5.2), and IPR and multi-beam sonar surveys from its onshore and offshore boundaries (Sections 3.1.1 and 3.6.2), this accuracy corresponds to a model bathymetric or bed depth resolution of about 15 m for a wide outlet glacier or seabed topography under an ice shelf. More conservative error budgets, taking the additional effects of geological variability into account, suggest the gravity method might effectively constrain cavity thickness to within ~175 m (Eisermann et al., 2020). In practice, uncertainties depend critically on co-solving gravity for elevation and complex geology, errors can be substantially larger, potentially hundreds of meters or more.Aircraft movement affects the gravity measurements, so inertial navigation system or GNSS measurements are needed to solve for kinematic acceleration along the flight trajectory. For a typical flight speed of 250–300 km h^{-1} (Table 3) and with the benefit of modern precise kinematic GNSS positioning, sub-mGal level data reproducibility can be achieved with an along-track spatial resolution of 5 km. Cross-track resolution achieved by interpolation cannot be finer than this value, but may be coarser depending on survey design. Flying slower with low ground clearance can increase the along-track resolution (e.g., Hinze et al., 2013), but increases fuel consumption. The use of UAS, which fly slowly and consume a fraction of the fuel needed for crewed platforms, may make 1-km resolution logistically feasible in Antarctica within the next few years (see Section 3.4).

Table 3: Key Aircraft used for airborne geophysics surveys in Antarctica. Range, survey speed, and survey altitude are nominal values of each airplane or typical values used for survey planning. Actual values may vary between individual aircraft.

Type	Aircraft	Range (km)	Surveying speed (km h^{-1})	Survey height above ice (m)	Common user organizations *
Fixed-wing jet	DC-8	10,000	850	460	NASA
	Gulfstream V	9,000	930	460	NASA
Fixed-wing propeller	Antonov An-2	1,000	180	300	PMGE
	Basler BT-67#	2,000	260	600	AAD, AWI, DTU, NASA, PRIC, USAP
	DHC-6 Twin Otter	1,000	240	600	BAS, DTU, USAP
	LC130H	2,600	590	700	USAP
	P3	7,040	740	460	CECs, NASA
Helicopters	AS 350B2	650	130	600	KOPRI
	Bell 412EP (sling)	980	60-80	100	ARC
	UH-60 (sling)	600	65	40	FACH

* Organization abbreviations are: AAD (Australian Antarctic Division), ARC (Armada Nacional de la República de Colombia), AWI (Alfred Wegener Institute, Germany), BAS (British Antarctic Survey), CECs (Centro de Estudios Científicos, Chile), DTU (Technical Univ. Denmark), FACH (Fuerza Aérea de Chile), KOPRI (Korea Polar Research Institute), NASA (National Aeroautics and Space Administration, USA), PRIC (Polar Research Institute of China), RMGE (Russian Polar Marine Geosurvey Expedition), USAP (United States Antarctic Program).

\# Basler BT-67 is also known as DC-3T.

To ensure consistency of the new data within ongoing Antarctica-wide compilations and reduce instrument drift effects to negligible levels (Scheinert et al., 2016), as well as improve the overall geological knowledge, airborne gravity measurements should be tied regularly to absolute gravity points available at several of the large Antarctic research stations.

A small hand-held gravimeter is necessary to tie to such points if the logistics of a measurement campaign allow one of the stations to be visited. Airborne absolute quantum accelerometers (Bidel et al., 2023), which do not require tie measurements, are a new development on the horizon.

3.1.5 Magnetic sensors

In coastal zone of the AIS, magnetic anomalies can be correlated with magnetic properties of outcropping rocks. Similarly to the Antarctic-wide gravity compilation (Scheinert et al., 2016), the Antarctic Digital Magnetic Anomaly Project (ADMAP) was launched in 1995 to compile near-surface magnetic anomaly data into a digital map and database for the Antarctic continent and surrounding oceans. The first version was published in 2001 and updated in several steps. The latest version, ADMAP-2, includes 3.5 million line-km of magnetic anomaly data collected over the past 50 years (e.g., Golynsky et al., 2018). Magnetic anomalies are also useful to describe the heterogeneity in geological boundary conditions that can affect ice-sheet flow (Tankersley et al., 2022). Such heterogeneity includes 1) basement faults or rift-basin controls on bed topography (Figure 7d; e.g., Bingham et al., 2012), 2) volcanic edifices and complexes (Behrendt, 2013), 3) sub-ice shelf shallow-level intrusions or basement highs (e.g., acting as pinning points, Eisermann et al., 2020), and 4) subglacial sediments vs crystalline bedrock beneath ice streams (e.g., Andrew M. Smith et al., 2013). The use of magnetic anomaly measurements for estimating GHF in Antarctica is outlined in Section 2.6.2.

Magnetic anomalies can be measured from a variety of airborne platforms. Helicopter-based aeromagnetic surveys are well-suited to reveal subglacial geology in areas of rugged terrain such as the Transantarctic Mountains, where outlet glaciers are flanked by steep ranges (e.g., Bozzo et al., 1999; Ferraccioli et al., 2009). Helicopters can be deployed from research vessels near the coastline (e.g., Gohl et al., 2013) so it can be convenient to survey highly rugged terrains in the coastal zone that are far away from research stations and runways (Section 3.2). For a sensor configuration, helicopter-borne surveys often use a total magnetic intensity optically pumped cesium vapor magnetometer sensor in a towed bird configuration. To reduce magnetic influences from the aircraft, the sensor is hung about 25 to 30 m below the helicopter.

Cesium-sensor configurations can also be flown on longer-range fixed-wing platforms such as a Twin Otter or Basler aircraft (Section 3.3). In such a case, the sensors may be installed in pods on the wings or in a tail—or nose—boom configuration for safer survey operations (e.g., Aitken et al., 2014; Ferraccioli et al., 2005). In this case, one installs an additional magnetometer that measures all magnetic field components that are felt during a controlled set of aircraft pitch, roll and yaw maneuvers within an area of known constant magnetic field. These components can then be applied to calculate a set of calibration coefficients used to actively compensate for aircraft influences (e.g. magnetization of the aircraft, magnetization induced by the engine; magnetic field set up by electrical circuit within the aircraft).

The sensors installed onboard the aircraft measure the total magnetic field that includes both the field generated within the Earth and the time-varying external field magnetic variations. In Antarctica these latter variations, known as diurnal variations, can be particularly strong and must therefore be measured independently at fixed stations on the ground to obtain a more reliable representation of the magnetic anomalies caused by changes in the geology. For these independent measurements, magnetic base stations (e.g., equipped with Overhauser magnetometer) should be installed within or near the survey area. These variations themselves typically show significant spatial structure, owing to variable Earth conductivity within the survey region, so that high frequency components in the ground station records must be filtered out before use, and the separation between the aircraft sensor and the nearest ground station should ideally not exceed 100 km (e.g., Aitken et al., 2020; Damaske et al., 2003). Aeromagnetic surveys are best flown during magnetically quiet periods of the day, with the flight window chosen based on inspection of ground-station records both prior to and during the aeromagnetic survey period. In practice, due to Antarctic logistic, weather, and survey-design constraints, the availability of multiple ground stations and chosen flight times rarely meet these ideal requirements, especially during longer-range surveys (e.g., Aitken et al., 2014; Forsberg et al., 2018).

Magnetic anomalies are typically measured over regular survey grids with survey lines and orthogonal tie lines rather than individual profiles. The availability of cross-overs between line pairs in a single survey campaign is crucial, as the true magnetic field strength can be assumed to be identical on each line. This is particularly important to remove the shorter wavelength residual magnetic field variations not removed by the filtered ground station correction (Aitken et al., 2020). The cross-overs are used in a statistical processing technique known as levelling (Ray, 1985). Generally, after levelling and microlevelling (a related frequency-domain technique; Fausto Ferraccioli et al., 1998), cross-over errors are significantly smaller (1–5 nT) than measurable anomalies caused by geological variability (10–1000 nT). A control (tie) line spacing with five times the flight line spacing has proven adequate for Antarctic surveys of regional-scale geology. The line spacing should ideally roughly equal the distance between the magnetic sensor and the geological source being investigated. For example, if the aircraft is flying at 1 km distance from the bed, ideally one would fly a 1 km line spacing to fully resolve the 3D heterogeneity in subglacial geology. Closer spacings than ice thickness may not reveal more bed features but do provide redundancy and improve accuracy in general.

High-resolution aeromagnetic surveys remain logistically challenging and very costly to fly in Antarctica, and hence typically a flight line spacing of about 5 km or wider is used (e.g., Golynsky et al., 2018 and refs. therein). However, the development of new ultralight magnetic sensors for drones could enable significantly higher resolution aeromagnetic surveys over the next few years. Thus, sub-kilometer scale aeromagnetic and aerogravity studies depicting the heterogeneity in subglacial geology, of both coastal regions of the grounded ice sheet and beneath ice shelves, are becoming a tantalizing new prospect.

3.1.6 Geoelectric and electromagnetic sensors

Geoelectric and electromagnetic (EM) sensors are increasingly used to explore the margin of the AIS, including the anatomies and formative processes of floating sea ice and ice shelves, hydrological systems within and below the ice sheet, groundwater and GHF in and through the underlying crust, and the viscosity of the upper mantle and its impact on isostatic change. EM methods can generally be classified as either active, passive, or hybrid, and seek to characterize the electrical conductivity structure below the ice surface, usually expressed in terms of its inverse, the electrical resistivity (Key & Siegfried, 2017). Glacier ice, firn, snow as well as subglacial permafrost and consolidated bedrock are usually highly resistive (Kulessa, 2007), so that relatively conductive features such as subglacial lakes or groundwater reservoirs are preferred targets for EM imaging. Because electrical resistivity generally scales inversely with temperature and water content and salinity of sediments and rocks, EM methods are also well suited to characterizing subglacial saltwater-freshwater interactions at ice stream grounding zones, and anomalies in crustal geothermal heat flow or mantle viscosities.

Currently the only EM techniques capable of airborne deployment are active-source frequency or time-domain soundings, with the latter often referred to as Transient EM (TEM). Frequency-domain sounding has been widely used in sea-ice imaging, especially using the EM Bird system (Haas et al., 2009). It is a small (~ 3.5 m long thin beam) and lightweight (~ 100 kg) system slung from aircraft ~ 10-20 m above the sea ice surface, with height measured using a laser altimeter whilst emitting a primary EM field of several kHz. The primary field induces eddy currents and therefore a secondary EM field in conductive seawater beneath relatively resistive sea ice and the overlying snow. The phase and amplitude of the secondary field relative to the primary field, corrected for elevation, can then indicate sea ice thicknesses every 5-6 m along flight tracks hundreds of kilometers long, and can furthermore identify the presence of platelet layers accreted from the ocean below (Haas et al., 2021).

The commercial airborne SkyTEM system (Foley et al., 2016) was more recently used for subglacial groundwater mapping beneath glaciers several hundreds of meters thick in the Dry Valleys of the Transantarctic Mountains (Mikucki et al., 2015). It uses a large transmitter loop of several hundreds of square meters and a receiver loop an order of magnitude smaller, both of which are slung by helicopter ~ 30-40 m above the ice surface. Using combined low and high transmitter moments, the TEM responses cover an equivalent frequency range from ~ 10 Hz to ~ 300 kHz, and as such are optimized to generate one subsurface sounding approximately every 50 m from the surface to depths of several hundreds of meters. Integrated TEM and hydrogeological analyses can infer subglacial groundwater flow pathways over tens of kilometers, as well as submarine groundwater discharge across the grounding line (Foley et al., 2019).

The EM Bird system can be flown from suitable Basler or Twin Otter aircraft, or helicopter, with little modification for sea-ice imaging around the Antarctic margin, whereby multi-sensor combination with, e.g., laser scanner and shallow-sounding IPR can yield information on sea-ice properties such as density as well as internal structures (Jutila et al., 2022). Two fundamental limitations affect SkyTEM type data. First, the inversion of EM data suffers from the principle of equivalence, whereby layer thickness and resistivity cannot be estimated independently of each other. Joint acquisition and inversion of SkyTEM type data together with airborne IPR, gravity and magnetic measurements promises to address this limitation, resulting in particularly complete characterization of the AIS margin and its substrate (Moorkamp et al., 2011) (Killingbeck et al., 2022). Second, the depth penetration of TEM sounding scales with transmitter loop size, with loops of 40 km^2 or more required to sound deep enough into the Earth’s crust beneath kilometers-thick ice (Siegert et al., 2018). Such large loops are prohibitive in airborne applications and necessitate ground-based EM data acquisition, and it is here where magnetotelluric measurements come into their own (Hill, 2020). Magnetotelluric data most recently revealed a large groundwater reservoir beneath the Whillans Ice Stream in the Siple Coast (Gustafson et al., 2022) and show clear potential in constraining sub-ice sheet GHF anomalies (Kulessa et al., 2019) as well as crustal and mantle structures and properties at the margins of both WAIS (Wannamaker et al., 2017) and EAIS (Peacock & Selway, 2016). Integrated airborne and ground-based EM sounding therefore promises to be a suitable approach in future exploration of Antarctica’s coastal regions.

3.1.7 Ocean instruments

In contrast to the relative ease of observing the ocean surface from space, observations of the ocean interior require in-situ deployment of instruments. In recent years, airborne techniques have been used to obtain depth profiles of temperature and salinity in front of the Greenland Ice Sheet and Antarctic ice shelves. In this way, airborne coastal surveys provide a unique approach to oceanic measurements. In addition, these instruments are highly cost-effective compared to traditional deployments of instruments from research icebreaker vessels, particularly when airborne surveys are made for other purposes nearby.

Two main types of airborne ocean instruments have been used. The first type are disposable probes such as the AXBT (airborne expendable bathy-thermograph) and the AXCTD (airborne expendable conductivity temperature depth) probes. The second type are float profilers like Argo floats and ALAMO floats (air-launched autonomous micro observer), which can be recovered after several cycles of data sampling and transmission. The Argo floats were first developed for tropical and subtropical oceans, but recently some floats were deployed under seasonal sea ice (van Wijk et al., 2022; Wong & Riser, 2011) and under sea ice and ice shelves (Girton et al., 2019), all from vessels. More recently, they were adapted for launching from airplanes along the front of the Ross Ice Shelf (Porter et al., 2019). These two types of instruments differ in their functionality and the number of profiles they can provide. Specifically the disposable probes produce a single profile and require the aircraft to linger during the descent, while float profiles can provide many profiles over months or years with the data telemetered via satellite.

The probe type instruments have a radio transmitter at the surface of the ocean and provides a single profile of the water column while transmitting the measurements in real time to a radio unit on the launching aircraft. These expendable and relatively inexpensive probes are well-suited for large-scale surveys in polar regions and can measure seabed depths of up to 1000 meters below the surface. Building up from AXBTs, which can only measure pressure and temperature, AXCTD probes can measure salinity as well and have been deployed from both fix wing aircraft and helicopters (Muilwijk et al., 2022; Nakayama et al., 2023) and they have been used around Greenland (Yang et al., 2020).

In contrast, the float type instruments can provide up to 300 profiles of the water column at a set cycle frequency (10-day cycles, providing an observational period of 3000 days). They have been launched in boxes from the cargo doors of large airplanes, as was done during the ROSETTA-ICE project (Porter et al., 2019). This launching method may not be widely available for Antarctic surveys. However, the ALAMO floats (Jayne & Bogue, 2017) were designed to also be launchable from sonobuoy launch tubes, and therefore they could be launched from small airplanes typical for Antarctic surveys. These float profilers, much like their larger typically ship-launched versions, go through cycles of data transmission and positioning at the surface, followed by descent to a specified parking depth (typically 1000 m). They drift for a specified number of days (typically 10), make a profile between the surface and 2000 m depth, and then start a new cycle. Since the early 2000s, nearly 4,000 Argo float profilers have been deployed from vessels worldwide (Freeland et al., 2010). In addition, several recent pilot studies have deployed Argo floats from airplanes (Jayne & Bogue, 2017; Porter et al., 2019). These floats provide real time data on temperature, salinity, and currents, as well as bio-optical properties. The Argo program revolutionized sampling of the interior of the oceans by launching drifting profiling platforms or profiling floats.

In summary, expendable probes like AXBTs and AXCTDs can make only one depth profile per deployment and require the airplane to circle back to retrieve data via radio link. Float profilers like Argo and ALAMO instead provide multiple profiles, communicating via satellite to servers on land and thus do not require the airplane to return for data retrieval. However, in the extreme conditions of the Antarctic shelf seas (sea ice, icebergs, ice shelves), most profilers may be lost before reaching the end of their battery life. Nevertheless, these platforms would likely collect a minimum of tens of profiles and up to 300 profiles with a single launch, and therefore should be able to measure spatio-temporal oceanic variability. In case of deployments in glacial rifts and permanent sea-ice cover, where surfacing is unlikely to occur, float profilers would not be able to send their data via satellite. In this case, AXCTDs would be the more suitable option.

3.2 Logistics for airborne surveys

Due to the remoteness and challenging environmental conditions, airborne surveys in Antarctica require extensive logistics support. Essential support structures include a remote camp with skiway, fuel, aircraft maintenance, weather forecasts, communications and navigation systems, search and rescue, and contingency planning - including medivacs. As presented in Section 4.3, data availability in the coastal regions strongly suggests that logistics support capability is the main limiting factor for data collection. Transportation and logistical support are integral and quite complicated due to the relatively few options and the short survey season during the Austral summer. Overcoming these numerous challenges while maintaining the highest safety standards necessitates significant resources and meticulous planning, sometimes several years in advance.

3.2.1 Remote camp and fuel cache

Logistical preparations for any survey depend on the accessibility of the survey area from existing logistical hubs, such as research stations or research vessels, the aircraft's range (Section 3.3), and the survey’s duration (i.e., the amount of fuel and general supplies needed for the survey). There are 29 active airfields within 100 km of the coastline (49% of all active airfields in Antarctica) and 35 within 200 km (Figure 16). When the survey area is situated further away from these airfields, establishing a field camp becomes necessary. For very distant locations, additional fuel caches might be needed along the way to the field camp. Fuel can be delivered by aircraft with airdropping fuel barrels or by landing at the remote site. Ground traverses from the station or the loading site at the ice-shelf front are also possible. In order to maximize seasonal efficiency, fuel caches can already be set up in the previous season, which can also be used to inspect and adjust possible camp and landing sites. A field camp needs to be self-sufficient for the survey's duration, with trained personnel, sufficient fuel, basic food provisions, satellite communication capability, and medical facilities, all of which need to be brought in advance, requiring several additional flights. Such a field camp extends the survey capability to a remote area, but requires significantly more planning and expenses.

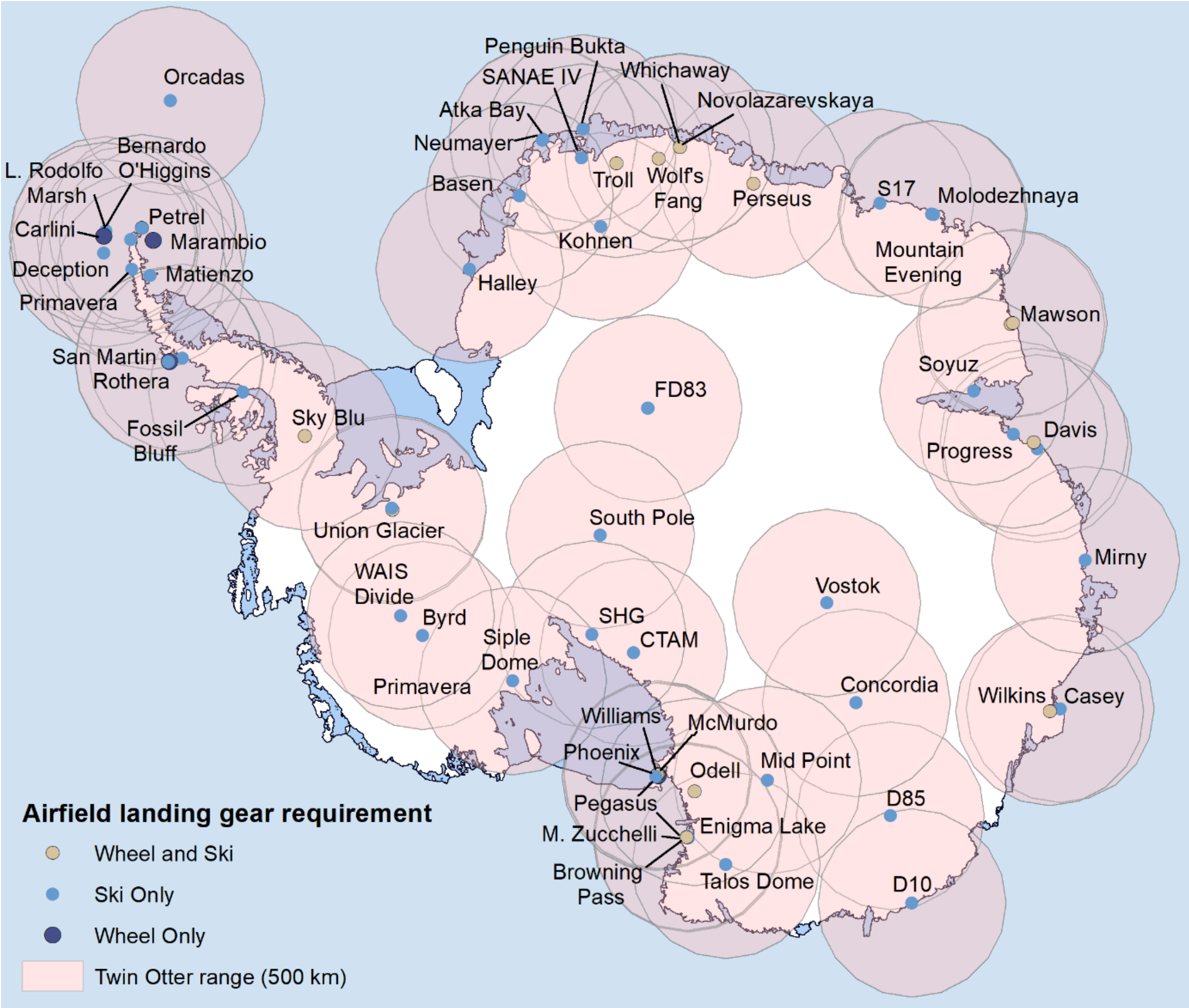

Figure 16: Currently active airfields (COMNAP, 2023). 500-km buffers from each airfield are shown as an approximate range of small survey airplanes (see Table 3). This map is made using Quantarctica (Matsuoka et al., 2021).

3.2.2 Weather forecast

Antarctic weather can be harsh and prone to rapid changes. While generally calm conditions are essential, terrain and survey specifications can further constrain the weather requirements for a safe and successful campaign. For example, mountainous terrain or a lidar survey both need cloud clearance below flight altitude, while other surveys may not. Consequently, reliable weather forecasts are paramount to minimizing risk and maximizing data quality.

Weather forecasts typically include information on white–out and cloud cover, wind velocity (both surface and upper), turbulence, drifting snow, and icing, for the coming hours and days. Making such reports for specific sites and flight tracks demands dedicated and experienced weather forecasters who can integrate streams of data from ground measurements, satellite imagery and meteorological models. This task is especially challenging because weather stations feeding data into these models are extremely sparse in Antarctica (Figure 5c), while some regions with highly variable terrain are particularly difficult to forecast.

Weather data for the forecasting models can come from the Global Telecommunications System maintained by World Meteorological Organization (WMO) as well as from more local networks of automatic weather stations and other surface weather reporting stations. Some research stations also make upper-air soundings of meteorological variables with vertical profiles from the surface to the lower stratosphere. Based on these data and regional climate models like the Antarctic Mesoscale Prediction System (AMPS; (Powers et al., 2012)), many national Antarctic programs operate weather forecasting services or collaborate with forecasting agencies. Their data and forecasts are often shared with the various Antarctic programs. For example, AMPS provides forecasts at various locations every 12 hours on the Internet (https://www2.mmm.ucar.edu/rt/amps/). The forecasters at the German Neumayer III Station provide weather forecasts for the DROMLAN consortium, which consists of 11 countries in the Dronning Maud Land region (Nöth, 2021). In addition to data from the German weather service's (DWD; https://www.dwd.de/) weather forecast model, these forecasters refer to the information provided by the European Centre for Medium-Range Weather Forecasts (ECMWF; https://www.ecmwf.int), the U.S. National Oceanic and Atmospheric Administration (NOAA; https://www.noaa.gov), and AMPS. Similar collaborative efforts should enable effective weather forecasting in other parts of Antarctica. Even after these efforts, the weather conditions can be hard to predict in the coastal regions and have considerable influence on the success or failure of a campaign. Detailed forecasts in remote areas are particularly important for large-scale surveys, while for surveys in smaller areas, such as those using helicopters it is often advantageous to observe and monitor rapidly changing local weather conditions or conditions that differ from predictions. One approach to address this issue would be to strategically increase the number of AWS with satellite data links for real-time data transmission along the coast.

3.2.3 Navigation, communication, and search and rescue

A survey requires precise navigational tools and robust communication routines for various standard functions and unexpected situations. These functions and situations include 1) to effectively coordinate a survey with prompt updates from off-site weather forecasters, 2) to monitor survey progress in real time, and 3) to promptly initiate search and rescue operations when needed. For navigation, GNSS systems are required, and since survey instruments also log location data, multiple GNSS units may be needed onboard. For communications, the most common devices are currently satellite-based phones, though satellite internet receivers are becoming more common as coverage expands across the continent. In addition, particularly when the aircraft are operated from research stations with permanent radio communication systems, HF and VHF radio communications are used. A robust communication routine such as an hourly check-in procedure to the base camp during the flights must also be set. Such a routine should also include communication of protocols to be followed in case of unforeseen events and emergencies.

Despite these precautionary measures, risks associated with air missions in Antarctica are inherently high. Particularly severe accidents including the crash of a Chilean C-130 aircraft into the Drake Passage with the loss of all 38 occupants on 9 December 2019. The cause of the crash is unknown (https://aviation-safety.net/database/record.php?id=20191209-1; Reuters, 2019). Another fatal aviation accident occurred under low-visibility conditions in January 2013 when a DHC-6 Twin Otter aircraft with a crew of three crashed into Mt. Elizabeth in the Queen Alexandra Range (https://aviation-safety.net/database/record.php?id=20130123-0; Patterson, 2013). Other accidents include a DC3T losing its landing gear while taxiing on an unprepared surface in November 2016 (https://avherald.com/h?article=4a2181ed), and a Basler BT-67 losing its landing gear while taking off in December 2012 (https://avherald.com/h?article=45ae28ad). In both cases, the landing gear struck unexpectedly hard snow drift and was damaged. There are tremendous efforts to mitigate such accidents through in-depth preparation and international coordination (Chilton, 2004). As a result of these efforts, such events have become rarer.

The Council of Managers of National Antarctic Programs (COMNAP; https://www.comnap.aq) is focused on reducing the risks of any emergency and asks all National Antarctic Programs and Antarctic operators conducting air activities to provide timely, current and accurate information for the purposes of maintaining the Antarctic Flight Information Manual, which is available to COMNAP member National Antarctic Programs and their affiliate organizations. As is the case elsewhere, aviation emergencies in Antarctica come under the same search-and-rescue obligations and principles set by the International Civil Aviation Organization (ICAO). In the event of an aviation accident in Antarctica, the pilot or crew of the aircraft will typically use emergency transmitters or personal beacons to alert authorities of the accident and its location. Also if an aircraft fails to report by agreed communication routines (HF and VHF radio) at an arranged time or the aircraft does not arrive at its destination within the time allocated for the flight, the flight follower must initiate a predefined emergency response plan. In either case, the Rescue Coordination Centre (RCC) responsible for the area will be alerted and coordinate the search-and-rescue effort. Seven RCCs cover Antarctica: in Cape Town and Johannesburg (South Africa), Canberra (Australia), Wellington (New Zealand), Punta Arenas (Chile), and Ushuaia and Comodoro Rivadavia (Argentina). Once alerted, the RCC then notifies the appropriate search-and-rescue assets and dispatches them to the location of the accident. Search-and-rescue assets may include aircraft, boats, and ground search and rescue teams. The type of assets deployed will depend on the location and circumstances of the accident. The RCC will continue to coordinate the search-and-rescue effort and provide updates to the appropriate authorities. Search-and-rescue operations in Antarctica can be more complex than that in other areas in the world, and their success often depends on the cooperation of multiple agencies and organizations.

3.2.4 Environmental considerations

Antarctica’s environment is sensitive (Chown et al., 2012; Hughes et al., 2011, 2016). Thus, careful consideration should be given to minimize human impacts. General environment management is regulated by the Protocol on Environmental Protection to the Antarctic Treaty (also known as the Madrid Protocol or the Environmental Protocol; The Secretariat of the Antarctic Treaty, 1991; https://www.ats.aq/e/protocol.html). This protocol consists of six annexes covering various aspects, including prevention, protection, assessment, and management of environmental resources. For this purpose, an application to conduct research in Antarctic areas south of 60°S must be submitted to the relevant national authority for environmental protection for approval. The protocol also designates certain areas as Antarctic specially protected areas (ASPAs) and Antarctic specially managed areas (ASMAs) (L.R. Pertierra & Hughes, 2013). These areas have special conservation or management objectives and may have additional restrictions on activities to protect their unique ecological, scientific, or cultural values. Additional permission is required to survey these areas, and implementation guidelines may apply to minimize environmental impacts (Pertierra et al., 2013).

Practical environmental considerations include fuel management protocols, as leakage and spills at remote camps can occur. Equipment and plans for on-site management and reporting of a spill must be well established before fieldwork begins (COMNAP Fuel

Manual; https://www.comnap.aq/handbooks-manuals-operational-guidelines). Also, special care should be taken while airdropping fuel barrels for setting up remote fuel caches.

Aircraft operations can disturb the physiology, behavior, and reproductive capacity of animals (The Secretariat of the Antarctic Treaty, 2004) (ATCPs, 2004). The severity of disturbance depends on various factors such as the species involved, their breeding season stage, the intensity, duration, and frequency of the disturbance. Conversely, aircraft flying near bird colonies may be struck by birds. Thus, it is important to know the location of such sites and assess possible disturbances in the project's planning phase. Special permits might be needed to conduct environmentally responsible science in such areas. In addition, with inter-continental flights, precautions should be taken to avoid the spread of non-native species in Antarctica (ATCPs, 2016). Particular attention should be given to aircraft that have also operated in the Arctic to not spread species that could survive in Antarctica. Checklists for the reduction in risk of transfer of non-native species developed by COMNAP and Scientific Committee on Antarctic Research (SCAR) in 2019 are available for the supply chain managers of National Antarctic Programs at https://www.comnap.aq/handbooks-manuals-operational-guidelines).

3.2.5 Challenges and opportunities

Currently available bed elevation data, and perhaps any airborne geophysical data, show clustering near research stations, with large data gaps in remote areas (Section 4.3). Overcoming this location bias requires coordinated international collaboration to secure the necessary resources for surveys in remote areas. Coastal surveys face particular challenges due to harsh weather conditions. The rough terrain, strong katabatic winds, and frequent storms along the coast make the weather in these areas challenging and hard to predict. With a mean total cloud cover of around 80%, coastal regions of Antarctica are one of the cloudiest regions in the world (Turner & Pendlebury, 2004).

Given these constraints, coastal surveys require careful coordination from the outset, involving scientists, logistics, and aviation specialists. Figure 16 maps existing logistics hubs and airfields, but not all coastal-region stations have sufficient capacity to support an airborne survey and their support capability varies year to year. Detailed mapping of station capabilities and coordinating contributions from various National Antarctic Programs are needed to prepare for future joint airborne surveys in the coastal regions. This requires close collaborations between various National Antarctic Programs, facilitated through SCAR and COMNAP, particularly COMNAP's Science Facilitation Expert Group and Air Operations Expert Group. As SCAR provides scientific oversight, COMNAP can provide a forum for sharing and discussing best practices on logistics, operations, and environmental protection, encouraging collaboration on both logistical and scientific aspects while adhering to the principles of the Antarctic Treaty.

3.3 Aircraft

Retrieval of large geophysical datasets relies on aircraft, several types of which are currently in use in Antarctica (Table 3). The Twin Otter is a high-wing, twin-engine, turbo-propeller aircraft that can operate in snow and icy terrain using mounted skis. The aircraft typically flies at ~60 m s^{-1} (or ~220 km h^{-1}) while collecting data, which can result in an along-track distance of 0.2 m between each tracked IPR trace (prior to processing) (Frémand et al., 2022). The aircraft can be equipped with gravimeter, magnetometer, IPR, GNSS, and lidar measurements (Section 3.1). All aerogeophysical data acquired by British Antarctic Survey have been obtained using the Twin Otter aircraft because of their versatility, remote capabilities, and long range (up to 1,000 km).

The Basler BT-67 can also provide necessary logistical and surveying support in Antarctica. This aircraft offers long range surveying and reconnaissance, short takeoff and landing capabilities (often ski-equipped), and can transport larger cargo (~4.5 ton). During survey operations, the Basler typically flies at ~80 m s^{-1} (or ~300 km h^{-1}) and has a range of ~1800 km. Much like the Twin Otter, the Basler can be equipped with an extensive range of geophysical equipment to provide necessary surveying capability. Kenn Borek Air in Canada has operated the Basler airplanes for the Australian, Chinese, German, Italian, and US Antarctic Programs on both scientific and logistics missions. Many of the Basler airplanes operating in Antarctica are bespoke conversions of older DC-3 airframes. Consequently, their specifications and scientific capabilities vary slightly.

Other airplanes that can be equipped with skis for airfields in Antarctica are the De Havilland Canada Dash 7 and the LC-130H "Skibird", and Antonov An-2/An-3. The Antonov airplanes are used by the Russian Antarctic expeditions. They benefit from a short take-off/landing capability and can survey at ~50 m s^{-1} (~180 km h^{-1}) with a maximum range of 1000 km. The Dash 7 has been used for transports between Punta Arenas, Chile, and the British Rothera Station on the Antarctic Peninsula. Similarly, the LC-130H transports provisions and personnel between Christchurch, New Zealand, and American McMurdo Station. Their long ranges and ability to land on blue-ice runways are attractive for airborne surveys in remote coastal regions. However, during each season, snow drifts must be cleared before the aircraft can land.

Helicopters are also used for airborne surveys; they are of advantage in steep fjords or in areas that are far away from any established logistics hubs but a vessel can approach nearby (Table 3). Their ranges are much shorter than fixed-wing aircraft but can be deployed from ice breakers near the coastline for aerial surveys (e.g., Gohl et al., 2013; Lindzey et al., 2020) and for supporting and retrieving field parties. The combination of an icebreaker and helicopters presents exceptional opportunities for exploring regions that were previously inaccessible to both fixed-wing aircraft and ground vehicles, such as the grounding zone of fast-flowing glaciers that are heavily crevassed with distinct terrains.

Overall, several types of aircraft of various ranges have been used for airborne geophysical surveys in Antarctica, but considering the sparse availability of logistics hubs (Figure 16), it is crucial to use ski-equipped airplanes that have a longer range and fly at cruise speeds suitable for scientific data collection. Ultra-long-range airplanes without skis such as Gulfstream V can also be operated from outside of Antarctica without any landing sites in Antarctica, provided that the transit time is small compared to survey time or can be utilized for other scientific purposes. These aircraft typically fly at altitudes and speeds that allow reliable operation of the instruments discussed in Section 3.1. Ideally, the aircraft range should be extended to ~4000 km, because such long-range aircraft would have the important environmental advantage of reducing the need for fuel cache in remote locations, which require many fuel transportation flights and more human activities.

3.4 Uncrewed aerial systems

Uncrewed aerial systems (UAS), also known as uncrewed aerial vehicles (UAV), remotely piloted aircraft systems (RPAS) and drones, have promising capabilities as a platform for light-weight airborne geophysical surveys. Although largely used in military applications, UAS and sensor technologies have also found many uses in research programs including cryosphere surveys (Bhardwaj et al., 2016; Gaffey & Bhardwaj, 2020). Most of these reported applications involved retrieving optical imagery or in-situ atmospheric samples using multi-rotor platforms. Most UAS-deployed systems are limited to near-surface investigations using low-power instruments on drones (Jenssen & Jacobsen, 2020, 2021; Prager et al., 2022; Tan et al., 2021; Vergnano et al., 2022). A few studies have deployed high-power sensors on longer-range UAS (Arnold et al., 2018; Keshmiri et al., 2017; Jordan et al., 2025), but these have been experimental, proof-of-concept surveys that need further development and testing to establish their value as replacements for crewed aircraft. However, should this technology become mature and its effectiveness demonstrated, it could transform scientific studies in polar regions.

UAS are typically classified according to size and operational characteristics such as maximum take-off weight, payload capacity, operating altitude, air speed, and range (Watts et al., 2012). Table 4 provides examples of drones used for scientific surveys in the polar regions. For surveys in the coastal zone of Antarctica, we can consider just three broad classes of drones: small single- or multi-rotor, mid-sized fixed-wing, and larger fixed-wing. Even larger fixed-wing drones such as the Northrop Grumman Global Hawk UAS have great potential but are not considered for use in Antarctica due to high acquisition and development costs and large logistical footprints.

Table 4: UAS that were used in polar regions. Power sources are: battery (B), single engine (S), and dual engine (D). Ranges largely depend on the payload. The takeoff modes are: vertical (V), ski (S), launcher (L), runway (R), and truck-pulled (P).

Type	Name	Power source	Payload (kg)	Range (km)	Take off mode	Common applications	Note
Helicopter	Vapor 55	B	4.5	8	V	Optical, IPR	#1
Hexacopter	Aurelia X6	B	5	15	V	Optical, IPR	#1
Fixed wing	CroWing	S	15	500	S, L	Lidar, optical	#2
	GIX	S	5	100	S	IPR	#3
	Meridian	S	55	1,700	S	IPR	#4
	Prion MK3	S	15	1,000	S, L		#5
	SealHunter	D	50	> 500	R	Lidar, optical, IPR	#6
	Sierra	S	45	1,000	R	Lidar, optical, IPR	#7
	Vanilla	S	70	5,000	P	Optical, IPR	#8
	WindRacers	D	100	1,000	R	Optical, IPR, gravity, magnetics	#9

#1: https://aurelia-aerospace.com/ Information is based on experiences by an author (CL) in Greenland, 2022.
#2: Solbø et al., 2013
#3: Keshmiri et al., 2017, Leuschen et al., 2014
#4: Keshmiri et al., 2017
#5: https://uave.co.uk/prion.php
#6: https://above.nasa.gov/meeting_anchorage/presentations/20160121/1340_Cahill.pdf
#7: https://www.arm.gov/publications/programdocs/doe-sc-arm-15-046.pdf
#8: https://www.nasa.gov/feature/goddard/2022/nasa-helps-fly-drone-in-alaska-to-study-sea-ice-thickness
#9: Watts et al., 2012; Jordan et al., 2025.

Helicopter and Hexacopter UAS in Table 4 are examples of relatively inexpensive single- or multi-rotor drones. These types have a payload of only a few kilograms and a typical endurance and range less than an hour and tens of kilometers. These UAS typically carries optical cameras or lightweight active sensors but the low coverage limits its use for a regional survey. GIX in Table 4 has made IPR measurements in both Antarctica and Greenland at HF and VHF frequencies (Arnold et al., 2018; Keshmiri et al., 2017; Leuschen et al., 2014). SeaHunter stands out as the University of Alaska has been routinary operating this platform in polar regions. Given access to a field camp, it possesses the payload and range capacities necessary to support airborne geophysical surveys including IPR. Vanilla provides an alternative approach with multi-day endurance. It can be launched from a fixed base and has wing hardpoints to mount antennas suitable for IPR. Finally, Meridian has been operated from fixed bases and field camps in both Antarctica and Greenland with a multi-channel VHF-range IPR.

Sensor integration with UAS must be carefully considered to maintain measurement performance with no interference from avionics and communications. The latter issue becomes increasingly difficult when considering IPR, which requires a large antenna structure to operate at the HF and VHF frequencies needed to sound warmer ice near the ice-sheet margins. These antennas can be mounted using wing hard points, as with most crewed aircraft, or integrated into the wing (Leuschen et al., 2014). In addition to antenna integration, IPR operates with large transmit power levels (up to a few kW), which must be ground tested to ensure electromagnetic interference does not compromise the UAS. The use of carbon fiber in surface and structural parts of modern UAS is a point of special consideration when integrating antennas because carbon fiber is dielectrically conductive and will essentially short the antenna if it is close. In these situations, it is essential to mount the antenna a significant fraction (~1/4) of the radio-wave wavelength away from the UAS, as well as to run simulations to ensure radiation efficiency and directivity, and to use matching networks to avoid interference of the radio-frequency signal within the UAS (Allen et al., 2012; Byers et al., 2012).

Operational constraints will affect the survey location and the type of UAS. Most large fixed-wing UAS will require a smooth runway (firn or snow-covered ice) of sufficient length for take-off and landing. When UAS are used for regional surveys, they can operate beyond the visible range, conducting surveys hundreds of kilometers away from the airfield. The success and safety of UAS operations depend on good regional communications and the ability to forecast weather over the duration and extent of the operations (Sections 3.2.2 and 3.2.3).

3.5 Ground- or vessel-based observations

Airborne surveys alone may not deliver the complete set of observations needed in the coastal zone of Antarctica. Here, we describe ground-based and vessel-based operations needed to complement airborne surveys.

3.5.1 Ice cores and ground-based radar surveys

Ice cores are a primary tool to reconstruct paleoclimate over a timescale ranging from tens to millions of years (Jouzel, 2013). Compared to other paleoclimate proxies such as marine sediment cores and geological methods, ice cores often have a higher temporal resolution, stratigraphic continuity, and the unique capacity to provide direct samples of past atmospheric gas compositions, as well as proxy data from insoluble particles, chemical constituents and water isotopes. Determining the chronology of the ice core, i.e., the depth-age relationship, allows one to convert the depth series of chemical, isotope, biological and physical measurements to a time series of paleoclimate proxies in the past. The chronology is also fundamental to dating radar-detected isochrones at depth. For example, shallow (< 100

m) radar reflectors are used to map recent SMB over large areas (Figure 15b), provided that the radar reflectors are continuous for a long distance without significant disturbance related to surface melting and crevasses (Section 3.6.3). Deeper radar reflectors are used to constrain or test ice-flow models from which we can learn about past ice dynamics and SMB (e.g., Sun et al., 2020).

Ice cores are usually drilled near ice domes or along prominent ridges. Compared to those drilled at inland sites, ice cores drilled in the coastal regions usually cover a shorter time span because of larger SMB and thinner ice than inland regions in general and provide more regional proxies because coastal climate is highly spatially variable (e.g., van Ommen & Morgan, 2010; Winstrup et al., 2019; Wauthy et al., 2024). Before drilling, IPR surveys can provide evidence of internal layer architecture (Figure 15). The upward arches observed beneath the ice ridge are made with anomalously low deviatoric stress in the vicinity of the ridge (Raymond, 1983). The shape of these Raymond Arches would indicate whether the location may yield a stratigraphically intact ice core. When repeated point measurements or multi-polarimetric measurements are made using autonomous phase-sensitive radio-echo sounder (ApRES), basal melting rates, vertical strain rates within the ice sheet, and alignments of ice crystals can be inferred (e.g., Jordan et al., 2022). Because of the often high SMB near the coast (Figure 5a and 5d), an ice core retrieved from an ice rise can provide proxy records with seasonal temporal resolution (e.g., Jong et al., 2022; Philippe et al., 2016), which would allow the reconstruction of climate variables such as SMB and chemical species on the seasonal to multidecadal timescales. These timescales are relevant to the detection and attribution of anthropogenic-induced climate change in proxy data (e.g., Dalaiden et al., 2022).

Ice-core sites are selected based on their ability to support answering the scientific questions of interest, and whether the glaciological conditions can ensure high-quality climate records, as well as considering logistics constraints. Glaciological conditions ideal for most climate science objectives are no surface melting, minimal ice-flow speed (i.e., located near a local ice flow divide), minimal basal melt, and minimal disturbance in ice stratigraphy in the targeted depth/age range. Also important are SMB and ice thickness, which are fundamental to estimating the timespan and temporal resolution of the ice core (e.g., Fischer et al., 2013; Van Liefferinge & Pattyn, 2013; Vance et al., 2016). Considering logistics, the choice of drilling systems is important. The choice largely depends on the targeted depth range (Table 5). A lightweight portable hand or electric auger can be used to drill tens of meters, whereas a heavier drill is needed for deeper cores (e.g., Mulvaney et al., 2021; Souney et al., 2021). For drilling over 200 m, an even heavier "wet-drilling" operation is needed. Such wet-drilling uses a drilling fluid to both lubricate the coring process in increasingly pressurized ice while also balancing ice overburden pressure, which keeps the borehole open and reducing fractures in the core due to the change in pressure. Such wet drilling also requires a casing of the borehole in the firn depths to avoid leakage of the drilling fluid into the firn (see Johnson et al., 2014).

Table 5: Examples of shallow drills routinely used by the projects under the US Antarctic Programs. The "Drilling period" column indicates the time required to reach the maximum depth for each drill. The "TO?" column specifies whether the drill system can be transported using DHC-6 Twin Otter airplane (Table 3). The "Fluid?" column indicates whether drilling fluid is required for operation.

Drill name	Maximum	Drilling	Shipping	TO?	Fluid?	Key reference

	depth (m)	period	weight (kg)			
IDP Hand Auger	20-40	1-2 days	~40	Yes	No	https://icedrill.org/long-range-science-plan
Foro 400	400	2-4 weeks	~820	Yes	Yes*1	https://icedrill.org/long-range-science-plan
Foro 1650	1,650	12 weeks (>1 season)	>13,610	No	Yes	https://icedrill.org/long-range-science-plan

*1: Drilling fluid is required only for depths exceeding 200 m. Twin Otter transportation considers the drill system alone, without accounting for the transport of drilling fluid and casing (see text).

When targeted time span is only a few decades so the length of the ice cores is limited to a few tens of meters, ice cores can be drilled over ice shelves. When targeted timespan is longer, ice rises, locally grounded isle and promontory at least partially surrounded by ice shelves, constitute interesting ice coring areas due to their stability and the presence of a prominent ridge over each ice rise which are ideal ice coring locations (Figure 15; e.g., Matsuoka et al., 2015). According to the inventory of ice rises in Antarctica (Moholdt & Matsuoka, 2015), inventoried ice rises are generally close to research stations and airfields. Exceptions are those along the Bellingshausen and Amundsen Sea coasts in West Antarctica. Ice cores drilled in these two remote, and harsh-weather coast regions, especially near Thwaites Glacier, are particularly important to survey because of ongoing rapid changes there (Neff, 2020), yet are located furthest from active airfields of any coastal sites (Figure 16). Shallow drilling at coastal ice rises may not extend back more than several hundred years due to the high coastal SMB. However, many of the larger ice rises can provide much longer timespans over the past millennia (e.g., Bertler et al., 2018) or even to the Last Glacial Maximum and the previous interglacial period Eemian (e.g., Mulvaney et al., 2007). These cores can contribute to the global network of ice core records in the past two thousand years set by the International Partnership of Ice Core Sciences (IPICS-2k array, https://pastglobalchanges.org/sites/default/files/download/docs/working_groups/ipics/white-papers/IPICS_2kArray.pdf). To optimally select sites for these ice cores, airborne IPR surveys are useful. In turn, the ice cores can provide reflector chronology, which enables ones to extrapolate the age distribution from the single location data obtained by the ice core. It eventually provides regional SMB in a large area (e.g., Medley et al., 2013). The relationship between core-derived SMB and regionally-representative SMB derived from IPR surveys is highly variable between ice rises (Cavitte et al., 2023). Mapping of SMB using IPR and ice cores is further discussed in Section 3.6.3.

There is an ongoing effort Antarchitecture under SCAR to develop a continent-wide age-depth model of AIS using englacial radar reflectors (Bingham et al., 2025; https://scar.org/science/cross/antarchitecture). For example, recent tracing of just one radar reflector across much of West Antarctica, dated to 4.72 ka by its intersection with the WAIS Divide Ice Core, has facilitated a data-constrained improved understanding of SMB variation since the mid Holocene, and indicates that SMB over the Amundsen-Ross-Weddell divide was on average 18% higher during the mid Holocene compared to the present (Bodart et al., 2023). Similar exercises elsewhere in Antarctica (e.g. Leysinger Vieli et al., 2004; Ashmore et al., 2020; Bodart et al., 2021; Cavitte et al., 2016; 2018) are steadily developing a continent-wide coverage for which the prospects of assimilating into SMB modelling are rapidly improving (Sutter et al., 2021).

3.5.2 Seismology

Active and passive seismological observations can provide constraints on the seabed topography beneath ice shelves, the geological structure under both ice sheets and ice shelves, and physical properties of the ice itself (e.g., Albert & Bentley, 1990). Although IPR can directly measure bed topography under grounded ice, it does not penetrate seawater. Consequently, IPR can measure only the thickness of ice shelves, but not seabed topography. Instead, airborne gravity data is often used to infer seawater column thickness under ice shelves, as well as in the sea-ice-covered or open-water areas where vessel-based bathymetry data are unavailable (e.g., Jordan et al., 2020). The gravity method works by modelling the effects of the strong density contrast between water and rocks at the seabed, but is subject to uncertainties because of geological density further below. Gravity models of seabed topography should therefore ideally be tuned by fitting seismic constraints on water column thickness (Section 3.1.4). Seismic surveys over grounded ice and floating ice are well suited to assess the presence and thickness of sediment layers (Anandakrishnan et al., 1998; Smith et al., 2020), which are important due to their large effect on the basal motion of fast-flowing glaciers (Sections 2.6.4 and 2.8.3). Overall, seismic survey data can complement and reduce uncertainties in the geological framework interpreted from airborne gravity and magnetic data (e.g., Kristoffersen et al., 2014). They also provide critical constraints on present-day basal boundary conditions (e.g., Hofstede et al., 2021; Horgan et al., 2021), and inform about paleo-ice dynamics, especially from present-day geomorphological structures (e.g., Oetting et al., 2022; Smith et al., 2007).

Seismic surveys are carried out using either an active or a passive source. An active source seismic survey may be collected as point measurements (a single set of measurements) or as linear profiles (multiple measurements along a line). Linear profiles are generally preferred as they facilitate more robust analysis; however, as active-source seismic measurements are time consuming, logistical constraints and scientific goals may dictate a different survey mode. When information about seabed topography is needed, point measurements are often made at many locations over a large area (e.g., Nøst, 2004; Rosier et al., 2018). Conversely, when information about geologic structure is needed, linear profiles may be collected (e.g., Horgan et al., 2013; Kristoffersen et al., 2014; Smith et al., 2020). For any active-source case, the most common sources are either a small explosive charge (~500 g or less) or a striking metal plate (Brisbourne et al., 2020). Reflected and refracted signals are recorded by a 200-400 m long string of cabled geophones. As the conventional active source seismic equipment is relatively light weight (~50 kg or less) and can be deployed quickly (~ 1 hour per point measurement), a team with just a few people and a small fixed wing aircraft such as a Twin Otter can acquire a relatively large seismic dataset in a single season (e.g., Brisbourne et al., 2020; Rosier et al., 2018). The vibroseis method, which uses a large mechanical source, is by far the most efficient means of active source seismic acquisition, allowing a data collection rate of 20 km day^{-1} (Kristoffersen et al., 2014; Smith et al., 2020). However, this method requires significant logistical infrastructure (tractor train), which may make it challenging to operate in some regions (Eisen et al., 2015). In recent years, the development of so-called autonomous seismic nodes, which are light-weight and relatively cheap, enabled the deployment of hundreds of such nodes in arrays for either passive or active seismic studies (Smith et al., 2015; Zhang et al., 2022). Distributed Acoustic Sensing (DAS) systems, which use fiber optic cables to detect acoustic vibrations, have the potential to significantly enhance our understanding of the Antarctic subsurface by providing detailed depth profiles of ice (e.g., Brisbourne et al., 2021) and bed. DAS systems are capable of detecting a wide range of signals, including seismic waves and ambient noise. However, the harsh environmental conditions in Antarctica pose challenges to the operation and maintenance of these systems, such as cable and equipment damage due to extreme cold and weather conditions.

Passive seismic observations differ from active source measurements in that networks of broadband seismometers or geophones are left to record seismic signals of discrete natural events (earthquakes and icequakes) and ambient noise such as from ocean waves and subglacial water flow (e.g., Winberry et al., 2009) or iceberg collisions (e.g., Pirli et al., 2017). The size of the networks depends on the dedicated target processes to investigate and can range from several square kilometers with a station spacing of tens to hundreds of meters for shallow and localized processes (e.g., grounding line cryoseismicity) to large-scale seismic networks with stations being 100s of kilometers apart. Such networks are particularly well suited for imaging sedimentary basins and overall geological structure. Seismic stations for deep-Earth studies, which could help determining mantle viscosity related to GIA and GHF (Section 2.6), are typically deployed for two years and often require a significant dedicated battery bank to support their operation through the polar night, resulting in relatively high total station weight (> 150 kg) (Hansen et al., 2015). However, summer only deployments can operate with a much lower total station weight (< 40 kg). Although such summer-only observations are not ideal for deep-Earth targets, these shorter-term deployments (1–2 months) provide an efficient way to image subglacial sedimentary basins (e.g., Gustafson et al., 2022). Whereas most seismological networks were deployed on grounded ice and outcrops, recent work has shown that seismological stations on ice shelves can provide insight into water-column thickness, although at a lower accuracy than active source observations (Phạm & Tkalčić, 2021; Zhan et al., 2014). Passive seismic observation can also be used to evaluate the stability of ice shelves against long-period ocean swells (Chen et al., 2019)

3.5.3 Marine and submarine instruments

The technology for polar marine observations has advanced recently. In addition to the traditional methods of observations from research icebreakers such as Swath multibeam, Rosette CTD, and moorings, a series of autonomous instruments have been developed. Originally, these new instruments were designed for the open ocean, but they have been modified for use in numerous polar deployments near and under sea ice and ice shelves. For more about the history of submarine instruments, see the Antarctic section of Rudnick et al. (2017) and Barker et al. (2020) for a review of the historical and remaining challenges for marine robotic technologies for exploring under ice.

Float profilers, instrumented seals, and gliders are light, relatively inexpensive, and optimized to explore the temporal variability in the ocean. They are relatively long-lasting but have a limited payload. Sensing capabilities are often limited to optical properties, temperature, conductivity, and pressure in the water column. These sensors can provide point observations of the system geometry (e.g., seabed and ice-base depth) with a relatively coarse spatial resolution; underwater geo-location can be determined using only acoustic solution, not GNSS (Girton et al., 2019). On the other end of the spectrum are high payload, low-endurance platforms such as autonomous underwater vehicles and remotely operated vehicles. Such platforms are often used on shorter spatial and temporal scales to examine processes and geometric features on the seabed and the ice base (e.g., Dutrieux et al., 2014; Jenkins et al., 2010).

Despite these inherent trade-offs, technological advances have significantly expanded the capability of autonomous platforms to observe polar oceans (e.g., Lee et al., 2022). Underwater gliders, for example, enable months-long autonomous sampling with high vertical and horizontal resolution in locations that are otherwise inaccessible or exposed to extreme environmental conditions (Webster et al., 2015; Rudnick et al., 2016). Their adaptive sampling strategies and diverse payloads, including optical (Camus et al., 2021), biogeochemical (Portela et al., 2025; Pickup et al., 2025) and acoustic (Baumgartner et al., 2020; Camus et al., 2021) sensors, make them uniquely suited for resolving multi-disciplinary fine-scale processes (Meyer, 2016; Friedrichs et al., 2022), tracking boundary-current variability (Testor et al., 2019), and characterizing under-ice environments using a quiet and energy-efficient platform (Rudnick, 2016; Testor et al., 2019). Gliders therefore increasingly complement ship-based and AUV operations, offering access to key areas where traditional platforms are limited (Rudnick et al., 2016; Lee et al., 2022).

Parallel advances in profiling float technology (e.g., Riser et al. 2018; Le Traon et al., 2020) have further opened opportunities for sustained observations beneath sea ice (Wallace et al., 2020; Hague and Vichi, 2021; Smith and Zhong, 2024), along ice-shelf margins (Porter el al., 2019), and even within ice-shelf cavities (Falco et al., 2024), providing new insight into basal melt and cavity-ocean exchange processes. Constrained-mode Argo floats, programmed to minimize drifting, can now deliver year-round profiles in regions that were historically inaccessible, particularly during winter (Porter et al., 2019; Wallace et al., 2020; Falco et al., 2024). These deployments demonstrate the growing potential of constrained-mode floats to resolve processes within and around ice-shelf cavities and to reduce the long-standing observational gap that persists during winter (Falco et al., 2024).

Together with airborne deployment of ocean instruments (Section 3.1.7), we now have a remarkable opportunity to fill many gaps in our current understanding of the large temporally and spatially variable Antarctic shelf seas.

3.6 Mapping topography and surface mass balance

3.6.1 Bed topography

Ice thickness and bed topography are most efficiently measured through airborne IPR (Section 3.1.1). While efficient and reliable, this method only provides a measurement of the bed topography directly underneath the aircraft at nadir in most cases. Some applications managed swath-mapping to see off-nadir measurements, but such measurements are not routinely available at this stage. Even at nadir, IPR can fail to detect the bed if the ice surface ice is heavily crevassed (Holt et al., 2006), if pockets of water exist on or in the ice (Figure 14), or if reflection from valley sidewall of outcrops superimpose the return signal. Water pockets limit the penetration of radio wave signals and produces a spurious signal that can be confused with the bed echo. Penetration of the radio wave can also be limited when ice is warm and attenuates radar signals. A fourth limitation is in regions of steep, rough, and entrenched bed topography where the basal reflection of the signal can be masked by reflection from escarpments or the side walls of valleys (Figure 14). Coastal regions are prone to all four limitations: this is where the basal topography is most complex, the surface is most crevassed, and where supraglacial lakes are most likely to be present.

Subglacial topography is a key boundary condition in ice sheet models to assess mass balance (Sections 2.6.4, 2.8, 3.8). Models require bed topography at the same spatial scale as the computational grid or mesh, which is typically at ~200–1000 m, and higher near grounding zones (Figure 10) in order to accurately capture grounding-line migration (e.g., Durand et al., 2009; Pattyn et al., 2013). To construct a complete, seamless map from data collected along flight lines, several approaches have been used. The simplest approach is by interpolation, using geostatistical methods such as kriging (Deutsch & Journel, 1997), and has produced the influential Bedmap (Lythe et al., 2001), Bedmap2 (Fretwell et al., 2013), and the most recent Bedmap3 (Pritchard et al., 2025) products, each based on more measured datapoints than its predecessors. However, numerical models rely on the conservation of mass to drive the dynamic evolution of the surface topography, and bed topography maps based on kriging tend to produce high anomalies in flux divergence, thereby introducing strong biases and artifacts in ice-flow models (Seroussi et al., 2011).

Another method to generate seamless maps from line measurements combines the IPR measurements with other datasets and invokes conservation of mass. This method was developed and applied to Greenland and Antarctic ice sheets by Morlighem et al. (2011, 2016, 2020) to overcome the difficulty of initializing numerical ice-flow models based on bed topography maps generated by geostatistical approaches. Similar approaches were applied to develop a regional bed topography map of the Antarctic Peninsula (Carrivick et al., 2019; Huss & Farinotti, 2014).

To interpolate ice thickness between IPR surveys, this method approximates the depth-averaged ice velocity with the satellite-measured surface velocity (similar to the mass flux calculation at the grounding line, Section 2.2). This velocity and the apparent mass balance are linked to the ice thickness. For apparent mass balance, the sum of SMB and the rate of ice-thickness change are considered, and subglacial melt under the grounded ice is ignored (Section 2.3). The inflow boundary is defined using the locations of IPR measurements. To constrain ice thickness over the entire domain, the mismatch between modeled and measured thickness along all surveys are minimized while the output ice thickness field remains smooth. The accuracy of the method depends on the modeled SMB (Section 2.4.2) and that of the satellite-measured ice velocity direction (Section 3.7.2). As a result, this method is currently applied only to the regions where ice flows faster than 20 m yr^{-1}, which is about 10% of the AIS, and a streamline diffusion method is applied elsewhere (Morlighem et al., 2020).

Both mapping methods can miss small-scale, yet important, topographic features particularly at large distances from survey measurements (Shackleton et al., 2023). Such features affect subglacial hydrology (Section 2.8.3) and ice flow, in particular near the grounding line (Section 2.8.2). Based on the roughness of the IPR-detected bed, small-scale features in the topography can be introduced using stochastic simulations (Section 4.7). This technique has been applied to map the bed of Thwaites Glacier (Goff et al., 2014), the AIS (Graham et al., 2017), Jakobshavn Isbræ in the Greenland Ice Sheet (MacKie et al., 2021), and Dome Fuji in the inland East Antarctica (Shackleton et al., 2023). However, the results are not unique and will change between each realization. Other physical constraints, such as the conservation of mass, are difficult to enforce and canyons may need to be manually introduced (Goff et al., 2014).

Finally, new methods are emerging for mapping bed topography based on surface data and deep learning models (Leong & Horgan, 2020; Ockenden et al., 2022; 2025). The approach assumes the existence of processes or properties that enable the ice sheet to transmit some information about the basal topography to its surface (Gudmundsson, 2008). Building on this assumption, Leong & Horgan (2020) developed DeepBedMap with the 0.25-km grids, a neural network could be developed to find relationships between surface observations (e.g., surface speed, surface topography, SMB, surface thinning rate) and local basal topography, which were applied to the Bedmap2 dataset with the 1-km grids (Fretwell et al., 2013). Recently, Ockenden et al. (2025) inverted subglacial topography across the entire AIS from a high-resolution surface DEM to produce the first map of continent-wide subglacial texture unbiased by the uneven distribution of existing IPR measurements. More research is needed to determine if this approach is a viable complement to existing techniques.

3.6.2 Seabed topography

Despite the importance of seabed topography data for understanding and predicting ice sheet mass loss, major problematic data gaps remain along most grounding lines (Section 4.4). The most accurate way to measure seabed is through shipborne multibeam sonar surveys. However, close to the ice sheet, the presence of thick sea ice makes shipborne surveys difficult or impossible. Seabed topography over Antarctica's continental shelves has also been reconstructed from satellite-derived gravity anomalies, providing large-scale (tens to hundreds of kilometers) constraints on previously undocumented seafloor features (Charrassin et al., 2025). The seabed topography under ice shelves is even more challenging to estimate because it requires the acquisition of seismic and or gravity data. Since the early 2010s, seabed topography beneath Antarctica's ice shelves has been reconstructed using inversion of airborne gravity data (e.g., Cochran & Bell, 2012; Tinto & Bell, 2011). Compared to direct measurements by ship-borne sonar surveys and ground-based seismic surveys (Section 3.5.2), airborne campaigns acquiring high-resolution gravity data are logistically more efficient and less time-consuming, but have larger uncertainties and lower spatial resolutions. Thus, it is crucial to co-solve gravity and geology for seabed elevation.

Over the past decade, various approaches to the inversion of gravity data for seabed topography have been used at various ice shelves of Antarctica (Section 4.4). The methodology in general is applicable wherever gravity data are available. The method's accuracy can be improved by adjusting the results to fit data better at the locations covered by a seismic survey (Section 3.5.2) or data from submarine probes (Section 3.5.3). The presence of density contrasts between different geological units produces gravity anomalies that are not related to seabed topography: deeper density contrasts affect long-wavelength part of the gravity field, whereas shallower density contrasts affect short-wavelength part. Thus, subglacial geology affects any seabed topography modelled from gravity. In the future, a comprehensive physical Earth model is needed to provide both seabed topography and water-column thickness under the ice shelves, as well as other geological characteristics such as GHF (Section 3.8.7).

The latest compilation of bathymetry data in the Southern Ocean is the International Bathymetry Chart of the Southern Ocean version 2 (IBCSO v2; Dorschel et al., 2022), which is a part of General Bathymetric Chart of the Ocean (GEBCO) seabed 2030 project. Following IBCSO's first version, which covered the area south of 60^{o}S (Arndt et al., 2013), geographical coverage of IBCSO V2 was extended to 50^{o}S, covering 2.4 times more of the seabed area (Figure 7a). Because of its highly variable data density, IBCSO V2 first re-interpolated all data at 2 km x 2 km resolution to create a coarse grid that captures large-scale features and removes noise. In regions where multibeam data are available, a separate 500 m x 500 m resolution grid was generated. These two data products were merged finally to generate a 500 m x 500 m grid for the entire Southern Ocean. IBCSO V2 is smoothly connected from seabed under the ice shelves to the bed under the AIS determined by BedMachine (Morlighem et al., 2020). IBCSO V2 has provided annual updates (https://ibcso.org/ibcso-2025-annual-release/).

3.6.3 Surface mass balance

Mapping and resolving spatial and temporal patterns in coastal SMB are crucial for reliable estimates of mass balance using the input-output method, for firn compaction in volume change estimates using satellite altimetry data, and for understanding the origin of a mass balance trend (Section 2.1). Most SMB models currently have spatial resolutions of tens of kilometers, so when field data are used to evaluate models, spatial representativeness of the stake- and core-based data, along with the short temporal coverage of the records, can be problematic (Section 2.4.2). To help fill these data gaps, one can use shallow-sounding IPR to measure SMB over large regions (Section 3.1.2 and Figure 15b). Here, we discuss how recent SMB can be retrieved in large areas using shallow-sounding IPR data and shallow ice (or firn) cores.

Ice-core data and IPR profiles are complementary in assessing SMB in the sense that ice cores locally provide absolute ages and densities at various depths whereas IPR profiles allow for spatializations over horizontal distances as long as the reflectors can be tracked continuity (e.g., Cavitte et al., 2022, 2023; Medley et al., 2013, 2014; Koch et al., 2024). This internal layering provides stratigraphic constraints inside the ice column: each reflector can generally be considered an isochrone (i.e., surface of uniform age) (Richardson et al., 1997; Spikes et al., 2004; Vaughan et al., 1999). However, assuming that the reflectors' age increases with depth in the sequence (i.e., no folding), the radar reflectors alone can only give relative ages. Furthermore, radar measures only two-way travel time to the reflectors. Converting this travel time to depth requires the radio-wave propagation speed, which depends on firn density (Kovacs et al., 1995; Cavitte et al., 2022) as well as water contents (Bradford et al., 2009). Although the density is essentially uniform in the deeper ice (and thus this is much less problematic for deep-sounding IPR to determine ice thickness), it varies significantly in the shallower ice that is relevant to SMB. A comprehensive error analysis showed that the principle error term in radar-derived SMB arises form uncertainties in the density profile used (Le Meur et al., 2018). In particular, in the coastal regions of Antarctica, the density varies from around 300–500 kg m^{-3} at the surface to about 830 kg m^{-3} (firn-ice transition) at depths typically shallower than 80–100 m (e.g., Hubbard et al., 2013). Radio-wave propagation speeds can be estimated by converting density measurements with ice cores (e.g., Eisen et al., 2002), by borehole optical logging (Hubbard et al., 2013), or by common-midpoint (wide-angle) IPR measurements (e.g., Arthern et al., 2013; Drews et al., 2016; Oraschewski et al., 2025).

For reflectors located at depths of within a few percent depth of the local ice thickness, the accumulated strain to this depth is minimal. As a result, SMB can be determined simply dividing the cumulated ice mass down to this reflector by the age of this reflector. This can also be applied to any layer located between two isochronous reflectors, where SMB is determined by dividing the mass within this layer by the number of years in this layer (Waddington et al., 2007). This "shallow-layer" assumption is widely used when a recent SMB is constrained using an ice core and radar reflectors (e.g., Cavitte et al., 2022; Goel et al., 2017; Kausch et al., 2020; Pratap et al., 2022; Moss et al., 2025). When radar reflectors are deeper and thus this assumption is no longer valid, accumulated strain rates need to be corrected. When horizontal advection of ice is negligible (i.e., small lateral advection due to slow motion or short period), this correction can be calculated one dimensionally locally at the site where SMB, called "local-layer approximation" (e.g., Bodart et al., 2023; Waddington et al., 2007). When the reflectors are too deep to simplify in these ways, ice-flow models are often used to remove accumulated strain and extract SMB, which is often non unique and requires many more assumptions (e.g., Koutnik et al., 2016). Extending these IPR and ice core SMB data further spatially is possible through data assimilation of these datasets with modelled SMB (e.g. Cavitte et al., 2025), which allows to reconstruct spatially and temporally consistent variations of SMB. In any case, dating radar reflectors using ice cores is crucial to derive SMB from shallow-sounding IPR data.

3.7 Satellite data

Satellite datasets and satellite-derived data products are crucial for characterizing Antarctic coastal zone and planning its ground-based and vessel-based surveys. In turn, satellite data analysis will be improved by any data collected by in-situ surveys. Here we review satellite data products for surface elevation and elevation changes (Section 3.7.1), ice-flow velocity (Section 3.7.2), surface melt (Section 3.7.3), and gravity (Section 3.7.4). Determination of the grounding line is further discussed in Section 4.1.

3.7.1 Surface elevation and elevation changes

For surface elevation and topography data, two satellite-derived datasets are useful; one is static products and the other is products of elevation changes. For the former, there are several pan-Antarctic products such as the reference elevation model of Antarctica (REMA; Howat et al., 2019) and TanDEM-X Polar DEM (Wessel et al., 2021), as well as a recent one for the Antarctic Peninsula (Dong et al., 2021). For example, REMA is a pan-Antarctic product of surface elevations derived from stereo-pair images from GeoEye-1, Worldview-1, -2, and -3 satellites (Howat et al., 2019) distributed at a ground sample distance of 2 m. Updates are released as they become available. REMA provides both a near-continuous continent-wide DEM mosaic of the AIS (now version 2, Howat et al., 2022) and time-stamped DEM strips (now version 4.1) with ~ 4 m accuracy in horizontal position. This horizontal accuracy can be reduced to <1 m with appropriate ground reference points. A vertical error is better than 1 m. The other dataset is from ICESat-2, NASA's Ice, Cloud, and land Elevation Satellite-2 (ICESat-2), which has the mission to measure the height of a changing Earth surface using a photon-counting laser altimeter (Markus et al., 2017). Various products useful for the AIS are generated from ICESat-2 data, including ATL06 (land-ice height; Smith et al., 2019, Smith et al., 2023a), ATL11 (land-ice-height change; Smith et al., 2023b) and ATL14/15 (gridded land-ice height and height-change, Smith et al., 2024a, 2024b, in review). These products constitute baseline datasets of surface topography and topographic change with the highest horizonal resolution of 2 m (REMA) and vertical precision < 0.1 m (ICESat-2 ATL06; Brunt et al., 2021). Another method to detect elevation changes is to combine existing DEM to interpret phase differences in the SAR (synthetic aperture radar) images (e.g., Seehaus et al., 2023; Shahateet et al., 2021).

Multiple data products provide estimates of continuous elevation changes in various time windows. Among these is the ICESat-2 ATL15 data product, which provides 1 km by 1 km resolution elevation estimates based on high-precision satellite laser altimetry (Smith et al., 2024b). The ATL15 time series begins 1st January 2019, with a temporal resolution of approximately three months, based on lower level ICESat-2 data that has ground-track spacing of 3 km and an individual footprint size of approximately ~ 11 m (Magruder et al., 2021). ITS_LIVE is one of NASA's Making Earth System Data Records for User in Research Environment (MEaSUREs) project to provide automated, low latency, global glacier flow and elevation change datasets. ITS_LIVE's data of AIS's elevation changes are based on a combination of satellite radar altimetry (Geosat, ERS-1, ERS-2, Envisat, and CryoSat-2 missions) and laser altimetry (ICESat and ICESat-2 missions) data from 1985 to 2020 and is posted at monthly time steps on a 1920 m x 1920 m grid with an effective spatial resolution of ~ 20 km (Nilsson et al., 2022). These long-term elevation-change estimates have an uncertainty near the coast of ~ 25 mm yr^{-1}, though uncertainty varies in both space, depending mainly on surface slope, and in time, depending on the available missions.

Oceanic ice-shelf basal melt–freeze rates at the continental scale are typically quantified using satellite radar altimetry (e.g., Adusumilli et al., 2020), with on-going work leveraging the higher spatial and vertical resolution of ICESat-2 mission datasets. This estimate assumes that ice shelves are freely afloat (Figure 10) and that firn density, SMB, and surface velocities are known. Basal melt rates are often highest near the grounding line (Section 2.7.2), where the freeboard assumption may not be valid due to non-local bridging stresses. Also, the higher surface elevation of the ice sheet inland of the grounding line, and in particular near the ice rises, may cause orographic precipitation that gets missed by RCMs (Lenaerts et al., 2014; Siegfried et al., 2017), which can result in additional uncertainty in firn density. Therefore, these estimates should be tested, particularly in the regions with significant variability in basal mass balance, where the basal mass balance is nearly zero, or where ice flow speed is very small. Ground-based measurements using ApRES revealed temporally variable basal melting rates over weeks to seasons (e.g., Lindbäck et al., 2019). Such data are being compiled all around Antarctica (Cook et al., 2023), which constitutes a very strong data constraint to constrain satellite-driven ice-shelf thickness changes and mass balance.

3.7.2 Ice-flow velocity

The most comprehensive ice-velocity product in Antarctica (Mouginot et al., 2019) is derived from a combination of three satellite-based methods for deriving ice velocity: optical image feature tracking, SAR speckle tracking, and interferometric SAR (InSAR). The NASA ITS_LIVE database provides time-resolved velocity from Landsat-based feature tracking over time windows of 6–546 days (Figure 7b; Gardner et al., 2018). Uncertainties in these feature-tracking velocity estimates can be as high as 20–30 m yr^{-1}, but are uncorrelated over large regions (Gardner et al., 2018). Glaciers in the west Antarctic Peninsula show significant speed up during the summer (Boxall et al., 2022; Wallis et al., 2023), which may bias satellite-based flow-field estimates.

As ice flows across the grounding zone, the ice-shelf flexure causes the surface elevation to change (Figure 10). Observing such change requires a high-precision, time-resolved, height-change product such as satellite laser altimetry (e.g., Fricker & Padman, 2006) or differential interferometric synthetic aperture radar (DInSAR; e.g., Rignot, 1998). Also, with appropriate quality control and vertical registration, REMA DEM strips may be used for this case (Chartrand & Howat, 2020). DInSAR uses two pairs of SAR images from past and current SAR imaging satellite missions (e.g., ERS-1, ERS-2, Envisat, RADARSAT, RADARSAT-2, Sentinel-1) to isolate and map differential vertical motion of ice near the grounding zone at two tidal heights (e.g., Rignot, 1998). Although current DInSAR missions can map changes in the grounding-line location over a tidal period in some cases (e.g., Milillo et al., 2017; Minchew et al., 2017), such mapping requires dedicated tasking of satellite assets and cannot be achieved continent-wide. The NASA-ISRO SAR (NISAR) mission launched in July 2025 may be able to provide a more complete assessment of grounding-zone variability across Antarctica.

3.7.3 Surface melt

Surface melt events (Figure 6) may trigger disintegration of ice shelves (Section 2.8.1), affect paleoclimate signals retrieved from ice cores (Section 3.5.1), and increase the surface density. A change in surface density, in turn, can influence estimates of elevation and mass changes as well as the thickness of ice shelves detected by satellite altimetry. Mapping strong surface melt areas before conducting airborne IPR surveys is crucial to minimize surface clutter that can lead to unusable data (Section 3.6.1). Continent-scale estimates of surface meltwater volume are currently derived from microwave backscatter methods, which has a relatively coarse spatial resolution of ~5 km (e.g., Trusel et al., 2013), and from depth-reflectance models applied to optical satellite imagery (e.g., Arthur et al., 2022). In addition to the amount of surface melt, the SMB is also poorly constrained by satellite products so far, so RCMs have been used to constrain these key parameters (Section 2.4.2), with validation from satellite tools (e.g., Smith et al., 2023b). Recent work using ICESat-2 satellite laser altimetry suggests that satellite data can supply useful data for estimating SMB, particularly at a short spatial scale where topography can drive small-scale variability in SMB processes (Medley et al., 2022). SMB observations using airborne shallow-sounding IPR will aid in the development of satellite-based methods for observing such surface processes with higher precision in the future.

3.7.4 Temporal variations of gravity

Temporal variations of gravity are useful to constrain mass balance of the AIS (Section 2.1.1). For this purpose, products are generated from GRACE, the gravity recovery and climate experiment (Tapley et al., 2004) and from GRACE-FO, the follow on to GRACE (Kornfeld et al., 2019). Also the datasets from GOCE, the gravity field and steady-state ocean circulation explorer, are of interest, particularly in relation with crust and mantle structure under the AIS (e.g., Ebbing et al., 2018).

The satellite gravity systems measure changes in the gravity field as the satellite orbits around the Earth, sampling its surface (in our case, the ice sheet) and the underlying crust and mantle. These gravity potential changes are provided as Level 2 spherical harmonic sets by three data centers: NASA Jet Propulsion Laboratory (JPL), Center for Space Research (CSR), and Helmholtz-Zentrum Potsdam (GFZ). These products are widely used in the GRACE science community due to their flexibility in geophysical corrections and ease of geodetic applications. A Level-3 product “mass concentration block (mascons)” in the form of gridded mass changes are provided by these data centers as well. Satellite gravity data inevitably have low spatial resolution of several hundred kilometers (Section 2.1.1), so it is necessary to remove any signals from other sources of mass movement from surrounding and far-field regions, such as ocean mass variability (e.g. tides), atmospheric vapor, land hydrology and GIA (e.g., Bamber et al., 2018; Chen et al., 2015; Kim et al., 2025; Loomis et al., 2019; Save et al., 2016; Watkins et al., 2015). Currently, the ICE-6G model (Peltier et al., 2018) is widely used for GIA corrections, but recent observations based on GNSS networks have shown that this model considerably underestimates the actual bedrock uplift, particularly in the glaciers near Amundsen Sea Embayment in West Antarctica, where most glaciers have been retreating rapidly over the past decades (Barletta et al., 2018).

GRACE/GRACE-FO and GOCE measure the gravity field in different ways. The GRACE/GRACE-FO consists of twin satellites, separated by about 220 km, which infer the gravity field from the variations in distance between both satellites due to the spatial changes in the gravity field. The distance between the satellites is measured using a precise microwave ranging system. GRACE-FO satellites also mount an experimental instrument that uses laser light instead of microwaves, aiming to improve the accuracy of future GRACE-like missions by tenfold or more (Jenny et al., 2025). By contrast, GOCE satellite employs the concept of gradiometry, i.e. the measurement of acceleration differences (gravity gradients) over short baselines between proof masses of a set of six 3-axis accelerometers of the electrostatic gravity gradiometer mounted by GRACE (Lu et al., 2025).

GRACE was operational over the period 2002-2017, while GOCE was during 2009-2013. The shorter lifetime of GOCE is due to its lower orbit altitude of 250-270 km and hence larger friction with the atmosphere (Michaelis et al., 2022), as compared with 500 km for GRACE. GRACE-FO was launched in 2018 and designed to operate for at least five years (the same as originally designed for GRACE, which finally lasted for 15 years). The lower orbit altitude of GOCE is a design concept, aimed at achieving a higher signal accuracy (10^{-2} m of geoid heights, and 10^{-5} m s^{-2} for gravity acceleration) and spatial resolution (half the wavelength) of about 100 km, as compared with the footprint of GRACE of about 300-400 km (Michaelis et al., 2022). Therefore, their spatial resolution is much lower than that of satellite altimetry (Section 3.7.1).

Both GRACE/GRACE-FO and GOCE systems have orbit periods of about 90 minutes, in near-polar orbits with inclinations of 89.5° and 96.7°, respectively. The latter implies a polar gap south of 83°S, where GOCE data are not available, whereas such a gap is negligible in the case of GRACE. The repeat cycles are of 30 days (GRACE) and 61 days (GOCE), the latter with a sub-cycle of 20 days.

In recent years, efforts have been made to enhance the spatial resolution of GRACE's Antarctic ice mass observations by integrating them with satellite altimetry data. Sasgen et al. (2019) combined GRACE and Cryosat-2 satellite altimetry observations in the spatial spectral domain, estimating ice mass trend from 2011 to 2017 at an approximate resolution of 40 km. Kim et al. (2022) developed a joint inversion approach, using multi-mission altimetry data as a-priori information, and provided monthly mass changes from 2003 to 2016 at a nominal resolution of about 27 km. However, these estimates do not fundamentally address the issue of GIA errors present in the gravity data (Jenny et al., 2025). As a result, enhancing the GIA model is crucial for improving ice mass change estimates derived from the satellite gravity data and reducing discrepancies with other mass balance estimates (Section 2.1.1).

3.8 Numerical models and reanalysis data

Numerical models help to shape our knowledge of how Antarctica responds to external forcing as well as the feedback between the ice sheet and other components, such as the ocean, atmosphere, and solid Earth. Observations from satellite remote sensing combined with in situ measurements play a significant role in improving ice-sheet and ice-shelf models by providing valuable physical constraints as well as mass-balance estimates. In turn, numerical models can provide valuable insights about defining priorities and targets for future fieldwork. Here we describe models and reanalysis data that are currently used for studying the coastal regions of the AIS. We also discuss the data needed in numerical models primarily for planning airborne surveys in the coastal regions.

3.8.1 Earth system models and global circulation models

Earth system models (ESMs) are advanced GCMs that also incorporate the carbon cycle in addition to the traditional components such as the atmosphere, ocean, and sea ice (e.g., Flato, 2011). At its most basic, Antarctica may be represented as a continent, simply a static ice-covered land, surrounded by an ocean with no ice shelves. More sophisticated representations of Antarctica in GCMs and ESMs may impose freshwater fluxes from melt and even solid ice fluxes, but these are often climatological values with no connection with regional circulation (Vizcaino, 2014). The most sophisticated ESMs include a coupled ice-sheet model with feedback between the ice sheet, the atmosphere, and the ocean components (e.g. Muntjewerf et al., 2021; Smith et al., 2021). Typically, this feedback takes the form of having SMB and oceanic basal melt under ice shelves imposed on the ice-sheet model, which then runs dynamically and outputs a new ice-sheet extent plus freshwater fluxes into the ocean. Few studies address the full coupling between the atmosphere, the ocean, and the ice sheets, while they are either limited in timespan (Pelletier et al., 2022) or limited by spatial resolution (Golledge et al., 2019; Sellevold et al., 2019). Besides the high computational cost, major issues in the fully coupled approach remain, such as how iceberg discharge relates to meltwater fluxes (Davison et al., 2020).

The rather coarse resolution of GCMs and ESMs means they are not ideal for forcing dynamical ice-sheet models, and thus RCM (Section 3.8.2) are frequently used where higher resolution atmospheric forcing is necessary. However, a new generation of global climate models with variable grid resolution are in development and have already been applied over the polar ice sheets, where they appear able to resolve important processes at least on the scale of tens of kilometers (e.g., Dunmire et al., 2022). These variable grids require a full surface energy balance scheme and firn model to calculate accurate SMB values. Recent work has focused on implementing these local components in GCMs (e.g., Datta et al., 2022b; Lipscomb et al., 2013).

Examples of commonly used ESMs and GCMs in Antarctica include the Alfred Wegener Institute Earth System Model (AWI-ESM2) (Sidorenko et al., 2019) used to simulate basal melt in the Totten Ice Shelf cavity (Song et al., 2025); LOVECLIM (Goosse et al., 2010), used to assess impact of Antarctic meltwater on ocean abyssal circulation (Moon et al., 2025). CMIP6 models (IPSL-CM6A-LR, UKESM1-0-LL, MPI-ESM1-2-HR and CNRM-CM6-1 have also been used (Davrinche et al., 2025) and there is an ESM in development (Villanueva and Shaffer, 2025).

3.8.2 Regional climate models

Regional Climate Models (RCMs) are typically atmosphere only, although some recent ones couple with ocean, sea-ice, and ice-sheet components (Smith et al., 2021c). Based on numerical weather prediction systems, RCMs are typically run over horizontal scales of tens of kilometers for climate projections, down to about one kilometer for process studies, depending on the physical scheme. Within the framework of the Polar CORDEX (i.e., the polar coordinated regional downscaling experiment, a World Climate Research Programme project), these models were typically run at 0.44° resolution over a domain covering the full continent and surrounding ocean. However, given improvements in computational power and interest in important process studies, the horizontal scale resolved by RCMs has improved to 5.5 km in the smaller sub-regions. However, van Wessem et al. (2018), and Arthur et al. (2022) pointed out that scales of ~10 km should be resolved to identify processes such as foehn and katabatic winds as well as to more realistically resolve the spatial variability in precipitation and local wind-driven ablation in high-relief topographically-complex regions like the Antarctic Peninsula and steep escarpment regions of ice-shelf grounding zones and ice rises in other coastal regions of Antarctica.

On the continental scale, Mottram et al. (2021) compare results from five RCMs running in eight versions, each version having distinct physical and dynamical schemes (see Figure 5 for the ensemble results). As the full pan-Antarctic domain is large, internal variability (RCM-predicted weather) starts to arise in unconstrained models, and the RCM starts to drift from the forcing model or reanalysis that gives spatial boundary conditions to the RCM. This drift tends to be large when the model's horizontal domain is larger, the temporal range is longer, and the horizontal resolution is finer. When run for weather forecasting, the models are re-initialized every 24–48 hours. Despite these efforts and the use of the same external forcing (e.g., ERA-Interim climate reanalysis), ensemble results spread widely (Figures 5b and 5d). Even when the models have similar resolution and similar physical parameterizations, the models show large variability in the spatial pattern of SMB. This points to the importance of running ensembles of models and using the ensemble mean for climate and ice-sheet studies.

Other RCMs commonly run in Antarctica include WRF (Deb et al., 2016) and NHM-SMAP (Niwano et al., 2018). Several studies note that RCMs may overestimate precipitation on the upward slope of high-relief topography, with a resulting dry bias on the downslope side (e.g., Kausch et al., 2020). Through the surface energy and moisture budgets, such bias affects estimates of SMB. Thus, to reduce such bias, new RCMs will include better prognostic precipitation schemes and non-hydrostatic physics. Another research direction is the development of machine learning techniques to emulate RCMs and enable the building of large ensembles of climate simulations. These were applied to Antarctica only by Meer et al. (2022), with promising preliminary results (Doury et al., 2023). Provided that they can be shown to represent regional climate accurately, their much lower computational cost and simplicity compared to RCMs make them attractive for broader use. This efficiency enables practical benefits such as running larger ensembles, extending simulations to longer time periods, or exploring higher spatial resolution without prohibitive resource demands. Better datasets, with finer spatial and longer temporal coverage of both atmospheric and surface processes will be key not only to assess these new models, but also as training data for Artificial Intelligence (AI) applications.

3.8.3 Reanalysis climate data

Climate reanalysis involves running a numerical weather prediction (NWP) model with full data assimilation in hindcast mode to give the closest possible approximation to observed weather. The result is a gridded dataset of model variables consistent with both the model dynamics and the weather observations. The model is nudged using data assimilation to reduce the stochastic variability that would otherwise be represented. The different variables under analysis can depend on the model and the ingested observations in varying ways. For instance, precipitation and fluxes are rarely assimilated, hence their values in the reanalysis can result entirely from the model. By contrast, winds, thermodynamic variables and mass variables are assimilated, thus the variables resulting from the reanalysis will combine the constraints of the ingested observations and the model dynamics (Section 16.2 in Warner, 2010). Reanalysis was originally a global product, with several products still commonly used in Antarctica including ERA-40 and ERA-Interim, now replaced by ERA5-LAND, CFSR, NCEP-NCAR, MERRA-2, and JRA-55 (e.g., Yang Wang et al., 2016). Differences between different reanalysis outputs can be large (Carter et al., 2022; Jones et al., 2016), which is a particular problem in polar regions due to the sparse observational data. Thus, the NWP models have a relatively large effect on the reanalysis outputs in Antarctica. However, reanalysis for the Antarctic Peninsula, having more AWS observations, generally performs better than in other parts of the continent (Wang et al., 2016). Different physical parameterizations, resolutions, and assimilation datasets used for different NWPs can all affect the reanalysis outputs within the region (e.g., Hines et al., 2000).

Reanalysis datasets can be used to determine climate trends and variability on a broad scale. Also, reanalysis datasets, through a method called downscaling, can produce higher resolution climate and weather information. There are two approaches to accomplish this. In statistical downscaling, the high-resolution subgrid-scale variability is derived from the grid-scale dataset using statistical-empirical relationships. In dynamic downscaling, the subgrid-scale variability results from the application to the grid-scale dataset of a dynamical model incorporating the key physical processes. Statistical downscaling is well suited for data-rich regions, while dynamical downscaling is best fitted to data-poor regions. In a typical dynamical downscaling, an RCM is driven from the lateral boundaries by a reanalysis dataset (Ghilain et al., 2022; van Lipzig et al., 2002). In general, the RCM hindcasts outperform the raw reanalysis because RCM has a higher resolution than the raw reanalysis data and RCM can resolve processes (e.g., Bozkurt et al., 2020). On the other hand, reanalysis is sometimes used to evaluate outputs of RCMs and GCMs. These evaluations are helpful, though many RCMs run in Antarctica use some kind of nudging within the model domain to keep the modelled climate close to the observed climate (Mottram et al., 2021), and thus there is a concern about circularity (i.e., reanalysis used to assess reanalysis data).

Earlier reanalysis datasets in the polar regions suffered from lower resolution and poor representations of some key processes, such as with sea ice and snow- or ice-covered surfaces. However, newer datasets like MERRA-2 have improved in both spatial resolution and polar relevant processes (Harrison et al., 2022). The development of higher resolution and regional reanalysis in the Arctic (e.g., ASR + CARRA; Køltzow et al., 2022; Steffensen Schmidt et al., 2023) and the insights gained from those efforts show that regional reanalysis with higher resolution and improved representation of polar processes can outperform more generic reanalysis products. As artificial intelligence tools continue to expand their applicability in numerical weather predictions and climate applications (e.g., Doury et al., 2023; Meer et al., 2022), a high-resolution regional Antarctic reanalysis dataset should be useful for training data.

3.8.4 Firn densification models

Firn densification models (FDMs) simulate the temporal variation of firn density, surface elevations, and the steady-state density profile. These models are used to estimate SMB and ice-mass changes from surface elevation changes observed by satellite altimetry (Section 3.7.1; Helsen et al., 2008). Thickness and thickness changes of ice shelves are often estimated from the surface elevations, assuming that the ice shelves are freely floating. This estimate requires firn density, which can change with time too (Ligtenberg et al., 2011). In addition, FDMs offer insights into mass and energy balances and the meltwater processes at the ice surface, which are crucial factors in interpreting historical climate records stored within ice cores (Veldhuijsen et al., 2023).

FDMs are often one dimensional and driven by the climate variables derived either from re-analysis data (Section 3.8.3) or from RCMs (Section 3.8.2). FDMs can be categorized into empirical and physical models. Empirical models are based on the observed correlations of densification rates with SMB and/or surface temperature. A commonly-used empirical model is the IMAU-FDM (Kaspers et al., 2004), which has been improved to include variables associated with liquid water process (Ligtenberg et al., 2011) and the densification process of fresh snow (Veldhuijsen et al., 2023). On the other hand, physical models account physical mechanisms in densification, such as grain growth and water vapor diffusion. Two examples of such models are CROCUS (Vionnet et al., 2012) and SNOWPACK (Bartelt & Lehning, 2002). Keenan et al. (2021) added the effect of wind drift-induced snow compaction to the SNOWPACK model, enhancing its ability to reproduce near-surface firn density within a depth of 10 meters. The community firn model (CFM; Stevens et al., 2020) includes eight FDMs and allows users to run these models in combination with their preferred SMB model (e.g., Medley et al., 2022). Another useful tool is the Glacier Energy and Mass Balance model (GEMB; Gardner et al., 2023). GEMB is one-way coupled with the atmosphere, and suitable to run offline with a diversity of climate forcing.

Despite these advancements, significant discrepancies persist between current FDM outputs and observations from firn cores or satellite altimeters. A major challenge lies in the long-term variability of simulated firn thickness changes, which lead to substantial uncertainties in estimating ice mass trends. This primarily depends on the setup of the reference period for the model's spin-up (Gardner et al., 2023; Helsen et al., 2008; Kuipers Munneke et al., 2015). Veldhuijsen et al. (2023) have shown that utilizing long-term climate conditions from ice core records can alleviate this issue. Furthermore, repeated observations using shallow-sounding IPR (Section 3.1.2) can provide data on firn density profiles and their variability, thereby aiding the evaluation of models (Chan, 2022; Ligtenberg et al., 2015).

3.8.5 Ice-flow models

Ice-sheet modelling has advanced considerably in the last decades, with substantial improvements in performance, capability, and resolution. Since the early 1990s (e.g., Huybrechts, 1990; Pattyn, 2018; Hanna et al., 2020). More than 10 three-dimensional ice-sheet models have been employed recently in ISMIP6, the ice-sheet model intercomparison project for CMIP6, the Coupled Model Intercomparison Project Phase 6 (Nowicki et al., 2016, 2020; Section 4.5), to determine the future contribution of the AIS to sea-level rise (Edwards et al., 2021; Seroussi et al., 2020). These models are shown in Table 6. Contrary to the earliest simpler ice-sheet models, models now approximate the full Stokes equations to a level where membrane stresses are included. Resolving these stresses is particularly important near grounding lines where the flow regime changes from grounded ice to floating shelf ice. However, to resolve them properly, and allow for grounding-line migration, high (~1 km) spatial resolutions are needed (Pattyn et al., 2012, 2013). To accomplish such resolution, some models allow for mesh refinement around the grounding zone (e.g., Cornford et al., 2013, 2016) or in the Amundsen Sea region (e.g., Johnson et al., 2022).

Table 6: Ice-sheet models included in ISMIP6. Where applicable, only model abbreviations is given in the column and its full names are given in the footnote. All models are three dimensional. SIA: shallow-ice approximation (Hutter, 1983); SSA: shallow-shelf approximation (Morland, 1987).

Model Name	Solutions	References
AISMPALEO	Hybrid of SIA and SSA	Huybrechts and de Wolde, 1999
BISICLES	Hybrid of SIA and SSA	Conford et al., 2013
CISM[*1]	Depth-integrated higher-order approximation	Lipscomb et al., 2019
Elmer/Ice	SIA, SSA, full-stokes	Gagliardini et al., 2013
f.ETISh[*2]	Hybrid of SIA and SSA	Pattyn, 2017
GRISLI	Hybrid of SIA and	Quiquet et al.,

	SSA	2018
IMAUICE	Hybrid of SIA and SSA	de Boer et al., 2014
ISSM*3	SIA, SSA, full-stokes	Larour et al., 2012
MALI*4	First-order “Blatter–Pattyn” momentum balance solver	Hoffman et al., 2018
PISM*5	Hybrid of SIA and SSA	Bueler and Brown, 2009
SICOPOLIS	SIA or hybrid shallow-ice–shelfy-stream dynamics for grounded ice, SSA for floating ice	Greve and SICOPOLIS Developer Team, 2019

*1: Community ice sheet model
*2: Fast Elementary Thermomechanical Ice Sheet model
*3: Ice-sheet and Sea-level System Model
*4: MPAS-Albany Land Ice
*5: Parallel Ice Sheet Model

An accurate representation of a transient grounding line is key to adequately model instabilities such as MISI. Grounding-line migration is complex and highly dependent on a precise knowledge of bed topography, ice-shelf buttressing and subglacial processes that govern basal sliding (Section 2.8). For fast-flowing areas of the AIS, horizontal ice-flow speed is dominated by basal sliding or till deformation. Most ice-sheet models employ viscous-type power-law sliding relationships (i.e., Weertman or Budd sliding laws) that have a linear-to-nonlinear relationship between sliding speed and basal drag (Figure 11c). However, recent studies have shown that sliding is plastic near the grounding line in Pine Island Glacier, Thwaites Glacier, and other fast-flowing areas of the Amundsen Sea (Brondex et al., 2019; Gillet-Chaulet et al., 2016; Joughin et al., 2019). It thus calls for a Coulomb-type sliding law (e.g., Schoof, 2010), which has already been implemented in some models (e.g., Bougamont et al., 2011; Pattyn, 2017). Schoof (2010) showed that solutions to the regularized Coulomb friction and power law problems converge to the Coulomb friction problem under appropriate parametric limits. Overall, a linear or near-linear Weertman sliding law may underestimate the ice mass flux across the grounding line (Brondex et al., 2017, 2019). Higher powers in the sliding law (representing cases closer to plastic flow) result in increased mass loss for a given forcing (Kazmierczak et al., 2022). For fixed power of the sliding law, spatial and temporal changes in water pressure or water flux at the base modulate basal sliding, especially for high-end emission scenarios for future projections (Kazmierczak et al., 2022). In general, subglacial hydrology increases the sensitivity in response to forcing compared with models ignoring subglacial hydrology. Difference assumptions on the subglacial water pressure in the regularized Coulomb law, especially near the grounding line, can lead to wide spread of projected mass loss (Zhao et al., 2024). Moreover, the uncertainty raised by subglacial hydrology models is comparable with that between different ice-sheet models under given RCP (representative concentration pathway) scenarios (Kazmierczak et al., 2022). The above discussion motivates the interest of a generalized sliding law combining processes of hard-bedded sliding and subglacial sediment deformation, while relating slip resistance, slip velocity and water pressure at the bed (see the last paragraph in Section 3.8.7 for further discussion). On the basis of laboratory experiments, Zoet & Iverson (2020) have proposed a sliding law for deformable beds, describing how slip resistance varies with slip velocity and till strength. While this work advances understanding of sliding mechanics, identifying where such conditions occur remains challenging, and subglacial hydrology plays an important role in these sediment systems.

Surface atmospheric melt and basal oceanic melt on ice shelves can weaken their structural integrity by reducing ice thickness and promoting hydrofracturing in the crevasses, when stresses approach the yield strength of the ice. This calls for the use of brittle physics to understand sudden ice-shelf breakup, a phenomenon that may accelerate grounding-line retreat (Bassis et al., 2021). When ice shelves break up and leave behind an exposed cliff in contact with the ocean, MICI may lead to unstable grounding-line retreat (Figure 11b; Bassis & Ma, 2015; DeConto et al., 2021; DeConto & Pollard, 2016)). However, these processes are not represented well in ice-flow models.

The use of data assimilation methods with observations (Arthern & Gudmundsson, 2010; S. L. Cornford et al., 2015) has facilitated improved parameterization of key unknown variables in ice flow, and a deeper understanding of the physical processes underlying (e.g., Millstein et al., 2022). For example, the inverse (or control) method has been used to obtain estimates of the basal friction coefficient in the friction law and ice rigidity in the flow relation (Fürst et al., 2015; Morlighem et al., 2013, Zhao et al., 2018), leading to improved modelling of surface flow. More recently, transient inverse methods have been used to show how variations in surface velocities are linked to changes in the subglacial water pressure, offering a tool to validate unknowns in the subglacial hydrological system (Derkacheva et al., 2021). Data assimilation methods also offer significant potential for constraining subglacial fields using observed surface fields, as recently demonstrated by Gillet-Chaulet (2020) who developed the ensemble Kalman filter method to jointly infer the basal friction coefficient and bed topography. Each of these studies demonstrate that high-accuracy and high-resolution surface velocity and subglacial topographic datasets, especially near the grounding line, are key to providing insights into the ice-dynamical processes in these regions. However, the inverse problem is heavily under-constrained so that a physical interpretation of the inferred parameters remains difficult. Moreover, these parameters often do not vary with time in the transient projections. This calls for high-fidelity observations which are preferably also resolved in time, so that time dependent initializations become feasible on the continental scale (Goldberg & Heimbach, 2013).

Improving ice-flow models, including interactions of the ice sheet and ice shelves with the ocean, the atmosphere, the subglacial hydrology, and the solid Earth, is crucial to better predict Antarctic contributions to the sea-level rise. Uncertainties in ice-sheet models stem from: poorly understood aspects of ice-sheet processes and unpredictable climate variability (Edwards et al., 2021); lack of high-resolution, precise bed topography; long-term records such as exposure dates and grounding line locations; and differences in ice-sheet-model initialization procedures. Major uncertainties also arise from both the forcing (atmosphere and ocean) and ice dynamics, particularly iceberg calving and the resulting damage and weakening of the ice shelves. Such damage reduces the buttressing from ice shelves (Lhermitte et al., 2020), potentially leading to sudden ice shelf collapse (Scambos, 2004). A key step in improving the projections in Antarctic contributions to the global sea-level rise is to clearly identify the primary sources that drive uncertainty through a combination of numerical modelling and observations (e.g., Barnes et al., 2021; Goldberg et al., 2019, 2020; Morlighem et al., 2021).

3.8.6 Ocean-circulation models

Large mass loss from the AIS is triggered by the basal melting of the ice shelves (Jenkins et al., 2018; The IMBIE team, 2018), which is sensitive to ocean circulation in the ice-shelf cavity (Figure 9, Section 2.7.2). Understanding the ice-ocean interaction beneath the ice shelf is essential for simulating the migration of the grounding line, changes in ice-discharge flux through the grounding line, and predicting the future of the AIS and its impact on global sea-level rise. Direct and fine-scale oceanographic observations in the cavities beneath ice shelves are key to understanding the ice-ocean interaction beneath the ice shelf, but is logistically challenging. Numerical models that include the ice-ocean interaction have an invaluable role in investigating the processes governing basal melting (Dinniman et al., 2016). More recent progress in ocean modeling has been applied to the development of idealized cases for simulating ice-shelf melting, including use of following models: ROMSIceShelf (Galton-Fenzi et al., 2012; Gladstone et al., 2021; Zhao et al., 2022), FVCOM (Zhou & Hattermann, 2020), NEMO (Smith et al., 2021c), MITgcm (Goldberg et al., 2018; Jordan et al., 2018; Liu et al., 2022), and POP2x (Asay-Davis et al., 2016). These ocean models have been coupled with an ice-sheet model for examining a moving ocean-ice boundary under the MISOMIP1 configuration (Asay-Davis et al., 2016) as well as for realistic simulations on regional configurations (Pelle et al., 2021; Seroussi et al., 2017; Timmermann & Goeller, 2017; Yan et al., 2023) and for circumpolar domains (Naughten et al., 2018; Pelletier et al., 2022 Nakayama et al., 2021; Kreuzer et al., 2021; Comeau et al., 2022).

However, there are still a number of challenges in developing a coupled ice-ocean model. Examples of these challenges are the coarse resolution in the bathymetry dataset beneath the sub-ice-shelf cavities (Section 4.4), determining the locations of ice rumples and their influence on the ocean circulation and ice-shelf buttressing, determining a method for parameterizing moving grounding lines, as well as the drastically different characteristic timescales of the ocean circulations (order of days to years) and ice flow (order of decades to centuries). Seabed topography with higher resolution is needed for regional studies compared with that for the large-scale applications (of 10-20 km horizontal resolution) because some physical processes, like internal tides and eddies, have been identified as critical in regional ocean models (Dinniman et al., 2016). To resolve heat transport by bathymetric troughs and eddy-scale circulation over continental shelves, a regional ocean model must have a horizontal resolution of 2 km or less (Richter et al., 2022).

3.8.7 Solid Earth models

As shown in Section 2.6, the solid Earth directly impacts ice flow by determining the basal boundary conditions. Therefore, coupling the solid Earth and ice sheet in numerical models requires a realistic representation of physical processes in solid Earth.

Traditional GIA models implement linear Maxwell rheology to represent the deformation process, with an instantaneous elastic response followed by long-term relaxation associated with viscous deformation (Peltier, 1974). Recent laboratory experiments indicate that the rheology is more complicated than this Maxwell rheology and depends on the frequency of the unloading process (Ivins et al., 2020). This nonlinear, time-dependent complexity depends on many mantle properties, including grain size, water content, melt, and temperature inhomogeneities (Ivins et al., 2023; Ranalli & Fischer, 1984). One-dimensional, depth-dependent viscosity field was used to describe interactions between ice and solid Earth (e.g., Nield et al., 2014). Recent works find evidence for lateral variations in temperature and the composition of the Antarctic lithosphere (Haeger et al., 2019; Pappa et al., 2019; Li et al., 2025). Both geophysical and GNSS-derived models suggest that viscosity varies by several orders of magnitude across the entire Antarctic continent (Barletta et al., 2018; Nield et al., 2016). For example, the Amundsen Sea Embayment has significantly lower mantle viscosity than the global average (Barletta et al., 2018). This improved understanding of lateral variations in solid-Earth properties has increased the need to incorporate 3D mantle viscosity into GIA models (van der Wal et al., 2015). However, due to the computation expense compared with 1D GIA models, the 3D GIA models are run with limited spatial resolutions (Larour et al., 2019; Wan et al., 2022).

Modelling the GIA process also requires robust knowledge of ice-sheet history, namely ice loading and unloading, though little is known about past ice-sheet history (Bentley et al., 2014). Geological observations have been used to constrain numerical models that simulate past ice-sheet history, although constraints in areas currently covered by ice shelves are needed (Pittard et al., 2022). GIA significantly affects predictions of future ice-sheet and sea-level changes. Regions with low mantle viscosity should exhibit rapid bedrock uplift, which causes local sea-level fall, despite eustatic sea-level rise (Van der Wal et al., 2023; Whitehouse et al., 2019, Zurbuchen and Simms, 2019). For example, when coupling GIA models with sea-level models, the models predict large uplift of the bed reducing areas of the ocean (ocean expulsion effect) due to low mantle viscosity in West Antarctica, which leads to an additional 1-meter of global sea-level rise within thousands of years after collapse of West Antarctica (Pan et al., 2021). The GIA effect, which reflects the interplay between reduced grounding-line retreat and water expulsion, strongly depends on future emission scenarios, with GIA reducing Antarctica's contribution to global sea-level rise under low emissions but amplifying it under high emissions (Gomez et al., 2024).

Another key solid Earth - ice-sheet interaction happens with subglacial sediment. The properties of this basal material impact ice-flow patterns by altering the basal friction law, suggesting another change in the grounding-line dynamics in response to external forcing (Koellner et al., 2019; Parizek et al., 2013). The spatial variation of basal material has shown a strong impact on the basal sliding, leading to a different buildup of paleo ice sheets (Gowan et al., 2023). When an ice-flow model was coupled with sediment and till dynamics, the reorganization of the subglacial hydrological system was found to influence the ice flow in the Kamb Ice Stream, leading to a transition from basin-wide mass gain to mass loss within two centuries (Bougamont et al., 2015; Retzlaff & Bentley, 1993). Numerical models reveal extensive, high-pressure, and near steady-state channels of subglacial meltwater passageways from interior of the ice sheet to the grounding line, which necessitates accounting for ice dynamics in conjunction with the hydrological system (Dow et al., 2022). The subglacial hydrogeological system in the subglacial sedimentary basins can change as a result of ice-sheet changes, depending on many factors including sediment permeability and the stratigraphy (Aitken et al., 2023; Gooch et al., 2016; Li et al., 2022a). These examples highlight the importance of coupling the ice sheet and solid Earth to represent processes over various timescales.

3.8.8 Data needed for modeling

Accurate bed topography is the fundamental input of ice-sheet models. In general, denser topographic data and finer bed-topography map products are needed. Because of MISI and the importance of small-scale topographic bumps in acting as pinning points (Section 2.8.4), enhancing knowledge of bed topography beneath marine ice sheets should be prioritized. In particular, across-flow bed topography data defines the flux gate to estimate ice discharge and thus is crucial (Sections 2.2 and 4.5). Although along-flow bed topography can be modeled using the mass conservation principle (Section 3.6.1) this relies on highly-uncertain SMB in the coastal regions (Sections 2.4.2 and 4.5.3) and does not always pick out higher resolution roughness that may be important for evaluating grounding-line stability.

Bed features at a scale finer than 0.5 km can affect ice flow and stability of the coastal regions (Hoffman et al., 2022; Kyrke-Smith et al., 2018; McCormack et al., 2025). Many recent ice-flow models use the ~0.5 km spatial grids near grounding lines, as this resolution is needed to resolve processes such as grounding line migration (e.g., Pattyn et al., 2013). This is a nominal spatial resolution of recent gridded bed topography datasets (e.g., Fretwell et al., 2013; Morlighem et al., 2020). However, many of these 0.5-km grid cells have no bed elevation data. As the required spatial resolution is inversely proportional to the local ice-flow speed, higher model resolutions may be required for certain fast-flowing areas or in areas with highly variable bed topography near the grounding line, such as stabilizing grounding zone wedges and outcrops (Mas e Braga et al., 2021). To get the necessary finer model resolution while saving computing time, models have used either structured triangular meshes or adaptive mesh refinement, which increases resolution near the moving grounding line while maintaining a coarser resolution elsewhere on the ice sheet (e.g., Cornford et al., 2013). Castleman et al. (2022) assessed vertical uncertainties and spatial resolutions of bed topography required to accurately model Thwaites Glacier. They used a sea-level uncertainty outlined by the 2017 Decadal Survey for Earth Science as a targeted accuracy (< ±0.1 mm yr^{-1} of sea-level-rise uncertainty, giving ± 2 cm sea-level-rise uncertainty over 200 years; Committee on the Decadal Survey for Earth Science and Applications from Space et al., 2018). In these experiments, they found that to meet this accuracy target, the bed topography must be known with the spatial resolution better than 2 km and the vertical uncertainty better than 8 m. Such highly accurate dense data are needed in the vicinity of the grounding line of fast-flowing glaciers, as well as over 10-20 km or even further inland of the grounding line where the glacier may retreat in the coming centuries. Such data are particularly needed when the bed is over-deepened or below sea level (i.e., MISI-prone).

Bathymetry measurements are needed beneath all ice shelves. Currently, many ice shelves lack sufficiently detailed data from any method (Section 4.3). Ice shelves that have not been surveyed are often assumed to have a constant water depth in numerical models and should be prioritized for future surveys. Ground-based seismic surveys on the ice shelves and multi-beam sonar surveys from autonomous vehicles are the most direct measurements, though few ice shelves have been covered with such direct measurements. Airborne gravity data, together with ice-thickness measurements from IPR, are used to invert to seabed topography (Section 3.6.2). As the accuracy of the inversion depends on the sediment density, basement faults, intrusions and other geological heterogeneities under the seawater, seismic or multi-beam sonar data are required to constrain the inversion model precisely. Magnetics data provide key insights into the varying geologic setting improving fidelity of the gravity inversions for seabed topography (Tinto et al., 2019). Additionally, the spatial resolution of gravity-derived bathymetry is limited by the wavelength of gravity anomalies relative to cavity depth, which can restrict the ability to resolve fine-scale features. Besides topography, sediment strength can strongly control the stability of the grounding line, but this is rarely known because measurements are taken using sediment coring at relatively few point locations around Antarctica.

Several other datasets are needed for the numerical models. ApRES measurements can collect a time series of precise thickness changes of grounded and floating ice (Cook et al., 2023; Nicholls et al., 2015; Vaňková et al., 2021). The data can provide sub-shelf melt rates, and thus help improve ice-sheet and ice-shelf models by providing observations on ice-ocean interactions. Other datasets required for modeling include grounding-line locations (Section 4.1) and SMB (Section 2.4.2). These can be retrieved from satellite data or models at different spatial scales (ESM or RCM), but need to be compared with observations because of their large temporal and spatial changes. Finally, AWS, firn cores, and shallow IPR data are all useful to constrain SMB and also near-surface density (Section 3.6.3), which are needed for estimating thickness of ice shelves using the freeboard assumption, and thus also help to improve model results.

Finally, satellite and other observations are needed to document changing environments and to use them to initialize models that project future evolution of the ice sheet. Such measurements include ocean temperature and currents (Wåhlin et al., 2020), sea ice extents (Liao et al., 2021), ice-sheet terminus positions (Miles et al., 2016), ice-shelf calving and oceanic melt rates (Greene et al., 2022), ice mass (Shepherd et al., 2019), ice velocity and discharge (Gardner et al., 2018; Rignot et al., 2019), and supraglacial melting (Banwell et al., 2023; de Roda Husman et al., 2024; Stokes et al., 2019). These observations are important because the current ice sheet is not in equilibrium and therefore the understanding of current and future grounding line stability is already pre-conditioned by those ongoing changes. Continued measurements of coastal glacier conditions are therefore important as model constraints.

For the modeling community, individual datasets should use consistent definitions and assumptions, include uncertainty estimates, and be all well documented. For example, there are several datasets showing the area of grounded ice (ice mask). Use of different ice masks alone adds 1.8–6.0% uncertainty of ensemble SMB integrated over the ice sheet, which directly impacts the estimate of mass balance of the AIS (Hansen et al., 2022).

3.9 Data management

Open science principles play an essential role in advancing polar research, improving the integrity and reproducibility of studies, and enabling broader use of datasets. These principles are increasingly mandated by funding agencies, particularly through adherence to the FAIR (Findable, Accessible, Interoperable, and Reusable) guidelines for data management (Wilkinson et al., 2016). FAIR practices ensure that datasets are not only accessible but also well-documented and easily integrated into diverse scientific workflows. While data policy remains variable across the National Antarctic Programs, SCAR's Data Policy (Scientific Committee on Antarctic Research, 2022) provides a strong baseline and serves as a guiding framework for improving data sharing and archiving in this highly interdependent international research community.

The FAIR guidelines emphasize several key aspects: datasets must have permanent identifiers (e.g., DOIs), adhere to open and widely accepted standards, and be accessible using free and universally implementable software. Metadata should clearly describe the dataset's origins, processing methods, and potential applications. Prominent repositories such as the National Snow and Ice Data Center (https://nsidc.org/home) and PANGAEA (https://www.pangaea.de/) serve as critical platforms for FAIR data dissemination. Zenodo is a well-used data depository and also hosts such as community whitepapers (https://zenodo.org/). Many National Antarctic Programs also maintain their own data centers to ensure compliance with these standards. Efforts to meet FAIR principles, however, demand sustained resources, disciplined data management, and skilled personnel. Large-scale satellite missions, backed by substantial funding and centralized organization, routinely achieve these goals. In contrast, smaller research projects often face challenges related to short-term funding cycles, making the sustainability of data curation a pressing concern (Daniels et al., 2022).

Polar datasets are typically categorized into four levels, reflecting their stages of processing and usability. Level 0 data consist of raw, unprocessed observations directly acquired by instruments, such as radar echoes or raw satellite telemetry. Level 1 data represents geotagged and processed outputs, such as radargrams (e.g., Figures 14 and 15) or geolocated satellite images, ready for further analysis but not yet translated into geophysical variables. There are often sub levels, such as 1a and 1b, to represent different stages of processing. Level 2 data products include derived geophysical variables—such as ice thickness or bed elevation profiles—extracted from level 1 data and essential for scientific interpretation (e.g., red curve in Figure 14b). Finally, Level 3 data products integrate multiple level 2 datasets into gridded products, such as continental-scale maps of ice thickness or surface velocity, enabling broad-scale analyses and modeling efforts (e.g., Figure 7). Each level contributes to the research lifecycle, from raw observation to actionable scientific insights.

Community-led efforts to compile the level 3 datasets play a pivotal role in enhancing data accessibility and interoperability. For example, the ADMAP project integrates magnetic data from many nations to produce a map of Antarctic magnetic anomalies (Figure 7f) (Golynsky et al., 2018), and the AntGG project integrates ground-based and airborne gravity data (Scheinert et al., 2016; Scheinert et al., 2024). Similarly, the International Bathymetric Chart of the Southern Ocean (IBCSO, Version 2) compiles over 1,500 datasets to create the most accurate seabed map (Figures 7a and 21) (Dorschel et al., 2022). Another key initiative is Bedmap, which has evolved over two decades to represent subglacial bed topography in Antarctica. While earlier versions of Bedmap used level 2 data submitted under confidentiality agreements (Lythe et al, 2001, Fretwell et al., 2013), the latest version Bedmap3 adheres to FAIR principles. It compiles level-2 datasets from numerous institutions as a FAIR-compliant compiled product (Frémand, Fretwell, et al., 2022), and generates a level-3 bed DEM of the AIS using only these FAIR-compliant level-2 data (Pritchard et al., 2025). This FAIR-compliant level-2 data is also used in other data compilations, such as the MEaSUREs BedMachine product (Morlighem et al., 2020). Other noteworthy examples of comprehensive Antarctic data efforts include the MEaSUREs ice-velocity map (Mouginot et al., 2019), ITS LIVE ice-velocity map (Gardner et al., 2018), and the REMA DEM (Howat et al., 2019).

Compiling individual level-3 datasets into integrated resources significantly enhances their accessibility, usability, and scientific value. Tools like the Antarctic Mapping Tools MATLAB package (Greene et al., 2017) improve the interoperability of these datasets by providing streamlined workflows for managing and visualizing community data products, though MATLAB itself is not strictly FAIR. Quantarctica, a free GIS-based data package, has brought together approximately 160 scientific datasets on Antarctica and the Southern Ocean, combining them with terrain models and satellite imagery on base maps optimized through advanced cartographic techniques (Matsuoka et al., 2021). Built on the QGIS platform, Quantarctica provides an integrated environment for browsing, analyzing, and visualizing data. Since its initial release in 2014, it has become a widely used tool, with an updated version (Quantarctica 4) planned for mid-2026 featuring newer datasets.

While high-level data products (e.g., level 2 and level 3) are undoubtedly valuable, proper archiving of lower-level data (e.g., level 0 and level 1) is critical because it preserves the foundation for future applications that may extend well beyond the lifespan of compiled products—a lifespan that is becoming increasingly short as data volumes grow and automated synthesis techniques advance. For example, digitizing analog radar records from the 1970s enabled comparisons of ice thickness in the rapidly changing Thwaites Glacier (Schroeder et al., 2019), an analysis that would not have been possible without the original data being preserved and subsequently rescued through extensive digitization efforts.

Advances in data processing algorithms continually improve our ability to extract meaningful insights from raw data. Also, earlier geophysical extractions in level 2 data, such as ice thickness or bed elevation, may include errors. These errors may arise from limitations in initial processing techniques, calibration inaccuracies, or manual mistakes. Identifying and correcting such errors is vital for ensuring the accuracy and reliability of scientific interpretations and subsequent analyses, which is only feasible if lower-level data are preserved. Despite their importance, open-access release of level-1 radargrams has been limited. Recent progress includes releases from the British Antarctic Survey (Fremand et al. (2022), the Center for Remote Sensing of Ice Sheets (CReSIS) at the Univ. Kansas (MacGregor et al., 2021), the Univ. Texas Institute of Geophysics (UTIG, Young et al., 2021), and Alfred Wegener Institute (Franke et al., 2025).

The Open Polar Radar project is an ongoing effort to establish a software ecosystem to consolidate polar radar software and services and make the associated datasets standardized and searchable. The target audiences are radioglaciology domain scientists, data scientists, and the software and data engineers behind the various satellite, airborne, and ground-based IPR data collected over ice sheets, mountain glaciers, sea ice, and planetary icy bodies (Paden et al., 2021).

Various file formats are currently used to share the data. Historically, IPR radargrams or any level-1 datasets were often released using the MATLAB proprietary format, but more recently, NetCDF has become more popular. NetCDF is an open format that works across different operating systems and includes information about the data, such as timestamps and units of measurement. However, NetCDF file types have size limits and inefficient compressibility (Delaunay et al., 2019). For sharing level-2 products, such as ice thickness along the flight profile, both CSV (or plain text) and shapefiles have been widely used. While CSV files are versatile, they often come with various standards, making data compilation complex when datasets are collected from different institutions. Shapefiles are more standardized but have limitations, such as being split across multiple files and offering limited attributes, which do not fully meet recent geospatial data standards. GeoPackage is increasingly being used as an alternative to shapefiles, as it is more compact, portable, and self-describing. Level-3 data are often distributed in formats like GeoTIFF or NetCDF file formats.

Machine learning and data science techniques are becoming more widely used and require large datasets with better interoperability and more compact data volumes. File formats such as ORC, AVRO, JSON, XML, and Parquet are often used for these purposes. For example, Parquet can be used easily with Python and MATLAB and can reduce file sizes by over 90% compared to CSV. Newer formats that support spatial datasets, including Spatial Parquet (Saeedan & Eldawy, 2022a), GeoParquet (Saeedan & Eldawy, 2022b), and GeoJSON (Butler et al., 2016), are also emerging as viable options. However, these recent data formats can be complex. Additionally, many NetCDF files archived at data centers are not fully compliant with the file-format requirements, which demonstrates that even NetCDF can be challenging for many scientists. This highlights the importance of not only selecting appropriate open file formats and developing rich metadata but also providing consistent and well-resourced data support to help researchers generate FAIR-compliant datasets. In summary, it is crucial to ensure both the scientific and technical quality of the data, to choose the appropriate open file format, to develop adequate metadata, and to fully comply with FAIR principles.

4. Quantifying data and knowledge gaps

In this section, we examine data and knowledge gaps using published datasets. First, the contemporary grounding line is determined as the geographical reference point in the following analysis (Section 4.1). Second, this grounding line is simplified as a flux gate to estimate ice discharge (Section 4.2). Third, availability of bed topography data is presented for the areas under the grounded ice (Section 4.3) and the ocean including ice shelf cavities (Section 4.4). Fourth, empirical assessments of ice-discharge flux are presented at different flux gate locations, including the simplified grounding line established in Section 4.2, for different sets of assumptions (Section 4.5). Fifth, grounding-line locations projected until 2100 are analyzed using results from ice-sheet models used for IPCC's 6th assessment report AR6 (Section 4.6). Finally, interpolation uncertainty of bed elevations is examined in terms of separation between survey profiles (Section 4.7). In this section, we describe the analysis and continent-wide characteristics of the obtained results. These results constitute the basis to identify the outstanding science priorities and relevant recommendations (Section 5). Results presented in this section are available as FAIR data; see the open data section.

4.1 Reference grounding line locations

The grounding line is where the grounded ice sheet meets the ocean (Figure 10). It is the reference location for assessments of ice discharge and contribution to sea-level change. The basic properties and dynamics of grounding lines are described in Section 2.8.2. Here, we focus on how to best delineate a contemporary grounding line to be used as a reference for the primary ring, one of three circum-Antarctic rings for the Antarctic RINGS initiative (Section 5), and the gridded products of Bedmap3 (Pritchard et al., 2025). This new RINGS/Bedmap3 grounding line outlines the grounded ice sheet, including permanently and transiently grounded areas within the ice shelves such as ice rises, rumples and pinning points. The coastline for margins with grounded ice or ice-free land are also included in this grounding line product (Figure 17).

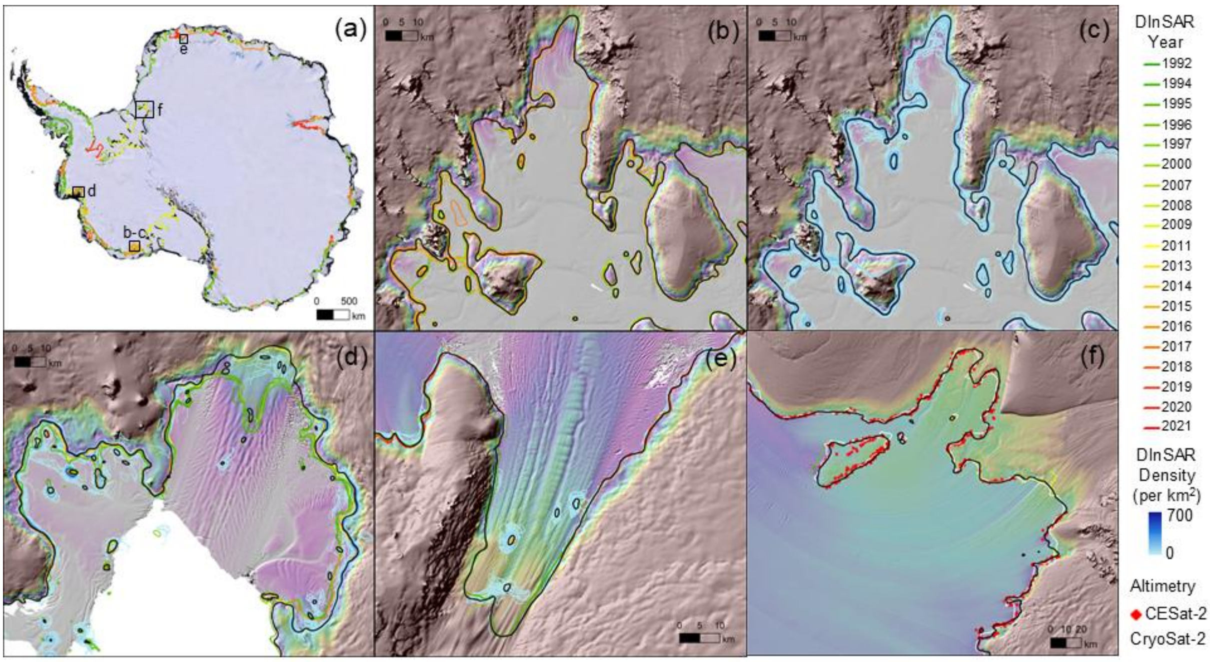

Figure 17: Grounding lines of the AIS. The RINGS/Bedmap-3 grounding line is shown with black curve in all panels together with various grounding line products. (a) Historic DInSAR grounding line data colored by year (Rignot et al., 2016; Floricioiu et al., 2021). Background images are the LIMA, Landsat image mosaic of Antarctica (Bindschadler et al., 2008). The locations of (b-f) are indicated with black frames in (a). (b) Historic DInSAR data for the inner parts of the Sulzberger Ice Shelf. (c) Heatmap derived from the density of DInSAR grounding lines from Sentinel-2 data in 2018 (Mohajerani et al., 2021), also for the inner parts of the Sultzberger Ice Shelf. (d) All DInSAR data for the ice shelf of the Pine Island Glacier. (e) All DInSAR data for the grounding zone of the Jutulstraumen Glacier. (f) All DInSAR data for the southeastern part of the Filchner Ice Shelf and additional grounding line data from altimetry using ICESat-2 (red dots, Li et al., 2022b) and CryoSat-2 (white line, Dawson and Bamber, 2020). The background of (b-f) the REMA surface elevations (Howat et al., 2019) shown in transparent color scale (0-200 m elevation) over a hillshade plot that is exaggerated by a factor five in the vertical scale.

The first grounding line maps of Antarctica were based on the break-in-slope of optical imagery (Scambos et al., 2007; Bindschadler et al., 2011), which is typically on the seaward side of the true grounding line (point I in Figure 10). Later grounding line maps have combined these data with scattered grounding line points and segments from repeat-track laser altimetry (e.g., Fricker & Padman, 2006) and DInSAR (e.g., Rignot et al., 2011a). With these two methods, ice-shelf height differences due to ocean tides are measured and used to map the inland limit of ice-shelf flexure, also known as the hinge line, which is slightly landward of the true grounding line (point F in Figure 10). The tide-based approach is often more accurate than the slope-based one but its coverage is limited. The actual grounding line (point G in Figure 10) is located between points I and F identified by these two approaches.

Neither the grounding line nor the hinge line are static features. They can retreat and advance over various time scales, from tidal to seasonal to multiyear, and not only depending on changes in sea level and ice thickness, but also from local constraints imposed by bed properties and ocean-ice dynamics (Chen et al., 2023). Such temporal variations of the grounding line and its non-deterministic nature have been recently well documented at continental scale using the high frequency of Sentinel-1 SAR acquisitions in combination with deep learning (Mohajerani et al., 2021; Floricioiu et al., 2021). Unlike the earlier grounding line datasets that were sampled sporadically over a few decades (Figure 17a), these new datasets can include tens to hundreds comparable estimates from within a year's time in many regions (Figure 17c and 17d). The densely observed short-term variability in grounding line position is often larger than the differences seen in the limited long-term data (Figure 17b and 17c), which makes it difficult to detect long-term grounding line migration and to define a single grounding line reference for RINGS and Bedmap3.

As a starting point for the reference grounding line, we used the composite grounding line product of Gardner et al. (2018), which is an update of that from Depoorter et al. (2013). This dataset was then manually updated and improved considering newer grounding line data, including multitemporal grounding line segments from DInSAR (Brancato et al., 2020; Mohajerani et al., 2021; Milillo et al., 2022 Floricioiu et al., 2021; Christie et al., 2022; Rignot et al., 2022) and altimetry-based grounding zone points from CryoSat-2 (Dawson & Bamber, 2020) and ICESat-2 (Wild et al., 2021; Li et al., 2022b). The altimetry data were particularly useful for the two largest ice shelves, Ross and Fichner-Ronne, where the availability of DInSAR data is limited (Figure 17a and 17f). Elevation data from REMA (Howat et al., 2019; Dong et al., 2022) and continent-wide ice flow maps (Rignot et al., 2022; Gardner et al., 2018) were used as further references to detect unrealistic grounding lines (e.g., where elevations or gradients were too high), to make the grounding line more consistent (e.g., following local fluctuations in topography rather than crossing them), and to delineate uncharted ice rumples and ice rises visible as surface scars or rounded features in hillshade plots (Matsuoka et al., 2015). In areas with dense coverage of DInSAR grounding lines (Mohajerani et al., 2021), a heat map of time-varying grounding line location was generated to better judge its spatial distribution (Figures 17c, 17d, and 17e). In such cases, the grounding line was digitized along the modal location of this mapped distribution rather than its extreme inner limit, which could be erroneous or a matter of extreme conditions related to ocean-ice dynamics. Delineating the reference line slightly seaward of its inner extremes also serves to somewhat compensate for the landward bias of the ice flexure limit relative to the true grounding line.

If we define the span of grounding line positions over a full tidal cycle as the grounding zone (Chen et al., 2023; Rignot et al., 2022), then our reference line is meant to demarcate the inner part of this zone where the ice is grounded most of the time, subject to the limitations in accuracy and frequency of the available data. In other areas, the line had to be set where data were available, irrespective of the (unknown) tidal variability. Some smaller regions and ice shelves did not have any available DInSAR or altimetry data and hence had to rely on past mappings from optical data or new interpretations using REMA and a complete catalogue of Landsat-8 imagery from summer 2022. The Landsat-8 imagery was further used to delineate a high-resolution coastline, which was connected to the ice-shelf grounding lines to form a continuous ocean boundary around the continent, including islands extracted from the Antarctic Digital Database (ADD), version 7.4 (https://data.bas.ac.uk/collections/e74543c0-4c4e-4b41-aa33-5bb2f67df389/, last access 24th March 2025).

4.2 Prescribing flux gate based on simplified grounding line

It is crucial to measure bed topography at the current grounding line locations for constraining current ice-discharge flux (Section 2.2) and at slightly inland locations for predicting grounding line retreat and measuring ice-discharge flux in the future. However, the contemporary grounding line has a very complex geometry (Figure 17), which is unpractical for the survey aircraft to exactly follow because of both navigational and scientific reasons. When an airplane turns, the airplane maneuvers and therefore an IPR cannot observe the nadir point. Furthermore, frequent maneuvers jeopardize collection of gravity data. Here, we simplify the contemporary grounding line, which can be considered as a guideline to plan future survey profiles where flux gates can be located.

The first guiding criterion of this geometry simplification is to composite the simplified grounding line with as long as possible line segments located landward of, and as close as possible to, the RINGS/Bedmap3 grounding line (Figure 18). At a typical cruising survey speed of airplanes at 250 – 300 km hr^{-1} (Table 3), the aircraft needs to turn every ~2 minutes if the segments are 10 km long and 10-12 minutes if the segments are 50 km long. So, we set the desired length of these line segments to 50 km and the minimum length to 10 km. In reality, it is hard to make the segment always longer than 10 km but we used these distances as a guideline when simplifying the grounding line. The second guiding criterion is to avoid turning points in the middle of the fast-flowing glaciers and ice streams so that the flux gate has a simpler geometry at such locations where large ice discharge flux is expected. The third guiding criterion is to make the turning angle as small as possible. For example, when two adjacent line segments have a turning angle of 70^{o} (i.e., the inner angle of 110^{o}) and the airplane can make a turn with a 500-m radius, the airplane starts the turn before it reaches the turning point and the actual flight path is about 100 m off the designated turn point, which we consider acceptable. However, when the turning angle is 140^o and the inner angle is 40^o, the actual path is about 800 m away from the designated turning point, which we consider unfavorable. For this case, the airplane will fly along the first segment beyond the turning point, and then make a large 290^o turn to adjust its heading to the next segment. Such turns require extra flight time and fuel and must be avoided when possible. We also considered the distance to rock outcrops to avoid strong radar clutters (side scattering) and aimed to avoid flying directly over larger outcrops where possible, as they require steep descending or ascending maneuvers. We did not consider flight regulations over ASPAs (Section 3.2.4), because the regulations can be site specific and different for different types of the aircraft and missions.

We implemented these three criteria into a computational procedure and made manual adjustments later. This computational procedure takes the contemporary grounding line projected to EPSG:3031 polar stereographic coordinates x and y as a starting point, and then follows these steps: (1) resampling (x, y) line vertices based on Euclidean distance around the continent with a 250 m increment; (2) smoothing the resampled grounding line by applying an 80-point (i.e., 20 km) moving window to the x- and y-coordinates of consecutive vertices; (3) computing the along-track distance along the smoothed grounding line using a centered differencing method (average of the forward and backward differences); (4) calculating the lateral offset from the smoothed (x, y) positions to the original grounding line using Euclidean distance; (5) disregarding points located seaward from the smoothed grounding line; (6) retaining points with the maximum landward distance from the RINGS/Bedmap3 grounding line within a 10 km window; (7) assigning final points for the simplified grounding line where the maximum onshore distance equaled the onshore distance; (8) interpolating between these points manually to meet the guiding criteria above. In many cases, it is hard to find a solution that fulfills all criteria so manual adjustments are needed to have the best-balanced product. In the final simplified grounding line product, 18% of the segments are longer than 50 km, 44% 20-50 km, 21% 10-20 km, and 17% less than 10 km.

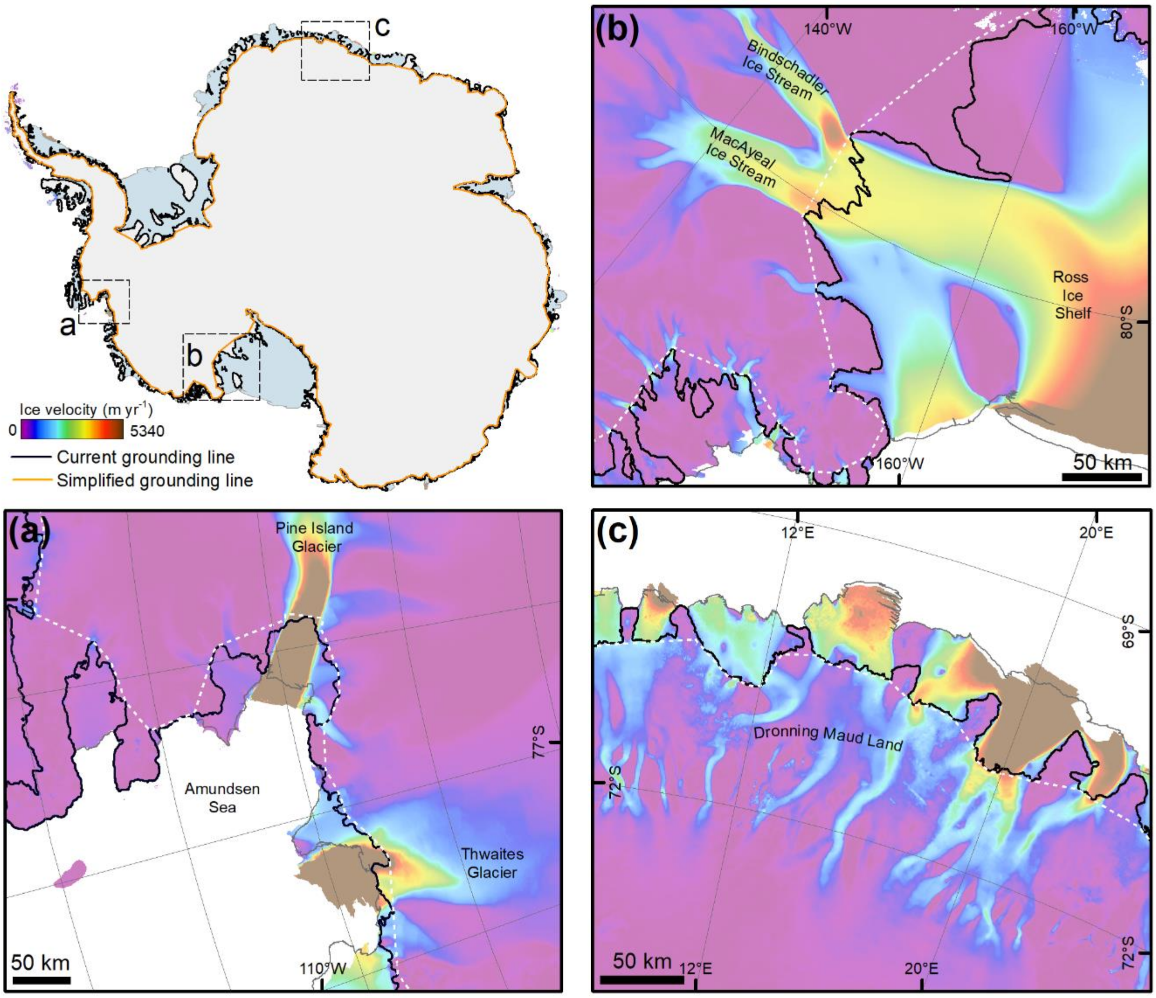

Figure 18: The proposed flux gate (primary ring) at the simplified grounding line of the AIS (red, Section 4.1) and contemporary RINGS/Bedmap3 grounding line of the AIS (black, Section 4.2). RINGS/Bedmap3 grounding line is also defined for ice rises but not shown in this map. (a-c) Regional views of these grounding lines together with ice-flow speed (Gardner et al., 2018).

Examples of simplified grounding lines are shown at three locations in Figure 18. To make these lines feasible for airborne IPR surveys, most of the small promontories must be removed from the simplified grounding-line geometry. As a consequence, when IPR surveys are conducted along this simplified grounding line and the resulting bed topography is used to define a flux gate for ice-discharge estimates, the SMB of the omitted promontories must be accounted for as additional mass flux, assuming these promontories are in balance. If they are not in balance, the net mass balance should also be accounted for. As presented in Figure 5 and further discussed in Section 4.5, RCM models show highly variable SMB values in the region bounded by the RINGS/Bedmap3 and simplified grounding lines. This highlights the need for SMB measurements using shallow-sounding IPR and ice cores over these promontories (Section 3.6.3), as well as additional local flights to outline large promontories, so that ice discharge from them can be directly estimated.

4.3 Bed topography data gaps under grounded ice

We analyzed bed-elevation data availability within a 100-km buffer zone landward of the contemporary grounding line position (Section 4.1) using the FAIR dataset compiled by the

Bedmap3 project (Fremand et al., 2023), which includes 77 million data points over the AIS. This analysis is more comprehensive than the previous RINGS analysis using the data compiled for BedMachine (Matsuoka et al., 2022).

Most datasets included in Bedmap2 and 3 were collected using modern GPS/GNSS techniques, with which the locations of individual data are accurately determined within a few meters or less. However, some datasets acquired between the mid to late 1990s were collected using older navigational techniques such as Omega VLF, which may give positioning uncertainties of kilometers or more. Here we are interested in data that have high accuracy both in terms of exact location and derived bed elevations, which can be used as a baseline dataset in the future. Importantly once the bed elevations are accurately determined, future ice thickness can be determined using this bed elevation and ice-surface elevation determined by satellite altimetry (Section 3.7.1). This is because bed elevation changes due to GIA over decades are presumably negligible, though significant sediment erosion and associated bed elevation lowering was observed and cannot be excluded.

For this purpose, we removed data collected before the 1990s because they are unlikely to have been collected with adequate positioning using modern GPS receivers. Such data include all data submitted as part of Bedmap1 (Lythe et al., 2001) and the re-processed SPRI-NSF-TUD data (Schroeder et al., 2019). We contacted providers of the data collected in the 1990s and included their data in the analysis if dual-frequency GPS was used for airborne missions, or if any types of GPS was used for ground-based missions. We assumed that all data collected after 2000 have adequate position accuracy. All points over ice shelves were removed as they provide only thickness of ice shelves, not the elevation of the seabed. Following these procedures, 52 out of 66 Bedmap2 datasets and 62 out of 84 Bedmap3 datasets acquired between 1994 and 1999 were removed from the Bedmap database (Fremand et al., 2023). Despite this data screening, an extremely large number of data points remain to analyze. As a result, instead of examining the exact locations of every single data point, we developed a data availability raster using a grid of 500 m by 500 m cells produced by the Bedmap3 project (Fremand et al., 2023), which allows us to analyze data availability with 0.5 km intervals, an adequate resolution for our purpose.

We categorized the data availability into three map-cell classes: (1) the cell does not include any reported data point (i.e., no IPR data exists there), (2) the cell includes at least one data point but none of these data points include valid ice thickness (i.e., the IPR survey was carried out but the bed was not picked), and (3) the cell includes at least one data point with valid ice thickness. The difference between class (2) and (3) can be seen in Figure 14b. When a radargram is produced, the bed-echo may not be identified at every location along the profile. For such a case, it is a common practice to report the location anyway without an ice-thickness value (i.e., invalid ice thickness) so that the radargram and reported ice thickness dataset have identical data lengths. When such a segment with invalid ice thickness is only a few hundred meters or less, a 500-m cell likely includes other data points with the valid ice thickness, resulting in a cell being assigned data class 3 in our analysis. The class-2 cells do not represent such short data gaps, and the cell has the class 2 only if none of the data points collected in the cell has a valid ice thickness value. We consider the class 2 useful because it shows the incompleteness of existing datasets and regional distributions of difficult targets with significant size (> ~0.5 km) surveyed but not detected successfully. Hereafter, we use the total distribution of classes 2 and 3 to see survey availability and class 3 distribution to see data availability.

Figure 19 shows all IPR profiles flown in the coastal zone and reported to Bedmap2 (Fretwell et al., 2013) and Bedmap3 (Fremand et al., 2023), with significant improvement in data coverage between the two Bedmap versions. In particular, improvements are significant in the Antarctic Peninsula, Weddell Sea Embayment, Ross Sea Embayment, Wilkes Land and Princess Elizabeth Land in East Antarctica. However, large data gaps still remain, particularly in Enderby Land and Oates Land in East Antarctica. Figure 20 shows pan-Antarctic survey availability (i.e., cell classes 2 and 3) and data availability (i.e., cell class 3 only) by distance away from the grounding line (< 1 km, 1-5 km, and > 5 km). For example, only 12% of the grounding line has a survey location within 1 km, and 63% of the grounding line has survey location within 5 km. However, 17% of the grounding line has no survey within 18 km, and many cases of this category have no survey within tens of kilometers. Because the bed echo is not detected at every location, the data availability is worse than the survey availability. For example, only 10% of the grounding line has data within 1 km (Figure 20b), which is 2% lower than the survey coverage (Figure 20a). Whereas 63% of the grounding line has a survey location within 5 km (Figure 20a), 10% of these surveys did not detect the bed echo clearly (Figure 20b).

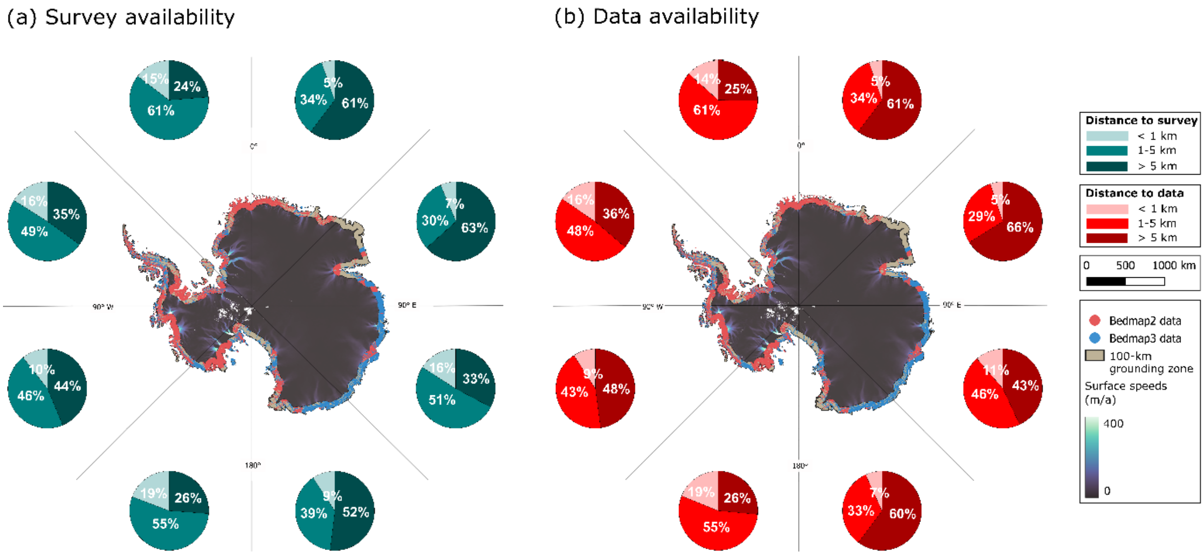

Figure 19: Overview of IPR survey availability (a) and bed-elevation data availability (b) under the AIS in the coastal zone (marked right brown), within 100 km landward from the RINGS/Bedmap3 grounding line (Section 4.1). This analysis is based on the syntheses by Bedmap2 (Fretwell et al., 2013) and Bedmap3 (Frémand et al., 2023) data, but used the data only those reported with precise locations using GPS/GNSS since 1990s. Survey availability shows the reported survey locations regardless of the bed detection (class 2 and class 3 in Figure 14), whereas data availability shows only the survey with valid bed elevation data (class 3 in Figure 14). See full discussion of these classes in Section 4.3. It is usual that one survey profile includes both classes and missing bed echo at some locations. On the maps, the Bedmap2 data is overlaid on top of the Bedmap3 data. Background further inland shows surface flow speeds from the MEaSUREs dataset (Rignot et al., 2017). For each 45-degree meridian, regional survey (a) and data (b) availabilities are shown.

Pie charts in Figure 19 show more details of regional survey availability and data availability. The basins with the poorest data coverage are Enderby Land and Princess Elizabeth Land (45-90°E), where 66% of the grounding line is not within 5 km of the data location. This is closely followed by Dronning Maud Land (60%; 0-45°E) and Wilkes Land (48%; 135-180°E) basins. This is primarily due to the difficult access of these basins (Figure 16). Overall, regions with better survey and data coverage are located in the Antarctic Peninsula and West Antarctica. In the Antarctic Peninsula, nearly two thirds of the grounding line have data within 5 km. The basins with the best data coverage are the western Ross Embayment and Marie Byrd Land (135-180°W) and Coates Land and the eastern Weddell Embayment (0-45°W), where approximately 75% of the grounding line contains data points located 5 km or less from its modern position. The Antarctic Peninsula and the western Weddell Embayment (45-90°W) have similar data coverage.

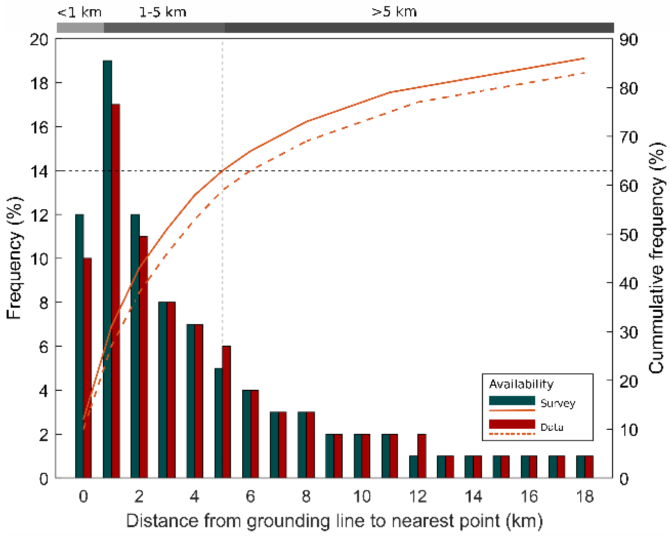

Figure 20: Histograms showing the IPR survey and bed-elevation data availabilities in the vicinity of the RINGS/Bedmap3 grounding line. Abscissa show the distance from the grounding line to the closest survey or data points. Both cases analyzed data with precise locations collected with GPS or GNSS since 1990s. Survey availability analyzed using both classes 2 and 3; the class 2 indicates locations where the bed echo is not identified though the survey is made, whereas the class 3 indicates locations where the bed echo is successfully identified (Figures 14b and 19, and Section 4.3). Data availability analyzed using only the class 3.

This analysis is most directly relevant to estimating ice-discharge flux, which requires ice thickness in the vicinity of the grounding line (Sections 2.2 and 4.5). Ice-flow modeling requires high-resolution bed topography particularly in the coastal regions and in fast-flowing glaciers (Section 3.8.5). For modeling the future evolution of the ice sheet, bed topography is needed in the landward section of the grounding line at an adequate spatial resolution (Section 4.7) and also under the ice shelves (Section 4.4). Based on this analysis, Figures 19 and 20 and further discussion in Section 4.7 on the data density needed for a prescribed data interpretation tolerance, we did not find a single basin where data coverage is sufficient for modeling future ice-mass discharge from the AIS. We further discuss uncertainties in the current ice-discharge flux estimated with these ice thickness data (Section 4.5).

More detailed regional characteristics of the data distribution are discussed in Matsuoka and Shackleton (2026). That study also covers regions that lie beyond the 100 km coastal buffer used in the analysis above, including the areas of projected 2100 grounding-line retreat from the ISMIP6 experiments (Section 4.6) and the regions where ice flow exceeds 100 m a^{-1}.

4.4 Data gaps of seabed topography

Because radio waves do not penetrate seawater, IPR works to detect the bed topography only under the grounded ice sheet. Instead, ground-based seismic surveys have been used to measure bed topography under the ice shelves (Section 3.5.2). Multi or single beam sonar surveys have been made by vessels in the open ocean. More recently, seabed topography has been inverted from airborne gravity data (Section 3.6.2). These datasets have been compiled under a worldwide initiative of Global Bathymetric Chart of the Oceans (GEBCO). In the Southern Ocean, International Bathymetry Chart of Southern Ocean (IBCSO) released its version 1 a decade ago (Arndt et al., 2013) and version 2 recently (Dorschel et al., 2022).

Figure 21 shows that only six ice shelves have dense bathymetry data inverted from airborne gravity data (nominal separation < 10 km) constrained with seismic surveys or with autonomous underwater vehicles. Seven other ice shelves have dense gravity data without such constraints. Eight more ice shelves have gravity-inverted seabed topography data but only sparse data coverage. Numerical models and datasets often assume a constant seabed elevation under the other ice shelves (Sections 3.8.5 and 3.8.6), which is obviously inadequate to model the ice-ocean interactions and evolution of the ice sheet in those regions. Ship-based bathymetry data distribution is highly uneven; in general the vicinity of major research hubs such as the McMurdo Station, the Neumayer Station, and the Rothera Station have relatively higher data coverage, as well as some regions of high interests, such as Amundsen Sea, Mertz Glacier Tongue, and Scotia Sea. To model the evolution of the AIS, seabed topography is particularly important over the continental shelf where the water column is only 0.5-1 km (Figure 7a; also, the continental shelf is outlined with ASC shown in Figure 8). Some of these regions are covered with heavy sea ice, which prevents voyage of ice breakers and remain as large data gaps, such as the western Weddell Sea along the Antarctic Peninsula.

Overall, seabed topography data, particularly beneath ice shelves, is even more limited than AIS bed topography data. It is crucial to carry out dense (~km spacing) airborne gravity and IPR surveys to reveal the thickness of the water column under ice shelves. Ground-based seismic surveys or autonomous underwater vehicle measurements are crucial to constrain this gravity inversion model as geological structure (e.g., sediment thickness and density) varies significantly and locally (see Section 2.6.3).

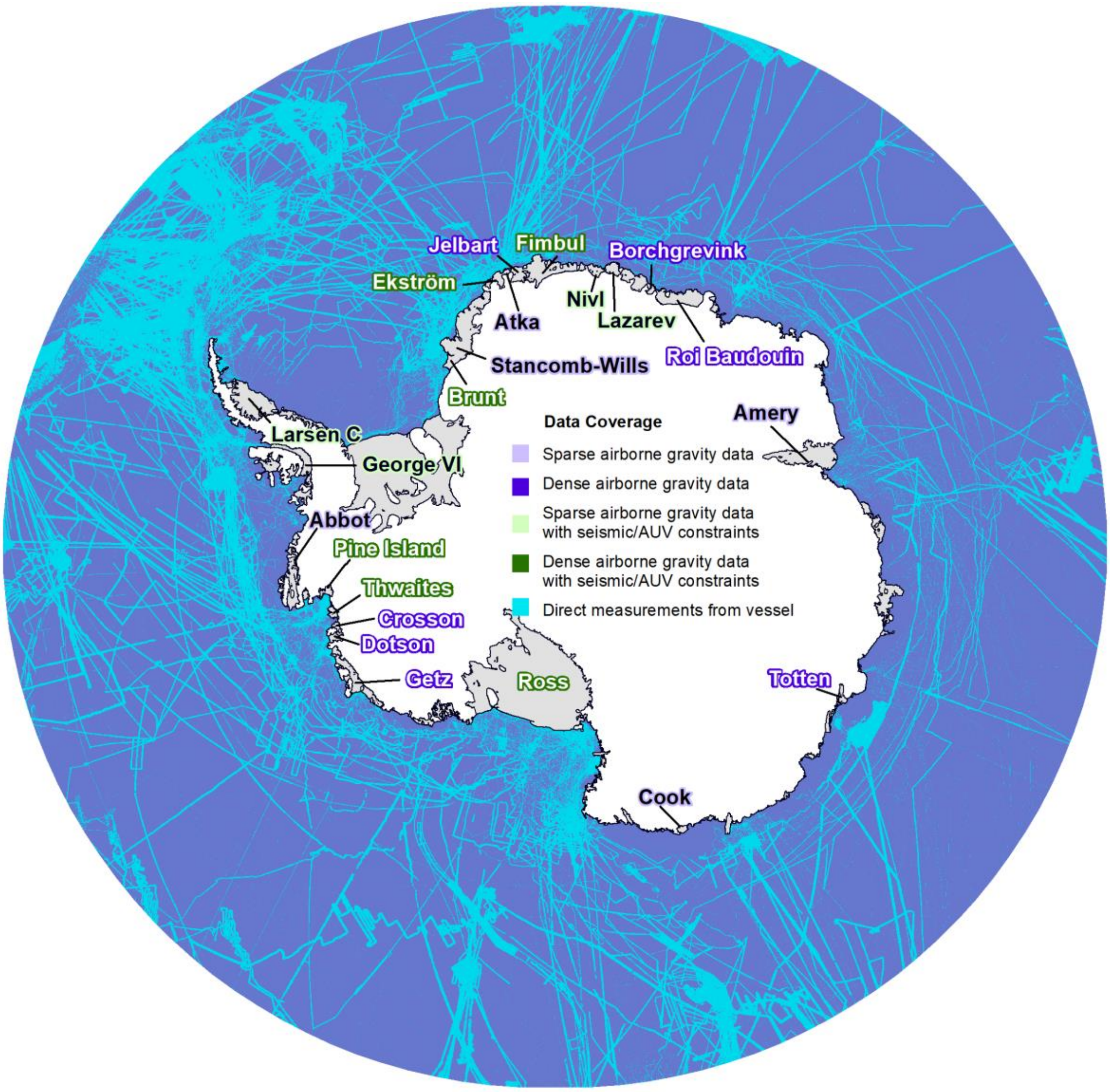

Figure 21: Seabed elevation data availability to 50°S. Over the open ocean, locations are shown only for ship-bone bathymetry data (excluding satellite gravity inversions). Airborne gravity data over ice shelves collected various line spacing; here, data collected with nominal spacing less than 10 km are shown as dense, otherwise sparse. Ice shelves shown with grey have no bathymetry data. Data sources are: Nøst (2004) for the Fimbul Ice Shelf, Eisermann et al. (2020 and 2021) for the other Dronning Maud Land ice shelves (Ekstrom, Atka, Jelbart, Borchgrevink and Baudouin), Yang et al. (2021) for the Amery Ice Shelf, Greenbaum et al. (2015) for the Totten Glacier Ice Shelf, Tinto et al. (2019) for the Ross Ice Shelf, Milan et al. (2020) for the Getz Ice Shelf, Constantino et al. (2020) for the George VI Sound, Millan et al. (2017) for Amundsen Sea ice shelves (Pine Island, Thwaites, Crosson, Dotson).

4.5 Empirical assessments of ice-discharge fluxes

Our review of published ice discharge estimates at continental scale (Section 2.2, Figure 4) shows large differences between studies and methods. These differences are not within stated uncertainties of individual estimates and are at the level of the total mass imbalance of the AIS. Uncertainty assessments are typically done by error propagation of input data variables, but this is difficult at continental scale because the origin of the input data is highly variable. Velocity data can be derived from multiple satellite sensors and methods, whereas ice thickness data stem from various airborne campaigns over several decades and are interpolated or modeled in areas with data voids. Assumptions or models are also needed concerning ice velocity at depth, temporal variations in ice thickness, and impacts of known and unknown deviations between the selected observational flux gate and the evolving grounding line location. Even more difficult is the separation between random errors that reduce by spatial averaging, and systematic errors that can be present for larger regions or the entire continent.

We do not discuss formal uncertainty analyses of ice discharge here, but rather focus on the variability of estimated ice discharge resulting from different combinations of current reference datasets applied to the same computational methodology. This is meant to highlight data-rooted uncertainties in ice discharge, which can be improved by coordinated surveys of bed topography along the Antarctic grounding line (Section 5.1 and Figure 13). The assessment also provides the first discharge estimates for the new RINGS/Bedmap3 reference grounding line (Section 4.1) and its simplified version (Section 4.2) which is meant to guide future survey lines that will ultimately become flux gates for future monitoring of ice discharge.

4.5.1 Assessment framework

We carry out a simple assessment where basin-scale ice discharge is consistently calculated for 12 combinations of 3 flux gates, 2 ice-thickness datasets and 2 ice-velocity datasets. As flux gates for discharge calculations, we use the RINGS/Bedmap3 reference grounding line (Section 4.1), the landward simplified grounding line (Section 4.2) and a hydrostatic line (Point H in Figure 10) representing the landward boundary of where ice shelves are freely floating. The reason for including the hydrostatic line as a flux gate is that ice thickness has been estimated all around Antarctica from inversion of satellite altimetry measurements of ice-shelf freeboard under assumption of hydrostatic equilibrium (e.g., Griggs & Bamber, 2011). For that reason, it has been used in discharge calculations for some areas with sparse or no data for grounded ice thickness (e.g., Rignot et al., 2019). As there is no complete observational dataset of the hydrostatic line, we estimate it using the MATLAB function iceflex_interp within the Antarctic Mapping Tools package (Greene et al., 2017), which is an implementation of the ice flexure model presented by Vaughan (1995). In areas with no ice shelves, the hydrostatic line is set equal to the RINGS/Bedmap3 grounding line, which follows the calving-front or land coastline.

For ice thickness along these three flux gates, we use the continuous gridded products of Bedmap2 (Fretwell et al., 2013) and Bedmachine version 3 (Morlighem et al., 2020). These products are for the most part based on the same surveyed ice thickness data and the latter includes newly collected data mainly in East Antarctic coastal regions. However, they both rely on different methods for filling data gaps in areas with no data (Section 3.6.1) which constitute ~80% of the physical grounding line (Gardner et al., 2018). Over free-floating parts of the ice shelves, Bedmap2 is based on the altimetry product of Griggs and Bamber (2011), whereas Bedmachine is based on hydrostatic inversion of the REMA (Howat et al., 2019) after accounting for firn air content (Ligtenberg, et al., 2011). Of relevance for both the hydrostatic and grounding-line flux gates is that both ice-thickness products have been adjusted around the grounding zone (Figure 10) to obtain a smooth thickness transition from grounded to floating ice, important for any modeling application.

Data gaps in surface velocity products are no longer a major issue thanks to the frequent image coverage of the Sentinel-1/2 and Landsat-8 missions (Section 3.7.2). For our discharge calculations, we use the version 1 of the ITS_LIVE multiyear velocity mosaic (Gardner et al., 2018), observationally centered around 2015-16, and the 2014-17 velocity mosaic of Rignot et al. (2022), both part of NASA's MEaSUREs program. We use the 240 m and 450 m resolution versions of the two products, respectively, which is somewhat finer than the ice thickness grids at 500 m resolution for Bedmachine and 1 km for Bedmap2. To ensure data continuity along the entire flux gates, which occasionally reach outside of the grid masks, we artificially extend the grids seaward by extrapolating from the nearest grid cells over ice.

Discharge calculations are done in a vector-based fashion where ice flux is calculated for each line segment of the flux gate by multiplying the extracted surface velocity vector with ice thickness and the projection-corrected segment length. These fluxes are summed up for each of the 27 drainage basins of Zwally et al. (2012) and for the ice sheet as a whole. A maximum segment distance of 400 m is enforced to ensure sufficient sampling of the input grid data extracted by linear interpolation. We use ice-equivalent values for thickness and convert to mass by assuming an ice density of 917 kg m^{-3}. To account for added mass in the area between the inland flux gate at the simplified grounding line and the RINGS/Bedmap3 grounding line, we integrate the SMB of five RCMs (Section 2.4.2; Figure 5) over all intermediate areas in each drainage basin and use the median one, which is RACMO. Thickness changes from dynamic imbalance in this zone represent a significant but smaller correction (Gardner et al., 2018), which we do not account for here. For the hydrostatic flux gate, no SMB correction is applied as it would be counterbalanced by ice-shelf basal melting which cannot be easily estimated in the flexure zone and represents a major uncertainty for this approach.

Antarctic-wide discharge estimates for the 12 combinations of datasets are summarized in Table 7 and discussed below, focusing on the main uncertainties rooted in ice thickness and SMB correction, with relative contributions depending on the choice of flux gate location. To further check the dependency of discharge estimates on flux gate location, we also make calculations with km-scale buffer migrations of the RINGS/Bedmap3 reference line (Figure 22). It should be noted that the different input datasets are not independent as they have common sources of the IPR data, satellite imagery or RCMs, implying that they will also share some inherent errors from the source data, and the difference between these estimates may not fully address the current uncertainty of the ice-discharge estimates.

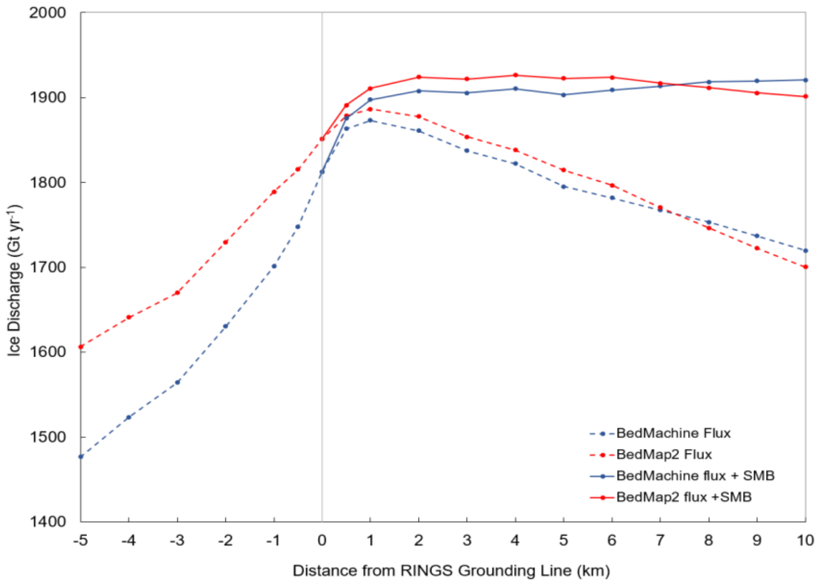

Figure 22: Ice discharge from the AIS determined for flux gates that are stepwise migrated by 0.5 or 1 km on either side of the RINGS/Bedmap3 grounding line, excluding ice rises. Dashed lines show ice flux through a given flux gate, whereas solid lines on the landward

side show estimated discharge at the grounding line after adding modeled SMB in the area between the grounding line and the flux gate. Blue lines are based on ice velocity from ITS_LIVE (Gardner et al., 2018) and ice thickness from Bedmachine version 3 (Morlighem et al., 2020), whereas red lines are based on ITS_LIVE and Bedmap2 (Fretwell et al., 2013). For SMB correction, we selected the ensemble model with median SMB from five RCM results (Mottram et al., 2021). The hydrostatic line is located 4.3 km seaward of the grounding line on average.

Table 7. Pan-Antarctic total ice discharge (Gt yr^{-1}) for the grounded ice sheet estimated at three different flux gates using two different ice thickness products and two different surface velocity products.

Prescribed flux gate locations	Bedmachine[*1] ice thickness		Bedmap2[*2] ice thickness	
	ITS_LIVE[*3] velocity	Rignot[*4] velocity	ITS_LIVE[*3] velocity	Rignot[*4] velocity
RINGS/Bedmap3 grounding line[*5]	1,812	1,769	1,851	1,800
RINGS simplified grounding line[*6]	1,884[*7, *8]	1,839[*7]	1,868[*7, *8]	1,816[*7]
Hydrostatic ice shelf line	1,518	1,480	1,657	1,607

*1: Bedmachine, version 3 Morlighem et al. (2020)
*2: Bedmap2, Fretwell et al. (2013)
*3:ITS_LIVE multiyear velocity mosaic version 1, 450 m Gardner et al. (2018)
*4: MEaSUREs 2014-2017 velocity mosaic, version 1, 450 m Rignot et al. (2022)
*5: Section 4.1. As shown by the black curves in Figure 18.
*6: Section 4.2. As shown by the red curves in Figure 18.
*7: These four estimates include a 160 Gt yr^{-1} correction for SMB in the area between the RINGS/Bedmap3 and simplified grounding lines, using the median RACMO model from five RCMs (Section 4.5.3). Figure 24 shows the regional distributions of this correction.
*8: Figure 23 shows the regional distributions of differences between these two estimates at the RINGS simplified grounding line, both calculated using the flow velocity from Gardner et al. (2018) but with two difference ice thickness datasets: Bedmachine (Morlighem et al., 2020) and Bedmap2 (Fretwell et al., 2013).

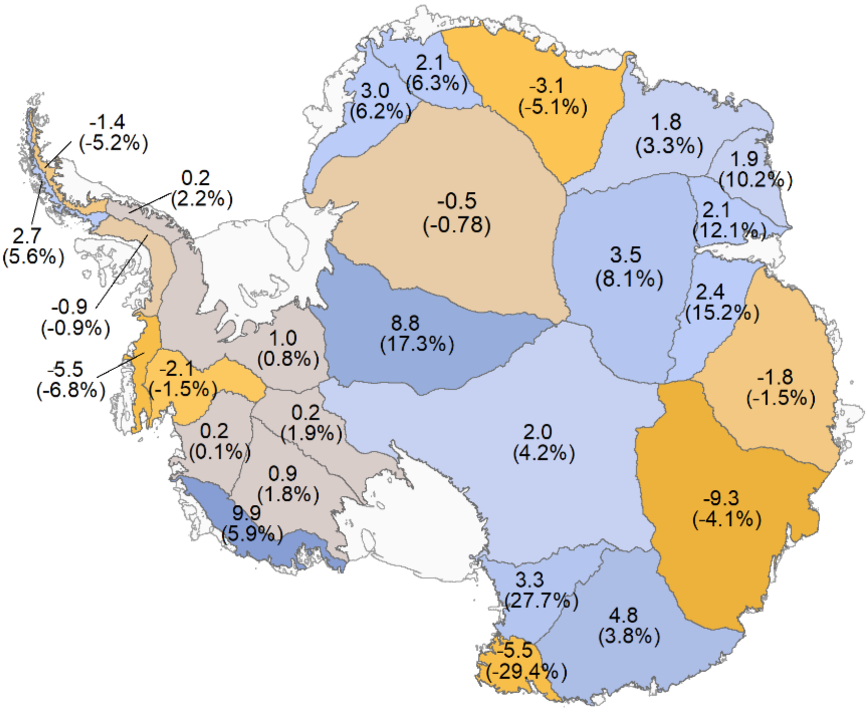

Figure 23: Comparison of two empirical ice-discharge estimates using Bedmap2 (Fretwell et al., 2013) and Bedmachine version 3 (Morlighem et al., 2020) bed topography at the primary ring (simplified grounding line (Figure 18 and Section 4.2), using ITS_LIVE velocity data (Gardner et al., 2018). The values are the excess of Bedmap2 case beyond BedMachine (Gt yr^{-1}) and percentage of this excess to the mean of these two values.

4.5.2 Uncertainties in mass flux rooted in ice-thickness uncertainty

For similar combinations of flux gates and thickness data, discharge estimates from the two velocity datasets have a near-constant offset of 38-52 Gt yr^{-1}, with ITS_LIVE being consistently higher (Table 7). It could reflect differences in timing of the two velocity products, up to several years in some regions, or it could be due to other small systematic effects related to different satellite sensors, processing techniques, and data filtering.

Keeping velocity datasets constant and varying ice thickness datasets or flux gate locations have a larger and more variable impact. When the RINGS/Bedmap3 grounding line is used as flux gate, Bedmap2 gives a higher discharge than Bedmachine, whereas the opposite is the case for the RINGS simplified grounding line. However, these differences are not systematic between drainage basins. For the hydrostatic line, the resulting discharge estimates using Bedmap2 are 127-140 Gt yr^{-1} higher than for Bedmachine, which can only be explained by systematic errors in the ice-shelf thickness data. It is likely dominated by the correction term for firn-air content, which gets scaled up by an order of magnitude when converting ice-shelf freeboard to thickness. Mismatch between hydrostatic ice thickness and measured ice thickness led to a recalibration of Bedmachine over ice shelves (Morlighem et al., 2020), which could explain some of the difference. Chartrand and Howat (2023) compared hydrostatic ice thickness from airborne laser altimetry with coincident ice thickness measurements from IPR. They found that ice shelves are on average 17 m (6%) thinner than their inferred hydrostatic thickness, but with high variability both within and between ice shelves. This is also evident at the basin scale for our discharge estimates.

Despite potential overestimation of hydrostatic ice thickness, total discharge estimates are much lower at the hydrostatic line (1,566 ± 67 Gt yr^{-1}, mean and mean absolute deviation of four estimates shown in Table 7) than at the grounding line (1,808 ± 24 Gt yr^{-1}) and the simplified line (1,852 ± 24 Gt yr^{-1}). Much of this difference is likely due to oceanic melting near the grounding line which locally can reach tens of gigatons per year for outlet glaciers with thick ice at the grounding lines (Rignot & Jacobs, 2002). Total discharge estimates at the grounding line and the simplified line are considerably lower than the published estimates of 1,929 ± 40 Gt yr^{-1} from Gardner et al. (2018) and 2,229 ± 142 Gt yr^{-1} from Rignot et al. (2019), see Figure 4 and Section 2.2 for a further comparison of these two studies. Gardner et al. (2018) also estimated discharge using the grounding line as flux gate, and from that they obtained a total discharge of 1,756 ± 99 Gt yr^{-1} , which is slightly lower than our estimates. If we replace the RINGS/Bedmap3 grounding line with theirs, we obtain total discharge estimates in the range 1,704-1,795 Gt yr^{-1} for the four combinations of ice thickness and velocity datasets of Table 7, consistent with their estimate as well as with Miles et al. (2022) who used the same grounding line in combination with Bedmachine version 1 for all the drainage basins of the WAIS and EAIS.

Migrating the flux gate seaward and landward of the reference grounding line (Figure 22) confirms the bias between Bedmachine and Bedmap2 over ice shelves, but shows consistent results when flux gates are migrated more than 1-2 km inland of the grounding line. Here, discharge estimates stabilize in the range 1,900 – 1,920 Gt yr^{-1} when SMB corrections are applied for the area between the grounding line and the migrated flux gate. This demonstrates the inherent challenges of interpolating and modeling ice thickness near grounding lines, where data gaps and boundary effects often introduce biases. In areas with no ice-thickness measurements, it is therefore better to move the flux gate 1-2 km inland of the grounding line to reduce the risk of biases in gridded ice-thickness products.

4.5.3 Uncertainties in mass flux rooted in SMB uncertainty

Selection of flux gate locations needs to be balanced between where accurate ice thickness data can be found and how well SMB and potential thickness changes are known for the area between the flux gate and the grounding line location. At the continental scale, the extracted SMB corrections in Figure 22 are balancing the decrease in ice-flux when the flux gate is migrated inland, but this can be different locally and for different RCM models. Considering all the five SMB ensembles (Figure 24), the inferred SMB correction for the area between the grounding line and the simplified flux gate (~357,000 km^2) varies from 85 Gt yr^{-1} to 213 Gt yr^{-1}, with mean and median values of 147 Gt yr^{-1} and 146 Gt yr^{-1}, respectively. This compares to values in the range 142-342 Gt yr^{-1} if we use the FG2 flux gate of Gardner et al. (2018) which represents an area of ~703,000 km^2 inland of the grounding line to the closest ice thickness measurements. Hence, when ice thickness is measured all along the simplified grounding line, then the remaining area and quantity for SMB correction of continental ice discharge will be roughly cut in half compared to the current estimate.

Further reduction of the uncertainty relies on better understanding of SMB distributions in the promontories that are excluded from the simplified grounding line (Figure 18). The high variability of SMB in the coastal zone and the large spread between RCMs underline the importance of collecting SMB data (Section 3.6.3). Such SMB measurements are important both for improving the remaining SMB correction of ice discharge at the grounding line, and for better constraining the firn pack over ice shelves, which is essential for flux-based calculations of oceanic melting that rely on hydrostatically inferred ice thickness from satellite data.

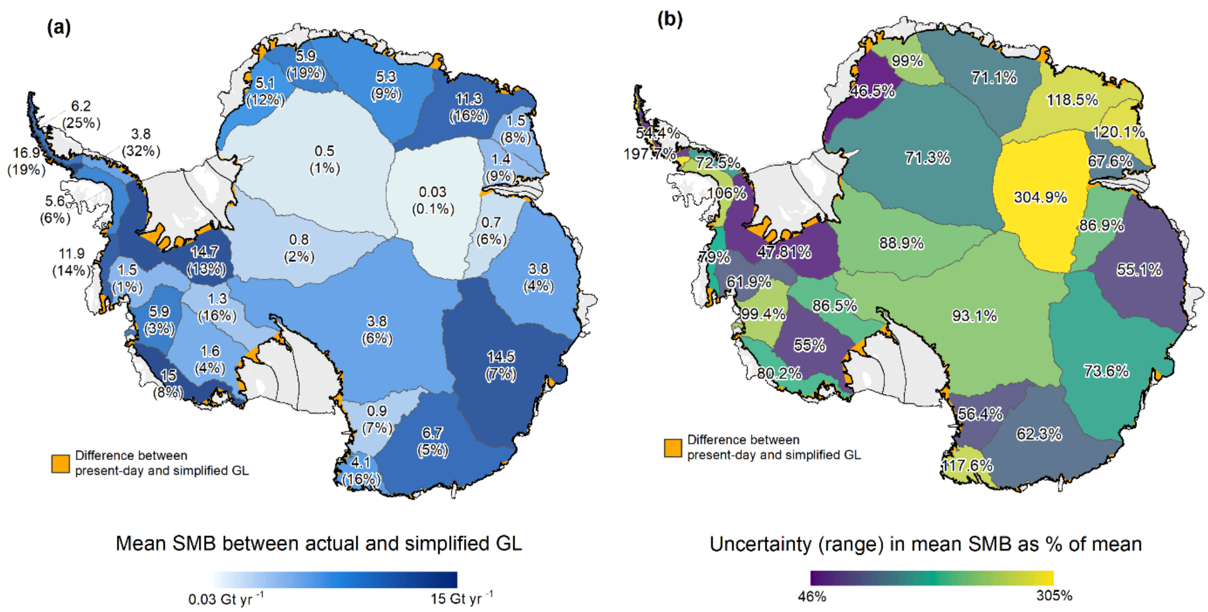

Figure 24: Magnitude and uncertainty of the SMB-correction term of the ice discharge. Ice-discharge from Antarctica is a combination of this SMB-correction term and ice discharge measured at the simplified grounding line. (a) Ensemble-mean SMB modeled by five RCMs (Figure 5a) integrated over the fringe regions (yellow) bounded by the RINGS/Bedmap3 grounding line and the RINGS simplified grounding line. The values are ensemble mean SMB (Gt yr^{-1}) and percentage of this SMB to the mean of the two ice-discharge estimates at the simplified grounding line using Bedmap2 (Fretwell et al., 2013) and Bedmachine (Morlighem et al., 2020) bed elevations together with the ITS_LIVE velocity data (Gardner et al., 2018). (b) The range of modeled SMB using five RCMs (Section 2.4.2) integrated over the fringe regions (yellow), shown as a relative value to the ensemble-mean SMB (a).

4.5.4 Summary and recommendations

Our assessment of ice discharge using different flux gate locations and gridded input data shows that discharge estimates can vary by >100 Gt yr^{-1} depending on how these datasets are combined (Table 7). This discrepancy is similar to the AIS mass balance (50-150 Gt yr^{-1} depending on year, Figure 2). Discharge estimates using the hydrostatic line are consistently lower than at the grounding line and show large relative biases depending on ice thickness products. This issue is also relevant around the grounding line as estimated discharge continues to increase for 1-2 km inland when flux gates are moved and corrected for the SMB contribution (Figure 22). This is likely also the reason why the estimated discharge using the simplified grounding line as flux gate is higher than when using the precise grounding line as a flux gate (Table 7).

Our new empirical estimates of ice fluxes using published datasets lead us to draw four recommendations. First, hydrostatically inferred ice thickness from ice shelves should not be used for ice-discharge flux estimates due to their high uncertainty and potential bias. Second, ice thickness measurements near grounding lines with no data should be prioritized, both to improve ice-flux calculations and to minimize the need for SMB corrections. Third, in areas with no thickness measurements in the vicinity of the grounding line, flux gates should be moved 1-2 km inland or to the closest thickness measurements. Fourth, discharge calculations should be done at high spatial resolutions (a few hundred meters) to ensure that sharp gradients in ice velocity and thickness are captured.

4.6 Projected grounding line locations by ISMIP6 models

Grounding line migration is a key characteristic of marine terminating regions of the AIS, and its evolution captures their overall dynamics (Weertman, 1974; Rignot et al., 2014). Ice-flow models have worked on designing and incorporating accurate grounding line dynamic evolution over the past couple of decades (Pattyn et al., 2006; Durand et al., 2009; Gladstone et al., 2010; Seroussi et al., 2014; Feldman et al., 2014; Seroussi and Morlighem, 2018). Different numerical schemes exist to track the evolution of grounding line migration, which have been extensively compared in several intercomparison projects (Pattyn et al., 2012; 2013; Cornford et al., 2020). This process is now systematically included in ice-flow simulations of the AIS and its marine terminating regions, both at regional scales (e.g., Joughin et al., 2014; Favier et al., 2014) and larger scales (e.g., Lipscomb et al., 2019; Golledge et al., 2019).

4.6.1 Ice Sheet Model Intercomparison Project for CMIP6 (ISMIP6)

The World Climate Research Program (WCRP) has led the Coupled Model Intercomparison Project (CMIP) since 1995 (Meehl et al., 2000; 2007; Taylor et al., 2012; Eyring et al., 2016). The overall objective of CMIP is to better understand the past, present and future changes of the coupled climate system caused by both natural and anthropogenic changes, using a multi-model ensemble approach. Climate models taking part in CMIP rely on various individual model components for the ocean, atmosphere, land surface, and sea ice, and use different model parameters and initial conditions, all contributing to the uncertainty in the simulated evolution of the future climate.

CMIP's sixth generation (CMIP6) includes the Ice Sheet Model Intercomparison Project for CMIP6 (ISMIP6), which is the first initiative focusing primarily on projections of the Antarctic and Greenland Ice Sheets (Nowicki et al., 2016; 2020). ISMIP6 investigates the response of the ice sheets to this evolving climate system, using oceanic and atmospheric forcings derived from the CMIP5 and CMIP6 ensembles (Barthel et al., 2020; Jourdain et al., 2020). Results from climate models forced with SSP1-2.6 and SSP5-8.5 emission scenarios (RCP2.6 and RCP8.5 for CMIP5 simulations) were used to derive the climate forcing; more specifically, ocean temperature and salinity for the oceanic forcing and surface temperature and SMB for the atmospheric forcing.

ISMIP6-2100 simulations of the AIS have been performed by 13 research groups using 10 different ice-flow models (Seroussi et al., 2020); these models are listed in Table 6. More recent ISMIP6-2300 simulations to the year 2300 have been performed by 16 research groups using 12 different ice-flow models (Seroussi et al., 2024). Different choices were made by the modelling groups for the initial conditions, model parameters, or processes to capture so that the main characteristics of each contributing ice sheet model outcomes vary greatly. For example, the mesh or grid size varies from 1 km to 32 km. Basal sliding over the bed was represented with different sliding laws: Weertman sliding law (Weertman, 1957), Budd sliding law (Budd et al., 1979) or a combination of the power law and Coulomb (Schoof, 2005) sliding laws. Calving was simulated with a minimum thickness, eigencalving (Albrecht and Levermann, 2012), or divergence and accumulated damage (Pollard et al., 2015). However, some models did not include calving simulations (Seroussi et al., 2020, Seroussi et al., 2024). Amongst several instability mechanisms to cause large and rapid retreat events (Section 2.8.4), MISI (Figures 11a and 12) is included in all ISMIP6 models. MICI (Figure 11b) has been included in a number of ice-flow models and studies (e.g., DeConto and Pollard, 2016) but was not included in any ISMIP6 simulations.

One of the few constraints imposed on the ice flow models for the ISMIP6 simulations was the ability to represent floating ice shelves as well as the evolution of grounding lines, making this ensemble suitable to assess future grounding line evolution. However, the exact treatment of the grounding line was left to the discretion of modelling groups, based on their typical practice, which included the flux parameterization (Winkelmann et al., 2011), the hydrostatic equilibrium (Huybrechts, 1990) or solving a contact problem (Durand et al., 2009).

All choices of model parameters and initial conditions have an impact on the simulated evolution of the AIS (Goelzer et al., 2017; Seroussi et al., 2019). However, preliminary results assessing the ice response to idealized forcings showed that the treatment of partially-floating cells and the model resolution at the grounding line had the largest impact on simulated grounding-line evolution and ice-mass loss (Seroussi et al., 2019). Theoretical results on both idealized and realistic cases suggest that model resolutions below 2 km should be used to accurately capture grounding line evolution, even when sub-grid parameterizations are used to continuously track the grounding line motion, for example using level-set methods (Seroussi et al., 2014; Seroussi and Morlighem, 2018). When mesh or grid resolution below 2 km are used in the vicinity of the grounding line, model results are primarily affected by choices in model parameters (e.g., sliding law) as opposed to numerical artifacts (Cornford et al., 2020). However, such high resolutions remain difficult to achieve at continental scales. Models rely on adaptive refinement in the key areas (Morlighem et al., 2010; Cornford et al., 2013), but few models have the ability to update their mesh following grounding line retreat (Cornford et al., 2015), causing limitations when grounding lines retreat over large areas. This is an active area of research (Dos Santos et al., 2021) and new schemes need to be integrated and used more routinely in large-scale simulations. Additionally, bed topography at a similar resolution to model grid resolution, i.e., of 2 km or below, is necessary to be able to feed the models with accurate data (Durand et al., 2011), which requires data measured roughly at the same spacing.

4.6.2 Projected grounding line retreat by the coming century

The ISMIP6-2100 experiments span the 2015-2100 period, and experiments were performed with 16 different ice-flow model configurations, and using climate forcings from 10 climate model simulations from CMIP5 and CMIP6. Results from 51 simulations are combined to assess the grounding line evolution simulated by 2100 and are shown in Figure 25.

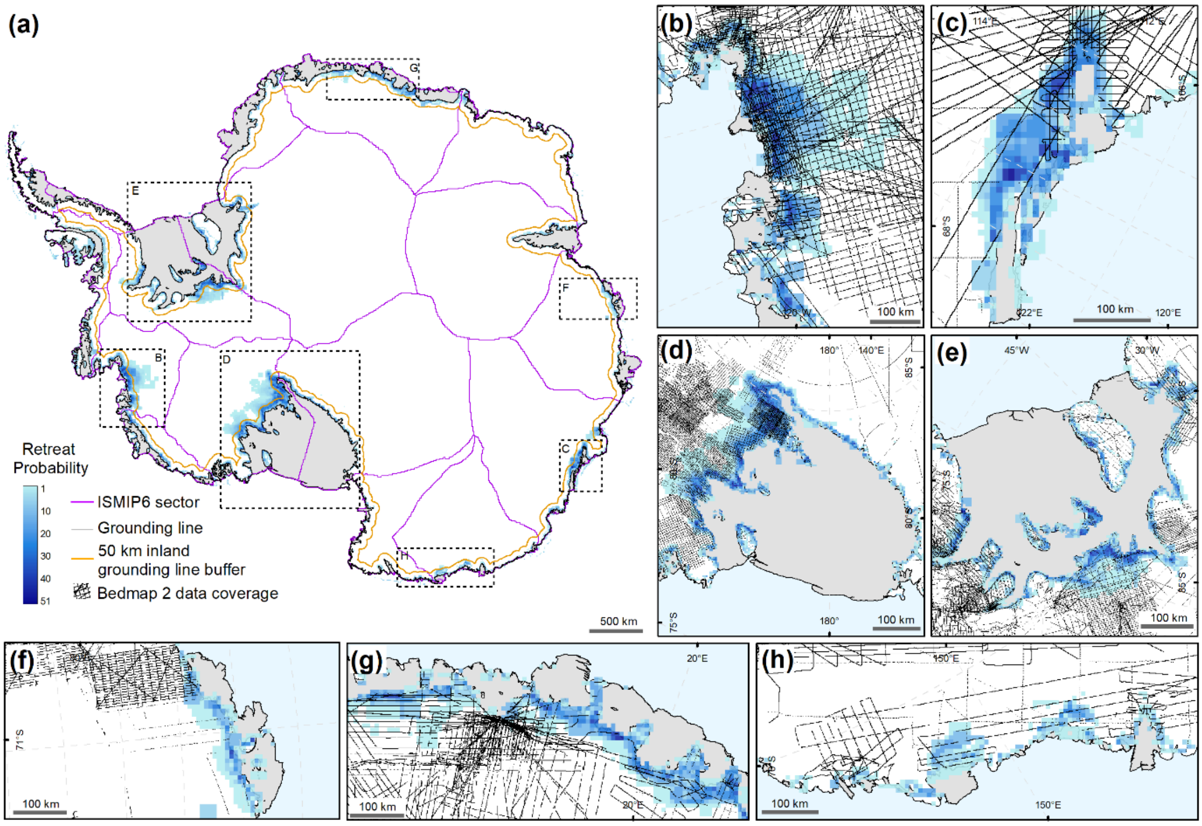

Figure 25: Projected Antarctic grounding line retreat from the ISMIP6 model ensembles by the end of 2100. Retreat probability represents the number of modeled retreat cells (see text). In total 51 ISMIP6 experiments were used to calculate retreat probability here, including 12 experiments based on RCP8.5 scenarios from 6 CMIP5 models; 4 experiments based on RCP 2.6 scenarios from 2 CMIP5 models; 2 experiments testing ice-shelf collapse; 2 experiments testing the uncertainty in the basal-melt parameterization, and 2 experiments testing the uncertainty in the melt calibration. All of these experiments except those testing basalt-melt parameterization and calibration were simulated with open and standard ocean melt frameworks. For full details of the participating models and experiments, see Seroussi et al. (2020). (a) Pan-Antarctic view, with the orange stroke denoting the 50 km inland limit from the RINGS/Bedmap3 grounding line and highlights regions of ≥ 50 km projected grounding line retreat. (b-h) regional views together with bed-elevation data locations used for Bedmap2 compilation (Fretwell et al., 2013), which was used for most of the ISMIP6 model experiments. Panel (g) on central Dronning Maud Land, (f) on the West Ice Shelf and panel (h) on Geroge V Land illustrate regions with sparse Bedmap2 data and limited reliability on the projected grounding line retreat.

In West Antarctica, retreats larger than 50 km occur in the Amundsen Sea basin (Figure 25b), in the Siple Coast basins (Figure 25d) as well as for some ice streams feeding in the Ronne-Filchner Ice Shelf (Figure 25e). In the Amundsen Sea basin, a small number of simulations suggest an extremely large retreat of Thwaites Glacier, reaching several hundreds of kilometers (Figure 25b). The majority of simulations, however, show a retreat of less than 100 km but there is a strong disagreement between models over the entire Thwaites basin. Results for the Pine Island Glacier, on the other hand, do not show any retreat past 40 km from the present-day grounding line, despite the large ice-shelf thinning (Seroussi et al., 2020), in agreement with previous regional results (e.g., Seroussi et al., 2014). Glaciers feeding into the Dotson and Crosson ice shelves experience a slightly larger retreat than the

Pine Island Glacier and up to 60 km for the largest retreats (Figure 25b). About half of the simulations suggest a retreat of at least 20 km in the region upstream of the grounding line of the Pope and Smith glaciers.

In the Siple Coast basin, simulated grounding line retreat can exceed 100 km for all the main ice streams feeding into the Ross Ice Shelf (Figure 25d). The majority of models predict a retreat of up to 50 km, except for the Whillans Ice Stream, for which the retreat is more pronounced. The grounding line retreat of ice streams feeding into the Ronne-Filchner Ice Shelf is more complex: the Institute, Moller and Evans ice streams experience significant retreats, while retreat is more limited for the other ones (Figure 25e). Ice flowing over the Bungenstock Ice Rise thins enough to detach from the ice rise in the majority of simulations, while the Berkner Island, Henry Ice Rise and Korff Ice Rise also see their area reduced significantly in most cases but stay grounded.

In East Antarctica, the retreat is less pronounced than in West Antarctica overall. The Totten, Moscow University and Vanderford glaciers in Wilkes Land, experience the largest retreats, with a grounding line retreat of about 50 km along most of the fast-flowing regions (Figure 25c). Agreement between models in this region is better than most regions, with relatively limited variations in retreat extent, except for the Vanderford Glacier. Small retreats are also simulated for the Cook, Ninnis and Merz ice shelves in George V Land (Figure 25h), the Shackleton Ice Shelf in Queen Mary Land and the Lazarev and Borchgrevink ice shelves in Dronning Maud Land (Figure 25g). Most models simulate a retreat of about 10 km in these regions, with no model simulating more than 50 km.

Finally, in the Antarctic Peninsula, the retreat is very limited and only a handful of simulations suggest a retreat of 10-20 km on both sides of the George IV Ice Shelf, as well as around the Bach Ice Shelf (Figure 25a). In this mountainous region, the bed topography is very steep and large forcing signals are needed before large retreats happen. The topography is also very uncertain in this region as the narrow valleys provide side echoes when acquiring bed topography from aircraft (Section 3.6.1).

Overall, grounding lines retreat by less than 50 km in most regions and for most simulations, with the largest retreat and also the largest uncertainties for Thwaites Glacier and the ice streams feeding into the Ross Ice Shelf. The total grounded ice area is reduced by 71,547 km^2 on average and up to 385,140 km^2 in the most extreme cases, including 27,570 km^2 on average in East Antarctica and 48,383 km^2 on average for West Antarctica.

Grounding lines retreat by less than 50 km in most regions and for most simulations, with the largest retreat and also the largest uncertainties for the Thwaites Glacier and the ice streams feeding into the Ross Ice Shelf. For example, in the Amundsen Sea sector, 34% of the grounding line is projected to retreat at least 50 km from the present-day grounding line, based on the ISMIP6 experiments we analyzed. Likewise, this fraction is just over 50% along the Siple Coast of the Ross Ice Shelf, about 25% in Dronning Maud Land, Wilkes Land and regions feeding into the Ronne Ice Shelf and the Filchner Ice Shelf, and 20% in George V Land. In other regions, this fraction is less than 5%.

We consider results to be more reliable when many models give consistent results. Nonetheless, if bed topography data are absent in the region, coincidence between models does not necessarily give an accurate prediction of the future grounding line retreat. Large uncertainties exist in bed topography under the AIS, caused by the sparse data coverage (see Figure 25 for IPR data used to generate bed topography for ISMIP6 simulations). This impacts simulations of grounding line retreats and adds uncertainty to the areas and rates of retreat (Durand et al., 2009). For example, many models consistently project relatively large grounding line retreat near the West Ice Shelf; however, this area lacks IPR-measured bed topography data, making the projection unreliable (Figure 25f). As the ISMIP6 ensemble of models all use similar underlying bed elevation, they do not capture bed-topography uncertainty and consequently underestimate the overall uncertainty in ice volume and grounding line locations for example. Improved spatial coverage and accurate bed elevations would reduce this uncertainty. Bed topography needs to be known at a spatial resolution better than 2 km near the grounding line (Castleman et al., 2022; Durand et al., 2011), which is rarely available in Antarctica (Figures 19 and 20). This would allow models to better reproduce changes linked to the actual topography everywhere rather than artificial features in regions with limited coverage (Seroussi et al., 2011, Durand et al., 2009).

4.7 Data density needed for a prescribed data interpretation tolerance

Our analysis presented in Section 4.3 highlights the fact that there are no coastal regions that have adequate topographic data coverage yet, despite the six decades of international efforts to map bed topography of the AIS. Numerical models require particularly high spatial resolution of the bed topography in the vicinity of the grounding line to project grounding line retreat and ice-volume change in the future. A case study of the Pine Island Glacier shows that bed topography must be known better than 2 km resolution (Durand et al., 2011). Another case study of the Thwaites Glacier shows that bed topography is needed at finer horizontal resolution than 2 km and at a vertical accuracy of 8 m to constrain sea-level rise projection uncertainties to within ±2 cm (Castleman et al., 2022). Also, numerical models need a horizontal resolution finer than 0.5 km to resolve physical processes that determine the grounding line positions and their changes (Section 3.8.8). In this section, we examine bed elevation uncertainty caused by spatial data interpolation in existing pan-Antarctic topography datasets, and then present a case study to infer profile spacing for a given elevation-uncertainty tolerance.

First we examined published uncertainties associated with bed topography maps. Bedmap2 uses 1-km grid cells, and uncertainty is defined using three landscape classes based on the standard deviation of the ice thickness grid over 50 km. For example, the uncertainty is estimated ± 59 m when the bed is smooth (representative of ice thickness distribution on the Siple Coast), ± 83 m when the bed is intermediate, ± 149 m when the bed is rough (the Gamburtsev Subglacial Mountains), ± 150 m over ice shelves and ± 1000 m when the bed elevations are estimated using satellite-gravity data (Fretwell et al., 2013). Uncertainty in each class is dependent on the presence or absence of ice thickness measurements. For cells that do not contain data, a single, average value of uncertainty is assigned within a class.

BedMachine used 0.5-km grid cells; bed-elevation uncertainty is derived using error propagation from satellite-derived flow speed and modeled SMB when mass conservation method is used (Section 3.6.1). Ensemble analysis of regional climate models show that SMB uncertainties provided by a single model do not represent true SMB uncertainties (Section 2.4.2) so that actual bed-elevation uncertainty can be larger than BedMachine's estimate. Because of the uncertainty of the flow velocity, the mass-conservation method can be used for about 13% of the area of the AIS. For the rest of the AIS, the bed elevation uncertainty is assigned, assuming a 2 % bed slope (mean slope derived from survey data used for BedMachine) so that bed-elevation uncertainty increases linearly with the distance from the IPR data points and reaches ±100 m at 10 km from the nearest data point (Morlighem et al., 2019). Overall, uncertainties provided in these compiled maps are not highly accurate and these errors may not be readily useful to estimate bed-elevation uncertainties between survey profiles.

Second, we considered an ensemble of bed topography representations generated through stochastic simulation. Values can be simulated between measurements based on a geostatistical model that describes spatial characteristics of bed elevations observed along the IPR profiles. This method was used to examine pan-Antarctic and regional bed topography (e.g., Graham et al., 2017; Law et al., 2023; MacKie et al., 2020 and 2021). Ensembles of the bed elevation representations show only small variations near input elevation data locations, whereas they have larger variability as it goes away from the data used to constrain the bed elevations. Bed roughness predicted by stochastic modeling gives the bed rougher than Bedmap2 by a factor of 2-8 (F. S. Graham et al., 2017) and by a factor of 5-6 (Shackleton et al., 2023).

Shackleton et al. (2023) applied this method to a compiled IPR data collected in the vicinity of Dome Fuji, inland EAIS, with a wide range of survey spacing between 0.25 to 10 km to generate the bed topography with 0.5-km map cells. Ensemble analysis gives median absolute difference (MAD) between simulated topography maps, which can be parameterized using local roughness (represented by Terrain Ruggedness Index or TRI, Riley et al., 1999) and the distance to the closest measurement. Using this parameterization, they developed an empirical relationship to determine a spacing between IPR profiles needed to constrain the bed elevation within a given uncertainty tolerance. When bed roughness is similar to Dome Fuji's median (median TRI = 213 m), the IPR profiles can be separated by 1.2 km, 5.7 km, and 27 km when the uncertainty tolerance is ± 50 m, ±100 m, and ±150 m respectively. However, if TRI is 330 m, median plus one standard deviation in the Dome Fuji region, the required survey spacing is reduced to 0.7 km, 1.9 km, and 14 km. This is a case study inland of the ice sheet, but it can be used at least as a reference case to evaluate a similar relationship in the coastal region.

Third, we carried out a case study using 2.5-km-spacing IPR data. This is one of the densest datasets in Antarctica reported to Bedmap3's FAIR database (Fremand et al., 2023). 2.5-km-spacing data are available at outlets of the Bailey, Slessor, Recovery and Academy Glaciers (Corr et al., 2021). 0.5-km-spacing data are available in tributaries of the Pine Island Glacier, but their spatial extents are much smaller than the former. As a test case to be examined here, we chose an area of 57 km by 57 km in the outlet of the Recovery Glacier (Figure 26), including the profile shown in Figure 14a. We removed every second profile to generate radar data with three different survey spacings of 5 km, 7.5 km and 10 km. Figure 26 shows four stochastic realizations of the bed topography. Only very little difference is found between these realizations using 2.5-km spacing data (Figure 26 upper row), whereas much larger difference is found when 10-km-spacing (Figure 26 lower row).

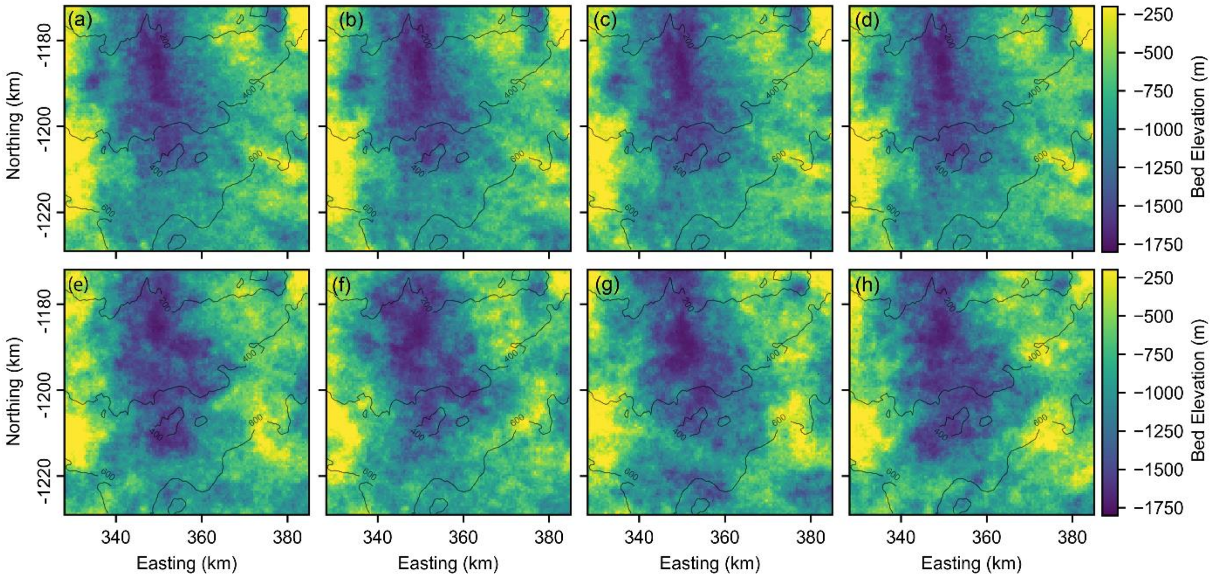

Figure 26: Stochastic simulations of bed topography in the vicinity of the Recovery Glacier outlet using 2.5-km spacing (upper row) and 10-km spacing (lower row) radar data. These radar profiles were acquired along grid east-west lines without any tie lines (Figure 27). The 10-km spacing dataset was made by using every fourth profile in the original 2.5-km spacing data (Corr et al., 2021). Four columns correspond to four snapshots of simulations. Videos showing all 100 results are available at doi.org/10.21334/npolar.2025.879398cd.

This difference is quantified as MAD across 100 simulations (Figure 27). MAD remains relatively low over the valley floor, regardless of the data spacing, whereas MAD tends to be higher in rougher regions outside of the valley floor. This indicates the effect of bed roughness on MAD. When nearest survey profile is within 1 km, the median MAD is about 50 m or less than 5% of the median ice thickness (~1000 m) in the study area (Figure 27e). This remains unchanged, when the survey spacing is larger (Figures 27 f-h). At 10-km profile spacing (where the nearest data point is ~5 km away), the median MAD rises to approximately 120 m, or 12% of the median ice thickness in the study area.

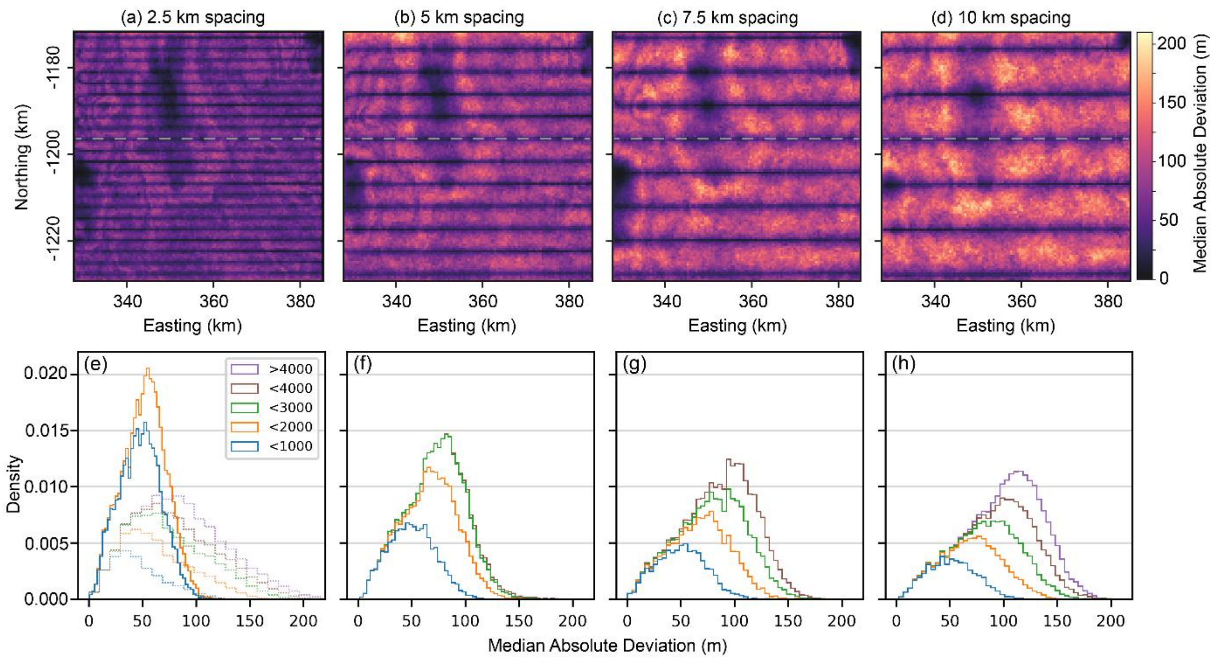

Figure 27: Median absolute deviations (MAD) derived from a stochastic analysis using an ensemble of 100 bed elevation grids simulated for different survey spacings in the vicinity of the outlet of the Recovery Glacier. This region is covered with 2.5-km profile spacing (a), and then subset of the data is used to simulate topography for sparser data: (b) 5-km spacing, (c) 7.5-km spacing, and (d) 10-km spacing. (e-h) Corresponding normalized histograms of MAD for different classes of distances to the radar profiles. In panel (e) dotted curves show this relationship derived using a similar analysis for Dome Fuji, inland EAIS (Shackleton et al., 2023). Radar data along the white dashed line (in a-d) are shown in Figure 14a.

MAD increases with distance from data points (Figures 27e-h) and with bed roughness (Figures 27a-d). To assess these efforts separately, we analyze data in 500 m distance bins (Figure 28a). Within each bin, MAD increases linearly with TRI. The slopes of these relationships steepen as distance from the nearest data point increases, following a logarithmic trend (Figure 28b):

(distance to the data point) = 10^((MAD/TRI – a) / b)

where (a, b) = (0.28, 0.54). A similar relationship holds for Dome Fuji data: (a, b) = (0.35, 0.74) (Shakleton et al., 2023).

Using this equation, we estimated required IPR profile spacing for a given median bed elevation tolerance (Figure 29). For simplicity, we assume all profiles are parallel, so the maximum distance to the nearest data point equals half the profile spacing (e.g., 2 km spacing results in a maximum 1 km distance to the nearest point). For a tolerance of ±10 m, profiles must be spaced closer than 200 m. For ±30 m tolerance, spacing must be under 600 m (TRI > 200 m), 1 km (TRI: 140–200 m), or 2 km (TRI = 100 m). Dome Fuji data suggest slightly different values (dashed curves in Figure 29), but a spacing of < 1 km is generally needed for ±20–30 m tolerance, except in very smooth regions. TRI should be derived from actual radar data or stochastic gridded topography, as smoothed datasets (e.g., Bedmap, Bedmachine) underestimate TRI by a factor of 2–8 (F. S. Graham et al., 2017) or 5–6 (Shackleton et al., 2023).

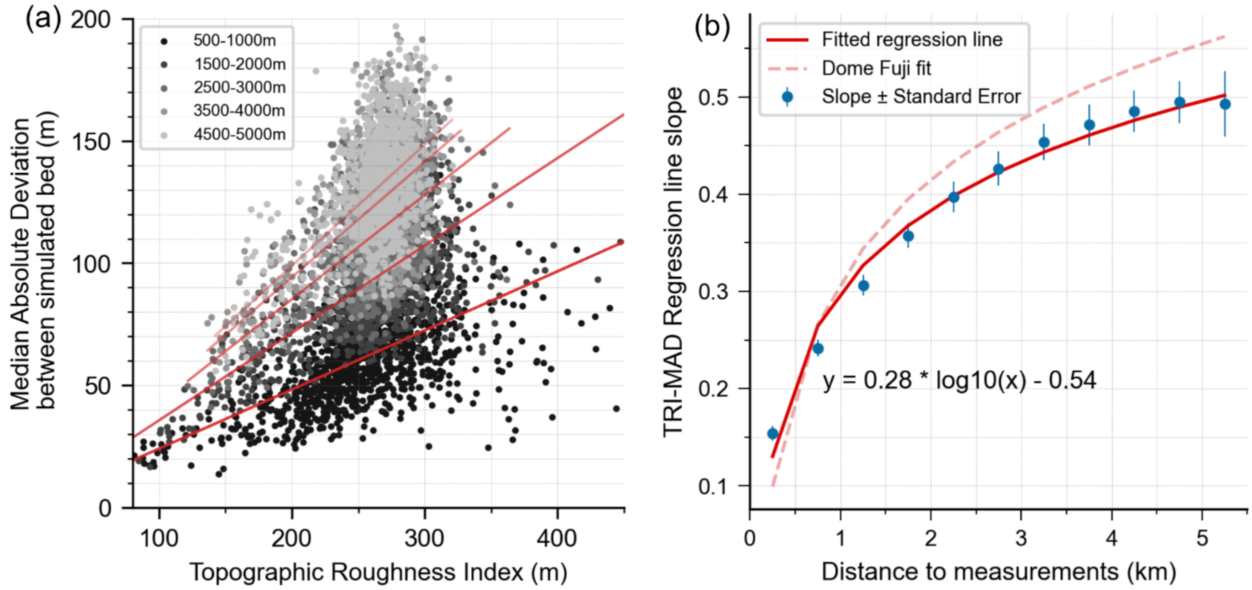

Figure 28: Bed topography uncertainty dependence on bed roughness and survey spacing. (a) Median absolute deviation (MAD) between simulated bed for increasing topographic roughness index binned at 0.5 km intervals in distance to measurements between 0 and 10 km. Only 5 of the 10 intervals are plotted to show overall trends. Red lines show their linear fit in each class. (b) Slopes of fitted regression lines in panel (a) for increasing distance to measurements. Error bars show the standard error of the linear fit, and the red curve shows a logarithmic fit. The red dotted curve shows this relationship near Dome Fuji, inland Antarctica (Shackleton et al., 2023).

The regionally-densest IPR profiles are spaced at 2.5 km at several glacier outlets to the Ronne-Filchner Ice Shelf (Corr et al., 2021). For TRI < 100 m, bed elevation uncertainty remains under ±30 m. However, for moderate roughness (TRI: 200 - 300 m), uncertainty increases to ± 60–100 m. More broadly, only 36% of the grounding lines have a radar-measured bed elevation data within 2 km (i.e., ~4 km profile spacing; Figure 20), resulting in bed elevation uncertainties of ± 40–100 m or more. Ice thickness at the grounding line has mean, median, and standard deviation of 456 m, 406 m and 323 m (Bedmap2) or 385 m, 321 m, and 391 m (Bedmachine), leading to ice-thickness uncertainties of ± 10–30 % or more.

This uncertainty significantly affects ice discharge and mass balance estimates. Since ice discharge is proportional to ice thickness, ice discharge at the current grounding line likely has uncertainties of ± 10–30 % or more. Ice discharge estimates using Bedmap and Bedmachine ice thickness products show that the choice of ice thickness product varies the ice discharge by a few percent or less, when the estimates are averaged for the entire ice sheet (Table 7). While some of the ±10–30% uncertainty at individual locations may statistically cancel out when integrated over a basin or the entire ice sheet, this does not imply that the true ice discharge is well constrained. In reality, both ice discharge and its uncertainty remain poorly quantified with currently available data, limiting confidence in large-scale mass balance assessments.

The close magnitude of SMB and ice discharge means that their difference (net mass balance) is relatively small, making uncertainty more pronounced (Sections 2.1.2 and 2.4.2). Nearly 50% of the grounding line lacks radar data within 5 km (~10 km spacing; Figure 20), making bed elevation uncertainty difficult to quantify but likely in the range of ±100–200 m (Figure 27h). This, in turn, could lead to ice discharge uncertainties of up to ±50% for half of the AIS. It is crucial to carry out more radar surveys in the ice sheet margin to more accurately estimate the current ice discharge and its future changes. While the difference of ice discharge using the smoothed bed products (Bedmap and Bedmachine) is only a few percent (Section 4.5; Table 7), that estimate presumably under represents ice-thickness-rooted ice discharge uncertainty.

In summary, data density requirements for targeted median bed elevation and ice thickness uncertainties can be estimated as follows:

1. Derive local bed roughness (TRI) using actual radar data or stochastic gridded topography. If unavailable, estimate TRI from smoothed datasets (e.g., Bedmap, Bedmachine) but adjust the values by a factor of 2-8 to account for smoothing effects.
2. Use the empirical equation to estimate required profile spacing for a given uncertainty tolerance (Figure 29). Since empirical relationships vary regionally and target only median uncertainty, actual radar profiles should be placed at narrower spacing than these estimates suggest.

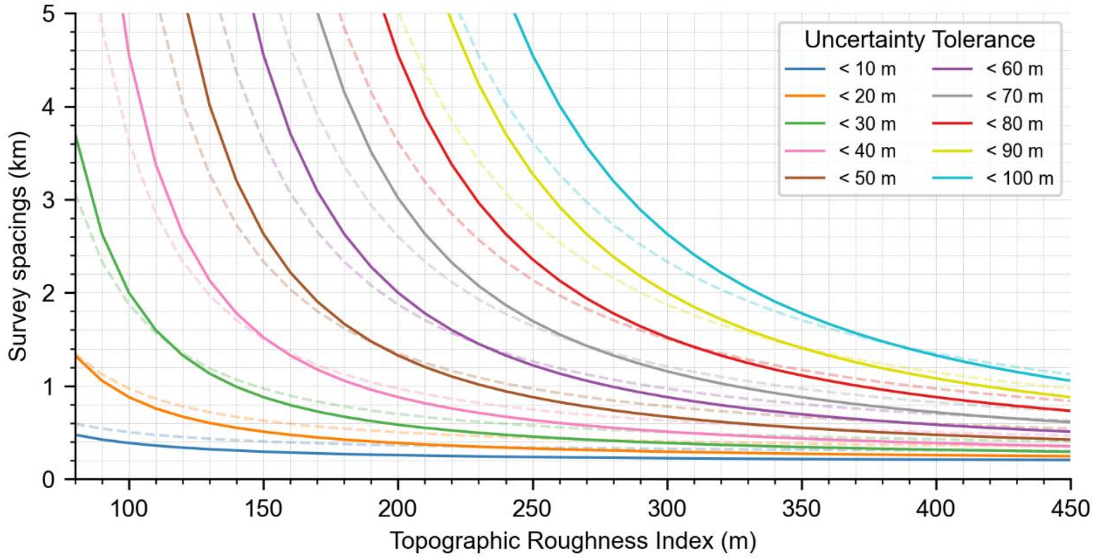

Figure 29: Survey spacings required to constrain bed elevation within various uncertainty tolerances, as a function of topographic roughness index, estimated using the parameterizations presented in Figure 28. Dashed curve shows this relationship derived near Dome Fuji, inland Antarctica (Shackleton et al., 2023).

5. Outstanding science priorities

Understanding the coastal zone of the AIS, where the ice interfaces with the Southern Ocean and warmer air masses, holds paramount importance in deciphering the intricate connections between Antarctica and the global climate system. Within this coastal zone lie multiple pivotal mechanisms that have the potential to induce significant, rapid, and conceivably irreversible transformations in the coming centuries (Section 2). Field surveys, satellite observations and numerical models are complementary interdependent tools to examine these regions (Section 3). Based on the synthesis of recent published results (Section 4), here, we discuss pan-Antarctic science priorities and approaches to address these for three different circum-Antarctic rings (Figure 13): one in the vicinity of the grounding line (primary ring, Section 5.1), one in the region slightly inland of the primary ring, where the grounding line may retreat to in the coming centuries (landward ring, Section 5.2), and one over ice shelves, ice rises and the surrounding open and sea-ice-covered ocean over the continental shelf (seaward ring, Section 5.3). These three rings represent distinct physical characteristics and science priorities. While other scientific questions are certainly not excluded, we emphasize that addressing the three key science priorities listed in Table 8 is fundamental and should be prioritized.

Table 8: Prioritized science questions for each of primary, landward and seaward rings.

	Primary ring (Section 5.1)	Landward ring (section 5.2)	Seaward ring (section 5.3)
First priority	Ice-flow discharge	Basal friction	Oceanic melt/refreeze rates
Second priority	Small-scale bed structure	SMB	Seabed topography
Third priority	Subglacial water discharge	Long-term ice-sheet evolution	Ice-shelf instability

Ice thickness along the primary ring paired with a contemporary surface velocity field will provide a glacier discharge baseline that avoids uncertainties from interpolated ice-thickness data (e.g., flux differences between bed grid products; see Table 7). This baseline enables operationally monitoring of temporal changes relative to a consistent reference. The landward and seaward rings provide important additional information about relevant processes that need to be considered for future projections. For example, differencing ice discharge estimates between the seaward and primary rings will provide sorely-needed quantification of ocean-induced melt rates in the tidal flexure zone. In this zone, melt rates are typically highest (section 2.7.2), yet are not straightforward to derive from remote sensing data because ice thickness cannot be inferred from hydrostatic equilibrium. The quantification of ocean-induced melting in the flexure zone will provide the required information for coupling of ice and ocean models (e.g. Asay-Davis et al., 2016). A landward ring enables investigation of relevant processes linked to fast ice flow and subglacial water discharge, which we discuss in section 5.2.

5.1 Primary ring

The primary ring is defined as the grounding zone identified by existing satellite products (Section 4.1) and extends a few kilometers inland to account for satellite-derived measurement uncertainties and potential short-term migrations, such as tidally-driven changes over gentle slopes. When necessary, the primary ring is defined slightly further inland as a simplified version of the grounding line to balance practical considerations for airborne surveys (Section 4.2) and possible uncertainties in ice-discharge estimates when flux gates are defined further inland (Section 4.5.4). The primary ring is the grounding zone where mass loss is concentrated and where both ice flow (Mouginot et al., 2019) and ice thinning rates (Pritchard et al., 2009; Shepherd et al., 2019) are highest. Rapid glaciological changes have been observed in this region, with rates of grounding line retreat exceeding 0.5 km yr^{-1} over most glaciers of the Amundsen Sea basin, as well as in some parts of the EAIS such as the Totten and Denman glaciers, and parts of the Antarctic Peninsula (Section 2.8.2).

The first science priority for the primary ring is the accurate quantification of ice discharge and its rate of change from individual drainage basins to the ocean (Section 2.2; see Table 8 for the priority summary). This is critical for determining Antarctica’s mass balance and its contribution to global sea level. Measurements of ice discharge are explicitly required in the input-output method, in which the discharge is compared to the total mass gain from SMB (Section 2.1.1). Partitioning mass balance into these two competing processes–ice dynamics and ice-atmosphere interactions–is critical to understand the future evolution of the AIS in a warmer climate. Separation between these processes can be achieved by directly calculating ice discharge from observations, by modelling SMB, or by removing one of those components from the net mass balance estimated from satellite altimetry or gravimetry. The large spread in projections of Antarctica's future sea-level contribution relates to the extent to which increased ice discharge driven by ocean warming will be compensated by increased snowfall arising from warmer air temperatures (Sections 2.1.3 and 2.4). This highlights the need for better observational constraints in the coming decades with more accurate and complete ice discharge measurements all around Antarctica.

Ice discharge can be estimated from satellite-measured velocity (Section 3.7.2) and ice thickness measured by airborne or ground-based IPR (Section 3.1.1). Though ice thicknesses change with time, once bed elevation is measured accurately using IPR, future ice thickness changes can be monitored by subtracting measured bed elevations from altimetry-measured ice-surface elevations (Section 3.7.1). Bed elevations also vary with time up to 10^{-2} m yr^{-1} in most areas due to GIA (Section 2.6.1), which is much less than the required accuracy of ice thickness for ice-discharge estimates or the uncertainty of most IPR systems. Critically, there are currently no Antarctic regions that have adequate bed-elevation data near the grounding line (Section 4.3).

The second science priority concerns how bed topography affects grounding line migration and related ice dynamics (Section 2.8.2). A bed slope that deepens inland is more prone to grounding-line retreat than a flat or upward-sloping bed through the MISI mechanism (Section 2.8.4). A local reverse (prograde) slope, or small bumps, can possibly stabilize the grounding line or prevent MISI-prone grounding line retreat (Figure 12). Small-scale bed roughness is also often indicative of easily deformable sediments or till (Section 2.6.4). These factors can have a large impact on ice-sheet stability, and we need higher resolution measurements of bed elevation to determine slope and roughness (Sections 4.6 and 4.7). Swath radar and UAS for ultra-dense local surveys are particularly valuable for this purpose. Seismic measurements on the ground can help to further resolve bed materials and friction parameters (Section 3.5.2), but this can only be carried out on a local scale. Furthermore, the seismic deployments are difficult in dynamic settings with fast moving ice. Ice-flow models that simulate ice-sheet behavior need continuous and realistic inputs of bed topography, which can be achieved by collating ice thickness measurements from airborne campaigns into geostatistical models that apply the roughness characteristics to unsurveyed areas, or by fusion with surface velocity and mass balance data in dynamic areas where mass conservation methods can be applied (Section 3.6.1). Either way, the quality of the output maps are highly dependent on the input ice thickness observations (Section 4.7), and addressing the existing observational gaps will contribute to improving those maps.

The third science priority is constraining subglacial meltwater discharge and its effects on ice dynamics in the grounding zone and oceanic melt of ice shelves. Subglacial meltwater discharge is poorly constrained by observations and a major unknown when considering AIS mass balance (Section 2.3). Meltwater supplied from upstream presumably lubricates the base of fast-flowing glaciers, enhancing ice flow and generating local subglacial meltwater through frictional heating (Section 2.8). Longitudinal features on ice-shelf surfaces, aligned to ice flow direction, are detectable in satellite images and digital elevation models (Section 2.3). These features represent local topographic depressions and thinner ice associated with channels incised upwards into the base of ice shelves. Many of these basal channels likely originate from subglacial water outlets. However, little is known about the impact of subglacial discharge on basal melting in the grounding zone, meaning the potential role of subglacial processes in future ice-sheet stability is highly uncertain (Section 2.3). High-resolution IPR data near the grounding line will help to identify basal channels and their extents (Figure 14c), which can provide further constraints on potential subglacial water volume. This information can be utilized by high-resolution models of ice-ocean interactions that incorporate subglacial meltwater plumes and channelized ice-shelf cavity interactions (Section 3.8.6). Upscaling these processes to the ice-sheet scale is another challenge, but improved observational constraints will be essential for doing so. Improved bed topography upstream of the grounding line (landward ring; Section 5.2) will also help to identify potential subglacial water sources which is needed to constrain subglacial hydrology models and potential impacts on ice-sheet dynamics.

Further scientific questions that could be explored within the survey framework of the primary ring relate to the impact of tides on ice flexure and grounding zone dynamics. Ocean-height variations during a tidal cycle can affect grounding line stability, as the grounding line can migrate several kilometers inland with tides in regions of low bed slope (Section 4.1). At the same time, downward flexure of the grounded ice leads to compaction of the subglacial till, helping stabilize the grounding line (Christianson et al., 2013; Section 2.6.3). The impact of ocean tides on ice flow velocities over ice shelves also propagates to the grounded ice upstream. Short-term fluctuations in surface velocity of 20 % have been observed over the Rutford Ice Stream over a two-week period (Gudmundsson, 2006) and tripled within a day over the Bindschadler Ice Stream (Anandakrishnan et al., 2003), causing fluctuations of ice discharge over short time-scales (Bindschadler et al., 2003). Finally, tidal fluctuations can lead to enhanced crevassing and damage over both ice shelves and the grounded ice upstream (Hulbe et al., 2016), which can further destabilize the grounding zone (Lhermitte et al., 2020). Airborne surveys within the primary ring will be an opportunity to build a high-resolution record of crevasses and damage in the grounding zone to help further investigate their impact on Antarctic ice dynamics.

The primary ring is primarily defined by its location near the grounding line. However, carrying out airborne surveys along the actual grounding line is not efficient and, in many cases, not logistically practical, given its complex geometry. Therefore, we define the primary ring slightly inland of the actual grounding line (Section 4.2). Simplifying the grounding line using long line segments highlighted that many promontories needed to be bypassed, resulting in the primary ring following the base of promontories (Figure 18). Therefore, we categorize science priorities associated with promontories (and their grounding line) in the seaward ring (Section 5.3).

5.2 Landward ring

The landward ring encompasses the region immediately upstream of the grounding line, feeding ice into the grounding zone and ultimately into the ocean. Unlike the primary ring, which is well-defined by the current grounding line position, the precise location or upstream range of the landward ring is less precisely defined and dependent on spatially-variable processes that dominate current and future ice flow. Three most significant science priorities for each of the three rings are summarized in Table 8.

The primary science priority for the landward ring is understanding and quantifying ice-sheet basal friction (Section 2.6.4). Present-day basal friction is typically inferred from observations of ice flow and surface slope, then used as a static parameter in ice-sheet models projecting future grounding-line retreat (Section 2.8.3). However, presently slowly-moving ice may flow faster in future. Basal friction is dynamic, evolving through interactions between the ice and its underlying deformable sediments and hard bedrock over various timescales, and is largely affected by subglacial hydrology (Section 2.6.3). The nature of the bed strongly affects ice motion, with weak, water-saturated sediments facilitating fast flow and stiff, high-friction beds promoting stability (Section 2.6.3). Improving constraints on bed properties through seismological surveys (Section 3.5.2) and better integration of observational data into numerical models (Section 3.6.1) will be critical for more accurate predictions of AIS behavior. In terms of airborne geophysics, it is crucial to infer geological properties of the lithosphere, including presence, thickness, and properties of sedimental basins, using gravity and magnetic fields (Section 2.6).

Closely linked to basal friction is the role of subglacial hydrology, the second scientific priority for the primary ring. Subglacial water exerts a key control on basal friction, lubricating ice flow and modulating ice dynamics at various temporal and spatial scales (Section 2.3). Water routing beneath the ice sheet follows hydraulic potential gradients, with network structures ranging from distributed water films to well-organized channelized flow systems. Large subglacial lakes, episodic drainage events, and persistent subglacial water pathways have been identified in several Antarctic regions, yet their influence on ice motion remains poorly constrained (Section 3.8.6). Mapping subglacial water pathways using radar sounding (Section 3.1.1) and linking these observations with ice velocity variations from satellite data (Section 3.7.2) will improve our ability to predict how basal water influences ice-sheet dynamics. Furthermore, understanding how subglacial water is routed towards the grounding line will help refine estimates of freshwater fluxes entering the ocean, which has implications for ice-shelf basal melt and ocean circulation (Section 5.3). The interactions between ice and the solid Earth are also critical, particularly the influence of hydrology on sediment processes and, ultimately, how geological constraints shape ice dynamics over various timescales (Section 2.6.4).

The second science priority for the landward ring is quantification of SMB (Section 2.4.2). The ice surface gains elevation within a short distance near the landward ring and orographic effects result in large snowfall in this region (Section 2.4.2). Large SMB in the coastal regions may counteract the increasing ice discharge from Antarctica and mitigate Antarctica's contribution to the global sea-level rise. The spatial and temporal variability of SMB (Section 2.4.2) must be constrained in a circum-polar manner, as it is the total continent-wide flux which determines global sea level, rather than variability in any single catchment. SMB records over the past few decades are useful to test RCMs constrained by reanalysis data (Sections 3.8.1, 3.8.2, and 3.8.3). Shallow sounding IPR is a viable method for constraining SMB (Sections 3.1.2 and 3.5.1), particularly when linked to shallow ice cores to date radar reflectors. This is most effectively conducted at ice rises, discussed for the seaward ring below (Section 3.6.3).

The third key science priority concerns the interplay between ice-sheet dynamics and evolving boundary conditions. The spatial pattern of stress transmission from the grounding zone inland dictates how rapidly the ice sheet will respond to perturbations. Ice-flow acceleration in outlet glaciers and ice streams can propagate upstream, reorganizing drainage networks and altering stress regimes in the ice-sheet interior (Section 2.8.2). Understanding these interactions requires improved mapping of bed topography as well as geological and tectonic factors, such as the distribution of superficial till layers, thicker sedimentary basins and other more robust lithologies, together with the broader tectonic setting, and crustal and lithospheric conditions (Section 2.6). This underlying geological template directly influences both basal friction and ice flow by providing a deformable or resistive substrate, and indirectly by providing controls on broad-scale topography, ground-water hydrology and geothermal heat flow. Such knowledge is particularly crucial in fast-flowing regions where mass loss is concentrated (Sections 4.6 and 4.7).

The precise location of the landward ring is largely variable between regions, reflecting topographic and glaciological settings, and governing mechanisms of ice flow and future ice-sheet evolution. Nonetheless, as a guideline, we define the landward limit of the landward ring based on the location of the future grounding line (Section 4.6.2) and current high-SMB coastal regions (Figure 5). The magnitude of grounding line retreat projected by ISMIP6 is highly variable between regions and in many cases retreat projections are based on inadequate bed topography (Figure 25; Section 4.6.2). Therefore, although it is hard to precisely define, we propose to locate the landward limit of the landward ring at the most inland location of the ISMIP6-projected grounding line location for 2100. The projected grounding line location is highly variable between models, so although the ISMIP6 projection is until 2100, the most extreme case can be used as a proxy for future grounding line retreat, such as the projected 2300 retreat position. This landward limit is approximate, and the survey region should be extended further inland in some locations where model projections show relatively consistent, limited retreat in regions with sparse bed topography data (Figure 25). Where no retreat is predicted, we suggest the landward ring should extend at least 10 km from the grounding line or grounded ice front to ensure basal conditions are adequately characterized, as it is possible that missing data may bias the ensemble model. The landward area where SMB is a significant and variable factor is a function of altitude, with higher altitudes showing more limited variability. It is therefore expected that RINGS studies of SMB will focus on lower altitudes (< 1500 m a.s.l.), or higher-altitude regions where ensemble models suggest significant SMB variability persists (Figure 5).

5.3 Seaward ring

The seaward ring primarily concerns the seabed topography under ice shelves, and sea-ice-covered or open ocean up to the continental shelf edge (Figure 7a). In some cases, the seaward ring may extend hundreds of kilometers beyond the current calving front, for example in the Ross Sea and Weddell Sea, or may be located close to the current ice-shelf calving front. Shallow seabed over the continental shelf largely controls ocean circulation that affects ice-ocean interactions, ice-sheet instability, and eventually the evolution of grounding line retreat and future Antarctic contributions to global sea-level rise. In regions with ice shelves, the seaward ring should preferably be located over them to examine ice-ocean interactions there. Overall, it is hard to prioritize a single location for the seaward ring and it is necessary to conduct surveys at multiple seaward ring locations between the grounding line and the continental shelf edge.

The primary science priority for the seaward ring is oceanic melt and refreeze rates under ice shelves (Table 8). Satellite altimetry has been used to map them based on freeboard assumptions. However, in the vicinity of the grounding line, the ice shelves are not often strictly in freeboard (Figure 10), leading to a larger uncertainty. Despite this, oceanic melt is often largest near the grounding line where ice shelves are thickest, meaning ocean water has a higher potential temperature to melt the ice-shelf base (Section 2.7.2). In-situ measurements using ApRES have revealed temporal series of basal melt rates over various timescales from days to years, though such surveys are only at limited locations (Section 3.7.1). To bridge pan-Antarctic satellite-based surveys and local point surveys, airborne surveys are highly useful to map ice thickness, ice-flux divergence, recent SMB and possibly near-surface firn density, all of which are needed to calculate oceanic melt or refreeze rates as residual of the mass balance of ice-shelf columns.

The second science priority is seabed topography, which largely affects ocean circulation driving oceanic melt of ice shelves and future grounding line retreat (Section 3.6.2). Existing seabed topography data are sparse (Figure 21), and current gridded map products smoothly interpolate seabed elevations across unsurveyed regions such as ice shelves and fast ice between multibeam bathymetric data in the open ocean and IPR-measured bed elevations beneath the grounded ice. This often results in shallow, featureless topography. However, surveys clearly indicate that the seabed under ice shelves is much more complicated, including deep troughs that allow the intrusion of CDW (Figure 9). Seabed topography is mainly achieved by gravity inversion using airborne data (Section 3.6.2). A dense and systematic collection of gravity data is therefore essential. In addition, accurate measurements of ice-shelf thickness and detailed geological structures—such as tectonic boundaries, rift systems, and sedimentary basins—are critical because they influence lithospheric density and, consequently, the thickness of the seawater column. Therefore, this science priority requires combined observations and analyses of the IPR and gravity, ideally together with lidar and magnetometer data. Over open ocean or relatively thin or seasonal sea ice regions, it is very useful to have multibeam vessel surveys synchronized with airborne surveys, or to re-occupy existing multibeam profiles by airborne surveys. In this way, gravity and geology are co-solved for seabed topography.

The third science priority is ice-shelf instability and its impact on grounding line positions and their vulnerability. This stems from a combination of the first and secondary science priorities discussed above. However, this question addresses other constraints (Figure 12) and requires data from the primary ring (small-scale bed structure). Roles of small pinning points (ice rumples) remain largely unknown, partly because their detailed topography is yet to be mapped accurately and their roles are largely variable, reflecting various glaciological conditions. Similarly, MISI and MICI instability mechanisms (Figure 11) need to be investigated both with more advanced, detailed surveys and computer models.

5.4 Cross-ring connections and shared challenges

Although each ring has distinct scientific priorities, many are closely related and not exclusive to a single ring. For example, while SMB is the second priority for the landward ring (Section 5.2), SMB over ice shelves is essential for determining ice-shelf mass balance—the top priority for the seaward ring (Section 5.3). Similarly, SMB over ice rises must be assessed independently because the simplified grounding line (proposed for the primary ring) excludes many ice rises (Section 5.1), making their mass balance unaccounted for by ice discharge measurements (Section 4.2). In addition, highly variable SMB in coastal regions (Section 2.4.2) cannot be captured by a single landward ring survey. Therefore, many priorities listed in Table 8 apply across multiple rings and should be considered collectively rather than in isolation.

When a fixed survey resource is available in a region, resources need to balance survey coverage density versus survey extent. Our analysis presented in Section 4.7 indicates that radar surveys of bed topography are needed with 2-4 km or better separations. Currently available resources are inadequate to make such dense surveys in the entire coastal zone around the AIS. Swath, side-looking radar is thus highly useful to extend the lateral coverage of the data and increase the profile separations, yielding a wider coverage of individual surveys. At the same time, urgent action is needed to map bed topography immediately landward of the current grounding line, because once these areas become seabed, only gravity measurements will be possible and they cannot resolve the fine details that radar provides.

Given the uncertainty in Antarctica's near-term contribution to global sea-level rise, prioritizing these surveys is an urgent task.

6. Summary

This review synthesizes current understanding of the Antarctic coastal zone where ice, ocean, atmosphere, and solid Earth interact, and evaluates how limitations in observations and models constrain predictions of Antarctica's future contribution to sea-level rise. Across the continent, rapid but spatially variable changes are underway: accelerated ice discharge, grounding-line retreat, enhanced ice-shelf thinning driven by intrusions of warm Circumpolar Deep Water, and episodic extreme atmospheric events that modulate snowfall and melt. Yet the processes most critical for determining Antarctica's future, such as ice-shelf buttressing, grounding-line dynamics, ice–ocean interactions, marine ice-sheet instability, and subglacial hydrology, remain poorly constrained because the coastal zone is among the least observed regions on Earth.

Our assessment of existing datasets shows that bed and seabed topography—fundamental boundary conditions for all ice-flow and ocean models—remain sparsely mapped along much of the Antarctic margin. Only a small portion of the grounding line lies within a kilometre of modern radar surveys, and cavity geometry beneath ice shelves is well constrained in only a handful of basins. These deficits lead directly to large uncertainties in key diagnostics: ice-discharge estimates can differ by several hundred gigatonnes per year, grounding-line projections vary by tens of kilometres even in the near future, and modeled basal melt rates depend strongly on unresolved sub-ice-shelf bathymetry.

The coastal environment is also strongly modulated by climate variability across multiple timescales. Regional atmospheric modes such as the Southern Annular Mode and Pacific–South American patterns influence snowfall, cloudiness, and surface melt; atmospheric rivers deliver both extreme precipitation and intense melt episodes; and ocean conditions fluctuate on seasonal to decadal scales, altering the delivery of warm water to ice-shelf cavities. The response of the ice sheet to these forcings depends on basal friction, subglacial water routing, sediment distribution, geothermal heat flux, and viscoelastic Earth structure. These are factors that can only be adequately resolved with denser, targeted observations.

To address these fundamental data gaps and enable a step-change in predictive skill, a coordinated, pan-Antarctic airborne geophysical survey framework, **RINGS**, was endorsed by SCAR in 2021 (Figure 13). The strategy is organized around three survey rings that jointly capture the critical processes governing mass loss.

The primary ring, aligned with a simplified grounding-line geometry (Section 4.2), focuses on obtaining high-resolution ice thickness, bed topography, subglacial hydrological pathways, and ice-flow velocity needed to constrain ice discharge and grounding-line stability. This ring directly reduces the dominant uncertainties in current mass-balance estimates and sea-level projections.

The landward ring, positioned tens of kilometres inland, targets basal friction, stress transmission, and the long-term evolution of ice geometry. It also enables spatially resolved mapping of SMB and firn processes in coastal regions, the areas that currently contribute nearly half of Antarctica's total SMB yet remain poorly observed. These data are essential for improving regional climate models, firn densification schemes, and dynamic ice-flow simulations.

The seaward ring, flown over ice shelves, ice rises, and sea ice addresses ocean-driven processes by mapping seabed topography, cavity circulation regimes, oceanic melt and refreezing patterns, pinning points, and fracture-prone zones. These observations are required to evaluate and parameterize ocean models, understand variability in basal melt, and diagnose mechanisms of ice-shelf weakening that can trigger rapid glacier acceleration.

Executing this framework requires integrated deployment of deep- and shallow-sounding radar, lidar, gravimetry, magnetics, electromagnetic sensors, and airborne ocean profilers, together with satellite products, improved numerical models. Although centered on airborne observations, RINGS relies on a broader suite of complimentary datasets collected through ship-based multibeam and hydrographic surveys and multidisciplinary ground-based measurements. Standardized data formats, open access, and adherence to FAIR principles will maximize the scientific return and support machine-learning applications that require large, coherent datasets.

A coordinated RINGS campaign will directly address the most consequential uncertainties in Antarctic sea-level projections. By delivering contiguous, high-quality, circum-Antarctic datasets for bed geometry, ice-shelf cavities, subglacial hydrology, SMB, and ice dynamics, RINGS provides a feasible and transformative path toward a physics-rich, observation-constrained understanding of the Antarctic coastal system.

Acknowledgements

Antarctic RINGS is an initiative supported by the Scientific Committee on Antarctic Research (SCAR) as an action group since 2021, jointly guided by the Physical Sciences Group and the Geo Sciences Group. The Council of Managers of National Antarctic Programs (COMNAP) established the COMNAP RINGS Collaboration Project in 2023 to contribute logistical expertise for efficient survey planning.

This review paper is based on the scientific presentations and discussions from the First International Workshop on Antarctic RINGS, hosted in 2022 by the Norwegian Polar Institute with contributions from SCAR, the Technical University of Denmark, the British Antarctic Survey, and the Research Council of Norway (POLARPROG 329765). We sincerely thank these supporting organizations and the many individuals who have encouraged and contributed to the growth of this large-scale international collaboration.

To the best of our knowledge, a concept similar to RINGS was first discussed at a SCAR logistics meeting in 1967. Since then, numerous attempts have been made to conduct RINGS-like surveys. The current and emerging Antarctic RINGS efforts greatly benefit from the lessons learned from these past initiatives and the robust, coordinated support from SCAR and COMNAP, making this unique collaboration possible.

Figures 1, and 8-13 were developed by Hasan Abbas, which was coordinated by Anna Sinisalo, both at Grid Arendal. Figures 4-6, 8a, 15a, 16, 18, 19, 21, and 23-25 were made using Quantarctica (Matsuoka et al., 2021). The bed elevation simulations presented in Figs. 26 and 27 were performed on resources provided by Sigma2 – the national infrastructure for High-Performance Computing and Data Storage in Norway (project No: NN10061k).

Various supports have been given to individual scientists to contribute to this article, which include: Agencia Estatal de Investigación (AEI) (#PID2020-113051RB-C31 for FN), Alfred Wegener Institute Helmholtz Centre for Polar and Marine Research (for GE), Australian Centre for Excellence in Antarctic Science (for ML, #SR200100008 for LL), Australian Research Council Special Research Initiative (for LL), Australian Research Council (ARC) Special Research Initiative Securing Antarctica's Environmental Future

(#SR200100005 for FSM) and ARC Discovery Early Career Research Award (#DE210101433 for ASM,# DE240100267 for CZ), European Research Council (ERC) (#101164392 for JLB and KS), Danish Government under the National Centre for Climate Research (for FB), Fonds de la recherche scientifique (FRS-FNRS) (for MGC), Deutsche Forschungsgemeinschaft (DFG) (#SE 3109/5-1 for TS), G. Unger Vetlesen Foundation (for DAY), Horizon 2020 Framework Programme (EU Framework Programme for Research and Innovation H2020) #101003472/EC (for JLB), Horizon Europe: OCEAN ICE (#101060452 for RM), Indian Ministry of Earth Sciences (PACER for VG and YR), Institutions of Eminence India (for MP), Jet Propulsion Laboratory, California Institute of Technology, under a contract with the National Aeronautics and Space Administration (80NM0018D0004 for ASG and CAG), Key Laboratory of Airborne Geophysics and Remote Sensing Geology (#2023YFL15 for JY), Korea Institute of Marine Science & Technology (Promotion RS-2023-00256677 for LWS), National Aeronautics and Space Administration (NASA), NASA (#80NSSC22K0387 for JG), NASA Cryospheric Sciences (for JAM and MS), NASA MEaSUREs ITS_LIVE (for AG and CAG), National Institute of Oceanography and Applied Geophysics (for FF), National Natural Science Foundation of China (#42376253 for XC, #42276257 for XT and 42476272 for JY), National Science Foundation (#OPP-2114454 for JG, OPP-2309648 for JG, #1745137 for DMS, #2317097 for RAV, #2303344 for RAV, #2049302 for MRS and HV, #2137099 for HV), Polar Science and Cryosphere (MoES-PACER), Research Council of Norway (FRINATEK #315246 for JA and CS), Natural Environment Research Council (#NE/S006613/1 for RB, #NE/S006621/1 for BK, #NE/R010838/1 for BK, PRESCIENT (for PD), for HP), Natural Environment Research Council Centre for Polar Observation and Modelling (AS, TS, #NE/Y006178/1 for INO), Swedish Research Council (VR) (#2024-04675 for APS), Swiss National Science Foundation (#211542 for JAB), University Parthenope of Naples (ESTRO Project PNRA_18_00258 for NK).

We thank the Editor Yusuke Yokoyama, Reviewer Alan Aitken, and two anonymous reviewers whose comments have improved this article significantly.

Data availability statements

All datasets used for this article are publicly available. Several common datasets are used to produce the figures in this manuscript, including

- Bedmap2 (Fretwell et al., 2013; doi.org/10.5194/tc-7-375-2013, https://secure.antarctica.ac.uk/data/bedmap2/);
- Bedmap3 (Frémand et al., 2023; doi.org/10.5194/essd-15-2695-2023, doi.org/jg6n, doi.org/jg8b);
- BedMachine version 3 (Morlighem, 2022; doi.org/10.5067/FPSU0V1MWUB69);
- ITS_LIVE ice velocity (Gardner et al., 2018; doi.org/10.5194/tc-12-521-2018, https://its-live.jpl.nasa.gov/);
- MEaSUREs ice velocity (doi.org/10.5067/9T4EPQXTJYW9);
- the Reference Elevation Model of Antarctica (Howat, et al., 2019; doi.org/10.5194/tc-13-665-2019, www.pgc.umn.edu/data/rema/);
- Antarctic surface mass balance regional climate model estimates (Mottram et al., 2021; doi.org/10.5194/tc-15-3751-2021, doi.org/10.5281/zenodo.4590263, doi.org/10.5281/zenodo.2539147, ensemblesrt3.dmi.dk/data/prudence/temp/RUM/HIRHAM/ANTARCTICA/ERAI/, doi.org/10.5281/zenodo.5195636).

Source datasets to used to produce additional figures include:

Rignot et al. (2019) ice discharge (doi.org/10.1073/pnas.1812883116, doi.pangaea.de/10.1594/PANGAEA.896940);

Miles et al. (2022) ice discharge (doi.org/10.1038/s41598-022-13517-2, doi.org/10.6075/J04Q7SHT);

Rodriguez-Morales et al. (2013, doi:10.1109/TGRS.2013.2266415);

Open Polar Radar (2023, doi.org/10.5281/zenodo.5683959);

Gardner et al. (2018) doi.org/10.5194/tc-12-521-2018;

Depoorter et al. (2013), doi.org/10.1038/nature12567, doi.org/10.1594/PANGAEA.819151, doi.org/10.1594/PANGAEA.819148, doi.org/10.1594/PANGAEA.819150, doi.org/10.1594/PANGAEA.819147);

Brancato et al. (2020, doi.org/10.1029/2019GL086291, doi.org/10.15146/zf0j-5m50),

Mohajerani et al. (2021, doi.org/10.1038/s41598-021-84309-3, doi.org/10.7280/D1VD6G),

Milillo et al. (2019, doi.org/10.1126/sciadv.aau3433, http://faculty.sites.uci.edu/erignot/data/),

Floricioiu et al. (2021, https://cryoportal.enveo.at/),

Christie et al. (2023, doi.org/10.1038/s41467-022-35471-3, doi.org/10.17863/CAM.90820),

Dawson & Bamber (2020, doi.org/10.5194/tc-14-2071-2020, doi.org/10.5285/40c0b0c6-533c-43e7-9761-38225dac3084),

Wild et al. (2022, doi.org/10.5194/tc-16-397-2022, doi.org/10.15784/601499),

Li. et al. (2022, doi.org/10.1038/s41561-022-00992-5, doi.org/10.5281/zenodo.6611940),

Howat et al. (2019, doi.org/10.5194/tc-13-665-2019, www.pgc.umn.edu/data/rema/),

Dong et al. (2021, doi.org/10.5194/tc-15-4421-2021, geoservice.dlr.de/web/),

Rignot et al. (2011b, doi.org/10.1126/science.1208336),

Rignot et al. (2022, doi.org/10.1029/2022GL100141, nsidc.org/data/nsidc-0761/versions/1),

Matsuoka et al. (2015, doi.org/10.1016/j.earscirev.2015.09.004, data.npolar.no/dataset/9174e644-3540-44e8-b00b-c629acbf1339),

Nøst (2004, doi.org/10.1029/2004JC002277),

Eisermann et al. (2020 and 2021, doi.org/10.1029/2019GL086724, doi.org/10.1029/2021JF006342, https://doi.pangaea.de/10.1594/PANGAEA.913742, doi.org/10.1594/PANGAEA.927545),

Yang et al. (2021, doi.org/10.1029/2021GL096215, doi.org/10.5281/zenodo.5651609),

Greenbaum et al. (2015, doi.org/10.1038/ngeo2388),

Tinto et al. (2019, doi.org/10.1038/s41561-019-0370-2, www.ldeo.columbia.edu/polar-geophysics-group/data.),

Milan et al. (2020, doi.org/10.1029/2019GL086522, doi.org/10.7280/D1XM31), Constantino et al. (2020, doi.org/10.1029/2020GL088654, pgg.ldeo.columbia.edu/data/operation-icebridge, nsidc.org/data/igbth3, nsidc.org/data/igbth4),

Millan et al. (2017, doi.org/10.1002/2016GL072071),

Seroussi et al. (2020, doi.org/10.5194/tc-14-3033-2020, doi.org/10.5281/zenodo.3940766, www.climate-cryosphere.org/wiki/index.php?title=ISMIP6_wiki_page), MacKie et al. (2023, doi.org/10.5194/gmd-16-3765-2023, doi.org/10.5281/zenodo.7274640),

Mälicke et al. (2021, doi.org/10.5281/zenodo.4835779),

Shackleton et al. (2023, doi.org/10.1029/2023JF007269).

Appendix 2 shows all the data generated and presented in this article (Table A2), which are FAIR datasets and downloadable from the Norwegian Polar Data Center (https://data.npolar.no/). Also, we provide QGIS project and style files with which these datasets can be used as “Quantarctica friendly” together with Quantarctica (Matsuoka et al., 2021).

Author contributions

This review is a collective effort by a large international community. The first three authors (KM, GM, and JA) are listed in order of their level of contribution, followed by three author groups, each listed alphabetically within the group based on the relative extent of their contributions.

The first three authors and the most significant contributor group (11 authors) led the conceptualization of the paper through their roles as members of the RINGS Action Group Steering Committee (KM, GM, XC, FF, RF, TJ, FM, KT), and conducted original and in-depth data analysis specifically for this review (KM, GM, JA, JB, VG, RM, HP, CS). They also contributed manuscript writing significantly.

The second group (40 authors) contributed to the manuscript by providing supplementary data analyses, drafting specific sections, or significantly revising earlier drafts by incorporating new perspectives or relevant literature. The third group (27 authors) primarily contributed through detailed reviews and constructive feedback that improved the clarity and completeness of the manuscript during the revision process.

Potential conflict of interest disclosure

The authors declare there are no conflicts of interest for this article.

Appendices

A1 Abbreviation used in this article

Table A1: List of all abbreviations used in this article in their alphabetical order, together with their full names and, where appropriate, sections that describe the term most significantly.

Abbreviation	Definition	Described in Section
AASW	Antarctic surface water	2.7.2
ACC	Antarctic circumpolar current	2.7.1
ADD	Antarctic digital database	4.1
ADMAP	Antarctic digital magnetic anomaly project	3.1.5
AIS	Antarctic Ice Sheet	
ALAMO	Air-launched autonomous micro observer	3.1.7
AMPS	Antarctic mesoscale prediction system	3.2.2
AP	Antarctic Peninsula	

ApRES	Autonomous phase-sensitive radio-echo sounder	3.5.1
ASC	Antarctic slope current	2.7.1
ASF	Antarctic slope front	2.7.1
a.s.l.	above sea level	
ASMA	Antarctic specially managed area	3.2.4
ASPA	Antarctic specially protected area	3.2.4
ATM	Airborne topographic mapper	3.1.3
AUV	Autonomous Underwater Vehicle	3.5.3
AWS	Automatic weather station	2.4.2
AXBT	Airborne expendable bathy-thermograph	3.1.7
AXCTD	Airborne expendable conductivity temperature depth	3.1.7
CDW	Circumpolar deep water	2.7.1
CFM	Community firn model	3.8.4
CMIP6	Coupled model intercomparison project phase 6	3.8.5
COMNAP	Council Of Managers of National Antarctic Program	3.2.3
CSV	Comma separated values (file format)	3.8
DAS	Distributed acoustic sensing	3.5.2
DEM	Digital elevation model	3.7.1
DInSAR	Differential interferometric synthetic aperture radar	3.7.2
DOI	Digital object identifier	
DROMLAN	Dronning Maud Land Air Network	3.2.2
EAIS	East Antarctic Ice Sheet	
ECMWF	European Centre for Medium-Range Weather Forecasts	3.2.2
EM	Geoelectric and electromagnetic	3.1.6
ENSO	El Niño–Southern Oscillation	2.4.1
ERA	ECMWF (European center for medium-range weather forecast) reanalysis	3.8.2
ESM	Earth system model	3.8.1
FAIR	Findable, accessible, interoperable, and reusable	3.9
FDM	Firn densification model	3.8.4
GCM	General circulation model	3.8.1
GEBCO	General Bathymetric Chart of the Ocean	3.6.2
GEMB	Glacier energy and mass balance model	3.8.4
GHF	Geothermal heat flow	2.6.2
GIA	Glacial isostatic adjustment	2.6.1
GNSS	Global navigation satellite system	

GOCE	Gravity field and steady-state ocean circulation explorer	3.7.4
GRACE	Gravity recovery and climate experiment	3.7.4
GRACE-FO	GRACE follow-on	3.7.4
HF	High frequency (3-30 MHz)	
HSSW	High-salinity shelf water	2.7.2
IBCSO	International Bathymetry Chart of the Southern Ocean	3.6.2
ICAO	International Civil Aviation Organization	3.2.3
ICESat-2	Ice, cloud, and land elevation satellite-2	3.7.1
InSAR	Interferometric synthetic aperture radar (SAR)	3.7.2
IPCC	Intergovernmental Panel on Climate Change	2.1.3
IPR	Ice-penetrating radar	3.1.1, 3.1.2
ISMIP6	Ice-sheet model intercomparison project for CMIP6	3.8.5
LIMA	Landsat image mosaic of Antarctica	
MAD	Median absolute deviation	4.7
mCDW	Modified circumpolar deep water	2.7.1
MEaSUREs	Making Earth System Data Records for Use in Research Environments	3.7.1
MICI	Marine ice cliff instability	2.8.4
MISI	Marine ice sheet instability	2.8.4
NetCDF	Network common data form	3.9
NISAR	NASA-ISRO (Indian space research organization) SAR	3.7.2
NWP	Numerical weather prediction	3.8.3
Polar CORDEX	Polar coordinated regional downscaling experiment	3.8.2
PSA	Pacific-South American patterns	2.4.1
RCC	Rescue Coordination Centre	3.2.3
RCM	Regional climate model	2.4.1
RCP	Representative concentration pathway	3.8.5, 4.6.1
REMA	Reference elevation model of Antarctica	3.7.1
RPAS	Remotely piloted aircraft systems	3.4
SAM	Southern Annular Mode	2.4.1
SAR	Synthetic aperture radar	3.7.2
SCAR	Scientific Committee on Antarctic Research	3.2.4
SMB	Surface mass balance	2.4.2
SSP	Shared socio-economic pathway	1
TEM	Transient geoelectric and electromagnetic (Transient EM)	3.1.6
UAS	Uncrewed aerial systems	3.4
UAV	Uncrewed aerial vehicles	3.4

VHF	Very high frequency (30-300 MHz)	
WAIS	West Antarctic Ice Sheet	
WCRP	World climate research programme	4.6.1

A2 Datasets generated in this article

Table A2: Eleven new datasets presented in this article and archived at the Norwegian Polar Data Center (https://data.npolar.no/).

Fig. No.	Dataset title	Data authors	DOI
4	Comparison of recent ice-discharge estimates for 27 drainage basins of the Antarctic Ice Sheet	Mahagaonkar, Arthur, and Matsuoka	doi.org/10.21334/NPOLAR.2025.742D0E9B
5	Modelled Antarctic annual surface mass balance averaged between 1987 and 2015	Arthur, Mottram, Boberg, and Matsuoka	doi.org/10.21334/NPOLAR.2025.75A66608
15	Deep-sounding radargram across Martin Peninsula in the Amundsen Embayment, West Antarctica	Li, Goel, and Matsuoka	doi.org/10.21334/NPOLAR.2025.A8C519F4
17	RINGS/Bedmap3 grounding line	Moholdt, Pritchard, and Maton	doi.org/10.21334/NPOLAR.2025.D1062D2A
18	Simplified Antarctic grounding line for primary ring surveys	Arthur, Moholdt, and Matsuoka	doi.org/10.21334/NPOLAR.2025.8CEC2D20
19, 20	Radar survey and bed elevation data availability in the Antarctic Ice Sheet margin, within 100 km landward from the RINGS/Bedmap3 grounding line	Bodart and Matsuoka	doi.org/10.21334/NPOLAR.2025.ECC09169
21	Seabed topography data availability under Antarctic ice shelves	Liebsch, Tinto, and Matsuoka	doi.org/10.21334/NPOLAR.2025.D6285F9C
23	Comparison of two empirical ice-discharge estimates using Bedmap2 and Bedmachine version 3 bed topography at the primary ring	Moholdt	doi.org/10.21334/NPOLAR.2025.B9AB2794
24	Magnitude and uncertainty of the surface mass balance-correction term of ice discharge at the simplified Antarctic grounding line	Arthur, Mottram, and Matsuoka	doi.org/10.21334/NPOLAR.2025.A4FF8348

25	Projected Antarctic grounding line retreat from the ISMIP6 model ensembles by the end of 2100	Arthur, Seroussi, and Matsuoka	doi.org/10.21334/NPOLAR.2025.8218FFFA
26, 27	Stochastic simulations of bed elevations at the outlet of Recovery Glacier, East Antarctica	Shackleton and Matsuoka	doi.org/10.21334/NPOLAR.2025.879398CD

References

Abdalati, W., Krabill, W., Frederick, E., Manizade, S., Martin, C., Sonntag, J., et al. (2002). Airborne laser altimetry mapping of the Greenland ice sheet. *Journal of Geodynamics*, *34*(3–4), 391–403. https://doi.org/10.1016/S0264-3707(02)00048-0

Adusumilli, S., Fricker, H. A., Medley, B., Padman, L., & Siegfried, M. R. (2020). Interannual variations in meltwater input to the Southern Ocean from Antarctic ice shelves. *Nature Geoscience*, *13*(9), 616–620. https://doi.org/10.1038/s41561-020-0616-z

Agosta, C., Amory, C., Kittel, C., Orsi, A., Favier, V., Gallée, H., et al. (2019). Estimation of the Antarctic surface mass balance using the regional climate model MAR (1979–2015) and identification of dominant processes. *The Cryosphere*, *13*(1), 281–296. https://doi.org/10.5194/tc-13-281-2019

Aitken, A. R. A., Young, D. A., Ferraccioli, F., Betts, P. G., Greenbaum, J. S., Richter, T. G., et al. (2014). The subglacial geology of Wilkes Land, East Antarctica. *Geophysical Research Letters*, *41*(7), 2390–2400. https://doi.org/10.1002/2014GL059405

Aitken, A. R. A., Roberts, J. L., van Ommen, T. D., Young, D. A., Golledge, N. R., Greenbaum, J. S., et al. (2016). Repeated large-scale retreat and advance of Totten Glacier indicated by inland bed erosion. *Nature*, *533*, 385–389. https://doi.org/10.1038/nature17447

Aitken, A. R. A., Ramos, L. N., Roberts, J. L., Greenbaum, J. S., Jong, L. M., Young, D. A., & Blankenship, D. D. (2020). A Magnetic Data Correction Workflow for Sparse, Four-Dimensional Data. *Journal of Geophysical Research: Solid Earth*, *125*(10), e2020JB019825. https://doi.org/10.1029/2020JB019825

Aitken, A. R. A., Li, L., Kulessa, B., Schroeder, D., Jordan, T. A., Whittaker, J. M., et al. (2023). Antarctic Sedimentary Basins and Their Influence on Ice-Sheet Dynamics. *Reviews of Geophysics*, *61*(3), e2021RG000767. https://doi.org/10.1029/2021RG000767

Albert, D. G., & Bentley, C. R. (1990). Seismic Studies on the Grid Eastern Half of the Ross Ice Shelf: RIGGS III and RIGGS IV. In *The Ross Ice Shelf: Glaciology and Geophysics* (pp. 87–108). American Geophysical Union (AGU). https://doi.org/10.1029/AR042p0087

Allen, C., Shi, L., Hale, R., Leuschen, C., Paden, J., Pazer, B., et al. (2012). Antarctic ice depthsounding radar instrumentation for the NASA DC-8. *IEEE Aerospace and*

Electronic Systems Magazine, *27*(3), 4–20. https://doi.org/10.1109/MAES.2012.6196253

Alley, K. E., Scambos, T. A., Siegfried, M. R., & Fricker, H. A. (2016). Impacts of Warm Water on Antarctic Ice Shelf Stability through Basal Channel Formation. *Nat. Geosci.*, *9*, 290–293. https://doi.org/10.1038/ngeo2675

Alley, R. B., Blankenship, D. D., Bentley, C. R., & Rooney, S. T. (1986). Deformation of till beneath ice stream B, West Antarctica. *Nature*, *322*(6074), 57–59. https://doi.org/10.1038/322057a0

Alley, R. B., Anandakrishnan, S., Dupont, T. K., Parizek, B. R., & Pollard, D. (2007). Effect of Sedimentation on Ice-Sheet Grounding-Line Stability. *Science*, *315*(5820), 1838–1841. https://doi.org/10.1126/science.1138396

An, M., Wiens, D. A., Zhao, Y., Feng, M., Nyblade, A., Kanao, M., et al. (2015). Temperature, lithosphere-asthenosphere boundary, and heat flux beneath the Antarctic Plate inferred from seismic velocities. *Journal of Geophysical Research: Solid Earth*, *120*(12), 8720–8742. https://doi.org/10.1002/2015JB011917

Anandakrishnan, S., Blankenship, D. D., Alley, R. B., & Stoffa, P. L. (1998). Influence of subglacial geology on the position of a West Antarctic ice stream from seismic observations. *Nature*, *394*(6688), 62–65. https://doi.org/10.1038/27889

Argyle, M., Ferguson, S., Sander, L., & Sander, S. (2000). AIRGrav results: a comparison of airborne gravity data with GSC test site data. *The Leading Edge*, *19*(10), 1134–1138. https://doi.org/10.1190/1.1438494

Armitage, T. W. K., Kwok, R., Thompson, A. F., & Cunningham, G. (2018). Dynamic Topography and Sea Level Anomalies of the Southern Ocean: Variability and Teleconnections. *Journal of Geophysical Research: Oceans*, *123*(1), 613–630. https://doi.org/10.1002/2017JC013534

Arndt, J. E., Schenke, H. W., Jakobsson, M., Nitsche, F. O., Buys, G., Goleby, B., et al. (2013). The International Bathymetric Chart of the Southern Ocean (IBCSO) Version 1.0-A new bathymetric compilation covering circum-Antarctic waters: IBCSO VERSION 1.0. *Geophysical Research Letters*, *40*(12), 3111–3117. https://doi.org/10.1002/grl.50413

Arnold, E., Rodriguez-Morales, F., Paden, J., Leuschen, C., Keshmiri, S., Yan, S., et al. (2018). HF/VHF Radar Sounding of Ice from Manned and Unmanned Airborne Platforms. *Geosciences*, *8*(5), 182. https://doi.org/10.3390/geosciences8050182

Arnold, E., Leuschen, C., Rodriguez-Morales, F., Li, J., Paden, J., Hale, R., & Keshmiri, S. (2020). CReSIS airborne radars and platforms for ice and snow sounding. *Annals of Glaciology*, *61*(81), 58–67. https://doi.org/10.1017/aog.2019.37

Arthern, R. J., & Gudmundsson, G. H. (2010). Initialization of ice-sheet forecasts viewed as an inverse Robin problem. *Journal of Glaciology*, *56*(197), 527–533. https://doi.org/10.3189/002214310792447699

Arthern, R. J., Winebrenner, D. P., & Vaughan, D. G. (2006). Antarctic snow accumulation mapped using polarization of 4.3-cm wavelength microwave emission. *Journal of Geophysical Research*, *111*(D6), D06107. https://doi.org/10.1029/2004JD005667

Arthern, R. J., J. Corr, H. F., Gillet-Chaulet, F., Hawley, R. L., & Morris, E. M. (2013). Inversion for the density-depth profile of polar firn using a stepped-frequency radar.

Journal of Geophysical Research: Earth Surface, *118*(3), 1257–1263. https://doi.org/10.1002/jgrf.20089

Arthur, J. F., Stokes, C. R., Jamieson, S. S. R., Miles, B. W. J., Carr, J. R., & Leeson, A. A. (2021). The triggers of the disaggregation of Voyeykov Ice Shelf (2007), Wilkes Land, East Antarctica, and its subsequent evolution. *Journal of Glaciology*, *67*(265), 933–951. https://doi.org/10.1017/jog.2021.45

Arthur, J. F., Stokes, C. R., Jamieson, S. S. R., Rachel Carr, J., Leeson, A. A., & Verjans, V. (2022). Large interannual variability in supraglacial lakes around East Antarctica. *Nature Communications*, *13*(1), 1711. https://doi.org/10.1038/s41467-022-29385-3

Arzeno, I. B., Beardsley, R. C., Limeburner, R., Owens, B., Padman, L., Springer, S. R., et al. (2014). Ocean variability contributing to basal melt rate near the ice front of Ross Ice Shelf, Antarctica. *Journal of Geophysical Research: Oceans*, *119*(7), 4214–4233. https://doi.org/10.1002/2014JC009792

Asay-Davis, X. S., Cornford, S. L., Durand, G., Galton-Fenzi, B. K., Gladstone, R. M., Gudmundsson, G. H., et al. (2016). Experimental design for three interrelated marine ice sheet and ocean model intercomparison projects: MISMIP v. 3 (MISMIP +), ISOMIP v. 2 (ISOMIP +) and MISOMIP v. 1 (MISOMIP1). *Geoscientific Model Development*, *9*(7), 2471–2497. https://doi.org/10.5194/gmd-9-2471-2016

Ashmore, D. W., & Bingham, R. G. (2014). Antarctic subglacial hydrology: current knowledge and future challenges. *Antarctic Science*, *26*(6), 758–773. https://doi.org/10.1017/S0954102014000546

ATCPs (Antarctic Treaty Consultative Parties), 2004. Resolution 2 (2004): Guidelines for the operation of aircraft near concentrations of birds in Antarctica. *Final Report of the XXVII Antarctic Treaty Consultative Meeting*, Cape Town, South Africa, 24 May– 4 June 2004

ATCPs (Antarctic Treaty Consultative Parties), 2006. Resolution 4 (2016): Non-native Species Manual. *Final Report of the XXXIX Antarctic Treaty Consultative Meeting*, Santiago, Chile, 23 May-1 June 2016

Aulicino, G., Fusco, G., Kern, S., & Budillon, G. (2014). Estimation of Sea-Ice Thickness in Ross and Weddell Seas from SSM/I Brightness Temperatures. *IEEE Transactions on Geoscience and Remote Sensing*, *52*(7), 4122–4140. https://doi.org/10.1109/TGRS.2013.2279799

Aulicino, G., Sansiviero, M., Paul, S., Cesarano, C., Fusco, G., Wadhams, P., & Budillon, G. (2018). A New Approach for Monitoring the Terra Nova Bay Polynya through MODIS Ice Surface Temperature Imagery and Its Validation during 2010 and 2011 Winter Seasons. *Remote Sensing*, *10*(3), 366. https://doi.org/10.3390/rs10030366

Austermann, J., & Forte, A. M. (2019). The importance of dynamic topography for understanding past sea-level changes. *Past Global Changes Magazine*, *27*(1). https://doi.org/10.22498/pages.27.1.18

Austermann, J., Pollard, D., Mitrovica, J. X., Moucha, R., Forte, A. M., DeConto, R. M., et al. (2015). The impact of dynamic topography change on Antarctic ice sheet stability during the mid-Pliocene warm period. *Geology*, *43*(10), 927–930. https://doi.org/10.1130/G36988.1

Bamber, J.L., Vaughan, D. G., & Joughin, I. (2000). Widespread complex flow in the interior of the Antarctic Ice Sheet. *Science*, *287*, 1248–1250. https://doi.org/10.1126/science.287.5456.1248

Bamber, Jonathan L, Westaway, R. M., Marzeion, B., & Wouters, B. (2018). The land ice contribution to sea level during the satellite era. *Environmental Research Letters*, *13*(6), 063008. https://doi.org/10.1088/1748-9326/aac2f0

Banwell, A. F., Wever, N., Dunmire, D., & Picard, G. (2023). Quantifying Antarctic-Wide Ice-Shelf Surface Melt Volume Using Microwave and Firn Model Data: 1980 to 2021. *Geophysical Research Letters*, 50(12), e2023GL102744. https://doi.org/10.1029/2023GL102744

Barker, L. D. L., Jakuba, M. V., Bowen, A. D., German, C. R., Maksym, T., Mayer, L., et al. (2020). Scientific Challenges and Present Capabilities in Underwater Robotic Vehicle Design and Navigation for Oceanographic Exploration Under-Ice. *Remote Sensing*, *12*(16), 2588. https://doi.org/10.3390/rs12162588

Barletta, V. R., Bevis, M., Smith, B. E., Wilson, T., Brown, A., Bordoni, A., et al. (2018). Observed rapid bedrock uplift in Amundsen Sea Embayment promotes ice-sheet stability. *Science*, *360*(6395), 1335–1339. https://doi.org/10.1126/science.aao1447

Barnes, J. M., Dias dos Santos, T., Goldberg, D., Gudmundsson, G. H., Morlighem, M., & De Rydt, J. (2021). The transferability of adjoint inversion products between different ice flow models. *The Cryosphere*, *15*(4), 1975–2000. https://doi.org/10.5194/tc-15-1975-2021

Bars, D. L., Drijfhout, S., & Vries, H. de. (2017). A high-end sea level rise probabilistic projection including rapid Antarctic ice sheet mass loss. *Environmental Research Letters*, *12*(4), 044013. https://doi.org/10.1088/1748-9326/aa6512

Bartelt, P., & Lehning, M. (2002). A physical SNOWPACK model for the Swiss avalanche warning: Part I: numerical model. *Cold Regions Science and Technology*, *35*, 123–145. https://doi.org/10.1016/S0165-232X(02)00074-5

Barthel, A., Agosta, C., Little, C. M., Hattermann, T., Jourdain, N. C., Goelzer, H., et al. (2020). CMIP5 model selection for ISMIP6 ice sheet model forcing: Greenland and Antarctica. *The Cryosphere*, *14*(3), 855–879. https://doi.org/10.5194/tc-14-855-2020

Bassis, J. N., & Ma, Y. (2015). Evolution of basal crevasses links ice shelf stability to ocean forcing. *Earth and Planetary Science Letters*, *409*, 203–211. https://doi.org/10.1016/j.epsl.2014.11.003

Bassis, J. N., Berg, B., Crawford, A. J., & Benn, D. I. (2021). Transition to marine ice cliff instability controlled by ice thickness gradients and velocity. *Science*, *372*(6548), 1342–1344. https://doi.org/10.1126/science.abf6271

Batchelor, Christine L., Christie, F. D. W., Ottesen, D., Montelli, A., Evans, J., Dowdeswell, E. K., et al. (2023). Rapid, buoyancy-driven ice-sheet retreat of hundreds of metres per day. *Nature*, *617*(7959), 105–110. https://doi.org/10.1038/s41586-023-05876-1

Batchelor, C.L., & Dowdeswell, J. A. (2015). Ice-sheet grounding-zone wedges (GZWs) on high-latitude continental margins. *Marine Geology*, *363*, 65–92. https://doi.org/10.1016/j.margeo.2015.02.001

Baumgartner, M. F., J. Bonnell, P. Corkeron, S. M. Van Parijs, C. Hotchkin, B. A. Hodges, and S. M. Bruner (2020), Slocum gliders provide accurate near–real-time estimates of baleen whale presence from human-reviewed passive acoustic detection information, *Front. Mar. Sci.*, 7, 100, https://doi.org/10.3389/fmars.2020.00100.

Beadling, R. L., Russell, J. L., Stouffer, R. J., Mazloff, M., Talley, L. D., Goodman, P. J., et al. (2020). Representation of Southern Ocean Properties across Coupled Model Intercomparison Project Generations: CMIP3 to CMIP6. *Journal of Climate*, *33*(15), 6555–6581. https://doi.org/10.1175/JCLI-D-19-0970.1

Beaumet, J., Déqué, M., Krinner, G., Agosta, C., Alias, A., & Favier, V. (2021). Significant additional Antarctic warming in atmospheric bias-corrected ARPEGE projections with respect to control run. *The Cryosphere*, *15*(8), 3615–3635. https://doi.org/10.5194/tc-15-3615-2021

Bebieva, Y., & Speer, K. (2021). Thermohaline Suppression of Upper Circumpolar Deep Water Eddies in the Ross Gyre. *Geophysical Research Letters*, *48*(18). https://doi.org/10.1029/2021GL094476

Behrendt, J. C. (2013). The aeromagnetic method as a tool to identify Cenozoic magmatism in the West Antarctic Rift System beneath the West Antarctic Ice Sheet — A review; Thiel subglacial volcano as possible source of the ash layer in the WAISCORE. *Tectonophysics*, *585*, 124–136. https://doi.org/10.1016/j.tecto.2012.06.035

Bell, R. E. (2008). The role of subglacial water in ice-sheet mass balance. *Nature Geoscience*, *1*(5), 297–304. https://doi.org/10.1038/ngeo186

Bell, R. E., Blankenship, D. D., Finn, C. A., Morse, D. L., Scambos, T. A., Brozena, J. M., & Hodge, S. M. (1998). Influence of subglacial geology on the onset of a West Antarctic ice stream from aerogeophysical observations. *Nature*, *394*(6688), 58–62. https://doi.org/10.1038/27883

Bell, R. E., Ferraccioli, F., Creyts, T. T., Braaten, D., Corr, H., Das, I., et al. (2011). Widespread Persistent Thickening of the East Antarctic Ice Sheet by Freezing from the Base. *Science*, *331*(6024), 1592–1595. https://doi.org/10.1126/science.1200109

Bell, Robin E., Chu, W., Kingslake, J., Das, I., Tedesco, M., Tinto, K. J., et al. (2017). Antarctic ice shelf potentially stabilized by export of meltwater in surface river. *Nature*, *544*(7650), 344–348. https://doi.org/10.1038/nature22048

Bell, Robin E., Banwell, A. F., Trusel, L. D., & Kingslake, J. (2018). Antarctic surface hydrology and impacts on ice-sheet mass balance. *Nature Climate Change*, *8*(12), 1044–1052. https://doi.org/10.1038/s41558-018-0326-3

Bentley, M. J., Ó Cofaigh, C., Anderson, J. B., Conway, H., Davies, B., Graham, A. G. C., et al. (2014). A community-based geological reconstruction of Antarctic Ice Sheet deglaciation since the Last Glacial Maximum. *Quaternary Science Reviews*, *100*, 1–9. https://doi.org/10.1016/j.quascirev.2014.06.025

Bergamasco, A., Defendi, V., Zambianchi, E., & Spezie, G. (2002). Evidence of dense water overflow on the Ross Sea shelf-break. *Antarctic Science*, *14*(3), 271–277. https://doi.org/10.1017/S0954102002000068

Berthier, E., Scambos, T. A., & Shuman, C. A. (2012). Mass loss of Larsen B tributary glaciers (Antarctic Peninsula) unabated since 2002. *Geophysical Research Letters*, *39*(13). https://doi.org/10.1029/2012GL051755

Bertler, N. A. N., Conway, H., Dahl-Jensen, D., Emanuelsson, D. B., Winstrup, M., Vallelonga, P. T., et al. (2018). The Ross Sea Dipole – temperature, snow accumulation and sea ice variability in the Ross Sea region, Antarctica, over the past 2700 years. *Climate of the Past*, *14*(2), 193–214. https://doi.org/10.5194/cp-14-193-2018

Bett, D. T., Holland, P. R., Naveira Garabato, A. C., Jenkins, A., Dutrieux, P., Kimura, S., & Fleming, A. (2020). The Impact of the Amundsen Sea Freshwater Balance on Ocean Melting of the West Antarctic Ice Sheet. *Journal of Geophysical Research: Oceans*, *125*(9). https://doi.org/10.1029/2020JC016305

Bhardwaj, A., Sam, L., Akanksha, Martín-Torres, F. J., & Kumar, R. (2016). UAVs as remote sensing platform in glaciology: Present applications and future prospects. *Remote Sensing of Environment*, *175*, 196–204. https://doi.org/10.1016/j.rse.2015.12.029

Biddle, L. C., Heywood, K. J., Kaiser, J., & Jenkins, A. (2017). Glacial Meltwater Identification in the Amundsen Sea. *Journal of Physical Oceanography*, *47*(4), 933–954. https://doi.org/10.1175/JPO-D-16-0221.1

Bidel, Y., Zahzam, N., Bresson, A., Blanchard, C., Bonnin, A., Bernard, J., et al. (2023). Airborne Absolute Gravimetry With a Quantum Sensor, Comparison With Classical Technologies. *Journal of Geophysical Research: Solid Earth*, *128*(4), e2022JB025921. https://doi.org/10.1029/2022JB025921

Bindschadler, R., Vornberger, P., Fleming, A., Fox, A., Mullins, J., Binnie, D., Paulsen, S.J., Granneman, B. and Gorodetzky, D., 2008. The Landsat image mosaic of Antarctica. *Remote Sensing of Environment*, 112(12), doi.org/10.1016/j.rse.2008.07.006

Bindschadler, R., Choi, H., Wichlacz, A., Bingham, R., Bohlander, J., Brunt, K., et al. (2011). Getting around Antarctica: new high-resolution mappings of the grounded and freely-floating boundaries of the Antarctic ice sheet created for the International Polar Year. *The Cryosphere*, *5*(3), 569–588. https://doi.org/10.5194/tc-5-569-2011

Bingham, R. G., & Siegert, M. J. (2007). Radio-Echo Sounding Over Polar Ice Masses. *Journal of Environmental and Engineering Geophysics*, *12*(1), 47–62. https://doi.org/10.2113/JEEG12.1.47

Bingham, R. G., Ferraccioli, F., King, E. C., Larter, R. D., Pritchard, H. D., Smith, A. M., & Vaughan, D. G. (2012). Inland thinning of West Antarctic Ice Sheet steered along subglacial rifts. *Nature*, *487*(7408), 468–471. https://doi.org/10.1038/nature11292

Bingham, R. G., Bodart, J. A., Cavitte, M. G. P., Chung, A., Sanderson, R. J., Sutter, J. C. R., et al. (2025). Review article: AntArchitecture – building an age–depth model from Antarctica's radiostratigraphy to explore ice-sheet evolution. *The Cryosphere*, *19*(10), 4611–4655. https://doi.org/10.5194/tc-19-4611-2025

Bintanja, R. (1999). On the glaciological, meteorological, and climatological significance of Antarctic blue ice areas. *Reviews of Geophysics*, *37*(3), 337–359. https://doi.org/10.1029/1999RG900007

Blankenship, D. D., Bell, R. E., Hodge, S. M., Brozena, J. M., Behrendt, J. C., & Finn, C. A. (1993). Active volcanism beneath the West Antarctic ice sheet and implications for ice-sheet stability. *Nature*, *361*(6412), 526–529. https://doi.org/10.1038/361526a0

Blankenship, D. D., Morse, D. L., Finn, C. A., Bell, R. E., Peters, M. E., Kempf, S. D., et al. (2001). Geologic Controls on the Initiation of Rapid Basal Motion for West Antarctic Ice Streams: A Geophysical Perspective Including New Airborne Radar Sounding and Laser Altimetry Results. In *The West Antarctic Ice Sheet: Behavior and Environment* (pp. 105–121). American Geophysical Union (AGU). https://doi.org/10.1029/AR077p0105

Bodart, J. A., Bingham, R. G., Young, D. A., MacGregor, J. A., Ashmore, D. W., Quartini, E., et al. (2023). High mid-Holocene accumulation rates over West Antarctica inferred from a pervasive ice-penetrating radar reflector. *The Cryosphere*, *17*(4), 1497–1512. https://doi.org/10.5194/tc-17-1497-2023

Boening, C., Lebsock, M., Landerer, F., & Stephens, G. (2012). Snowfall-driven mass change on the East Antarctic ice sheet. *Geophysical Research Letters*, *39*(21), n/a-n/a. https://doi.org/10.1029/2012GL053316

Boger, S. D. (2011). Antarctica — Before and after Gondwana. *Gondwana Research*, *19*(2), 335–371. https://doi.org/10.1016/j.gr.2010.09.003

Boghosian, A. L., Pitcher, L. H., Smith, L. C., Kosh, E., Alexander, P. M., Tedesco, M., & Bell, R. E. (2021). Development of ice-shelf estuaries promotes fractures and calving. *Nature Geoscience*, *14*(12), 899–905. https://doi.org/10.1038/s41561-021-00837-7

Bons, P. D., de Riese, T., Franke, S., Llorens, M.-G., Sachau, T., Stoll, N., et al. (2021). Comment on “Exceptionally high heat flux needed to sustain the Northeast Greenland Ice Stream” by Smith-Johnsen et al. (2020). *The Cryosphere*, *15*(5), 2251–2254. https://doi.org/10.5194/tc-15-2251-2021

Bougamont, M., Price, S., Christoffersen, P., & Payne, A. J. (2011). Dynamic patterns of ice stream flow in a 3-D higher-order ice sheet model with plastic bed and simplified hydrology. *Journal of Geophysical Research*, *116*(F4), F04018. https://doi.org/10.1029/2011JF002025

Bougamont, M., Christoffersen, P., Price, S. F., Fricker, H. A., Tulaczyk, S., & Carter, S. P. (2015). Reactivation of Kamb Ice Stream tributaries triggers century-scale reorganization of Siple Coast ice flow in West Antarctica. *Geophysical Research Letters*, *42*(20), 8471–8480. https://doi.org/10.1002/2015GL065782

Boxall, K., Christie, F. D. W., Willis, I. C., Wuite, J., & Nagler, T. (2022). Seasonal land-ice-flow variability in the Antarctic Peninsula. *The Cryosphere*, *16*(10), 3907–3932. https://doi.org/10.5194/tc-16-3907-2022

Bozkurt, D., Bromwich, D. H., Carrasco, J., Hines, K. M., Maureira, J. C., & Rondanelli, R. (2020). Recent Near-surface Temperature Trends in the Antarctic Peninsula from Observed, Reanalysis and Regional Climate Model Data. *Advances in Atmospheric Sciences*, *37*(5), 477–493. https://doi.org/10.1007/s00376-020-9183-x

Bozzo, E., Ferraccioli, F., Gambetta, M., Caneva, G., Spano, M., Chiappini, M., & Damaske, D. (1999). Recent progress in magnetic anomaly mapping over Victoria Land (Antarctica) and the GITARA 5 survey. *Antarctic Science*, *11*(2), 209–216. https://doi.org/10.1017/S0954102099000279

Bracegirdle, T. J., Holmes, C. R., Hosking, J. S., Marshall, G. J., Osman, M., Patterson, M., & Rackow, T. (2020). Improvements in Circumpolar Southern Hemisphere Extratropical Atmospheric Circulation in CMIP6 Compared to CMIP5. *Earth and Space Science*, *7*(6). https://doi.org/10.1029/2019EA001065

Bradford, J. H., Harper, J. T., & Brown, J. (2009). Complex dielectric permittivity measurements from ground-penetrating radar data to estimate snow liquid water content in the pendular regime. *Water Resources Research*, *45*(8). https://doi.org/10.1029/2008WR007341

Brancato, V., Rignot, E., Milillo, P., Morlighem, M., Mouginot, J., An, L., et al. (2020). Grounding Line Retreat of Denman Glacier, East Antarctica, Measured With COSMO-SkyMed Radar Interferometry Data. *Geophysical Research Letters*, *47*(7), e2019GL086291. https://doi.org/10.1029/2019GL086291

Braun, J. (2010). The many surface expressions of mantle dynamics. *Nature Geoscience*, *3*(12), 825–833. https://doi.org/10.1038/ngeo1020

Brinkerhoff, D. J., & Johnson, J. V. (2015). Dynamics of thermally induced ice streams simulated with a higher-order flow model. *Journal of Geophysical Research: Earth Surface*, *120*(9), 1743–1770. https://doi.org/10.1002/2015JF003499

Brisbourne, A., Kulessa, B., Hudson, T., Harrison, L., Holland, P., Luckman, A., et al. (2020). An updated seabed bathymetry beneath Larsen C Ice Shelf, Antarctic Peninsula. *Earth System Science Data*, *12*(2), 887–896. https://doi.org/10.5194/essd-12-887-2020

Brisbourne, A. M., Kendall, M., Kufner, S.-K., Hudson, T. S., & Smith, A. M. (2021). Downhole distributed acoustic seismic profiling at Skytrain Ice Rise, West Antarctica. *The Cryosphere*, *15*(7), 3443–3458. https://doi.org/10.5194/tc-15-3443-2021

Brondex, J., Gagliardini, O., Gillet-Chaulet, F., & Durand, G. (2017). Sensitivity of grounding line dynamics to the choice of the friction law. *Journal of Glaciology*, *63*(241), 854–866. https://doi.org/10.1017/jog.2017.51

Brondex, J., Gillet-Chaulet, F., & Gagliardini, O. (2019). Sensitivity of centennial mass loss projections of the Amundsen basin to the friction law. *The Cryosphere*, *13*(1), 177–195. https://doi.org/10.5194/tc-13-177-2019

Brozena, J. M. (1992). The Greenland Aerogeophysics Project: Airborne Gravity, Topographic and Magnetic Mapping of an Entire Continent. In O. L. Colombo (Ed.), *From Mars to Greenland: Charting Gravity With Space and Airborne Instruments* (Vol. 110, pp. 203–214). New York, NY: Springer New York. https://doi.org/10.1007/978-1-4613-9255-2_19

Budd, W. F., & Jacka, T. H. (1989). A review of ice rheology for ice sheet modelling. *Cold Regions Science and Technology*, *16*(2), 107–144. https://doi.org/10.1016/0165-232X(89)90014-1

Budillon, G., Fusco, G., & Spezie, G. (2000). A study of surface heat fluxes in the Ross Sea (Antarctica). *Antarctic Science*, *12*(2), 243–254. https://doi.org/10.1017/S0954102000000298

Budillon, G., Castagno, P., Aliani, S., Spezie, G., & Padman, L. (2011). Thermohaline variability and Antarctic bottom water formation at the Ross Sea shelf break. *Deep Sea Research Part I: Oceanographic Research Papers*, *58*(10), 1002–1018. https://doi.org/10.1016/j.dsr.2011.07.002

Burgard, C., Jourdain, N. C., Mosbeux, C., Caillet, J., Mathiot, P., & Kittel, C. (2025). Ocean warming threatens the viability of 60% of Antarctic ice shelves. *Nature*, 647(8088), 102–108. https://doi.org/10.1038/s41586-025-09657-w

Burton-Johnson, A., Halpin, J. A., Whittaker, J. M., Graham, F. S., & Watson, S. J. (2017). A new heat flux model for the Antarctic Peninsula incorporating spatially variable upper crustal radiogenic heat production. *Geophysical Research Letters*, *44*(11), 5436–5446. https://doi.org/10.1002/2017GL073596

Burton-Johnson, A., Dziadek, R., & Martin, C. (2020). Review article: Geothermal heat flow in Antarctica: current and future directions. *The Cryosphere*, *14*(11), 3843–3873. https://doi.org/10.5194/tc-14-3843-2020

Butler, H., Daly, M., Doyle, A., Gillies, S., Schaub, T., & Hagen, S. (2016). *The GeoJSON Format* (Request for Comments No. RFC 7946). Internet Engineering Task Force. Retrieved from https://datatracker.ietf.org/doc/rfc7946/

Byers, K. J., Harish, A. R., Seguin, S. A., Leuschen, C. J., Rodriguez-Morales, F., Paden, J., et al. (2012). A Modified Wideband Dipole Antenna for an Airborne VHF Ice-Penetrating Radar. *IEEE Transactions on Instrumentation and Measurement*, *61*(5), 1435–1444. https://doi.org/10.1109/TIM.2011.2181780

Camus, L., H. Andrade, A. S. Aniceto, M. Aune, K. Bandara, S. L. Basedow, K. H. Christensen, J. Cook, M. Daase, and K. Dunlop (2021), Autonomous surface and underwater vehicles as effective ecosystem monitoring and research platforms in the Arctic—The Glider Project, *Sensors*, 21, 6752, https://doi.org/10.3390/s21206752.

Cairns, G.J., Benham, G.P. and Hewitt, I.J., 2025. Groundwater dynamics beneath a marine ice sheet. The Cryosphere, 19(9), pp.3725-3747. https://doi.org/10.5194/tc-19-3725-2025

Caron, L., & Ivins, E. R. (2020). A baseline Antarctic GIA correction for space gravimetry. *Earth and Planetary Science Letters*, *531*, 115957. https://doi.org/10.1016/j.epsl.2019.115957

Carrivick, J. L., Davies, B. J., James, W. H. M., McMillan, M., & Glasser, N. F. (2019). A comparison of modelled ice thickness and volume across the entire Antarctic Peninsula region. *Geografiska Annaler: Series A, Physical Geography*, *101*(1), 45–67. https://doi.org/10.1080/04353676.2018.1539830

Carter, J., Leeson, A., Orr, A., Kittel, C., & van Wessem, J. M. (2022). Variability in Antarctic surface climatology across regional climate models and reanalysis datasets. *The Cryosphere*, *16*(9), 3815–3841. https://doi.org/10.5194/tc-16-3815-2022

Castagno, P., Falco, P., Dinniman, M. S., Spezie, G., & Budillon, G. (2017). Temporal variability of the Circumpolar Deep Water inflow onto the Ross Sea continental shelf. *Journal of Marine Systems*, *166*, 37–49. https://doi.org/10.1016/j.jmarsys.2016.05.006

Castagno, P., Capozzi, V., DiTullio, G. R., Falco, P., Fusco, G., Rintoul, S. R., et al. (2019). Rebound of shelf water salinity in the Ross Sea. *Nature Communications*, *10*(1), 5441. https://doi.org/10.1038/s41467-019-13083-8

Castleman, B. A., Schlegel, N.-J., Caron, L., Larour, E., & Khazendar, A. (2022). Derivation of bedrock topography measurement requirements for the reduction of uncertainty in ice-sheet model projections of Thwaites Glacier. *The Cryosphere*, *16*(3), 761–778. https://doi.org/10.5194/tc-16-761-2022

Caton Harrison, T., Biri, S., Bracegirdle, T. J., King, J. C., Kent, E. C., Vignon, É., & Turner, J. (2022). Reanalysis representation of low-level winds in the Antarctic near-coastal region. *Weather and Climate Dynamics*, *3*(4), 1415–1437. https://doi.org/10.5194/wcd-3-1415-2022

Cavitte, M. G. P., Blankenship, D. D., Young, D. A., Schroeder, D. M., Parrenin, F., Lemeur, E., et al. (2016). Deep radiostratigraphy of the East Antarctic plateau: connecting the Dome C and Vostok ice core sites. *Journal of Glaciology*, *62*(232), 323–334. https://doi.org/10.1017/jog.2016.11

Cavitte, M. G. P., Goosse, H., Wauthy, S., Kausch, T., Tison, J.-L., Liefferinge, B. V., et al. (2022). From ice core to ground-penetrating radar: representativeness of SMB at three ice rises along the Princess Ragnhild Coast, East Antarctica. *Journal of Glaciology*, *68*(272), 1221–1233. https://doi.org/10.1017/jog.2022.39

Cavitte, M. G. P., Goosse, H., Matsuoka, K., Wauthy, S., Goel, V., Dey, R., et al. (2023). Investigating the spatial representativeness of Antarctic ice cores: A comparison of ice core and radar-derived surface mass balance. *The Cryosphere Discussions*, 1–24. https://doi.org/10.5194/tc-2023-65

Cavitte, M. G. P., Goosse, H., Dalaiden, Q., & Ghilain, N. (2025). Brief communication: Annual variability of the atmospheric circulation at large spatial scale reconstructed from a data assimilation framework cannot explain local East Antarctic ice rises' surface mass balance records. *The Cryosphere*, 19, 6483–6492. https://doi.org/10.5194/tc-19-6483-2025

Chan, K. (2022). Mapping ice in firn with airborne ice-penetrating radar. *Nature Reviews Earth & Environment*, *3*(5), 291–291. https://doi.org/10.1038/s43017-022-00290-z

Chartrand, A. M., & Howat, I. M. (2020). Basal Channel Evolution on the Getz Ice Shelf, West Antarctica. *Journal of Geophysical Research: Earth Surface*, *125*(9). https://doi.org/10.1029/2019JF005293

Chartrand, Allison M., & Howat, I. M. (2023). A comparison of contemporaneous airborne altimetry and ice-thickness measurements of Antarctic ice shelves. *Journal of Glaciology*, 1–14. https://doi.org/10.1017/jog.2023.49

Charrassin, R., Millan, R., Rignot, E., & Scheinert, M. (2025). Bathymetry of the Antarctic continental shelf and ice shelf cavities from circumpolar gravity anomalies and other data. *Scientific Reports*, 15(1), 1214. https://doi.org/10.1038/s41598-024-81599-1

Chen, H., Rignot, E., Scheuchl, B., & Ehrenfeucht, S. (2023). Grounding Zone of Amery Ice Shelf, Antarctica, From Differential Synthetic-Aperture Radar Interferometry. *Geophysical Research Letters*, *50*(6), e2022GL102430. https://doi.org/10.1029/2022GL102430

Chen, J. L., Wilson, C. R., Li, J., & Zhang, Z. (2015). Reducing leakage error in GRACE-observed long-term ice mass change: a case study in West Antarctica. *Journal of Geodesy*, *89*(9), 925–940. https://doi.org/10.1007/s00190-015-0824-2

Chen, Z., Bromirski, P. D., Gerstoft, P., Stephen, R. A., Lee, W. S., Yun, S., et al. (2019). Ross Ice Shelf Icequakes Associated With Ocean Gravity Wave Activity. *Geophysical Research Letters*, *46*(15), 8893–8902. https://doi.org/10.1029/2019GL084123

Chilton, M. (2004). *Antarctic Aviation: Accidents and Safety Policy*. University of Canterbury. http://hdl.handle.net/10092/13999

Chown, S. L., Lee, J. E., Hughes, K. A., Barnes, J., Barrett, P. J., Bergstrom, D. M., et al. (2012). Challenges to the Future Conservation of the Antarctic. *Science*, *337*(6091), 158–159. https://doi.org/10.1126/science.1222821

Christiansen, B. (2020). Understanding the Distribution of Multimodel Ensembles. *Journal of Climate*, *33*(21), 9447–9465. https://doi.org/10.1175/JCLI-D-20-0186.1

Christianson, K., Jacobel, R. W., Horgan, H. J., Alley, R. B., Anandakrishnan, S., Holland, D. M., & DallaSanta, K. J. (2016). Basal conditions at the grounding zone of Whillans

Ice Stream, West Antarctica, from ice-penetrating radar. *Journal of Geophysical Research: Earth Surface*, *121*(11), 1954–1983. https://doi.org/10.1002/2015JF003806

Christie, F. D. W., Bingham, R. G., Gourmelen, N., Tett, S. F. B., & Muto, A. (2016). Four-decade record of pervasive grounding line retreat along the Bellingshausen margin of West Antarctica. *Geophysical Research Letters*, *43*(11), 5741–5749. https://doi.org/10.1002/2016GL068972

Christie, F. D. W., Steig, E. J., Gourmelen, N., Tett, S. F. B., & Bingham, R. G. (2023). Inter-decadal climate variability induces differential ice response along Pacific-facing West Antarctica. *Nature Communications*, *14*(1), 93. https://doi.org/10.1038/s41467-022-35471-3

Christoffersen, P., Bougamont, M., Carter, S.P., Fricker, H.A. and Tulaczyk, S., 2014. Significant groundwater contribution to Antarctic ice streams hydrologic budget. *Geophysical Research Letters*, 41(6), 2003-2010, https://doi.org/10.1002/2014GL059250

Chu, W., Hilger, A. M., Culberg, R., Schroeder, D. M., Jordan, T. M., Seroussi, H., et al. (2021). Multisystem Synthesis of Radar Sounding Observations of the Amundsen Sea Sector From the 2004–2005 Field Season. *Journal of Geophysical Research: Earth Surface*, *126*(10), e2021JF006296. https://doi.org/10.1029/2021JF006296

Church, J. A., Monselesan, D., Gregory, J. M., & Marzeion, B. (2013). Evaluating the ability of process based models to project sea-level change. *Environmental Research Letters*, *8*(1), 014051. https://doi.org/10.1088/1748-9326/8/1/014051

Clarke, G. (2005). Subglacial processes. *Annu. Rev. Earth Planet. Sci.*, *33*, 247–276. https://doi.org/10.1146/annurev.earth.33.092203.122621

Clerc, F., Minchew, B. M., & Behn, M. D. (2019). Marine Ice Cliff Instability Mitigated by Slow Removal of Ice Shelves. *Geophysical Research Letters*, *46*(21), 12108–12116. https://doi.org/10.1029/2019GL084183

Cochran, J. R., & Bell, R. E. (2012). Inversion of IceBridge gravity data for continental shelf bathymetry beneath the Larsen Ice Shelf, Antarctica. *Journal of Glaciology*, *58*(209), 540–552. https://doi.org/10.3189/2012JoG11J033

Colgan, W., MacGregor, J. A., Mankoff, K. D., Haagenson, R., Rajaram, H., Martos, Y. M., et al. (2021). Topographic Correction of Geothermal Heat Flux in Greenland and Antarctica. *Journal of Geophysical Research: Earth Surface*, *126*(2). https://doi.org/10.1029/2020JF005598

Colomb, A., Cammas, B., Linden, E., Heymes, G., Kreitz, M., & Gourand, F. (2022). Coup de chaud en Antarctique Est. *La Météorologie*, (117), 085. https://doi.org/10.37053/lameteorologie-2022-0045

Comeau, D., Asay‐Davis, X.S., Begeman, C.B., Hoffman, M.J., Lin, W., Petersen, M.R., Price, S.F., Roberts, A.F., Van Roekel, L.P., Veneziani, M. and Wolfe, J.D., 2022. The DOE E3SM v1. 2 cryosphere configuration: Description and simulated Antarctic ice‐shelf basal melting. *Journal of Advances in Modeling Earth Systems*, 14(2), p.e2021MS002468, https://doi.org/10.1029/2021MS002468

Committee on the Decadal Survey for Earth Science and Applications from Space, Space Studies Board, Division on Engineering and Physical Sciences, & National Academies of Sciences, Engineering, and Medicine. (2018). *Thriving on Our*

Changing Planet: A Decadal Strategy for Earth Observation from Space (p. 24938). Washington, D.C.: National Academies Press. https://doi.org/10.17226/24938

Constantino, R.R., Tinto, K.J., Bell, R.E., Porter, D.F. and Jordan, T.A., 2020. Seafloor depth of George VI Sound, Antarctic Peninsula, from inversion of aerogravity data. *Geophysical Research Letters*, 47(21), p.e2020GL088654, https://doi.org/10.1029/2020GL088654

Cook, A. J., Holland, P. R., Meredith, M. P., Murray, T., Luckman, A., & Vaughan, D. G. (2016). Ocean forcing of glacier retreat in the western Antarctic Peninsula. *Science*, *353*(6296), 283–286. https://doi.org/10.1126/science.aae0017

Cook, S., Nicholls, K. W., Vaňková, I., Thompson, S. S., & Galton-Fenzi, B. K. (2023). Data initiatives for ocean-driven melt of Antarctic ice shelves. *Annals of Glaciology*, 1–6. https://doi.org/10.1017/aog.2023.6

Cooper, M. G., Smith, L. C., Rennermalm, A. K., Tedesco, M., Muthyala, R., Leidman, S. Z., et al. (2021). Spectral attenuation coefficients from measurements of light transmission in bare ice on the Greenland Ice Sheet. *The Cryosphere*, *15*(4), 1931–1953. https://doi.org/10.5194/tc-15-1931-2021

Cornford, S. L., Martin, D. F., Payne, A. J., Ng, E. G., Le Brocq, A. M., Gladstone, R. M., et al. (2015). Century-scale simulations of the response of the West Antarctic Ice Sheet to a warming climate. *The Cryosphere*, *9*(4), 1579–1600. https://doi.org/10.5194/tc-9-1579-2015

Cornford, S. L., Martin, D. F., Lee, V., Payne, A. J., & Ng, E. G. (2016). Adaptive mesh refinement versus subgrid friction interpolation in simulations of Antarctic ice dynamics. *Annals of Glaciology*, *57*(73), 1–9. https://doi.org/10.1017/aog.2016.13

Cornford, Stephen L., Martin, D. F., Graves, D. T., Ranken, D. F., Le Brocq, A. M., Gladstone, R. M., et al. (2013). Adaptive mesh, finite volume modeling of marine ice sheets. *Journal of Computational Physics*, *232*(1), 529–549. https://doi.org/10.1016/j.jcp.2012.08.037

Cornford, Stephen L., Seroussi, H., Xylar S Asay-Davis, G. Hilmar Gudmundsson, Arthern, R., Borstad, C., et al. (2020). Supplementary data for “Results of the third Marine Ice Sheet Model Intercomparison Project (MISMIP+)” (Version TC accepted) [Data set]. Zenodo. https://doi.org/10.5281/ZENODO.3611935

Corr, H., Robinson, C., Jordan, T., Nicholls, K., & Brisbourne, A. (2021). Processed bed elevation picks from airborne radar depth sounding from the FISS 2016 survey covering the Filchner and Halley Ice Shelves (2016/2017) (Version 1.0) [Data set]. NERC EDS UK Polar Data Centre. https://doi.org/10.5285/e7851bba-21ff-4645-b557-d8eafdf89462

Cox, S.C., Smith Lyttle, B., Elkind, S., Smith Siddoway, C., Morin, P., Capponi, G., Abu-Alam, T., Ballinger, M., Bamber, L., Kitchener, B. and Lelli, L., 2023. A continent-wide detailed geological map dataset of Antarctica. *Scientific Data*, 10(1), https://doi.org/10.1038/s41597-023-02152-9

CReSIS. 2024. Open Polar Server [computer software], Lawrence, Kansas, USA. Retrieved from https://github.com/CReSIS/.

Crosta, X., Etourneau, J., Orme, L. C., Dalaiden, Q., Campagne, P., Swingedouw, D., et al. (2021). Multi-decadal trends in Antarctic sea-ice extent driven by ENSO–SAM over the last 2,000 years. *Nature Geoscience*, *14*(3), 156–160. https://doi.org/10.1038/s41561-021-00697-1

Culberg, R., Schroeder, D. M., & Chu, W. (2021). Extreme melt season ice layers reduce firn permeability across Greenland. *Nature Communications*, *12*(1), 2336. https://doi.org/10.1038/s41467-021-22656-5

Culberg, R., Schroeder, D. M., & Steinbrügge, G. (2022). Double ridge formation over shallow water sills on Jupiter's moon Europa. *Nature Communications*, *13*(1), 2007. https://doi.org/10.1038/s41467-022-29458-3

Dalaiden, Q., Goosse, H., Lenaerts, J. T. M., Cavitte, M. G. P., & Henderson, N. (2020). Future Antarctic snow accumulation trend is dominated by atmospheric synoptic-scale events. *Communications Earth & Environment*, *1*(1), 62. https://doi.org/10.1038/s43247-020-00062-x

Dalaiden, Q., Schurer, A. P., Kirchmeier-Young, M. C., Goosse, H., & Hegerl, G. C. (2022). West Antarctic Surface Climate Changes Since the Mid-20th Century Driven by Anthropogenic Forcing. *Geophysical Research Letters*, *49*(16). https://doi.org/10.1029/2022GL099543

Damaske, D., Ferraccioli, F., & Bozzo, E. (2003). Aeromagnetic anomaly investigations along the Antarctic coast between Yule Bay and Mertz Glacier. *Terra Antartica*, *10*, 85–96, https://hdl.handle.net/20.500.14083/27215

Damiani, T. M., Jordan, T. A., Ferraccioli, F., Young, D. A., & Blankenship, D. D. (2014). Variable crustal thickness beneath Thwaites Glacier revealed from airborne gravimetry, possible implications for geothermal heat flux in West Antarctica. *Earth and Planetary Science Letters*, *407*, 109–122. https://doi.org/10.1016/j.epsl.2014.09.023

Daniels, Mike; de La Beaujardière, J-F; Downs, Robert R.; Fulker, Dave; Hills, Denise J.; Jacobs, Gwen; Jha, Shantenu; Jones, Matt; Kinkade, Danie; Kuehn, Steve; Schreiber, Lynne; Walker, Doug; Cramer, Catherine (2022). EarthCube Sustainability Panel Report. In EarthCube Organization Materials. UC San Diego Library Digital Collections. https://doi.org/10.6075/J0CR5TJF

Das, I., Padman, L., Bell, R. E., Fricker, H. A., Tinto, K. J., Hulbe, C. L., et al. (2020). Multidecadal Basal Melt Rates and Structure of the Ross Ice Shelf, Antarctica, Using Airborne Ice Penetrating Radar. *Journal of Geophysical Research: Earth Surface*, *125*(3). https://doi.org/10.1029/2019JF005241

Datta, R. T., Herrington, A., Lenaerts, J. T. M., Schneider, D., Yin, Z., & Dunmire, D. (2022a). *Evaluating the Impact of Enhanced Horizontal Resolution over the Antarctic Domain Using a Variable-Resolution Earth Systems Model* (preprint). Ice sheets/Antarctic. https://doi.org/10.5194/egusphere-2022-1311

Datta, R. T., Herrington, A., Lenaerts, J., Schneider, D., Yin, Z., & Dunmire, D. (2022b). Evaluating the Impact of Enhanced Horizontal Resolution over the Antarctic Domain Using a Variable-Resolution Earth Systems Model. *The Cryosphere*, 17(9) 3847-3866, https://doi.org/10.5194/tc-17-3847-2023

Dattler, M. E., Lenaerts, J. T. M., & Medley, B. (2019). Significant Spatial Variability in Radar-Derived West Antarctic Accumulation Linked to Surface Winds and Topography. *Geophysical Research Letters*, *46*(22), 13126–13134. https://doi.org/10.1029/2019GL085363

Davies, D. R., Valentine, A. P., Kramer, S. C., Rawlinson, N., Hoggard, M. J., Eakin, C. M., & Wilson, C. R. (2019). Earth's multi-scale topographic response to global mantle flow. *Nature Geoscience*, *12*(10), 845–850. https://doi.org/10.1038/s41561-019-0441-4

Davis, C. H., Li, Y., McConnell, J. R., Frey, M. M., & Hanna, E. (2005). Snowfall-Driven Growth in East Antarctic Ice Sheet Mitigates Recent Sea-Level Rise. *Science*, *308*(5730), 1898–1901. https://doi.org/10.1126/science.1110662

Davison, B. J., Cowton, T. R., Cottier, F. R., & Sole, A. J. (2020). Iceberg melting substantially modifies oceanic heat flux towards a major Greenlandic tidewater glacier. *Nature Communications*, *11*(1), 5983. https://doi.org/10.1038/s41467-020-19805-7

Davrinche, C., Orsi, A., Amory, C., Kittel, C. and Agosta, C. (2025). Future changes in Antarctic near-surface winds: regional variability and key drivers under a high-emission scenario. *The Cryosphere*, 19(11), 6023-6042. https://doi.org/10.5194/tc-19-6023-2025.

Dawson, E. J., Schroeder, D. M., Chu, W., Mantelli, E., & Seroussi, H. (2022). Ice mass loss sensitivity to the Antarctic ice sheet basal thermal state. *Nature Communications*, *13*(1), 4957. https://doi.org/10.1038/s41467-022-32632-2

Dawson, G. J., & Bamber, J. L. (2020). Measuring the location and width of the Antarctic grounding zone using CryoSat-2. *The Cryosphere*, *14*(6), 2071–2086. https://doi.org/10.5194/tc-14-2071-2020

Deb, P., Orr, A., Hosking, J.S., Phillips, T., Turner, J., Bannister, D., Pope, J.O. and Colwell, S., 2016. An assessment of the Polar Weather Research and Forecasting (WRF) model representation of near - surface meteorological variables over West Antarctica. *Journal of Geophysical Research: Atmospheres*, 121(4), 1532-1548, https://doi.org/10.1002/2015JD024037

DeConto, R. M., & Pollard, D. (2003). Rapid Cenozoic glaciation of Antarctica induced by declining atmospheric CO2. *Nature*, *421*(6920), 245–249. https://doi.org/10.1038/nature01290

DeConto, R. M., & Pollard, D. (2016). Contribution of Antarctica to past and future sea-level rise. *Nature*, *531*(7596), 591–597. https://doi.org/10.1038/nature17145

DeConto, R. M., Pollard, D., Alley, R. B., Velicogna, I., Gasson, E., Gomez, N., et al. (2021). The Paris Climate Agreement and future sea-level rise from Antarctica. *Nature*, *593*(7857), 83–89.

Delaunay, X., Courtois, A., & Gouillon, F. (2019). Evaluation of lossless and lossy algorithms for the compression of scientific datasets in netCDF-4 or HDF5 files. *Geoscientific Model Development*, *12*(9), 4099–4113. https://doi.org/10.5194/gmd-12-4099-2019

Depoorter, M. A., Bamber, J. L., Griggs, J. A., Lenaerts, J. T. M., Ligtenberg, S. R. M., van den Broeke, M. R., & Moholdt, G. (2013). Calving fluxes and basal melt rates of Antarctic ice shelves. *Nature*, *502*(7469), 89–92. https://doi.org/10.1038/nature12567

de Roda Husman, S., Lhermitte, S., Bolibar, J., Izeboud, M., Hu, Z., Shukla, S., et al. (2024). A high-resolution record of surface melt on Antarctic ice shelves using multi-source remote sensing data and deep learning. *Remote Sensing of Environment*, 301, 113950. https://doi.org/10.1016/j.rse.2023.113950

Derkacheva, A., Gillet-Chaulet, F., Mouginot, J., Jager, E., Maier, N., & Cook, S. (2021). Seasonal evolution of basal environment conditions of Russell sector, West Greenland, inverted from satellite observation of surface flow. *The Cryosphere*, *15*(12), 5675–5704. https://doi.org/10.5194/tc-15-5675-2021

Deutsch, C., & Journel, A. (1997). *GSLIB: Geostatistical Software Library and User's Guide* (2nd ed.). New York: Oxford University Press.

Ding, Q., Steig, E. J., Battisti, D. S., & Küttel, M. (2011). Winter warming in West Antarctica caused by central tropical Pacific warming. *Nature Geoscience*, *4*(6), 398–403. https://doi.org/10.1038/ngeo1129

Dinniman, M. S., Asay-Davis, X. S., Galton-Fenzi, B. K., Holland, P. R., Jenkins, A., & Timmermann, R. (2016). Modeling ice shelf/ocean interaction in Antarctica: A review. *Oceanography*, *29*(4), 144–153, https://www.jstor.org/stable/24862289

Dirscherl, M., Dietz, A. J., Dech, S., & Kuenzer, C. (2020). Remote sensing of ice motion in Antarctica – A review. *Remote Sensing of Environment*, *237*, 111595. https://doi.org/10.1016/j.rse.2019.111595

Domack, E., D. Duran, A. Leventer, S. Ishman, S. Doane, S. McCallum, D. Amblas, J. Ring, R. Gilbert, and M. Prentice (2005), Stability of the Larsen B ice shelf on the Antarctic Peninsula during the Holocene epoch, *Nature*, *436*, 681–685, https://doi.org/10.1038/nature03908.

Dong, Y., Zhao, J., Floricioiu, D., Krieger, L., Fritz, T., & Eineder, M. (2021). High-resolution topography of the Antarctic Peninsula combining the TanDEM-X DEM and Reference Elevation Model of Antarctica (REMA) mosaic. *The Cryosphere*, *15*(9), 4421–4443. https://doi.org/10.5194/tc-15-4421-2021

Dorschel, B., Hehemann, L., Viquerat, S., Warnke, F., Dreutter, S., Tenberge, Y. S., et al. (2022). The International Bathymetric Chart of the Southern Ocean Version 2. *Scientific Data*, *9*(1), 275. https://doi.org/10.1038/s41597-022-01366-7

Doury, A., Somot, S., Gadat, S., Ribes, A., & Corre, L. (2023). Regional climate model emulator based on deep learning: concept and first evaluation of a novel hybrid downscaling approach. *Climate Dynamics*, *60*(5), 1751–1779. https://doi.org/10.1007/s00382-022-06343-9

Dow, C. F., McCormack, F., Young, D., Greenbaum, J., Roberts, J., & Blankenship, D. (2020). Totten Glacier subglacial hydrology determined from geophysics and modeling. *Earth and Planetary Science Letters*, *531*, 115961. https://doi.org/10.1016/j.epsl.2019.115961

Dow, C. F., Ross, N., Jeofry, H., Siu, K., & Siegert, M. J. (2022). Antarctic basal environment shaped by high-pressure flow through a subglacial river system. *Nature Geoscience*, *15*(11), 892–898. https://doi.org/10.1038/s41561-022-01059-1

Dow, Christine F. (2023). The role of subglacial hydrology in Antarctic ice sheet dynamics and stability: a modelling perspective. *Annals of Glaciology*, 1–6. https://doi.org/10.1017/aog.2023.9

Dowdeswell, J. A., Batchelor, C. L., Montelli, A., Ottesen, D., Christie, F. D. W., Dowdeswell, E. K., & Evans, J. (2020). Delicate seafloor landforms reveal past Antarctic grounding-line retreat of kilometers per year. *Science*, *368*(6494), 1020–1024. https://doi.org/10.1126/science.aaz3059

Drewry, D. J. (Ed.). (1983). *Antarctica: Glaciological and Geophysical Folio*. Cambridge: Scott Polar Research Institute, University of Cambridge. ISBN 0901021040 / 9780901021045.

Drewry, D. J. (2023). *The Land Beneath the Ice*. Retrieved from https://press.princeton.edu/books/hardcover/9780691237916/the-land-beneath-the-ice

Drews, R., Pattyn, F., Hewitt, I. J., Ng, F. S. L., Berger, S., Matsuoka, K., et al. (2017). Actively evolving subglacial conduits and eskers initiate ice shelf channels at an Antarctic grounding line. *Nature Communications*, *8*(1), 15228. https://doi.org/10.1038/ncomms15228

Drews, Reinhard, Brown, J., Matsuoka, K., Witrant, E., Philippe, M., Hubbard, B., & Pattyn, F. (2016). Constraining variable density of ice shelves using wide-angle radar measurements. *The Cryosphere*, *10*(2), 811–823. https://doi.org/10.5194/tc-10-811-2016

Dunmire, D., Lenaerts, J. T. M., Datta, R. T., & Gorte, T. (2022). Antarctic surface climate and surface mass balance in the Community Earth System Model version 2 during the satellite era and into the future (1979–2100). *The Cryosphere*, *16*(10), 4163–4184. https://doi.org/10.5194/tc-16-4163-2022

Durand, G., Gagliardini, O., de Fleurian, B., Zwinger, T., & Le Meur, E. (2009). Marine ice sheet dynamics: Hysteresis and neutral equilibrium. *Journal of Geophysical Research: Earth Surface*, *114*(F3). https://doi.org/10.1029/2008JF001170

Durand, G., Gagliardini, O., Favier, L., Zwinger, T., & le Meur, E. (2011). Impact of bedrock description on modeling ice sheet dynamics. *Geophysical Research Letters*, *38*(20), n/a-n/a. https://doi.org/10.1029/2011GL048892

Dutrieux, P., Stewart, C., Jenkins, A., Nicholls, K. W., Corr, H. F. J., Rignot, E., & Steffen, K. (2014). Basal terraces on melting ice shelves *Geophysical Research Letters*, *41*(15), 5506–5513. https://doi.org/10.1002/2014GL060618

Dutrieux, P., De Rydt, J., Jenkins, A., Holland, P. R., Ha, H. K., Lee, S. H., et al. (2014). Strong Sensitivity of Pine Island Ice-Shelf Melting to Climatic Variability. *Science*, *343*(6167), 174–178. https://doi.org/10.1126/science.1244341

Dziadek, R., Ferraccioli, F., & Gohl, K. (2021). High geothermal heat flow beneath Thwaites Glacier in West Antarctica inferred from aeromagnetic data. *Communications Earth & Environment*, *2*(1), 162. https://doi.org/10.1038/s43247-021-00242-3

Eagles, G., & Jokat, W. (2014). Tectonic reconstructions for paleobathymetry in Drake Passage. *Tectonophysics*, *611*, 28–50. https://doi.org/10.1016/j.tecto.2013.11.021

Eagles, G., Karlsson, N. B., Ruppel, A., Steinhage, D., Jokat, W., & Läufer, A. (2018). Erosion at extended continental margins: Insights from new aerogeophysical data in eastern Dronning Maud Land. *Gondwana Research*, *63*, 105–116. https://doi.org/10.1016/j.gr.2018.05.011

Eayrs, C., Holland, D., Francis, D., Wagner, T., Kumar, R., & Li, X. (2019). Understanding the Seasonal Cycle of Antarctic Sea Ice Extent in the Context of Longer-Term Variability. *Reviews of Geophysics*, *57*(3), 1037–1064. https://doi.org/10.1029/2018RG000631

Eayrs, C., Li, X., Raphael, M. N., & Holland, D. M. (2021). Rapid decline in Antarctic sea ice in recent years hints at future change. *Nature Geoscience*, *14*(7), 460–464. https://doi.org/10.1038/s41561-021-00768-3

Ebbing, J., Haas, P., Ferraccioli, F., Pappa, F., Szwillus, W., & Bouman, J. (2018). Earth tectonics as seen by GOCE - Enhanced satellite gravity gradient imaging. *Scientific Reports*, *8*(1), 16356. https://doi.org/10.1038/s41598-018-34733-9

Edwards, T. L., Brandon, M. A., Durand, G., Edwards, N. R., Golledge, N. R., Holden, P. B., et al. (2019). Revisiting Antarctic Ice Loss Due to Marine Ice-Cliff Instability. *Nature*, *566*(7742), 58. https://doi.org/10.1038/s41586-019-0901-4

Edwards, T. L., Nowicki, S., Marzeion, B., Hock, R., Goelzer, H., Seroussi, H., et al. (2021). Projected land ice contributions to twenty-first-century sea level rise. *Nature*, *593*(7857), 74–82. https://doi.org/10.1038/s41586-021-03302-y

Eerola, K., (2013) Twenty-one years of verification from the HIRLAM NWP system. *Weather and forecasting*, 28(1), 270-285. https://doi.org/10.1175/WAF-D-12-00068.1

Egholm, D. L., Jansen, J. D., Brædstrup, C. F., Pedersen, V. K., Andersen, J. L., Ugelvig, S. V., et al. (2017). Formation of plateau landscapes on glaciated continental margins. *Nature Geoscience*, *10*(8), 592–597. https://doi.org/10.1038/ngeo2980

Ehrenfeucht, S., Dow, C., McArthur, K., Morlighem, M., & McCormack, F. S. (2025). Antarctic Wide Subglacial Hydrology Modeling. *Geophysical Research Letters*, 52(1), e2024GL111386. https://doi.org/10.1029/2024GL111386

Eisen, O., Nixdorf, U., Wilhelms, F., & Miller, H. (2002). Electromagnetic wave speed in polar ice: validation of the common-midpoint technique with high-resolution dielectric-profiling and γ-density measurements. *Annals of Glaciology*, *34*, 150–156. https://doi.org/10.3189/172756402781817509

Eisen, Olaf, Frezzotti, M., Genthon, C., Isaksson, E., Magand, O., Van Den Broeke, M. R., et al. (2008). Ground-based measurements of spatial and temporal variability of snow accumulation in East Antarctica. *Reviews of Geophysics*, *46*(2), RG2001. https://doi.org/10.1029/2006RG000218

Eisen, Olaf, Hofstede, C., Diez, A., Kristoffersen, Y., Lambrecht, A., Mayer, C., et al. (2015). On-ice vibroseis and snowstreamer systems for geoscientific research. *Polar Science*, *9*(1), 51–65. https://doi.org/10.1016/j.polar.2014.10.003

Eisen, Olaf, Winter, A., Steinhage, D., Kleiner, T., & Humbert, A. (2020). Basal roughness of the East Antarctic Ice Sheet in relation to flow speed and basal thermal state. *Annals of Glaciology*, *61*(81), 162–175. https://doi.org/10.1017/aog.2020.47

Eisermann, H., Eagles, G., Ruppel, A., Smith, E. C., & Jokat, W. (2020). Bathymetry Beneath Ice Shelves of Western Dronning Maud Land, East Antarctica, and Implications on Ice Shelf Stability. *Geophysical Research Letters*, *47*(12). https://doi.org/10.1029/2019GL086724

Eisermann, H., Eagles, G., Ruppel, A.S., Läufer, A. and Jokat, W., 2021. Bathymetric control on Borchgrevink and Roi Baudouin ice shelves in East Antarctica. *Journal of Geophysical Research: Earth Surface*, 126(10), p.e2021JF006342, https://doi.org/10.1029/2021JF006342

Evans, D. J. A., Phillips, E. R., Hiemstra, J. F., & Auton, C. A. (2006). Subglacial till: Formation, sedimentary characteristics and classification. *Earth-Science Reviews*, *78*(1), 115–176. https://doi.org/10.1016/j.earscirev.2006.04.001

Fair, Z., Flanner, M., Neumann, T., Vuyovich, C., Smith, B., & Schneider, A. (2024). Quantifying volumetric scattering bias in ICESat-2 and Operation IceBridge altimetry over Greenland firn and aged snow. *Earth and Space Science*, 11(6), e2022EA002479. https://doi.org/10.1029/2022EA002479

Falco, P., & Zambianchi, E. (2011). Near-surface structure of the Antarctic Circumpolar Current derived from World Ocean Circulation Experiment drifter data. *Journal of Geophysical Research*, *116*(C5), C05003. https://doi.org/10.1029/2010JC006349

Falco, P., Krauzig, N., Castagno, P., Garzia, A., Martellucci, R., Cotroneo, Y., Flocco, D., Menna, M., Pirro, A., Mauri, E., Memmola, F., Solidoro, C., Pacciaroni, M., Notarstefano, G., Budillon, G., & Zambianchi, E. (2024). Winter thermohaline evolution along and below the Ross Ice Shelf. *Nature Communications*, 15, 10581. https://doi.org/10.1038/s41467-024-54751-8

Favier, L., Durand, G., Cornford, S. L., Gudmundsson, G. H., Gagliardini, O., Gillet-Chaulet, F., et al. (2014). Retreat of Pine Island Glacier controlled by marine ice-sheet instability. *Nature Climate Change*, *4*(2), 117–121. https://doi.org/10.1038/nclimate2094

Favier, V., Agosta, C., Parouty, S., Durand, G., Delaygue, G., Gallée, H., et al. (2013). An updated and quality controlled surface mass balance dataset for Antarctica. *The Cryosphere*, *7*(2), 583–597. https://doi.org/10.5194/tc-7-583-2013

Fernández Villanueva, E. and Shaffer, G. (2025). Presentation, calibration and testing of the DCESS II Earth system model of intermediate complexity (version 1.0). *Geoscientific Model Development*, 18(7), 2161-2192. https://doi.org/10.5194/gmd-18-2161-2025.

Ferraccioli, F., Jones, P. C., Curtis, M. L., & Leat, P. T. (2005). Subglacial imprints of early Gondwana break-up as identified from high resolution aerogeophysical data over western Dronning Maud Land, East Antarctica. *Terra Nova*, *17*(6), 573–579. https://doi.org/10.1111/j.1365-3121.2005.00651.x

Ferraccioli, Fausto, Gambetta, M., & Bozzo, E. (1998). Microlevelling procedures applied to regional aeromagnetic data: an example from the Transantarctic Mountains (Antarctica). *Geophysical Prospecting*, *46*(2), 177–196. https://doi.org/10.1046/j.1365-2478.1998.00080.x

Ferraccioli, Fausto, Armadillo, E., Jordan, T., Bozzo, E., & Corr, H. (2009). Aeromagnetic exploration over the East Antarctic Ice Sheet: A new view of the Wilkes Subglacial Basin. *Tectonophysics*, *478*(1–2), 62–77. https://doi.org/10.1016/j.tecto.2009.03.013

Ferraccioli, Fausto, Finn, C. A., Jordan, T. A., Bell, R. E., Anderson, L. M., & Damaske, D. (2011). East Antarctic rifting triggers uplift of the Gamburtsev Mountains. *Nature*, *479*(7373), 388–392. https://doi.org/10.1038/nature10566

Fischer, H., Severinghaus, J., Brook, E., Wolff, E., Albert, M., Alemany, O., et al. (2013). Where to find 1.5 million yr old ice for the IPICS "'Oldest-Ice'" ice core. *Clim. Past*.

Fitzgerald, P. G. (1992). The Transantarctic Mountains of southern Victoria Land: The application of apatite fission track analysis to a rift shoulder uplift. *Tectonics*, *11*(3), 634–662. https://doi.org/10.1029/91TC02495

Fitzgerald, P. G., & Goodge, J. W. (2022). Exhumation and tectonic history of inaccessible subglacial interior East Antarctica from thermochronology on glacial erratics. *Nature Communications*, *13*(1), 6217. https://doi.org/10.1038/s41467-022-33791-y

Flato, G. M. (2011). Earth system models: an overview. *WIREs Climate Change*, *2*(6), 783–800. https://doi.org/10.1002/wcc.148

Floricioiu, D., Krieger, L., Chowdhury, T. A., & Bässler, M. (2021). *ESA Antarctic Ice Sheet Climate Change Initiative (Antarctic_Ice_Sheet_cci): Grounding line location for key glaciers, Antarctica, 1994–2020, v2.0*. NERC EDS Centre for Environmental Data Analysis. https://catalogue.ceda.ac.uk/uuid/7b3bddd5af4945c2ac508a6d25537f0a

Fogt, R. L., & Marshall, G. J. (2020). The Southern Annular Mode: Variability, trends, and climate impacts across the Southern Hemisphere. *WIREs Climate Change*, *11*(4). https://doi.org/10.1002/wcc.652

Fogt, R. L., Sleinkofer, A. M., Raphael, M. N., & Handcock, M. S. (2022). A regime shift in seasonal total Antarctic sea ice extent in the twentieth century. *Nature Climate Change*, *12*(1), 54–62. https://doi.org/10.1038/s41558-021-01254-9

Foley, N., Tulaczyk, S., Auken, E., Schamper, C., Dugan, H., Mikucki, J., et al. (2016). Helicopter-borne transient electromagnetics in high-latitude environments: An application in the McMurdo Dry Valleys, Antarctica. *Geophsyics*, *81*(1), WA87–WA99. https://doi.org/10.1190/geo2015-0186.1

Foley, N., Tulaczyk, S. M., Grombacher, D., Doran, P. T., Mikucki, J., Myers, K. F., et al. (2019). Evidence for Pathways of Concentrated Submarine Groundwater Discharge in East Antarctica from Helicopter-Borne Electrical Resistivity Measurements. *Hydrology*, *6*(2), 54. https://doi.org/10.3390/hydrology6020054

Forsberg, R., Olesen, A. V., Ferraccioli, F., Jordan, T. A., Matsuoka, K., Zakrajsek, A., et al. (2018). Exploring the Recovery Lakes region and interior Dronning Maud Land, East Antarctica, with airborne gravity, magnetic and radar measurements. *Geological Society, London, Special Publications*, *461*(1), 23–34. https://doi.org/10.1144/SP461.17

Fowler, A. C. (1986). Sub-Temperate Basal Sliding. *Journal of Glaciology*, *32*(110), 3–5. https://doi.org/10.3189/S0022143000006808

Fox, M., Clinger, A., Smith, A. G., Cuffey, K., Shuster, D., & Herman, F. (2024) Antarctic Peninsula glaciation patterns set by landscape evolution and dynamic topography. *Nature Geoscience*, 17(1), 73-78. https://doi.org/10.1038/s41561-023-01336-7

Fox-Kemper, B., Hewitt, H. T., Xiao, C., Aoalgeirsdottir, G., Drijfhout, S. S., Edwards, T. L., et al. (2021). Chapter 9: Ocean, Cryosphere and Sea Level Change. In V. Masson-Delmotte, P. Zhai, A. Pirani, S. L. Connors, C. Pean, S. Berger, et al. (Eds.), *Climate Change 2021: The Physical Science Basis. Contribution of Working Group I to the Sixth Assessment Report of the Intergovernmental Panel on Climate Change*. Cambridge University Press, Cambridge, United Kingdom and New York, NY, USA. https://doi.org/10.1017/9781009157896.011

Franke, S., M. Wolovick, R. Drews, D. Jansen, K. Matsuoka, and P. D. Bons (2024), Sediment freeze-on and transport near the onset of a fast-flowing glacier in East Antarctica, *Geophys. Res. Lett.*, 51, e2023GL107164, https://doi.org/10.1029/2023GL107164.

Franke, S., Steinhage, D., Helm, V., Binder, T., Nixdorf, U., Miller, H., Humbert, A., Jansen, D., Eagles, G., Eisermann, H., Jokat, W., Ruppel, A., Drews, R., Zuhr, A., Driemel, A., Walter, A., Konopatzky, P., Heß, R., Haas, A., Koppe, R., Andreas, P. H., & Eisen, O. (2025). 30 years of airborne radar surveys on the Antarctic and Greenland ice sheets by the Alfred Wegener Institute. *The Cryosphere* (in review). https://doi.org/10.5194/egusphere-2025-5328

Freeland, H. J., Roemmich, D., Garzoli, S. L., Le Traon, P.-Y., Ravichandran, M., Riser, S., et al. (2010). ARGO - a decade of progress. Presented at the OceanObs'09: Sustained Ocean Observations and Information for Society (Vol. 2), Venice, Italy, 21-25 September 2009. Retrieved from https://archimer.ifremer.fr/doc/00029/14038/

Frémand, A. C., Bodart, J. A., Jordan, T. A., Ferraccioli, F., Robinson, C., Corr, H. F. J., et al. (2022). British Antarctic Survey's aerogeophysical data: releasing 25 years of airborne gravity, magnetic, and radar datasets over Antarctica. *Earth System Science Data*, *14*(7), 3379–3410. https://doi.org/10.5194/essd-14-3379-2022

Frémand, A. C., Fretwell, P., Bodart, J. A., Pritchard, H. D., Aitken, A., Bamber, J. L., et al. (2023). Antarctic Bedmap data: Findable, Accessible, Interoperable, and Reusable (FAIR) sharing of 60 years of ice bed, surface, and thickness data. *Earth System Science Data*, *15*(7), 2695–2710. https://doi.org/10.5194/essd-15-2695-2023

Fretwell, P., Pritchard, H. D., Vaughan, D. G., Bamber, J. L., Barrand, N. E., Bell, R., et al. (2013). Bedmap2: improved ice bed, surface and thickness datasets for Antarctica. *The Cryosphere*, *7*(1), 375–393. https://doi.org/10.5194/tc-7-375-2013

Fricker, H.A., Allison, I., Craven, M., Hyland, G., Ruddell, A., Young, N., Coleman, R., King, M., Krebs, K. and Popov, S., 2002. Redefinition of the Amery ice shelf, East Antarctica, grounding zone. *Journal of Geophysical Research: Solid Earth*, 107(B5), pp.ECV-1. https://doi.org/10.1029/2001JB000383

Fricker, H. A., & Padman, L. (2006). Ice shelf grounding zone structure from ICESat laser altimetry. *Geophysical Research Letters*, *33*(15). https://doi.org/10.1029/2006GL026907

Fricker, H. A., Scambos, T., Bindschadler, R., & Padman, L. (2007). An active subglacial water system in West Antarctica mapped from space. *Science*, *315*, 1544–1548. https://doi.org/10.1126/science.1136897

Fricker, H. A., Scambos, T., Carter, S., Davis, C., Haran, T., & Joughin, I. (2010). Synthesizing multiple remote-sensing techniques for subglacial hydrologic mapping: application to a lake system beneath MacAyeal Ice Stream, West Antarctica. *Journal of Glaciology*, *56*(196), 187–199. https://doi.org/10.3189/002214310791968557

Fricker, H. A., Siegfried, M. R., Carter, S. P., & Scambos, T. A. (2016). A decade of progress in observing and modelling Antarctic subglacial water systems. *Phil. Trans. R. Soc. A*, *374*(20140294). https://doi.org/10.1098/rsta.2014.0294

Friedrichs, D. M., J. B. T. McInerney, H. J. Oldroyd, W. S. Lee, S. Yun, S.-T. Yoon, C. L. Stevens, C. J. Zappa, C. F. Dow, D. Mueller, O. Sepúlveda Steiner, and A. L. Forrest (2022), Observations of submesoscale eddy-driven heat transport at an ice shelf calving front, *Commun. Earth Environ.*, 3, 140, https://doi.org/10.1038/s43247-022-00460-3.

Fudge, T. J., Markle, B. R., Cuffey, K. M., Buizert, C., Taylor, K. C., Steig, E. J., et al. (2016). Variable relationship between accumulation and temperature in West

Antarctica for the past 31,000 years. Geophysical Research Letters, 43(8), 3795–3803. https://doi.org/10.1002/2016GL068356

Fürst, J. J., Durand, G., Gillet-Chaulet, F., Merino, N., Tavard, L., Mouginot, J., et al. (2015). Assimilation of Antarctic velocity observations provides evidence for uncharted pinning points. *The Cryosphere*, *9*(4), 1427–1443. https://doi.org/10.5194/tc-9-1427-2015

Fusco, G., Budillon, G., & Spezie, G. (2009). Surface heat fluxes and thermohaline variability in the Ross Sea and in Terra Nova Bay polynya. *Continental Shelf Research*, *29*(15), 1887–1895. https://doi.org/10.1016/j.csr.2009.07.006

Fusco, G., Cotroneo, Y., & Aulicino, G. (2018). Different Behaviours of the Ross and Weddell Seas Surface Heat Fluxes in the Period 1972–2015. *Climate, 6*(1), 17. https://doi.org/10.3390/cli6010017

Gaffey, C., & Bhardwaj, A. (2020). Applications of Unmanned Aerial Vehicles in Cryosphere: Latest Advances and Prospects. *Remote Sensing*, *12*(6), 948. https://doi.org/10.3390/rs12060948

Galton-Fenzi, B. K., Hunter, J. R., Coleman, R., Marsland, S. J., & Warner, R. C. (2012). Modeling the basal melting and marine ice accretion of the Amery Ice Shelf. *Journal of Geophysical Research: Oceans*, *117*(C9). https://doi.org/10.1029/2012JC008214

Gardner, A., Schlegel, N.-J., & Larour, E. (2022). *Glacier Energy and Mass Balance (GEMB v1.0): A model of firn processes for cryosphere research* (preprint). Cryosphere. https://doi.org/10.5194/egusphere-2022-674

Gardner, A. S., Moholdt, G., Scambos, T., Fahnstock, M., Ligtenberg, S., van den Broeke, M., & Nilsson, J. (2018). Increased West Antarctic and unchanged East Antarctic ice discharge over the last 7 years. *The Cryosphere*, *12*(2), 521–547. https://doi.org/10.5194/tc-12-521-2018

Gardner, A. S., Schlegel, N.-J., & Larour, E. (2023). Glacier Energy and Mass Balance (GEMB): a model of firn processes for cryosphere research. *Geoscientific Model Development*, *16*(8), 2277–2302. https://doi.org/10.5194/gmd-16-2277-2023

Genthon, C., Six, D., Favier, V., Lazzara, M., & Keller, L. (2011). Atmospheric Temperature Measurement Biases on the Antarctic Plateau. *Journal of Atmospheric and Oceanic Technology*, *28*(12), 1598–1605. https://doi.org/10.1175/JTECH-D-11-00095.1

Ghilain, N., Vannitsem, S., Dalaiden, Q., Goosse, H., De Cruz, L., & Wei, W. (2022). Large ensemble of downscaled historical daily snowfall from an earth system model to 5.5 km resolution over Dronning Maud Land, Antarctica. *Earth System Science Data*, *14*(4), 1901–1916. https://doi.org/10.5194/essd-14-1901-2022

Gilbert, E., & Kittel, C. (2021). Surface Melt and Runoff on Antarctic Ice Shelves at 1.5°C, 2°C, and 4°C of Future Warming. *Geophysical Research Letters*, *48*(8). https://doi.org/10.1029/2020GL091733

Gill, A. E. (1973). Circulation and bottom water production in the Weddell Sea. *Deep Sea Research and Oceanographic Abstracts*, *20*(2), 111–140. https://doi.org/10.1016/0011-7471(73)90048-X

Gillet-Chaulet, F., Durand, G., Gagliardini, O., Mosbeux, C., Mouginot, J., Rémy, F., & Ritz, C. (2016). Assimilation of surface velocities acquired between 1996 and 2010 to constrain the form of the basal friction law under Pine Island Glacier. *Geophysical Research Letters*, *43*(19), 10–311.

Gillet-Chaulet, Fabien. (2020). Assimilation of surface observations in a transient marine ice sheet model using an ensemble Kalman filter. *The Cryosphere*, *14*(3), 811–832. https://doi.org/10.5194/tc-14-811-2020

Gillet-Chaulet, Fabien, & Durand, G. (2010). Ice–sheet advance in Antarctica. *Nature*, *467*(7317), 794–795. https://doi.org/10.1038/467794a

Girton, J. B., Christianson, K., Dunlap, J., Dutrieux, P., Gobat, J., Lee, C., & Rainville, L. (2019). Buoyancy-adjusting Profiling Floats for Exploration of Heat Transport, Melt Rates, and Mixing in the Ocean Cavities Under Floating Ice Shelves. In *OCEANS 2019 MTS/IEEE SEATTLE* (pp. 1–6). Seattle, WA, USA: IEEE. https://doi.org/10.23919/OCEANS40490.2019.8962744

Gladstone, R., Galton-Fenzi, B., Gwyther, D., Zhou, Q., Hattermann, T., Zhao, C., et al. (2021). The Framework For Ice Sheet–Ocean Coupling (FISOC) V1.1. *Geoscientific Model Development*, *14*(2), 889–905. https://doi.org/10.5194/gmd-14-889-2021

Goel, V., Brown, J., & Matsuoka, K. (2017). Glaciological settings and recent mass balance of Blåskimen Island in Dronning Maud Land, Antarctica. *The Cryosphere*, *11*(6), 2883–2896. https://doi.org/10.5194/tc-11-2883-2017

Goff, J. A., Powell, E. M., Young, D. A., & Blankenship, D. D. (2014). Conditional simulation of Thwaites Glacier (Antarctica) bed topography for flow models: Incorporating inhomogeneous statistics and channelized morphology. *Journal of Glaciology*, *60*(222), 635–646. https://doi.org/10.3189/2014JoG13J200

Gogineni, S., Yan, J.-B., Paden, J., Leuschen, C., Li, J., Rodriguez-Morales, F., et al. (2014). Bed topography of Jakobshavn Isbræ, Greenland, and Byrd Glacier, Antarctica. *Journal of Glaciology*, *60*(223), 813–833. https://doi.org/10.3189/2014JoG14J129

Gohl, K., Denk, A., Eagles, G., & Wobbe, F. (2013). Deciphering tectonic phases of the Amundsen Sea Embayment shelf, West Antarctica, from a magnetic anomaly grid. *Tectonophysics*, *585*, 113–123. https://doi.org/10.1016/j.tecto.2012.06.036

Goldberg, D. N., & Heimbach, P. (2013). Parameter and state estimation with a time-dependent adjoint marine ice sheet model. *The Cryosphere*, *7*(6), 1659–1678. https://doi.org/10.5194/tc-7-1659-2013

Goldberg, D. N., Snow, K., Holland, P., Jordan, J. R., Campin, J.-M., Heimbach, P., et al. (2018). Representing grounding line migration in synchronous coupling between a marine ice sheet model and a z-coordinate ocean model. *Ocean Modelling*, *125*, 45–60. https://doi.org/10.1016/j.ocemod.2018.03.005

Goldberg, D. N., Gourmelen, N., Kimura, S., Millan, R., & Snow, K. (2019). How Accurately Should We Model Ice Shelf Melt Rates? *Geophysical Research Letters*, *46*(1), 189–199. https://doi.org/10.1029/2018GL080383

Goldberg, D. N., Smith, T. A., Narayanan, S. H. K., Heimbach, P., & Morlighem, M. (2020). Bathymetric Influences on Antarctic Ice-Shelf Melt Rates. *Journal of Geophysical Research: Oceans*, *125*(11), e2020JC016370. https://doi.org/10.1029/2020JC016370

Golledge, N. R., Keller, E. D., Gomez, N., Naughten, K. A., Bernales, J., Trusel, L. D., & Edwards, T. L. (2019). Global environmental consequences of twenty-first-century ice-sheet melt. *Nature*, *566*(7742), 65–72. https://doi.org/10.1038/s41586-019-0889-9

Golynsky, A. V., Ferraccioli, F., Hong, J. K., Golynsky, D. A., von Frese, R. R. B., Young, D. A., et al. (2018). New Magnetic Anomaly Map of the Antarctic. *Geophysical Research Letters*, *45*(13), 6437–6449. https://doi.org/10.1029/2018GL078153

Gomez, N., Mitrovica, J. X., Huybers, P., & Clark, P. U. (2010). Sea level as a stabilizing factor for marine-ice-sheet grounding lines. *Nature Geoscience*, *3*(12), 850–853. https://doi.org/10.1038/ngeo1012

Gomez, N., Pollard, D., Mitrovica, J. X., Huybers, P., & Clark, P. U. (2012). Evolution of a coupled marine ice sheet-sea level model: COUPLED ICE SHEET, SEA LEVEL MODEL. *Journal of Geophysical Research: Earth Surface*, *117*(F1), n/a-n/a. https://doi.org/10.1029/2011JF002128

Gomez, N., Pollard, D., & Holland, D. (2015). Sea-level feedback lowers projections of future Antarctic Ice-Sheet mass loss. *Nature Communications*, *6*(1), 8798. https://doi.org/10.1038/ncomms9798

Gomez, N., Latychev, K., & Pollard, D. (2018). A Coupled Ice Sheet–Sea Level Model Incorporating 3D Earth Structure: Variations in Antarctica during the Last Deglacial Retreat. *Journal of Climate*, *31*(10), 4041–4054. https://doi.org/10.1175/JCLI-D-17-0352.1

Gomez, N., Weber, M. E., Clark, P. U., Mitrovica, J. X., & Han, H. K. (2020). Antarctic ice dynamics amplified by Northern Hemisphere sea-level forcing. *Nature*, *587*(7835), 600–604. https://doi.org/10.1038/s41586-020-2916-2

Gomez, N., Yousefi, M., Pollard, D., DeConto, R. M., Sadai, S., Lloyd, A., et al. (2024). The influence of realistic 3D mantle viscosity on Antarctica's contribution to future global sea levels. Science Advances, 10(31), eadn1470. https://doi.org/10.1126/sciadv.adn1470

Gooch, B. T., Young, D. A., & Blankenship, D. D. (2016). Potential groundwater and heterogeneous heat source contributions to ice sheet dynamics in critical submarine basins of East Antarctica. *Geochemistry, Geophysics, Geosystems*, *17*(2), 395–409. https://doi.org/10.1002/2015GC006117

Goosse, H. et al. (2010). Description of the Earth system model of intermediate complexity LOVECLIM version 1.2. *Geosci. Model Dev*. 3, 603–633, https://doi.org/10.5194/gmd-3-603-2010.

Goosse, H., & Zunz, V. (2014). Decadal trends in the Antarctic sea ice extent ultimately controlled by ice–ocean feedback. *The Cryosphere*, *8*(2), 453–470. https://doi.org/10.5194/tc-8-453-2014

Gorodetskaya, I. V., Van Lipzig, N. P. M., Van den Broeke, M. R., Mangold, A., Boot, W., & Reijmer, C. H. (2013). Meteorological regimes and accumulation patterns at Utsteinen, Dronning Maud Land, East Antarctica: Analysis of two contrasting years. *Journal of Geophysical Research: Atmospheres*, *118*(4), 1700–1715. https://doi.org/10.1002/jgrd.50177

Gorodetskaya, Irina V., Tsukernik, M., Claes, K., Ralph, M. F., Neff, W. D., & Van Lipzig, N. P. M. (2014). The role of atmospheric rivers in anomalous snow accumulation in East Antarctica. *Geophysical Research Letters*, *41*(17), 6199–6206. https://doi.org/10.1002/2014GL060881

Gorte, T., Lenaerts, J. T. M., & Medley, B. (2020). Scoring Antarctic surface mass balance in climate models to refine future projections. *The Cryosphere*, *14*(12), 4719–4733. https://doi.org/10.5194/tc-14-4719-2020

Gourmelen, N., Goldberg, D. N., Snow, K., Henley, S. F., Bingham, R. G., Kimura, S., et al. (2017). Channelized Melting Drives Thinning Under a Rapidly Melting Antarctic Ice Shelf. *Geophysical Research Letters*, *44*(19), 9796–9804. https://doi.org/10.1002/2017GL074929

Gourmelen, N., Jakob, L., Holland, P.R., Dutrieux, P., Goldberg, D., Bevan, S., Luckman, A. and Malczyk, G., 2025. The influence of subglacial lake discharge on Thwaites Glacier ice-shelf melting and grounding-line retreat. *Nature Communications*, 16(1), 2272, https://doi.org/10.1038/s41467-025-57417-1

Gowan, E. J., Niu, L., Knorr, G., & Lohmann, G. (2019). Geology datasets in North America, Greenland and surrounding areas for use with ice sheet models. *Earth System Science Data*, *11*(1), 375–391. https://doi.org/10.5194/essd-11-375-2019

Gowan, E. J., Hinck, S., Niu, L., Clason, C., & Lohmann, G. (2023). The impact of spatially varying ice sheet basal conditions on sliding at glacial time scales. *Journal of Glaciology*, 1–15. https://doi.org/10.1017/jog.2022.125

Graham, A. G. C., Dutrieux, P., Vaughan, D. G., Nitsche, F. O., Gyllencreutz, R., Greenwood, S. L., et al. (2013). Seabed corrugations beneath an Antarctic ice shelf revealed by autonomous underwater vehicle survey: Origin and implications for the history of Pine Island Glacier. *Journal of Geophysical Research: Earth Surface*, *118*(3), 1356–1366. https://doi.org/10.1002/jgrf.20087

Graham, A. G. C., Wåhlin, A., Hogan, K. A., Nitsche, F. O., Heywood, K. J., Totten, R. L., et al. (2022). Rapid retreat of Thwaites Glacier in the pre-satellite era. *Nature Geoscience*, *15*(9), 706–713. https://doi.org/10.1038/s41561-022-01019-9

Graham, F. S., Roberts, J. L., Galton-Fenzi, B. K., Young, D., Blankenship, D., & Siegert, M. J. (2017). A high-resolution synthetic bed elevation grid of the Antarctic continent. *Earth System Science Data*, *9*(1), 267–279. https://doi.org/10.5194/essd-9-267-2017

Greenbaum, J. S., Blankenship, D. D., Young, D. A., Richter, T. G., Roberts, J. L., Aitken, A. R. A., et al. (2015). Ocean access to a cavity beneath Totten Glacier in East Antarctica. *Nature Geoscience*, *8*(4), 294–298. https://doi.org/10.1038/ngeo2388

Greene, C. A., Gwyther, D. E., & Blankenship, D. D. (2017). Antarctic Mapping Tools for Matlab. *Computers & Geosciences*, *104*, 151–157. https://doi.org/10.1016/j.cageo.2016.08.003

Greene, C. A., Blankenship, D. D., Gwyther, D. E., Silvano, A., & van Wijk, E. (2017). Wind causes Totten Ice Shelf melt and acceleration. *Science Advances*, *3*(11), e1701681. https://doi.org/10.1126/sciadv.1701681

Greene, C. A., Young, D. A., Gwyther, D. E., Galton-Fenzi, B. K., & Blankenship, D. D. (2018). Seasonal dynamics of Totten Ice Shelf controlled by sea ice buttressing. *The Cryosphere*, *12*(9), 2869–2882. https://doi.org/10.5194/tc-12-2869-2018

Greene, C. A., Gardner, A. S., Schlegel, N.-J., & Fraser, A. D. (2022). Antarctic calving loss rivals ice-shelf thinning. *Nature*, *609*(7929), 948–953. https://doi.org/10.1038/s41586-022-05037-w

Griggs, J. A., & Bamber, J. L. (2011). Antarctic ice-shelf thickness from satellite radar altimetry. *Journal of Glaciology*, *57*(203), 485–498. https://doi.org/10.3189/002214311796905659

Gudmundsson, G. H. (2008). Analytical solutions for the surface response to small amplitude perturbations in boundary data in the shallow-ice-stream approximation. *The Cryosphere*, *2*(2), 77–93. https://doi.org/10.5194/tc-2-77-2008

Gudmundsson, G. Hilmar, Paolo, F. S., Adusumilli, S., & Fricker, H. A. (2019). Instantaneous Antarctic ice sheet mass loss driven by thinning ice shelves. *Geophysical Research Letters*, *46*(23), 13903–13909. https://doi.org/10.1029/2019GL085027

Gustafson, C. D., Key, K., Siegfried, M. R., Winberry, J. P., Fricker, H. A., Venturelli, R. A., & Michaud, A. B. (2022). A dynamic saline groundwater system mapped beneath an Antarctic ice stream. *Science*, *376*(6593), 640–644. https://doi.org/10.1126/science.abm3301

Haas, C., Lobach, J., Hendricks, S., Rabenstein, L., & Pfaffling, A. (2009). Helicopter-borne measurements of sea ice thickness, using a small and lightweight, digital EM system. *Journal of Applied Geophysics*, *67*(3), 234–241. https://doi.org/10.1016/j.jappgeo.2008.05.005

Haas, C., Langhorne, P. J., Rack, W., Leonard, G. H., Brett, G. M., Price, D., et al. (2021). Airborne mapping of the sub-ice platelet layer under fast ice in McMurdo Sound, Antarctica. *The Cryosphere*, *15*(1), 247–264. https://doi.org/10.5194/tc-15-247-2021

Haeger, C., Kaban, M. K., Tesauro, M., Petrunin, A. G., & Mooney, W. D. (2019). 3-D Density, Thermal, and Compositional Model of the Antarctic Lithosphere and Implications for Its Evolution. *Geochemistry, Geophysics, Geosystems*, *20*(2), 688–707. https://doi.org/10.1029/2018GC008033

Hale R and 11 others (2016) Multi-channel ultra-wideband radar sounder and imager. 2016 IEEE Int’l Geosci. Remote Sens. Sym. (IGARSS), Beijing. pp. 2112–2115. doi: 10.1109/IGARSS.2016.7729545.

Handcock, M. S., & Raphael, M. N. (2020). Modeling the annual cycle of daily Antarctic sea ice extent. *The Cryosphere*, *14*(7), 2159–2172. https://doi.org/10.5194/tc-14-2159-2020

Hanna, E., Pattyn, F., Navarro, F., Favier, V., Goelzer, H., Van Den Broeke, M. R., et al. (2020). Mass balance of the ice sheets and glaciers – Progress since AR5 and challenges. *Earth-Science Reviews*, *201*, 102976. https://doi.org/10.1016/j.earscirev.2019.102976

Hansen, N., Langen, P. L., Boberg, F., Forsberg, R., Simonsen, S. B., Thejll, P., et al. (2021). Downscaled surface mass balance in Antarctica: impacts of subsurface processes and large-scale atmospheric circulation. *The Cryosphere*, *15*(9), 4315–4333. https://doi.org/10.5194/tc-15-4315-2021

Hansen, N., Simonsen, S. B., Boberg, F., Kittel, C., Orr, A., Souverijns, N., et al. (2022). Brief communication: Impact of common ice mask in surface mass balance estimates over the Antarctic ice sheet. *The Cryosphere*, *16*(2), 711–718. https://doi.org/10.5194/tc-16-711-2022

Hansen, S. E., Reusch, A. M., Parker, T., Bloomquist, D. K., Carpenter, P., Graw, J. H., & Brenn, G. R. (2015). The Transantarctic Mountains Northern Network (TAMNNET):

Deployment and Performance of a Seismic Array in Antarctica. *Seismological Research Letters*, *86*(6), 1636–1644. https://doi.org/10.1785/0220150117

Haseloff, M., & Sergienko, O. V. (2018). The effect of buttressing on grounding line dynamics. *Journal of Glaciology*, *64*(245), 417–431. https://doi.org/10.1017/jog.2018.30

Hattermann, T., Nøst, O. A., Lilly, J. M., & Smedsrud, L. H. (2012). Two years of oceanic observations below the Fimbul Ice Shelf, Antarctica. *Geophysical Research Letters*, *39*(12), n/a-n/a. https://doi.org/10.1029/2012GL051012

Hague, M., and M. Vichi (2021), Southern Ocean biogeochemical Argo detect under-ice phytoplankton growth before sea ice retreat, *Biogeosciences*, 18, 25–38, https://doi.org/10.5194/bg-18-25-2021.

Hazzard, J. A., & Richards, F. D. (2024). Antarctic geothermal heat flow, crustal conductivity and heat production inferred from seismological data. Geophysical Research Letters, 51(7), e2023GL106274, https://doi.org/10.1029/2023GL106274

Hazzard, J. A. N., Richards, F. D., Goes, S. D. B., & Roberts, G. G. (2023). Probabilistic Assessment of Antarctic Thermomechanical Structure: Impacts on Ice Sheet Stability. *Journal of Geophysical Research: Solid Earth*, *128*(5), e2023JB026653. https://doi.org/10.1029/2023JB026653

Helsen, M. M., van den Broeke, M. R., van de Wal, R. S. W., van de Berg, W. J., van Meijgaard, E., Davis, C. H., et al. (2008). Elevation Changes in Antarctica Mainly Determined by Accumulation Variability. *Science*, *320*(5883), 1626–1629. https://doi.org/10.1126/science.1153894

Herraiz-Borreguero, L., & Naveira Garabato, A. C. (2022). Poleward shift of Circumpolar Deep Water threatens the East Antarctic Ice Sheet. *Nature Climate Change*, *12*(8), 728–734. https://doi.org/10.1038/s41558-022-01424-3

Herraiz-Borreguero, L., Coleman, R., Allison, I., Rintoul, S. R., Craven, M., & Williams, G. D. (2015). Circulation of modified Circumpolar Deep Water and basal melt beneath the A mery Ice Shelf, East Antarctica. *Journal of Geophysical Research: Oceans*, *120*(4), 3098–3112. https://doi.org/10.1002/2015JC010697

Heuzé, C. (2021). Antarctic Bottom Water and North Atlantic Deep Water in CMIP6 models. *Ocean Science*, *17*(1), 59–90. https://doi.org/10.5194/os-17-59-2021

Hewitt, I. J. (2013). Seasonal changes in ice sheet motion due to melt water lubrication. *Earth Planet. Sci. Lett.*, *371–372*(0), 16–25. http://dx.doi.org/10.1016/j.epsl.2013.04.022

Hill, G. J. (2020). On the Use of Electromagnetics for Earth Imaging of the Polar Regions. *Surveys in Geophysics*, *41*(1), 5–45. https://doi.org/10.1007/s10712-019-09570-8

Hills, B. H., Christianson, K., Jacobel, R. W., Conway, H., & Pettersson, R. (2022). Radar attenuation demonstrates advective cooling in the Siple Coast ice streams. *Journal of Glaciology*, 1–11. https://doi.org/10.1017/jog.2022.86

Hills, B. H., M. R. Siegfried, and D. M. Schroeder (2024), Entrained water in basal ice suppresses radar bed-echo power at active subglacial lakes, Geophys. Res. Lett., 51, e2024GL109248, https://doi.org/10.1029/2024GL109248.

Hines, K. M., Bromwich, D. H., & Marshall, G. J. (2000) Artificial Surface Pressure Trends in the NCEP–NCAR Reanalysis over the Southern Ocean and Antarctica. *Journal of*

Climate, *13*(22), 3940–3952. https://doi.org/10.1175/1520-0442(2000)013<3940:ASPTIT>2.0.CO;2

Hinze, W. J., Von Frese, R., & Saad, A. H. (2013) *Gravity and magnetic exploration: principles, practices, and applications*. New York: Cambridge University Press.

Houriez, L., Larour, E., Caron, L., Schlegel, N.J., Adhikari, S., Ivins, E., Pelle, T., Seroussi, H., Darve, E. and Fischer, M., 2025. Capturing Solid Earth and Ice Sheet Interactions: Insights from Reinforced Ridges in Thwaites Glacier. *The Cryosphere* 19 (10) https://doi.org/10.5194/tc-19-4355-2025

Hobbs, W. R., Massom, R., Stammerjohn, S., Reid, P., Williams, G., & Meier, W. (2016). A review of recent changes in Southern Ocean sea ice, their drivers and forcings. *Global and Planetary Change*, *143*, 228–250. https://doi.org/10.1016/j.gloplacha.2016.06.008

Hochmuth, K., Gohl, K., Leitchenkov, G., Sauermilch, I., Whittaker, J. M., Uenzelmann-Neben, G., et al. (2020). The Evolving Paleobathymetry of the Circum-Antarctic Southern Ocean Since 34 Ma: A Key to Understanding Past Cryosphere-Ocean Developments. *Geochemistry, Geophysics, Geosystems*, *21*(8). https://doi.org/10.1029/2020GC009122

Hofer, S., Amory, C., Kittel, C., Carlsen, T., Le Toumelin, L., & Storelvmo, T. (2021). The Contribution of Drifting Snow to Cloud Properties and the Atmospheric Radiative Budget Over Antarctica. *Geophysical Research Letters*, *48*(22). https://doi.org/10.1029/2021GL094967

Hoffman, A. O., Christianson, K., Holschuh, N., Case, E., Kingslake, J., & Arthern, R. (2022). The Impact of Basal Roughness on Inland Thwaites Glacier Sliding. *Geophysical Research Letters*, *49*(14). https://doi.org/10.1029/2021GL096564

Hofstede, C., Beyer, S., Corr, H., Eisen, O., Hattermann, T., Helm, V., et al. (2021). Evidence for a grounding line fan at the onset of a basal channel under the ice shelf of Support Force Glacier, Antarctica, revealed by reflection seismics. *The Cryosphere*, *15*(3), 1517–1535. https://doi.org/10.5194/tc-15-1517-2021

Hogg, A. E., & Gudmundsson, G. H. (2017). Impacts of the Larsen-C Ice Shelf calving event. *Nature Climate Change*, *7*(8), 540–542. https://doi.org/10.1038/nclimate3359

Holland, P. R. (2014). The seasonality of Antarctic sea ice trends. *Geophysical Research Letters*, *41*(12), 4230–4237. https://doi.org/10.1002/2014GL060172

Holland, P. R., & Kwok, R. (2012). Wind-driven trends in Antarctic sea-ice drift. *Nature Geoscience*, *5*(12), 872–875. https://doi.org/10.1038/ngeo1627

Holland, P. R., Bracegirdle, T. J., Dutrieux, P., Jenkins, A., & Steig, E. J. (2019). West Antarctic ice loss influenced by internal climate variability and anthropogenic forcing. *Nature Geoscience*, *12*(9), 718–724. https://doi.org/10.1038/s41561-019-0420-9

Holland, P. R., O'Connor, G. K., Bracegirdle, T. J., Dutrieux, P., Naughten, K. A., Steig, E. J., et al. (2022). Anthropogenic and internal drivers of wind changes over the Amundsen Sea, West Antarctica, during the 20th and 21st centuries. *The Cryosphere*, *16*(12), 5085–5105. https://doi.org/10.5194/tc-16-5085-2022

Holschuh, N., Christianson, K., Paden, J., Alley, R. B., & Anandakrishnan, S. (2020). Linking postglacial landscapes to glacier dynamics using swath radar at Thwaites Glacier, Antarctica. *Geology*, *48*(3), 268–272. https://doi.org/10.1130/G46772.1

Holt, J. W., Peters, M. E., Kempf, S. D., Morse, D. L., & Blankenship, D. D. (2006). Echo source discrimination in single-pass airborne radar sounding data from the Dry Valleys, Antarctica: Implications for orbital sounding of Mars. *Journal of Geophysical Research*, *111*(E6), E06S24. https://doi.org/10.1029/2005JE002525

Horgan, H. J., Alley, R. B., Christianson, K., Jacobel, R. W., Anandakrishnan, S., Muto, A., et al. (2013). Estuaries beneath ice sheets. *Geology*, *41*(11), 1159–1162. https://doi.org/10.1130/G34654.1

Horgan, H. J., Christianson, K., Jacobel, R. W., Anandakrishnan, S., & Alley, R. B. (2013). Sediment deposition at the modern grounding zone of Whillans Ice Stream, West Antarctica. *Geophysical Research Letters*, *40*(15), 3934–3939. https://doi.org/10.1002/grl.50712

Horgan, H. J., van Haastrecht, L., Alley, R. B., Anandakrishnan, S., Beem, L. H., Christianson, K., et al. (2021). Grounding zone subglacial properties from calibrated active-source seismic methods. *The Cryosphere*, *15*(4), 1863–1880. https://doi.org/10.5194/tc-15-1863-2021

Howat, I., Porter, C., Noh, M.-J., Husby, E., Khuvis, S., Danish, E., et al. (2022). The Reference Elevation Model of Antarctica - Mosaics, Version 2 [Data set]. Harvard Dataverse. https://doi.org/10.7910/DVN/EBW8UC

Howat, I. M., Porter, C., Smith, B. E., Noh, M.-J., & Morin, P. (2019). The Reference Elevation Model of Antarctica. *The Cryosphere*, *13*(2), 665–674. https://doi.org/10.5194/tc-13-665-2019

Hubbard, B., Tison, J.-L., Philippe, M., Heene, B., Pattyn, F., Malone, T., & Freitag, J. (2013). Ice shelf density reconstructed from optical televiewer borehole logging. *Geophysical Research Letters*, *40*(22), 5882–5887. https://doi.org/10.1002/2013GL058023

Hughes, K. A., Fretwell, P., Rae, J., Holmes, K., & Fleming, A. (2011). Untouched Antarctica: mapping a finite and diminishing environmental resource. *Antarctic Science*, *23*(6), 537–548. https://doi.org/10.1017/S095410201100037X

Hughes, K. A., López-Martínez, J., Francis, J. E., Crame, J. A., Carcavilla, L., Shiraishi, K., et al. (2016). Antarctic geoconservation: a review of current systems and practices. *Environmental Conservation*, *43*(2), 97–108. https://doi.org/10.1017/S0376892915000387

Huss, M. (2013). Density assumptions for converting geodetic glacier volume change to mass change. *The Cryosphere*, *7*(3), 877–887. https://doi.org/10.5194/tc-7-877-2013

Huss, M., & Farinotti, D. (2014). A high-resolution bedrock map for the Antarctic Peninsula. *The Cryosphere*, *8*(4), 1261–1273. https://doi.org/10.5194/tc-8-1261-2014

Huybrechts, P. (1990). A 3-D model for the Antarctic ice sheet: a sensitivity study on the glacial-interglacial contrast. *Climate Dynamics*, *5*(2), 79–92. https://doi.org/10.1007/BF00207423

Intergovernmental Panel on Climate Change (Ed.). (2014). Sea Level Change. In *Climate Change 2013 – The Physical Science Basis* (1st ed., pp. 1137–1216). Cambridge University Press. https://doi.org/10.1017/CBO9781107415324.026

Intergovernmental Panel On Climate Change (Ipcc). (2022). *The Ocean and Cryosphere in a Changing Climate: Special Report of the Intergovernmental Panel on Climate*

Change (1st ed.). Cambridge University Press. https://doi.org/10.1017/9781009157964

Irving, D., & Simmonds, I. (2016). A New Method for Identifying the Pacific–South American Pattern and Its Influence on Regional Climate Variability. *Journal of Climate*, *29*(17), 6109–6125. https://doi.org/10.1175/JCLI-D-15-0843.1

Ivins, E. R., Caron, L., Adhikari, S., Larour, E., & Scheinert, M. (2020). A linear viscoelasticity for decadal to centennial time scale mantle deformation. *Reports on Progress in Physics*, *83*(10), 106801. https://doi.org/10.1088/1361-6633/aba346

Ivins, E. R., van der Wal, W., Wiens, D. A., Lloyd, A. J., & Caron, L. (2023). Antarctic upper mantle rheology. *Geological Society, London, Memoirs*, *56*(1), 267–294. https://doi.org/10.1144/M56-2020-19

Jackson, R. H., & Straneo, F. (2016). Heat, Salt, and Freshwater Budgets for a Glacial Fjord in Greenland. *Journal of Physical Oceanography*, *46*(9), 2735–2768. https://doi.org/10.1175/JPO-D-15-0134.1

Jacobs, S., Giulivi, C., Dutrieux, P., Rignot, E., Nitsche, F., & Mouginot, J. (2013). Getz Ice Shelf melting response to changes in ocean forcing.*Journal of Geophysical Research: Oceans*, *118*(9), 4152–4168. https://doi.org/10.1002/jgrc.20298

Jacobs, S. S. (1991). On the nature and significance of the Antarctic Slope Front. *Marine Chemistry*, *35*(1–4), 9–24. https://doi.org/10.1016/S0304-4203(09)90005-6

Jacobs, S. S., Fairbanks, R. G., & Horibe, Y. G. (1985). Origin and evolution of water masses near the Antarctic continental margin: Evidence from H218O/H216O ratios in seawater. In S. Jacobs (Ed.), *Antarctic Research Series* (Vol. 43, pp. 59–85). Washington, D. C.: American Geophysical Union. https://doi.org/10.1029/AR043p0059

Jacobs, S. S., Helmer, H. H., Doake, C. S. M., Jenkins, A., & Frolich, R. M. (1992). Melting of ice shelves and the mass balance of Antarctica. *Journal of Glaciology*, *38*(130), 375–387. https://doi.org/10.3189/S0022143000002252

Jacobs, S. S., Hellmer, H. H., & Jenkins, A. (1996). Antarctic Ice Sheet melting in the southeast Pacific. *Geophysical Research Letters*, *23*(9), 957–960. https://doi.org/10.1029/96GL00723

Jacobs, S. S., Jenkins, A., Giulivi, C. F., & Dutrieux, P. (2011). Stronger ocean circulation and increased melting under Pine Island Glacier ice shelf. *Nature Geoscience*, *4*(8), 519–523. https://doi.org/10.1038/ngeo1188

Jacobs, S. S., Giulivi, C. F., & Dutrieux, P. (2022). Persistent Ross Sea Freshening From Imbalance West Antarctic Ice Shelf Melting. *Journal of Geophysical Research: Oceans*, *127*(3). https://doi.org/10.1029/2021JC017808

Jakobs, C. L., Reijmer, C. H., Smeets, C. J. P. P., Trusel, L. D., van de Berg, W. J., van den Broeke, M. R., & van Wessem, J. M. (2020). A benchmark dataset of in situ Antarctic surface melt rates and energy balance. *Journal of Glaciology*, *66*(256), 291–302. https://doi.org/10.1017/jog.2020.6

Jamieson, S. S. R., Sugden, D. E., & Hulton, N. R. J. (2010). The evolution of the subglacial landscape of Antarctica. *Earth and Planetary Science Letters*, *293*(1–2), 1–27. https://doi.org/10.1016/j.epsl.2010.02.012

Jamieson, S. S. R., Stokes, C. R., Ross, N., Rippin, D. M., Bingham, R. G., Wilson, D. S., et al. (2014). The glacial geomorphology of the Antarctic ice sheet bed. *Antarctic Science*, *26*(6), 724–741. https://doi.org/10.1017/S0954102014000212

Jansen, D., Luckman, A. J., Cook, A., Bevan, S., Kulessa, B., Hubbard, B., & Holland, P. R. (2015). Brief Communication: Newly developing rift in Larsen C Ice Shelf presents significant risk to stability. *The Cryosphere*, *9*(3), 1223–1227. https://doi.org/10.5194/tc-9-1223-2015

Jayne, S., & Bogue, N. (2017). Air-Deployable Profiling Floats. *Oceanography*, *30*(2), 29–31. https://doi.org/10.5670/oceanog.2017.214

Jenkins, A., & Jacobs, S. (2008). Circulation and melting beneath George VI Ice Shelf, Antarctica. *Journal of Geophysical Research*, *113*(C4), C04013. https://doi.org/10.1029/2007JC004449

Jenkins, A., Dutrieux, P., Jacobs, S. S., McPhail, S. D., Perrett, J. R., Webb, A. T., & White, D. (2010). Observations beneath Pine Island Glacier in West Antarctica and implications for its retreat. *Nature Geoscience*, *3*(7), 468–472. https://doi.org/10.1038/ngeo890

Jenkins, A., Dutrieux, P., Jacobs, S., Steig, E., Gudmundsson, H., Smith, J., & Heywood, K. (2016). Decadal Ocean Forcing and Antarctic Ice Sheet Response: Lessons from the Amundsen Sea. *Oceanography*, *29*(4), 106–117. https://doi.org/10.5670/oceanog.2016.103

Jenny, B., Jensen, T.E. and René, F. (2025). Mass Change in Antarctica from 2002 to 2025 Using GRACE and GRACE-FO. *Remote Sensing*, 17(23), 3870. https://doi.org/10.3390/rs17233870

Jenkins, A., Shoosmith, D., Dutrieux, P., Jacobs, S., Kim, T. W., Lee, S. H., et al. (2018). West Antarctic Ice Sheet retreat in the Amundsen Sea driven by decadal oceanic variability. *Nature Geoscience*, *11*(10), 733–738. https://doi.org/10.1038/s41561-018-0207-4

Jensen, T. E., Olesen, A. V., Forsberg, R., Olsson, P.-A., & Josefsson, Ö. (2019). New Results from Strapdown Airborne Gravimetry Using Temperature Stabilisation. *Remote Sensing*, *11*(22), 2682. https://doi.org/10.3390/rs11222682

Jenssen, R. O. R., & Jacobsen, S. (2020). Drone-mounted UWB snow radar: technical improvements and field results. *Journal of Electromagnetic Waves and Applications*, *34*(14), 1930–1954. https://doi.org/10.1080/09205071.2020.1799871

Jenssen, R. O. R., & Jacobsen, S. K. (2021). Measurement of Snow Water Equivalent Using Drone-Mounted Ultra-Wide-Band Radar. *Remote Sensing*, *13*(13), 2610. https://doi.org/10.3390/rs13132610

Johnson, A., Hock, R., & Fahnestock, M. (2022). Spatial variability and regional trends of Antarctic ice shelf surface melt duration over 1979–2020 derived from passive microwave data. *Journal of Glaciology*, *68*(269), 533–546. https://doi.org/10.1017/jog.2021.112

Johnson, J. A., Shturmakov, A. J., Kuhl, T. W., Mortensen, N. B., & Gibson, C. J. (2014). Next generation of an intermediate depth drill. *Annals of Glaciology*, *55*(68), 27–33. https://doi.org/10.3189/2014AoG68A011

Johnson, J. S., Pollard, D., Whitehouse, P. L., Roberts, S. J., Rood, D. H., & Schaefer, J. M. (2021). Comparing Glacial-Geological Evidence and Model Simulations of Ice Sheet

Change since the Last Glacial Period in the Amundsen Sea Sector of Antarctica. *Journal of Geophysical Research: Earth Surface*, *126*(6), e2020JF005827. https://doi.org/10.1029/2020JF005827

Jones, J. M., Gille, S. T., Goosse, H., Abram, N. J., Canziani, P. O., Charman, D. J., et al. (2016). Assessing recent trends in high-latitude Southern Hemisphere surface climate. *Nature Climate Change*, *6*(10), 917–926. https://doi.org/10.1038/nclimate3103

Jones, M. E., Bromwich, D. H., Nicolas, J. P., Carrasco, J., Plavcová, E., Zou, X., & Wang, S.-H. (2019). Sixty Years of Widespread Warming in the Southern Middle and High Latitudes (1957–2016). *Journal of Climate*, *32*(20), 6875–6898. https://doi.org/10.1175/JCLI-D-18-0565.1

Jong, L. M., Plummer, C. T., Roberts, J. L., Moy, A. D., Curran, M. A. J., Vance, T. R., et al. (2022). 2000 years of annual ice core data from Law Dome, East Antarctica. *Earth System Science Data*, *14*(7), 3313–3328. https://doi.org/10.5194/essd-14-3313-2022

Jordan, J. R., Holland, P. R., Goldberg, D., Snow, K., Arthern, R., Campin, J.-M., et al. (2018). Ocean-Forced Ice-Shelf Thinning in a Synchronously Coupled Ice-Ocean Model. *Journal of Geophysical Research: Oceans*, *123*(2), 864–882. https://doi.org/10.1002/2017JC013251

Jordan, T. A., Ferraccioli, F., Armadillo, E., & Bozzo, E. (2013). Crustal architecture of the Wilkes Subglacial Basin in East Antarctica, as revealed from airborne gravity data. *Tectonophysics*, *585*, 196–206. https://doi.org/10.1016/j.tecto.2012.06.041

Jordan, T. A., Martin, C., Ferraccioli, F., Matsuoka, K., Corr, H., Forsberg, R., et al. (2018). Anomalously high geothermal flux near the South Pole. *Scientific Reports*, *8*(1), 16785. https://doi.org/10.1038/s41598-018-35182-0

Jordan, T. A., Porter, D., Tinto, K., Millan, R., Muto, A., Hogan, K., et al. (2020). New gravity-derived bathymetry for the Thwaites, Crosson, and Dotson ice shelves revealing two ice shelf populations. *The Cryosphere*, *14*(9), 2869–2882. https://doi.org/10.5194/tc-14-2869-2020

Jordan, T. A., Riley, T. R., & Siddoway, C. S. (2020). The geological history and evolution of West Antarctica. *Nature Reviews Earth & Environment*, *1*(2), 117–133. https://doi.org/10.1038/s43017-019-0013-6

Jordan, T. M., Martín, C., Brisbourne, A. M., Schroeder, D. M., & Smith, A. M. (2022). Radar Characterization of Ice Crystal Orientation Fabric and Anisotropic Viscosity Within an Antarctic Ice Stream. *Journal of Geophysical Research: Earth Surface*, *127*(6). https://doi.org/10.1029/2022JF006673

Jordan, T. A., & Becker, D. (2018). Investigating the distribution of magmatism at the onset of Gondwana breakup with novel strapdown gravity and aeromagnetic data. *Physics of the Earth and Planetary Interiors*, *282*, 77–88. https://doi.org/10.1016/j.pepi.2018.07.007

Jordan, T., Robinson, C., Reed, T., Toomey, R., Jelev, N., Waters, J., et al. (2025). Successful deployment of a large uncrewed aerial vehicle for multidisciplinary science from Rothera Research Station, Antarctica: 2024 season overview and lessons learned. Antarctic Science, 37(4), 291–308. https://doi.org/10.1017/S0954102025000136

Joughin, I. (2003). Melting and freezing beneath Filchner-Ronne Ice Shelf, Antarctica. *Geophysical Research Letters*, *30*(9), 1477. https://doi.org/10.1029/2003GL016941

Joughin, I., & Tulaczyk, S. (2002). Positive mass balance of the Ross Ice Streams, West Antarctica. *Science*, *295*(5554), 476–480. https://doi.org/10.1126/science.1066875

Joughin, I., Tulaczyk, S., Bamber, J., Blankenship, D., Holt, J., Scambos, T., & Vaughan, D. (2009). Basal conditions for Pine Island and Thwaites Glaciers, West Antarctica, determined using satellite and airborne data. *J. Glaciol.*, *55*(190), 245–257.

Joughin, I., Smith, B. E., & Medley, B. (2014). Marine Ice Sheet Collapse Potentially Under Way for the Thwaites Glacier Basin, West Antarctica. *Science*, *344*(6185), 735–738. https://doi.org/10.1126/science.1249055

Joughin, I., Smith, B. E., & Schoof, C. G. (2019). Regularized Coulomb friction laws for ice sheet sliding: Application to Pine Island Glacier, Antarctica. *Geophysical Research Letters*, *46*(9), 4764–4771.

Jourdain, N. C., Mathiot, P., Merino, N., Durand, G., Le Sommer, J., Spence, P., et al. (2017). Ocean circulation and sea-ice thinning induced by melting ice shelves in the Amundsen Sea. *Journal of Geophysical Research: Oceans*, *122*(3), 2550–2573. https://doi.org/10.1002/2016JC012509

Jourdain, N. C., Asay-Davis, X., Hattermann, T., Straneo, F., Seroussi, H., Little, C. M., & Nowicki, S. (2020). A protocol for calculating basal melt rates in the ISMIP6 Antarctic ice sheet projections. *The Cryosphere*, *14*(9), 3111–3134. https://doi.org/10.5194/tc-14-3111-2020

Jouzel, J. (2013). A brief history of ice core science over the last 50 yr. *Climate of the Past*, *9*(6), 2525–2547. https://doi.org/10.5194/cp-9-2525-2013

Jullion, L., Garabato, A. C. N., Meredith, M. P., Holland, P. R., Courtois, P., & King, B. A. (2013). Decadal Freshening of the Antarctic Bottom Water Exported from the Weddell Sea. *Journal of Climate*, *26*(20), 8111–8125. https://doi.org/10.1175/JCLI-D-12-00765.1

Jutila, A., Hendricks, S., Ricker, R., Von Albedyll, L., Krumpen, T., & Haas, C. (2022). Retrieval and parameterisation of sea-ice bulk density from airborne multi-sensor measurements. *The Cryosphere*, *16*(1), 259–275. https://doi.org/10.5194/tc-16-259-2022

Kachuck, S. B., Martin, D. F., Bassis, J. N., & Price, S. F. (2020). Rapid Viscoelastic Deformation Slows Marine Ice Sheet Instability at Pine Island Glacier. *Geophysical Research Letters*, *47*(10), e2019GL086446. https://doi.org/10.1029/2019GL086446

Kamb, B. (2001). Basal Zone of the West Antarctic Ice Streams and its Role in Lubrication of Their Rapid Motion. In *The West Antarctic Ice Sheet: Behavior and Environment* (pp. 157–199). American Geophysical Union (AGU). https://doi.org/10.1029/AR077p0157

Karlsson, N. B., Solgaard, A. M., Mankoff, K. D., Gillet-Chaulet, F., MacGregor, J. A., Box, J. E., et al. (2021). A First Constraint on Basal Melt-Water Production of the Greenland Ice Sheet. *Nature Communications*, *12*(1), 3461. https://doi.org/10.1038/s41467-021-23739-z

Kaspers, K. A., van de Wal, R. S. W., van den Broeke, M. R., Schwander, J., van Lipzig, N. P. M., & Brenninkmeijer, C. a. M. (2004). Model calculations of the age of firn air across the Antarctic continent. *Atmospheric Chemistry and Physics*, *4*(5), 1365–1380. https://doi.org/10.5194/acp-4-1365-2004

Kausch, T., Lhermitte, S., Lenaerts, J. T. M., Wever, N., Inoue, M., Pattyn, F., et al. (2020). Impact of coastal East Antarctic ice rises on surface mass balance: insights from observations and modeling. *The Cryosphere*, *14*(10), 3367–3380. https://doi.org/10.5194/tc-14-3367-2020

Kazmierczak, E., Sun, S., Coulon, V., & Pattyn, F. (2022). Subglacial hydrology modulates basal sliding response of the Antarctic ice sheet to climate forcing. *The Cryosphere*, *16*(10), 4537–4552. https://doi.org/10.5194/tc-16-4537-2022

Kazmierczak, E., Gregov, T., Coulon, V., & Pattyn, F. (2024). A fast and simplified subglacial hydrological model for the Antarctic Ice Sheet and outlet glaciers. *The Cryosphere*, 18(12), 5887–5911. https://doi.org/10.5194/tc-18-5887-2024

Keenan, E., Wever, N., Dattler, M., Lenaerts, J. T. M., Medley, B., Kuipers Munneke, P., & Reijmer, C. (2021). Physics-based SNOWPACK model improves representation of near-surface Antarctic snow and firn density. *The Cryosphere*, *15*(2), 1065–1085. https://doi.org/10.5194/tc-15-1065-2021

Keshmiri, S., Arnold, E., Blevins, A., Ewing, M., Hale, R., Leuschen, C., et al. (2017). Radar ECHO sounding of russell glacier at 35 MHz using compact radar systems on small unmanned aerial vehicles. In *2017 IEEE International Geoscience and Remote Sensing Symposium (IGARSS)* (pp. 5900–5903). Fort Worth, TX: IEEE. https://doi.org/10.1109/IGARSS.2017.8128352

Key, K., & Siegfried, M. R. (2017). The feasibility of imaging subglacial hydrology beneath ice streams with ground-based electromagnetics. *Journal of Glaciology*, *63*(241), 755–771. https://doi.org/10.1017/jog.2017.36

Khazendar, A., Rignot, E., & Larour, E. (2009). Roles of marine ice, rheology, and fracture in the flow and stability of the Brunt/Stancomb-Wills Ice Shelf. *Journal of Geophysical Research*, *114*(F4), F04007. https://doi.org/10.1029/2008JF001124

Khazendar, A., Schodlok, M. P., Fenty, I., Ligtenberg, S. R. M., Rignot, E., & van den Broeke, M. R. (2013). Observed thinning of Totten Glacier is linked to coastal polynya variability. *Nature Communications*, *4*(1), 2857. https://doi.org/10.1038/ncomms3857

Khazendar, A., Borstad, C. P., Scheuchl, B., Rignot, E., & Seroussi, H. (2015). The evolving instability of the remnant Larsen B Ice Shelf and its tributary glaciers. *Earth Planet. Sci. Lett.* https://doi.org/10.1016/j.epsl.2015.03.014

Killingbeck, S. F., Dow, C. F., & Unsworth, M. J. (2022). A quantitative method for deriving salinity of subglacial water using ground-based transient electromagnetics. *Journal of Glaciology*, *68*(268), 319–336. https://doi.org/10.1017/jog.2021.94

Kim, B.-H., Seo, K.-W., Eom, J., Chen, J., & Wilson, C. R. (2020). Antarctic ice mass variations from 1979 to 2017 driven by anomalous precipitation accumulation. *Scientific Reports*, *10*(1), 20366. https://doi.org/10.1038/s41598-020-77403-5

Kim, B.-H., Seo, K.-W., Lee, C.-K., Kim, J.-S., Chen, J., & Wilson, C. R. (2022). Antarctic Ice Mass Change (2003–2016) Jointly Estimated by Satellite Gravimetry and Altimetry. *Journal of Geophysical Research: Solid Earth*, *127*(9), e2021JB023297. https://doi.org/10.1029/2021JB023297

Kim, C.-S., Kim, T.-W., Cho, K.-H., Ha, H. K., Lee, S., Kim, H.-C., & Lee, J.-H. (2016). Variability of the Antarctic Coastal Current in the Amundsen Sea. *Estuarine, Coastal and Shelf Science*, *181*, 123–133. https://doi.org/10.1016/j.ecss.2016.08.004

Kim, H.R., Golynsky, A.V., Golynsky, D.A., Leftwich, T.E., Von Frese, R.R.B., Hong, J.K. and Lee, M. (2025). Antarctic magnetic anomalies and their gradients differentially reduced to the geomagnetic pole for enhanced crustal analysis. *Journal of Geophysical Research: Solid Earth*, 130(5), p.e2024JB029687. https://doi.org/10.1029/2024JB029687

Kingslake, J., Martín, C., Arthern, R. J., Corr, H. F. J., & King, E. C. (2016). Ice-flow reorganization in West Antarctica 2.5 kyr ago dated using radar-derived englacial flow velocities. *Geophysical Research Letters*, *43*(17), 9103–9112. https://doi.org/10.1002/2016GL070278

Kingslake, J., Ely, J. C., Das, I., & Bell, R. E. (2017). Widespread movement of meltwater onto and across Antarctic ice shelves. *Nature*, *544*(7650), 349–352. https://doi.org/10.1038/nature22049

Kittel, C., Amory, C., Hofer, S., Agosta, C., Jourdain, N. C., Gilbert, E., et al. (2022). Clouds drive differences in future surface melt over the Antarctic ice shelves. *The Cryosphere*, *16*(7), 2655–2669. https://doi.org/10.5194/tc-16-2655-2022

Koch I, Drews R, Franke S, et al. (2024). Radar internal reflection horizons from multisystem data reflect ice dynamic and surface accumulation history along the Princess Ragnhild Coast, Dronning Maud Land, East Antarctica. *Journal of Glaciology*. 70:e18. https://doi.org/10.1017/jog.2023.93

Koellner, S., Parizek, B. R., Alley, R. B., Muto, A., & Holschuh, N. (2019). The impact of spatially-variable basal properties on outlet glacier flow. *Earth and Planetary Science Letters*, *515*, 200–208. https://doi.org/10.1016/j.epsl.2019.03.026

Køltzow, M., Schyberg, H., Støylen, E., & Yang, X. (2022). Value of the Copernicus Arctic Regional Reanalysis (CARRA) in representing near-surface temperature and wind speed in the north-east European Arctic. *Polar Research*, *41*. https://doi.org/10.33265/polar.v41.8002

Konrad, H., Gilbert, L., Cornford, S. L., Payne, A., Hogg, A., Muir, A., & Shepherd, A. (2017). Uneven onset and pace of ice-dynamical imbalance in the Amundsen Sea Embayment, West Antarctica. *Geophysical Research Letters*, *44*(2), 910–918. https://doi.org/10.1002/2016GL070733

Konrad, H., Shepherd, A., Gilbert, L., Hogg, A. E., McMillan, M., Muir, A., & Slater, T. (2018). Net Retreat of Antarctic Glacier Grounding Lines. *Nature Geoscience*, *11*(4), 258–262. https://doi.org/10.1038/s41561-018-0082-z

Kopp, R. E., DeConto, R. M., Bader, D. A., Hay, C. C., Horton, R. M., Kulp, S., et al. (2017). Evolving Understanding of Antarctic Ice-Sheet Physics and Ambiguity in Probabilistic Sea-Level Projections. *Earth's Future*, *5*(12), 1217–1233. https://doi.org/10.1002/2017EF000663

Kornfeld, R. P., Arnold, B. W., Gross, M. A., Dahya, N. T., Klipstein, W. M., Gath, P. F., & Bettadpur, S. (2019). GRACE-FO: The Gravity Recovery and Climate Experiment Follow-On Mission. *Journal of Spacecraft and Rockets*, *56*(3), 931–951. https://doi.org/10.2514/1.A34326

Koutnik, M. R., Fudge, T. J., Conway, H., Waddington, E. D., Neumann, T. A., Cuffey, K. M., et al. (2016). Holocene accumulation and ice flow near the West Antarctic Ice Sheet Divide ice core site. *Journal of Geophysical Research: Earth Surface*, *121*(5), 907–924. https://doi.org/10.1002/2015JF003668

Kovacs, A., Gow, A. J., & Morey, R. M. (1995). The in-situ dielectric constant of polar firn revisited. *Cold Regions Science and Technology*, *23*(3), 245–256. https://doi.org/10.1016/0165-232X(94)00016-Q

Krabbendam, M., & Glasser, N. F. (2011). Glacial erosion and bedrock properties in NW Scotland: Abrasion and plucking, hardness and joint spacing. *Geomorphology, 130*(3), 374–383. https://doi.org/10.1016/j.geomorph.2011.04.022

Krabill, W. B., Abdalati, W., Frederick, E. B., Manizade, S. S., Martin, C. F., Sonntag, J. G., et al. (2002). Aircraft laser altimetry measurement of elevation changes of the greenland ice sheet: technique and accuracy assessment. *Journal of Geodynamics, 34*(3–4), 357–376. https://doi.org/10.1016/S0264-3707(02)00040-6

Kreuzer, M., Reese, R., Huiskamp, W.N., Petri, S., Albrecht, T., Feulner, G. and Winkelmann, R., 2021. Coupling framework (1.0) for the PISM (1.1. 4) ice sheet model and the MOM5 (5.1. 0) ocean model via the PICO ice shelf cavity model in an Antarctic domain. *Geoscientific Model Development*, 14(6), 3697-3714. https://doi.org/10.5194/gmd-14-3697-2021

Kristoffersen, Y., Hofstede, C., Diez, A., Blenkner, R., Lambrecht, A., Mayer, C., & Eisen, O. (2014). Reassembling Gondwana: A new high quality constraint from vibroseis exploration of the sub-ice shelf geology of the East Antarctic continental margin. *Journal of Geophysical Research: Solid Earth*, *119*(12), 9171–9182. https://doi.org/10.1002/2014JB011479

Kuipers Munneke, P., Ligtenberg, S. R. M., Noël, B. P. Y., Howat, I. M., Box, J. E., Mosley-Thompson, E., et al. (2015). Elevation change of the Greenland Ice Sheet due to surface mass balance and firn processes, 1960–2014. *The Cryosphere*, *9*(6), 2009–2025. https://doi.org/10.5194/tc-9-2009-2015

Kuipers Munneke, Peter, Ligtenberg, S. R. M., Van Den Broeke, M. R., & Vaughan, D. G. (2014). Firn air depletion as a precursor of Antarctic ice-shelf collapse. *Journal of Glaciology*, *60*(220), 205–214. https://doi.org/10.3189/2014JoG13J183

Kulessa, B. (2007). A Critical Review of the Low-Frequency Electrical Properties of Ice Sheets and Glaciers. *Journal of Environmental and Engineering Geophysics*, *12*(1), 23–36. https://doi.org/10.2113/JEEG12.1.23

Kulessa, B., Jansen, D., Luckman, A. J., King, E. C., & Sammonds, P. R. (2014). Marine ice regulates the future stability of a large Antarctic ice shelf. *Nature Communications*, *5*(1), 3707. https://doi.org/10.1038/ncomms4707

Kulessa, B., Key, K., Thompson, S., & Siegert, M. (2019). Heat and groundwater transport between the Antarctic Ice Sheet and subglacial sedimentary basins from electromagnetic geophysical measurements. In *SEG Technical Program Expanded Abstracts 2019* (pp. 4819–4823). San Antonio, Texas: Society of Exploration Geophysicists. https://doi.org/10.1190/segam2019-3215566.1

Kusahara, K., Reid, P., Williams, G. D., Massom, R., & Hasumi, H. (2018). An ocean-sea ice model study of the unprecedented Antarctic sea ice minimum in 2016. *Environmental Research Letters*, *13*(8), 084020. https://doi.org/10.1088/1748-9326/aad624

Kyrke-Smith, T. M., Gudmundsson, G. H., & Farrell, P. E. (2018). Relevance of Detail in Basal Topography for Basal Slipperiness Inversions: A Case Study on Pine Island Glacier, Antarctica. *Frontiers in Earth Science*, *6*, 33. https://doi.org/10.3389/feart.2018.00033

LaCoste, L., Ford, J., Bowles, R., & Archer, K. (1982). Gravity measurements in an airplane using state-of-the-art navigation and altimetry. *Geophysics*, *47*(5), 832–838. https://doi.org/10.1190/1.1441351

Lai, C.-Y., Kingslake, J., Wearing, M. G., Chen, P.-H. C., Gentine, P., Li, H., et al. (2020). Vulnerability of Antarctica's ice shelves to meltwater-driven fracture. *Nature*, *584*(7822), 574–578. https://doi.org/10.1038/s41586-020-2627-8

Larour, E., Seroussi, H., Adhikari, S., Ivins, E., Caron, L., Morlighem, M., & Schlegel, N. (2019). Slowdown in Antarctic mass loss from solid Earth and sea-level feedbacks. *Science*, *364*(6444), eaav7908. https://doi.org/10.1126/science.aav7908

de Lavergne, C., Madec, G., Roquet, F., Holmes, R. M., & McDougall, T. J. (2017). Abyssal ocean overturning shaped by seafloor distribution. *Nature*, *551*(7679), 181–186. https://doi.org/10.1038/nature24472

Le Brocq, A. M., Ross, N., Griggs, J. A., Bingham, R. G., Corr, H. F. J., Ferraccioli, F., et al. (2013). Evidence from ice shelves for channelized meltwater flow beneath the Antarctic Ice Sheet. *Nature Geoscience*, *6*(11), 945–948. https://doi.org/10.1038/ngeo1977

Le Meur, E., & Huybrechts, P. (1996). A comparison of different ways of dealing with isostasy: examples from modelling the Antarctic ice sheet during the last glacial cycle. *Annals of Glaciology*, *23*, 309–317. https://doi.org/10.3189/S0260305500013586

Le Meur, E., Magand, O., Arnaud, L., Fily, M., Frezzotti, M., Cavitte, M., et al. (2018). Spatial and temporal distributions of surface mass balance between Concordia and Vostok stations, Antarctica, from combined radar and ice core data: first results and detailed error analysis. *The Cryosphere*, *12*(5), 1831–1850. https://doi.org/10.5194/tc-12-1831-2018

Le Traon, P. Y., F. D'Ortenzio, M. Babin, E. Leymarie, C. Marec, S. Pouliquen, X. Xing, and colleagues (2020), Preparing the new phase of Argo: Scientific achievements of the NAOS project, *Front. Mar. Sci.*, 7, 577408, https://doi.org/10.3389/fmars.2020.577408.

Lee, C. M., M. DeGrandpre, J. Guthrie, V. Hill, R. Kwok, J. Morison, C. J. Cox, H. Singh, T. P. Stanton, and J. Wilkinson (2022), Emerging technologies and approaches for in situ, autonomous observing in the Arctic, *Oceanography*, 35, 210–221, https://doi.org/10.5670/oceanog.2022.127.

Lemieux, J.-M., Sudicky, E. A., Peltier, W. R., & Tarasov, L. (2008). Dynamics of groundwater recharge and seepage over the Canadian landscape during the Wisconsinian glaciation. *Journal of Geophysical Research*, *113*(F1), F01011. https://doi.org/10.1029/2007JF000838

Lenaerts, J. T. M., Meijgaard, E., Broeke, M. R., Ligtenberg, S. R. M., Horwath, M., & Isaksson, E. (2013). Recent snowfall anomalies in Dronning Maud Land, East Antarctica, in a historical and future climate perspective. *Geophysical Research Letters*, *40*(11), 2684–2688. https://doi.org/10.1002/grl.50559

Lenaerts, J. T. M., Brown, J., Van Den Broeke, M. R., Matsuoka, K., Drews, R., Callens, D., et al. (2014). High variability of climate and surface mass balance induced by Antarctic ice rises. *Journal of Glaciology*, *60*(224), 1101–1110. https://doi.org/10.3189/2014JoG14J040

Lenaerts, J. T. M., Medley, B., Van Den Broeke, M. R., & Wouters, B. (2019). Observing and Modeling Ice Sheet Surface Mass Balance. *Reviews of Geophysics*, *57*(2), 376–420. https://doi.org/10.1029/2018RG000622

Leong, W. J., & Horgan, H. J. (2020). DeepBedMap: a deep neural network for resolving the bed topography of Antarctica. *The Cryosphere*, *14*(11), 3687–3705. https://doi.org/10.5194/tc-14-3687-2020

Lepp, A.P., Simkins, L.M., Anderson, J.B., Clark, R.W., Wellner, J.S., Hillenbrand, C.D., Smith, J.A., Lehrmann, A.A., Totten, R., Larter, R.D. and Hogan, K.A., 2022. Sedimentary signatures of persistent subglacial meltwater drainage from Thwaites Glacier, Antarctica. Frontiers in Earth Science, 10, p.863200, https://doi.org/10.3389/feart.2022.863200

Leuschen, C., Hale, R., Keshmiri, S., Yan, J. B., Rodriguez-Morales, F., Mahmood, A., & Gogineni, S. (2014). UAS-Based Radar Sounding of the Polar Ice Sheets. *IEEE Geoscience and Remote Sensing Magazine*, *2*(1), 8–17. https://doi.org/10.1109/MGRS.2014.2306353

Levermann, A., Winkelmann, R., Albrecht, T., Goelzer, H., Golledge, N. R., Greve, R., et al. (2020). Projecting Antarctica's contribution to future sea level rise from basal ice shelf melt using linear response functions of 16 ice sheet models (LARMIP-2). *Earth System Dynamics*, *11*(1), 35–76. https://doi.org/10.5194/esd-11-35-2020

Lhermitte, S., Sun, S., Shuman, C., Wouters, B., Pattyn, F., Wuite, J., et al. (2020). Damage accelerates ice shelf instability and mass loss in Amundsen Sea Embayment. *Proceedings of the National Academy of Sciences*, *117*(40), 24735–24741. https://doi.org/10.1073/pnas.1912890117

Li, J., Paden, J., Leuschen, C., Rodriguez-Morales, F., Hale, R. D., Arnold, E. J., et al. (2013). High-Altitude Radar Measurements of Ice Thickness Over the Antarctic and Greenland Ice Sheets as a Part of Operation IceBridge. *IEEE Transactions on Geoscience and Remote Sensing*, *51*(2), 742–754. https://doi.org/10.1109/TGRS.2012.2203822

Li, L., & Aitken, A. R. A. (2024) Crustal heterogeneity of Antarctica signals spatially variable radiogenic heat production. *Geophysical Research Letters,* 51(2), e2023GL106201. https://doi.org/10.1029/2023GL106201

Li, Q., England, M. H., Hogg, A. M., Rintoul, S. R., & Morrison, A. K. (2023). Abyssal ocean overturning slowdown and warming driven by Antarctic meltwater. *Nature*, *615*(7954), 841–847. https://doi.org/10.1038/s41586-023-05762-w

Li, L., Aitken, A. R. A., Lindsay, M. D., & Kulessa, B. (2022a). Sedimentary basins reduce stability of Antarctic ice streams through groundwater feedbacks. *Nature Geoscience*, *15*(8), 645–650. https://doi.org/10.1038/s41561-022-00992-5

Li, L., Aitken, A.R., Gross, L. and Codd, A., 2025. Resolving mantle composition suggests a warmer East Antarctic mantle. *Journal of Geophysical Research: Solid Earth*, 130(3), p.e2024JB029677.

Li, T., Dawson, G. J., Chuter, S. J., & Bamber, J. L. (2022b). A high-resolution Antarctic grounding zone product from ICESat-2 laser altimetry. *Earth System Science Data*, *14*(2), 535–557. https://doi.org/10.5194/essd-14-535-2022

Li, W., Wu, Y., & Hu, X. (2023). The Processes-Based Attributes of Four Major Surface Melting Events over the Antarctic Ross Ice Shelf. *Advances in Atmospheric Sciences*. https://doi.org/10.1007/s00376-023-2287-3

Li, X., Rignot, E., Morlighem, M., Mouginot, J., & Scheuchl, B. (2015). Grounding line retreat of Totten Glacier, East Antarctica, 1996 to 2013. *Geophysical Research Letters*, *42*(19), 8049–8056. https://doi.org/10.1002/2015GL065701

Ligtenberg, S. R. M., Helsen, M. M., & Van Den Broeke, M. R. (2011). An improved semi-empirical model for the densification of Antarctic firn. *The Cryosphere*, *5*(4), 809–819. https://doi.org/10.5194/tc-5-809-2011

Ligtenberg, S. R. M., Medley, B., Broeke, M. R. V. D., & Munneke, P. K. (2015). Antarctic firn compaction rates from repeat-track airborne radar data: II. Firn model evaluation. *Annals of Glaciology*, *56*(70), 167–174. https://doi.org/10.3189/2015AoG70A204

Liljedahl, L. C., Meierbachtol, T., Harper, J., van As, D., Näslund, J.-O., Selroos, J.-O., et al. (2021). Rapid and sensitive response of Greenland’s groundwater system to ice sheet change. *Nature Geoscience*, *14*(10), 751–755. https://doi.org/10.1038/s41561-021-00813-1

Lindbäck, K., Moholdt, G., Nicholls, K. W., Hattermann, T., Pratap, B., Thamban, M., & Matsuoka, K. (2019). Spatial and temporal variations in basal melting at Nivlisen ice shelf, East Antarctica, derived from phase-sensitive radars. *The Cryosphere*, *13*(10), 2579–2595. https://doi.org/10.5194/tc-13-2579-2019

Lindzey, L. E., Beem, L. H., Young, D. A., Quartini, E., Blankenship, D. D., Lee, C.-K., et al. (2020). Aerogeophysical characterization of an active subglacial lake system in the David Glacier catchment, Antarctica. *The Cryosphere, 14*(7), 2217–2233. https://doi.org/10.5194/tc-14-2217-2020

Liao, S., Luo, H., Wang, J., Shi, Q., Zhang, J. and Yang, Q., 2021. An Evaluation of Antarctic Sea Ice Thickness from the Global Ice-Ocean Modeling and Assimilation System based on In-situ and Satellite Observations. *The Cryosphere*, 16, 1807-1819. https://doi.org/10.5194/tc-16-1807-2022

Lipscomb, W. H., Fyke, J. G., Vizcaíno, M., Sacks, W. J., Wolfe, J., Vertenstein, M., et al. (2013). Implementation and Initial Evaluation of the Glimmer Community Ice Sheet Model in the Community Earth System Model. *Journal of Climate*, *26*(19), 7352–7371. https://doi.org/10.1175/JCLI-D-12-00557.1

Lipscomb, W.H., Price, S.F., Hoffman, M.J., Leguy, G.R., Bennett, A.R., Bradley, S.L., Evans, K.J., Fyke, J.G., Kennedy, J.H., Perego, M. and Ranken, D.M., 2019. Description and evaluation of the community ice sheet model (CISM) v2. 1. *Geoscientific Model Development*, 12(1), 387-424, https://doi.org/10.5194/gmd-12-387-2019.

van Lipzig, N. P. M., Meijgaard, E. van, & Oerlemans, J. (2002). The spatial and temporal variability of the surface mass balance in Antarctica: results from a regional atmospheric climate model. *International Journal of Climatology*, *22*(10), 1197–1217. https://doi.org/10.1002/joc.798

Liu, C., Wang, Z., Liang, X., Li, X., Li, X., Cheng, C., & Qi, D. (2022). Topography-mediated Transport of Warm Deep Water across the Continental Shelf Slope, East Antarctica. *Journal of Physical Oceanography*. https://doi.org/10.1175/JPO-D-22-0023.1

Liu, Y., Moore, J. C., Cheng, X., Gladstone, R. M., Bassis, J. N., Liu, H., et al. (2015). Ocean-driven thinning enhances iceberg calving and retreat of Antarctic ice shelves. *Proceedings of the National Academy of Sciences*, *112*(11), 3263–3268. https://doi.org/10.1073/pnas.1415137112

Livingstone, S. J., Clark, C. D., Woodward, J., & Kingslake, J. (2013). Potential subglacial lake locations and meltwater drainage pathways beneath the Antarctic and Greenland ice sheets. *Cryosphere*, *7*(6), 1721–1740. https://doi.org/10.5194/tc-7-1721-2013

Livingstone, Stephen J., Li, Y., Rutishauser, A., Sanderson, R. J., Winter, K., Mikucki, J. A., et al. (2022). Subglacial lakes and their changing role in a warming climate. *Nature Reviews Earth & Environment*, *3*(2), 106–124. https://doi.org/10.1038/s43017-021-00246-9

Lloyd, A. J., Wiens, D. A., Zhu, H., Tromp, J., Nyblade, A. A., Aster, R. C., et al. (2020). Seismic Structure of the Antarctic Upper Mantle Imaged with Adjoint Tomography. *Journal of Geophysical Research: Solid Earth*, *125*(3), 2019JB017823. https://doi.org/10.1029/2019JB017823

Loomis, B. D., Luthcke, S. B., & Sabaka, T. J. (2019). Regularization and error characterization of GRACE mascons. *Journal of Geodesy*, *93*(9), 1381–1398. https://doi.org/10.1007/s00190-019-01252-y

Lösing, M., Aitken, A., Ebbing, J., Halpin, J. A., Li, L., Moorkamp, M., et al. (2025). Linking Tectonics and Crustal Thermal Properties in Southwestern Australia and East Antarctica Through Coupled Gravity and Magnetic Analysis. *Journal of Geophysical Research: Solid Earth*, *130*(12), e2024JB030770. https://doi.org/10.1029/2024JB030770

Lösing, M. (2022). Antarctic Geothermal Heat Flow: Investigations by Geophysical and Statistical Analyses. Retrieved from https://macau.uni-kiel.de/receive/macau_mods_00003271

Lösing, M., & Ebbing, J. (2021). Predicting Geothermal Heat Flow in Antarctica With a Machine Learning Approach. *Journal of Geophysical Research: Solid Earth*, *126*(6). https://doi.org/10.1029/2020JB021499

Lösing, M., Ebbing, J., & Szwillus, W. (2020). Geothermal Heat Flux in Antarctica: Assessing Models and Observations by Bayesian Inversion. *Frontiers in Earth Science*, *8*, 105. https://doi.org/10.3389/feart.2020.00105

Lösing, M., Moorkamp, M., & Ebbing, J. (2022). Joint inversion based on variation of information—a crustal model of Wilkes Land, East Antarctica. *Geophysical Journal International*, *232*(1), 162–175. https://doi.org/10.1093/gji/ggac334

Lowe, M., Mather, B., Green, C., Jordan, T.A., Ebbing, J. and Larter, R., 2023. Anomalously high heat flow regions beneath the Transantarctic Mountains and Wilkes Subglacial Basin in East Antarctica inferred from curie depth. *Journal of Geophysical Research: Solid Earth*, *128*(1), p.e2022JB025423. https://doi.org/10.1029/2022JB025423
Lumpkin, R., & Speer, K. (2007). Global Ocean Meridional Overturning. *Journal of Physical Oceanography*, *37*(10), 2550–2562. https://doi.org/10.1175/JPO3130.1

Lu, T., Zhang, S., Xiao, F., Li, J., Geng, T., Luo, H., Yang, Y. and Wu, H. (2025). Determination of mass changes in the Totten Glacier Basin, East Antarctica, using an improved mascon method with GRACE/GRACE-FO data. *Journal of Geophysical*

Research: Solid Earth, 130(12), p.e2025JB031384. https://doi.org/10.1029/2025JB031384.

Luthcke, S. B., Zwally, H. J., Abdalati, W., Rowlands, D. D., Ray, R. D., Nerem, R. S., et al. (2006). Recent Greenland Ice Mass Loss by Drainage System from Satellite Gravity Observations. *Science*, *314*(5803), 1286–1289. https://doi.org/10.1126/science.1130776

Lythe, M. B., Vaughan, D. G., and the BEDMAP consortium (2001). BEDMAP: A new ice thickness and subglacial topographic model of Antarctica. *Journal of Geophysical Research: Solid Earth*, *106*(B6), 11335–11351. https://doi.org/10.1029/2000JB900449

Macelloni, G., Leduc-Leballeur, M., Montomoli, F., Brogioni, M., Ritz, C., & Picard, G. (2019). On the retrieval of internal temperature of Antarctica Ice Sheet by using SMOS observations. *Remote Sensing of Environment*, *233*, 111405. https://doi.org/10.1016/j.rse.2019.111405

MacFerrin, M., Machguth, H., As, D. van, Charalampidis, C., Stevens, C. M., Heilig, A., et al. (2019). Rapid expansion of Greenland's low-permeability ice slabs. *Nature*, *573*(7774), 403–407. https://doi.org/10.1038/s41586-019-1550-3

MacGregor, J. A., Winebrenner, D. P., Conway, H., Matsuoka, K., Mayewski, P. A., & Clow, G. D. (2007). Modeling englacial radar attenuation at Siple Dome, West Antarctica, using ice chemistry and temperature data. *Journal of Geophysical Research*, *112*(F3), F03008. https://doi.org/10.1029/2006JF000717

MacGregor, J. A., Boisvert, L. N., Medley, B., Petty, A. A., Harbeck, J. P., Bell, R. E., et al. (2021). The Scientific Legacy of NASA's Operation IceBridge. *Reviews of Geophysics*, *59*(2). https://doi.org/10.1029/2020RG000712

MacKie, E. J., Schroeder, D. M., Zuo, C., Yin, Z., & Caers, J. (2021). Stochastic modeling of subglacial topography exposes uncertainty in water routing at Jakobshavn Glacier. *Journal of Glaciology*, *67*(261), 75–83. https://doi.org/10.1017/jog.2020.84

Maclennan, M. L., Lenaerts, J. T. M., Shields, C. A., Hoffman, A. O., Wever, N., Thompson-Munson, M., et al. (2023). Climatology and surface impacts of atmospheric rivers on West Antarctica. *The Cryosphere*, *17*(2), 865–881. https://doi.org/10.5194/tc-17-865-2023

Magruder, L., Brunt, K., Neumann, T., Klotz, B. and Alonzo, M., 2021. Passive ground-based optical techniques for monitoring the on-orbit ICESat-2 altimeter geolocation and footprint diameter. *Earth and Space Science*, 8(10), p.e2020EA001414.

Mantelli, E., & Schoof, C. (2019). Ice sheet flow with thermally activated sliding. Part 2: the stability of subtemperate regions. *Proceedings of the Royal Society A: Mathematical, Physical and Engineering Sciences*, *475*(2231), 20190411. https://doi.org/10.1098/rspa.2019.0411

Mantelli, E., Haseloff, M., & Schoof, C. (2019). Ice sheet flow with thermally activated sliding. Part 1: the role of advection. *Proceedings of the Royal Society A: Mathematical, Physical and Engineering Sciences*, *475*(2230), 20190410. https://doi.org/10.1098/rspa.2019.0410

Maritati, A., Danišík, M., Halpin, J. A., Whittaker, J. M., & Aitken, A. R. A. (2020). Pangea Rifting Shaped the East Antarctic Landscape. *Tectonics*, *39*(8). https://doi.org/10.1029/2020TC006180

Markus, T., Neumann, T., Martino, A., Abdalati, W., Brunt, K., Csatho, B., et al. (2017). The Ice, Cloud, and land Elevation Satellite-2 (ICESat-2): Science requirements, concept, and implementation. *Remote Sensing of Environment*, *190*, 260–273. https://doi.org/10.1016/j.rse.2016.12.029

Marshall, G. J. (2003). Trends in the Southern Annular Mode from Observations and Reanalyses. *Journal of Climate*, *16*(24), 4134–4143. https://doi.org/10.1175/1520-0442(2003)016<4134:TITSAM>2.0.CO;2

Marshall, J., & Speer, K. (2012). Closure of the meridional overturning circulation through Southern Ocean upwelling. *Nature Geoscience*, *5*(3), 171–180. https://doi.org/10.1038/ngeo1391

Martin, C., Gudmundsson, G. H., & King, E. C. (2014). Modelling of Kealey Ice Rise, Antarctica, reveals stable ice-flow conditions in East Ellsworth Land over millennia. *Journal of Glaciology*, *60*(219), 139–146. https://doi.org/10.3189/2014JoG13J089

Martos, Y. M., Catalán, M., Jordan, T. A., Golynsky, A., Golynsky, D., Eagles, G., & Vaughan, D. G. (2017). Heat Flux Distribution of Antarctica Unveiled. *Geophysical Research Letters*, *44*(22), 11,417-11,426. https://doi.org/10.1002/2017GL075609

Mas E Braga, M., Selwyn Jones, R., Newall, J. C. H., Rogozhina, I., Andersen, J. L., Lifton, N. A., & Stroeven, A. P. (2021). Nunataks as barriers to ice flow: implications for palaeo ice sheet reconstructions. *The Cryosphere*, *15*(10), 4929–4947. https://doi.org/10.5194/tc-15-4929-2021

Massom, R. A., Scambos, T. A., Bennetts, L. G., Reid, P., Squire, V. A., & Stammerjohn, S. E. (2018). Antarctic ice shelf disintegration triggered by sea ice loss and ocean swell. *Nature*, *558*(7710), 383–389. https://doi.org/10.1038/s41586-018-0212-1

Matsuoka, K., Furukawa, T., Fujita, S., Maeno, H., Uratsuka, S., Naruse, R., & Watanabe, O. (2003). Crystal orientation fabrics within the Antarctic ice sheet revealed by a multipolarization plane and dual-frequency radar survey. *Journal of Geophysical Research: Solid Earth*, *108*(B10). https://doi.org/10.1029/2003JB002425

Matsuoka, K., MacGregor, J. A., & Pattyn, F. (2012). Predicting radar attenuation within the Antarctic ice sheet. *Earth and Planetary Science Letters*, *359–360*, 173–183. https://doi.org/10.1016/j.epsl.2012.10.018

Matsuoka, K., Hindmarsh, R. C. A., Moholdt, G., Bentley, M. J., Pritchard, H. D., Brown, J., et al. (2015). Antarctic ice rises and rumples: their properties and significance for ice-sheet dynamics and evolution. *Earth Sci. Rev.*, *150*, 724–745. https://doi.org/10.1016/j.earscirev.2015.09.004

Matsuoka, K., Skoglund, A., Roth, G., De Pomereu, J., Griffiths, H., Headland, R., et al. (2021). Quantarctica, an integrated mapping environment for Antarctica, the Southern Ocean, and sub-Antarctic islands. *Environmental Modelling & Software*, *140*, 105015. https://doi.org/10.1016/j.envsoft.2021.105015

Matsuoka, K., Forsberg, R., Ferraccioli, F., Moholdt, G., & Morlighem, M. (2022). Circling Antarctica to Unveil the Bed Below Its Icy Edge. *Eos*, *103*. https://doi.org/10.1029/2022EO220276

Matsuoka, K. and C. Shackleton (2026). Bed topography data gaps in the Antarctic Ice Sheet margin zone revealed by new analysis of Bedmap3 database for Antarctic RINGS, *Phiol. Trans. A*, https://doi.org/ 10.1098/rsta.2025.0371

Maule, C. F., Purucker, M. E., Olsen, N., & Mosegaard, K. (2005). Heat Flux Anomalies in Antarctica Revealed by Satellite Magnetic Data. *Science*, *309*(5733), 464–467. https://doi.org/10.1126/science.1106888

McCormack, F. S., Roberts, J. L., Gwyther, D. E., Morlighem, M., Pelle, T., & Galton-Fenzi, B. K. (2021). The Impact of Variable Ocean Temperatures on Totten Glacier Stability and Discharge. *Geophysical Research Letters*, *48*(10), e2020GL091790. https://doi.org/10.1029/2020GL091790

McCormack, F. S., Roberts, J. L., Dow, C. F., Stål, T., Halpin, J. A., Reading, A. M., & Siegert, M. J. (2022). Fine-Scale Geothermal Heat Flow in Antarctica Can Increase Simulated Subglacial Melt Estimates. *Geophysical Research Letters*, *49*(15), e2022GL098539. https://doi.org/10.1029/2022GL098539

McCormack, F. S., Warner, R. C., Seroussi, H., Dow, C. F., Roberts, J. L., & Treverrow, A. (2022). Modeling the Deformation Regime of Thwaites Glacier, West Antarctica, Using a Simple Flow Relation for Ice Anisotropy (ESTAR). *Journal of Geophysical Research: Earth Surface*, *127*(3), e2021JF006332. https://doi.org/10.1029/2021JF006332

McCormack, F. S., Stål, T., Shao, N., MacKie, E., Fabela, A., Lösing, M., et al. (2025). Synthetic bed topographies for Antarctica and their utility in ice sheet modelling. *Philosophical Transactions A.* https://doi.org/10.1098/rsta.2024-0537, accepted.

Medley, B., & Thomas, E. R. (2019). Increased snowfall over the Antarctic Ice Sheet mitigated twentieth-century sea-level rise. *Nature Climate Change*, *9*(1), 34–39. https://doi.org/10.1038/s41558-018-0356-x

Medley, B., Joughin, I., Das, S. B., Steig, E. J., Conway, H., Gogineni, S., et al. (2013). Airborne-radar and ice-core observations of annual snow accumulation over Thwaites Glacier, West Antarctica confirm the spatiotemporal variability of global and regional atmospheric models. *Geophysical Research Letters*, *40*(14), 3649–3654. https://doi.org/10.1002/grl.50706

Medley, B., Joughin, I., Smith, B. E., Das, S. B., Steig, E. J., Conway, H., et al. (2014). Constraining the recent mass balance of Pine Island and Thwaites glaciers, West Antarctica, with airborne observations of snow accumulation. *The Cryosphere*, *8*(4), 1375–1392. https://doi.org/10.5194/tc-8-1375-2014

Medley, B., Ligtenberg, S. R. M., Joughin, I., Van den Broeke, M. R., Gogineni, S., & Nowicki, S. (2015). Antarctic firn compaction rates from repeat-track airborne radar data: I. Methods. *Annals of Glaciology*, *56*(70), 155–166. https://doi.org/10.3189/2015AoG70A203

Medley, B., McConnell, J. R., Neumann, T. A., Reijmer, C. H., Chellman, N., Sigl, M., & Kipfstuhl, S. (2018). Temperature and Snowfall in Western Queen Maud Land Increasing Faster Than Climate Model Projections. *Geophysical Research Letters*, *45*(3), 1472–1480. https://doi.org/10.1002/2017GL075992

Medley, B., Neumann, T. A., Zwally, H. J., Smith, B. E., & Stevens, C. M. (2022). Simulations of firn processes over the Greenland and Antarctic ice sheets: 1980–2021. *The Cryosphere*, *16*(10), 3971–4011. https://doi.org/10.5194/tc-16-3971-2022

Meehl, G. A., Arblaster, J. M., Chung, C. T. Y., Holland, M. M., DuVivier, A., Thompson, L., et al. (2019). Sustained ocean changes contributed to sudden Antarctic sea ice retreat in late 2016. *Nature Communications*, *10*(1), 14. https://doi.org/10.1038/s41467-018-07865-9

Van Der Meer, M., de Roda Husman, S. and Lhermitte, S., 2023. Deep learning regional climate model emulators: A comparison of two downscaling training frameworks. *Journal of Advances in Modeling Earth Systems*, *15*(6), p.e2022MS003593. https://doi.org/10.1029/2022MS003593 Mengel, M., & Levermann, A. (2014). Ice plug prevents irreversible discharge from East Antarctica. *Nature Climate Change*, *4*(6), 451–455. https://doi.org/10.1038/nclimate2226

Mercer, J. H. (1978). West Antarctic ice sheet and CO2 greenhouse effect: a threat of disaster. *Nature*, *271*(5643), 321–325. https://doi.org/10.1038/271321a0

Michaelis, I., Styp-Rekowski, K., Rauberg, J. et al. (2022). Geomagnetic data from the GOCE satellite mission. *Earth Planets Space* 74, 135. https://doi.org/10.1186/s40623-022-01691-6

Mikucki, J. A., Auken, E., Tulaczyk, S., Virginia, R. A., Schamper, C., Sørensen, K. I., et al. (2015). Deep groundwater and potential subsurface habitats beneath an Antarctic dry valley. *Nature Communications*, *6*(1), 6831. https://doi.org/10.1038/ncomms7831

Miles, B. W. J., Stokes, C. R., & Jamieson, S. S. R. (2016). Pan–ice-sheet glacier terminus change in East Antarctica reveals sensitivity of Wilkes Land to sea-ice changes. *Science Advances*, *2*(5), e1501350. https://doi.org/10.1126/sciadv.1501350

Miles, B. W. J., Stokes, C. R., & Jamieson, S. S. R. (2017). Simultaneous disintegration of outlet glaciers in Porpoise Bay (Wilkes Land), East Antarctica, driven by sea ice break-up. *The Cryosphere*, *11*(1), 427–442. https://doi.org/10.5194/tc-11-427-2017

Miles, B. W. J., Jordan, J. R., Stokes, C. R., Jamieson, S. S. R., Gudmundsson, G. H., & Jenkins, A. (2021). Recent acceleration of Denman Glacier (1972–2017), East Antarctica, driven by grounding line retreat and changes in ice tongue configuration. *The Cryosphere*, *15*(2), 663–676. https://doi.org/10.5194/tc-15-663-2021

Miles, B. W. J., Stokes, C. R., Jamieson, S. S. R., Jordan, J. R., Gudmundsson, G. H., & Jenkins, A. (2022). High spatial and temporal variability in Antarctic ice discharge linked to ice shelf buttressing and bed geometry. *Scientific Reports*, *12*(1), 10968. https://doi.org/10.1038/s41598-022-13517-2

Milillo, P., Rignot, E., Rizzoli, P., Scheuchl, B., Mouginot, J., Bueso-Bello, J., & Prats-Iraola, P. (2019). Heterogeneous retreat and ice melt of Thwaites Glacier, West Antarctica. *Science Advances*, *5*(1), eaau3433. https://doi.org/10.1126/sciadv.aau3433

Milillo, Pietro, Rignot, E., Mouginot, J., Scheuchl, B., Morlighem, M., Li, X., & Salzer, J. T. (2017). On the Short-term Grounding Zone Dynamics of Pine Island Glacier, West Antarctica, Observed With COSMO-SkyMed Interferometric Data: PIG Grounding Line Dynamics. *Geophysical Research Letters*, *44*(20), 10,436-10,444. https://doi.org/10.1002/2017GL074320

Millan, R., Rignot, E., Bernier, V., Morlighem, M., & Dutrieux, P. (2017). Bathymetry of the Amundsen Sea Embayment sector of West Antarctica from Operation IceBridge gravity and other data. *Geophysical Research Letters*, *44*(3), 1360–1368. https://doi.org/10.1002/2016GL072071

Millstein, J. D., Minchew, B. M., & Pegler, S. S. (2022). Ice Viscosity Is More Sensitive to Stress than Commonly Assumed. *Communications Earth & Environment*, *3*(1), 1–7. https://doi.org/10.1038/s43247-022-00385-x

Minchew, B. M., Simons, M., Riel, B., & Milillo, P. (2017). Tidally induced variations in vertical and horizontal motion on Rutford Ice Stream, West Antarctica, inferred from remotely sensed observations. *Journal of Geophysical Research: Earth Surface*, *122*(1), 167–190. https://doi.org/10.1002/2016JF003971

Minchew, B. M., Meyer, C. R., Robel, A. A., Gudmundsson, G. H., & Simons, M. (2018). Processes Controlling the Downstream Evolution of Ice Rheology in Glacier Shear Margins: Case Study on Rutford Ice Stream, West Antarctica. *Journal of Glaciology*, 1–12, https://doi.org/10.1017/jog.2018.47

Minowa, M., Sugiyama, S., Ito, M., Yamane, S., & Aoki, S. (2021). Thermohaline structure and circulation beneath the Langhovde Glacier ice shelf in East Antarctica. *Nature Communications*, *12*(1), 4209. https://doi.org/10.1038/s41467-021-23534-w

Mohajerani, Y., Jeong, S., Scheuchl, B., Velicogna, I., Rignot, E., & Milillo, P. (2021). Automatic delineation of glacier grounding lines in differential interferometric synthetic-aperture radar data using deep learning. *Scientific Reports*, *11*(1), 4992. https://doi.org/10.1038/s41598-021-84309-3

Moholdt, G., & Matsuoka, K. (2015). Inventory of Antarctic ice rises and rumples (version 1) [Data set]. npolar.no. https://doi.org/10.21334/NPOLAR.2015.9174E644

Moorkamp, M., Heincke, B., Jegen, M., Roberts, A. W., & Hobbs, R. W. (2011). A framework for 3-D joint inversion of MT, gravity and seismic refraction data: 3-D joint inversion. *Geophysical Journal International*, *184*(1), 477–493. https://doi.org/10.1111/j.1365-246X.2010.04856.x

Moon, JY., An, SI., Mandal, G. et al. (2025). Antarctic meltwater spread pattern and its duration modulate abyssal circulation. *Commun Earth Environ* 6, 586. https://doi.org/10.1038/s43247-025-02589-3

Morioka, Y., Iovino, D., Cipollone, A., Masina, S., & Behera, S. K. (2022). Decadal Sea Ice Prediction in the West Antarctic Seas with Ocean and Sea Ice Initializations. *Communications Earth & Environment*, *3*(1), 189. https://doi.org/10.1038/s43247-022-00529-z

Morlighem, M., Rignot, E., Seroussi, H., Larour, E., Ben Dhia, H., & Aubry, D. (2011). A mass conservation approach for mapping glacier ice thickness, *Geophysical Research Letters*, *38*(19), https://doi.org/10.1029/2011GL048659

Morlighem, M., Seroussi, H., Larour, E., & Rignot, E. (2013). Inversion of basal friction in Antarctica using exact and incomplete adjoints of a higher-order model. *Journal of Geophysical Research: Earth Surface*, *118*(3), 1746–1753. https://doi.org/10.1002/jgrf.20125

Morlighem, M., Rignot, E., & Willis, J. (2016). Improving Bed Topography Mapping of Greenland Glaciers Using NASA's Oceans Melting Greenland (OMG) Data. *Oceanography*, *29*(4), 62–71. https://doi.org/10.5670/oceanog.2016.99

Morlighem, M., Rignot, E., Binder, T., Blankenship, D., Drews, R., Eagles, G., et al. (2020). Deep glacial troughs and stabilizing ridges unveiled beneath the margins of the Antarctic ice sheet. *Nature Geoscience*, *13*(2), 132–137. https://doi.org/10.1038/s41561-019-0510-8

Morlighem, M., Goldberg, D., Santos, T. D. D., Lee, J., & Sagebaum, M. (2021). Mapping the sensitivity of the Amundsen Sea Embayment to changes in external forcings using Automatic Differentiation. *Geophysical Research Letters, 48*(23). https://doi.org/10.1029/2021GL095440

Morlighem, M., Goldberg, D., Barnes, J.M., Bassis, J.N., Benn, D.I., Crawford, A.J., Gudmundsson, G.H. and Seroussi, H. (2024) The West Antarctic Ice Sheet may not be vulnerable to marine ice cliff instability during the 21st century. *Science Advances*, 10(34), p.eado7794, https://doi.org/10.1126/sciadv.ado7794

Moss, G., Višnjević, V., Eisen, O., Oraschewski, F. M., Schröder, C., Macke, J. H., & Drews, R. (2025). Simulation-based inference of surface accumulation and basal melt rates of an Antarctic ice shelf from isochronal layers. *Journal of Glaciology*, 71, e44. https://doi.org/10.1017/jog.2025.13

Mottram, R., Hansen, N., Kittel, C., van Wessem, J. M., Agosta, C., Amory, C., et al. (2021). What is the surface mass balance of Antarctica? An intercomparison of regional climate model estimates. *The Cryosphere*, *15*(8), 3751–3784. https://doi.org/10.5194/tc-15-3751-2021

Mouginot, J., Rignot, E., & Scheuchl, B. (2014). Sustained increase in ice discharge from the Amundsen Sea Embayment, West Antarctica, from 1973 to 2013. *Geophysical Research Letters*, *41*(5), 1576–1584. https://doi.org/10.1002/2013GL059069

Mouginot, J., Rignot, E., Scheuchl, B., & Millan, R. (2017). Comprehensive Annual Ice Sheet Velocity Mapping Using Landsat-8, Sentinel-1, and RADARSAT-2 Data. *Remote Sensing*, *9*(4), 364. https://doi.org/10.3390/rs9040364

Mouginot, J., Rignot, E., & Scheuchl, B. (2019). Continent-Wide, Interferometric SAR Phase, Mapping of Antarctic Ice Velocity. *Geophysical Research Letters, 46*(16), 9710–9718. https://doi.org/10.1029/2019GL083826

Muilwijk, M., Straneo, F., Slater, D. A., Smedsrud, L. H., Holte, J., Wood, M., et al. (2022). Export of Ice Sheet Meltwater from Upernavik Fjord, West Greenland. *Journal of Physical Oceanography*, *52*(3), 363–382. https://doi.org/10.1175/JPO-D-21-0084.1

Mulder, J. A., Halpin, J. A., Daczko, N. R., Orth, K., Meffre, S., Thompson, J. M., & Morrissey, L. J. (2019). A Multiproxy provenance approach to uncovering the assembly of East Gondwana in Antarctica. *Geology*, *47*(7), 645–649. https://doi.org/10.1130/G45952.1

Mulvaney, R., Alemany, O., & Possenti, P. (2007). The Berkner Island (Antarctica) ice-core drilling project. *Annals of Glaciology*, *47*, 115–124. https://doi.org/10.3189/172756407786857758

Mulvaney, R., Rix, J., Polfrey, S., Grieman, M., Martìn, C., Nehrbass-Ahles, C., et al. (2021). Ice drilling on Skytrain Ice Rise and Sherman Island, Antarctica. *Annals of Glaciology*, *62*(85–86), 311–323. https://doi.org/10.1017/aog.2021.7

Muntjewerf, L., Sacks, W. J., Lofverstrom, M., Fyke, J., Lipscomb, W. H., Ernani da Silva, C., et al. (2021). Description and Demonstration of the Coupled Community Earth System Model v2 – Community Ice Sheet Model v2 (CESM2-CISM2). *Journal of Advances in Modeling Earth Systems*, 13(6), e2020MS002356. https://doi.org/10.1029/2020MS002356

Muto, A., Anandakrishnan, S., Alley, R. B., Horgan, H. J., Parizek, B. R., Koellner, S., et al. (2019). Relating bed character and subglacial morphology using seismic data from

Thwaites Glacier, West Antarctica. *Earth and Planetary Science Letters*, *507*, 199–206. https://doi.org/10.1016/j.epsl.2018.12.008

Nakayama, Y., Schröder, M., & Hellmer, H. H. (2013). From circumpolar deep water to the glacial meltwater plume on the eastern Amundsen Shelf. *Deep Sea Research Part I: Oceanographic Research Papers*, *77*, 50–62. https://doi.org/10.1016/j.dsr.2013.04.001

Nakayama, Y., Menemenlis, D., Zhang, H., Schodlok, M., & Rignot, E. (2018). Origin of Circumpolar Deep Water intruding onto the Amundsen and Bellingshausen Sea continental shelves. *Nature Communications*, *9*(1), 3403. https://doi.org/10.1038/s41467-018-05813-1

Nakayama, Y., Greene, C. A., Paolo, F. S., Mensah, V., Zhang, H., Kashiwase, H., et al. (2021). Antarctic Slope Current Modulates Ocean Heat Intrusions Towards Totten Glacier. *Geophysical Research Letters*, *48*(17), e2021GL094149. https://doi.org/10.1029/2021GL094149

Nakayama, Y., Cai, C., & Seroussi, H. (2021). Impact of Subglacial Freshwater Discharge on Pine Island Ice Shelf. *Geophysical Research Letters*, *48*(18), e2021GL093923. https://doi.org/10.1029/2021GL093923

Nakayama, Yoshihiro, Wongpan, P., Greenbaum, J. S., Yamazaki, K., Noguchi, T., Simizu, D., et al. (2023). Helicopter-Based Ocean Observations Capture Broad Ocean Heat Intrusions Toward the Totten Ice Shelf. *Geophysical Research Letters*, *50*(17), e2022GL097864. https://doi.org/10.1029/2022GL097864

Naughten, K. A., Meissner, K. J., Galton-Fenzi, B. K., England, M. H., Timmermann, R., & Hellmer, H. H. (2018). Future Projections of Antarctic Ice Shelf Melting Based on CMIP5 Scenarios. *Journal of Climate*, *31*(13), 5243–5261. https://doi.org/10.1175/JCLI-D-17-0854.1

Naughten, K. A., De Rydt, J., Rosier, S. H. R., Jenkins, A., Holland, P. R., & Ridley, J. K. (2021). Two-timescale response of a large Antarctic ice shelf to climate change. *Nature Communications*, *12*(1), 1991. https://doi.org/10.1038/s41467-021-22259-0

Naughten, K. A., Holland, P. R., Dutrieux, P., Kimura, S., Bett, D. T., & Jenkins, A. (2022). Simulated Twentieth-Century Ocean Warming in the Amundsen Sea, West Antarctica. *Geophysical Research Letters*, *49*(5). https://doi.org/10.1029/2021GL094566

Needell, C., & Holschuh, N. (2023). Evaluating the Retreat, Arrest, and Regrowth of Crane Glacier Against Marine Ice Cliff Process Models. *Geophysical Research Letters*, *50*(4). https://doi.org/10.1029/2022GL102400

Neff, P. (2020). Amundsen Sea Coastal Ice Rises: Future Sites for Marine-Focused Ice Core Records. *Oceanography*, *33*(2). https://doi.org/10.5670/oceanog.2020.215

Nettleton, L. L., LaCoste, L., & Harrison, J. C. (1960) Tests of an airborne gravity meter *Geophysics*, *25*(1), 181–202. https://doi.org/10.1190/1.1438685

Newman, Hancock, Hofmann, Williams, Henley, Moreau, et al. (2022) SOOS Science and Implementation Plan 2021-2025. https://doi.org/10.5281/ZENODO.6324359

Newman, L., Heil, P., Trebilco, R., Katsumata, K., Constable, A., van Wijk, E., et al. (2019). Delivering Sustained, Coordinated, and Integrated Observations of the Southern

Ocean for Global Impact. *Frontiers in Marine Science*, *6*, 433. https://doi.org/10.3389/fmars.2019.00433

Nias, I. J., Cornford, S. L., Edwards, T. L., Gourmelen, N., & Payne, A. J. (2019). Assessing Uncertainty in the Dynamical Ice Response to Ocean Warming in the Amundsen Sea Embayment, West Antarctica. *Geophysical Research Letters*, *46*(20), 11253–11260. https://doi.org/10.1029/2019GL084941

Nicholls, K. W., Corr, H. F. J., Stewart, C. L., Lok, L. B., Brennan, P. V., & Vaughan, D. G. (2015). A ground-based radar for measuring vertical strain rates and time-varying basal melt rates in ice sheets and shelves. *Journal of Glaciology*, *61*(230), 1079–1087. https://doi.org/10.3189/2015JoG15J073

Nield, G. A., Barletta, V. R., Bordoni, A., King, M. A., Whitehouse, P. L., Clarke, P. J., et al. (2014). Rapid bedrock uplift in the Antarctic Peninsula explained by viscoelastic response to recent ice unloading. *Earth and Planetary Science Letters*, *397*, 32–41. https://doi.org/10.1016/j.epsl.2014.04.019

Nield, G. A., Whitehouse, P. L., King, M. A., & Clarke, P. J. (2016). Glacial isostatic adjustment in response to changing Late Holocene behaviour of ice streams on the Siple Coast, West Antarctica. *Geophysical Journal International*, *205*(1), 1–21. https://doi.org/10.1093/gji/ggv532

Nilsson, J., Gardner, A. S., & Paolo, F. S. (2022). Elevation change of the Antarctic Ice Sheet: 1985 to 2020. *Earth System Science Data*, *14*(8), 3573–3598. https://doi.org/10.5194/essd-14-3573-2022

Niwano, M., Aoki, T., Hashimoto, A., Matoba, S., Yamaguchi, S., Tanikawa, T., Fujita, K., Tsushima, A., Iizuka, Y., Shimada, R. and Hori, M., 2018. NHM–SMAP: spatially and temporally high-resolution nonhydrostatic atmospheric model coupled with detailed snow process model for Greenland Ice Sheet. *The Cryosphere*, *12*(2), 635-655, https://doi.org/10.5194/tc-12-635-2018

Noble, T. L., Rohling, E. J., Aitken, A. R. A., Bostock, H. C., Chase, Z., Gomez, N., et al. (2020). The Sensitivity of the Antarctic Ice Sheet to a Changing Climate: Past, Present, and Future. *Reviews of Geophysics*, *58*(4), e2019RG000663. https://doi.org/10.1029/2019RG000663

Nøst, O. A. (2004). Measurements of ice thickness and seabed topography under the Fimbul Ice Shelf, Dronning Maud Land, Antarctica. *Journal of Geophysical Research*, *109*(C10), C10010. https://doi.org/10.1029/2004JC002277

Nöth, G. (2021). Wetter und Klima - Deutscher Wetterdienst - Feature für Medien - Aktualisierte Fassung: Meteorologie in der Antarktis. Retrieved from https://www.dwd.de/DE/presse/feature/20210126_feature_dromlan.html?nn=644266

Nowicki, S., Payne, A., Larour, E., Seroussi, H., Goelzer, H., Lipscomb, W., et al. (2016). Ice Sheet Model Intercomparison Project (ISMIP6) contribution to CMIP6. *Geoscientific Model Development*, *9*(12), 4521–4545. https://doi.org/10.5194/gmd-9-4521-2016

Nowicki, S., Goelzer, H., Seroussi, H., Payne, A. J., Lipscomb, W. H., Abe-Ouchi, A., et al. (2020). Experimental protocol for sea level projections from ISMIP6 stand-alone ice sheet models. *The Cryosphere*, *14*(7), 2331–2368. https://doi.org/10.5194/tc-14-2331-2020

Ockenden, H., Bingham, R. G., Curtis, A., & Goldberg, D. (2022). Inverting ice surface elevation and velocity for bed topography and slipperiness beneath Thwaites Glacier. *The Cryosphere*, *16*(9), 3867–3887. https://doi.org/10.5194/tc-16-3867-2022

Ockenden, H., R. G. Bingham, D. Goldberg, A. Curtis, and M. Morlighem (2025), Complex mesoscale landscapes beneath Antarctica mapped from space, *Science*, Accepted 25 Nov. 2025.

Oetting, A., Smith, E. C., Arndt, J. E., Dorschel, B., Drews, R., Ehlers, T. A., et al. (2022). Geomorphology and shallow sub-sea-floor structures underneath the Ekström Ice Shelf, Antarctica. *The Cryosphere*, *16*(5), 2051–2066. https://doi.org/10.5194/tc-16-2051-2022

Ohshima, K. I., Nihashi, S., & Iwamoto, K. (2016). Global view of sea-ice production in polynyas and its linkage to dense/bottom water formation. *Geoscience Letters*, *3*(1), 13. https://doi.org/10.1186/s40562-016-0045-4

van Ommen, T. D., & Morgan, V. (2010). Snowfall increase in coastal East Antarctica linked with southwest Western Australian drought. *Nature Geoscience*, *3*(4), 267–272. https://doi.org/10.1038/ngeo761

Oraschewski, F. M., Ershadi, M. R., & Drews, R. (2025). Polarimetric wide-angle radar detects competing signatures of ice fabric and structural firn anisotropy. *Geophysical Research Letters*, 52, e2024GL113096. https://doi.org/10.1029/2024GL113096

Orr, A., Deb, P., Clem, K. R., Gilbert, E., Bromwich, D. H., Boberg, F., et al. (2023a). Characteristics of Surface "Melt Potential" over Antarctic Ice Shelves based on Regional Atmospheric Model Simulations of Summer Air Temperature Extremes from 1979/80 to 2018/19. *Journal of Climate*, *36*(10), 3357–3383. https://doi.org/10.1175/JCLI-D-22-0386.1

Orr, A., Deb, P., Clem, K. R., Gilbert, E., Bromwich, D. H., Boberg, F., et al. (2023b). Characteristics of Surface "Melt Potential" over Antarctic Ice Shelves based on Regional Atmospheric Model Simulations of Summer Air Temperature Extremes from 1979/80 to 2018/19. *Journal of Climate*, *36*(10), 3357–3383. https://doi.org/10.1175/JCLI-D-22-0386.1

Orsi, A. H., & Wiederwohl, C. L. (2009). A recount of Ross Sea waters. *Deep Sea Research Part II: Topical Studies in Oceanography*, *56*(13–14), 778–795. https://doi.org/10.1016/j.dsr2.2008.10.033

Orsi, A. H., Whitworth, T., & Nowlin, W. D. (1995). On the meridional extent and fronts of the Antarctic Circumpolar Current. *Deep Sea Research Part I: Oceanographic Research Papers*, *42*(5), 641–673. https://doi.org/10.1016/0967-0637(95)00021-W

Orsi, A. H., Johnson, G. C., & Bullister, J. L. (1999). Circulation, mixing, and production of Antarctic Bottom Water. *Progress in Oceanography*, *43*(1), 55–109. https://doi.org/10.1016/S0079-6611(99)00004-X

Otosaka, I. N., Shepherd, A., Ivins, E. R., Schlegel, N.-J., Amory, C., Van Den Broeke, M. R., et al. (2023). Mass balance of the Greenland and Antarctic ice sheets from 1992 to 2020. *Earth System Science Data*, *15*(4), 1597–1616. https://doi.org/10.5194/essd-15-1597-2023

Paden, J., Akins, T., Dunson, D., Allen, C., & Gogineni, P. (2010). Ice-sheet bed 3-D tomography. *Journal of Glaciology*, *56*(195), 3–11. https://doi.org/10.3189/002214310791190811

Paden, J., Tinto, K., Young, D., Christianson, K., Schroeder, D., Rahnemoonfar, M., Li, J., Talasila, H.M., Eisen, O. and Jordan, T.(2021) Open polar radar software and services to standardize radar echograms and integrate into a geospatial database. In *AGU Fall Meeting Abstracts* (Vol. 2021, C51A-08).

Padman, L., Siegfried, M. R., & Fricker, H. A. (2018). Ocean Tide Influences on the Antarctic and Greenland Ice Sheets. *Reviews of Geophysics*, *56*(1), 142–184. https://doi.org/10.1002/2016RG000546

Palm, S. P., Kayetha, V., Yang, Y., & Pauly, R. (2017). Blowing snow sublimation and transport over Antarctica from 11 years of CALIPSO observations. *The Cryosphere*, *11*(6), 2555–2569. https://doi.org/10.5194/tc-11-2555-2017

Palmer, M. D., Domingues, C. M., Slangen, A. B. A., & Dias, F. B. (2021). An ensemble approach to quantify global mean sea-level rise over the 20th century from tide gauge reconstructions. *Environmental Research Letters*, *16*(4), 044043. https://doi.org/10.1088/1748-9326/abdaec

Pan, L., Powell, E. M., Latychev, K., Mitrovica, J. X., Creveling, J. R., Gomez, N., et al. (2021). Rapid postglacial rebound amplifies global sea level rise following West Antarctic Ice Sheet collapse. *Science Advances*, *7*(18), eabf7787. https://doi.org/10.1126/sciadv.abf7787

Pappa, F., Ebbing, J., Ferraccioli, F., & van der Wal, W. (2019). Modeling Satellite Gravity Gradient Data to Derive Density, Temperature, and Viscosity Structure of the Antarctic Lithosphere. *Journal of Geophysical Research: Solid Earth*, *124*(11), 12053–12076. https://doi.org/10.1029/2019JB017997

Parizek, B. R., Christianson, K., Anandakrishnan, S., Alley, R. B., Walker, R. T., Edwards, R. A., et al. (2013). Dynamic (in)stability of Thwaites Glacier, West Antarctica.*Journal of Geophysical Research: Earth Surface*, *118*(2), 638–655. https://doi.org/10.1002/jgrf.20044

Park, Y.-H., & Gambéroni, L. (1995). Large-scale circulation and its variability in the south Indian Ocean from TOPEX/POSEIDON altimetry. *Journal of Geophysical Research*, *100*(C12), 24911. https://doi.org/10.1029/95JC01962

Parkinson, C. L. (2019). A 40-y record reveals gradual Antarctic sea ice increases followed by decreases at rates far exceeding the rates seen in the Arctic. *Proceedings of the National Academy of Sciences*, *116*(29), 14414–14423. https://doi.org/10.1073/pnas.1906556116

Parkinson, C. L., & Cavalieri, D. J. (2012). Antarctic sea ice variability and trends, 1979–2010. *The Cryosphere*, *6*(4), 871–880. https://doi.org/10.5194/tc-6-871-2012

Patterson, M. (2013). Aviation Accidents in Antarctica -A review of literature and examination of dimensions. University of Canterbury, https://ir.canterbury.ac.nz/server/api/core/bitstreams/75e487f6-5881-4a83-80c2-fa70752fed65/content

Pattyn, F. (2010). Antarctic subglacial conditions inferred from a hybrid ice sheet/ice stream model. *Earth and Planetary Science Letters*, *295*(3), 451–461. https://doi.org/10.1016/j.epsl.2010.04.025

Pattyn, F. (2017). Sea-level response to melting of Antarctic ice shelves on multi-centennial timescales with the fast Elementary Thermomechanical Ice Sheet model (f.ETISh v1.0). *The Cryosphere*, *11*(4), 1851–1878. https://doi.org/10.5194/tc-11-1851-2017

Pattyn, F. (2018). The paradigm shift in Antarctic ice sheet modelling. *Nature Communications*, *9*(1), 2728. https://doi.org/10.1038/s41467-018-05003-z

Pattyn, F., Schoof, C., Perichon, L., Hindmarsh, R. C. A., Bueler, E., de Fleurian, B., et al. (2012). Results of the Marine Ice Sheet Model Intercomparison Project, MISMIP. *The Cryosphere*, *6*(3), 573–588. https://doi.org/10.5194/tc-6-573-2012

Pattyn, F., Perichon, L., Durand, G., Favier, L., Gagliardini, O., Hindmarsh, R. C. A., et al. (2013). Grounding-line migration in plan-view marine ice-sheet models: results of the ice2sea MISMIP3d intercomparison. *Journal of Glaciology*, *59*(215), 410–422. https://doi.org/10.3189/2013JoG12J129

Pattyn, F., Favier, L., Sun, S., & Durand, G. (2017). Progress in Numerical Modeling of Antarctic Ice-Sheet Dynamics. *Current Climate Change Reports*, *3*(3), 174–184. https://doi.org/10.1007/s40641-017-0069-7

Paxman, G. J. G., Jamieson, S. S. R., Ferraccioli, F., Bentley, M. J., Forsberg, R., Ross, N., et al. (2017). Uplift and tilting of the Shackleton Range in East Antarctica driven by glacial erosion and normal faulting: Flexural Uplift of the Shackleton Range. *Journal of Geophysical Research: Solid Earth*. https://doi.org/10.1002/2016JB013841

Paxman, G. J. G., Jamieson, S. S. R., Hochmuth, K., Gohl, K., Bentley, M. J., Leitchenkov, G., & Ferraccioli, F. (2019). Reconstructions of Antarctic topography since the Eocene–Oligocene boundary. *Palaeogeography, Palaeoclimatology, Palaeoecology*, *535*, 109346. https://doi.org/10.1016/j.palaeo.2019.109346

Paxman, G. J. G., Gasson, E. G. W., Jamieson, S. S. R., Bentley, M. J., & Ferraccioli, F. (2020). Long-Term Increase in Antarctic Ice Sheet Vulnerability Driven by Bed Topography Evolution. *Geophysical Research Letters*, *47*(20). https://doi.org/10.1029/2020GL090003

Payne, A. J. (1999). A thermomechanical model of ice flow in West Antarctica. *Climate Dynamics*, *15*(2), 115–125. https://doi.org/10.1007/s003820050271

Payne, A. J., & Dongelmans, P. W. (1997). Self-organization in the thermomechanical flow of ice sheets. *Journal of Geophysical Research: Solid Earth*, *102*(B6), 12219–12233. https://doi.org/10.1029/97JB00513

Peacock, J. R., & Selway, K. (2016). Magnetotelluric investigation of the Vestfold Hills and Rauer Group, East Antarctica. *Journal of Geophysical Research: Solid Earth*, *121*(4), 2258–2273. https://doi.org/10.1002/2015JB012677

Pelle, T., Morlighem, M., Nakayama, Y., & Seroussi, H. (2021). Widespread Grounding Line Retreat of Totten Glacier, East Antarctica, Over the 21st Century. *Geophysical Research Letters*, *48*(17), e2021GL093213. https://doi.org/10.1029/2021GL093213

Pelle, Tyler, Greenbaum, J. S., Dow, C. F., Jenkins, A., & Morlighem, M. (2023). Subglacial discharge accelerates future retreat of Denman and Scott Glaciers, East Antarctica. *Science Advances*, 9(43), eadi9014. https://doi.org/10.1126/sciadv.adi9014

Pelle, T., Greenbaum, J. S., Ehrenfeucht, S., Dow, C. F., & McCormack, F. S. (2024). Subglacial Discharge Accelerates Dynamic Retreat of Aurora Subglacial Basin Outlet Glaciers, East Antarctica, Over the 21st Century. *Journal of Geophysical Research: Earth Surface*, 129(7), e2023JF007513. https://doi.org/10.1029/2023JF007513

Pelletier, C., Fichefet, T., Goosse, H., Haubner, K., Helsen, S., Huot, P.-V., et al. (2022). PARASO, a circum-Antarctic fully coupled ice-sheet–ocean–sea-ice–atmosphere–

land model involving f.ETISh1.7, NEMO3.6, LIM3.6, COSMO5.0 and CLM4.5. *Geoscientific Model Development*, *15*(2), 553–594. https://doi.org/10.5194/gmd-15-553-2022

Pellichero, V., Sallée, J.-B., Chapman, C. C., & Downes, S. M. (2018). The southern ocean meridional overturning in the sea-ice sector is driven by freshwater fluxes. *Nature Communications*, *9*(1), 1789. https://doi.org/10.1038/s41467-018-04101-2

Peltier, W. R. (1974). The impulse response of a Maxwell Earth. *Reviews of Geophysics*, *12*(4), 649–669. https://doi.org/10.1029/RG012i004p00649

Person, M., Bense, V., Cohen, D., & Banerjee, A. (2012). Models of ice-sheet hydrogeologic interactions: a review: Ice-Sheet Hydrogeologic Model Review. *Geofluids*, *12*(1), 58–78. https://doi.org/10.1111/j.1468-8123.2011.00360.x

Pertierra, L.R., & Hughes, K. A. (2013). Management of Antarctic Specially Protected Areas: permitting, visitation and information exchange practices. *Antarctic Science*, *25*(4), 553–564. https://doi.org/10.1017/S0954102012001204

Pertierra, Luis R., Hughes, K. A., Benayas, J., Justel, A., & Quesada, A. (2013). Environmental management of a scientific field camp in Maritime Antarctica: reconciling research impacts with conservation goals in remote ice-free areas. *Antarctic Science*, *25*(2), 307–317. https://doi.org/10.1017/S0954102012001083

Peters, M. E. (2005). Analysis techniques for coherent airborne radar sounding: Application to West Antarctic ice streams. *Journal of Geophysical Research*, *110*(B6), B06303. https://doi.org/10.1029/2004JB003222

Phạm, T., & Tkalčić, H. (2021). Constraining Floating Ice Shelf Structures by Spectral Response of Teleseismic P-Wave Coda: Ross Ice Shelf, Antarctica. *Journal of Geophysical Research: Solid Earth*, *126*(4). https://doi.org/10.1029/2020JB021082

Philippe, M., Tison, J.-L., Fjøsne, K., Hubbard, B., Kjær, H. A., Lenaerts, J. T. M., et al. (2016). Ice core evidence for a 20th century increase in surface mass balance in coastal Dronning Maud Land, East Antarctica. *The Cryosphere*, *10*(5), 2501–2516. https://doi.org/10.5194/tc-10-2501-2016

Pickup, D. D., D. C. E. Bakker, K. J. Heywood, F. Glassup, E. M. Hammermeister, S. E. Stammerjohn, G. A. Lee, S. Loucaides, B. Y. Queste, B. G. M. Webber, and P. L. Yager (2025), Cold lenses in the Amundsen Sea: Impacts of sea ice formation on subsurface pH and carbon, *Ocean Sci.*, 21, 2727–2741, https://doi.org/10.5194/os-21-2727-2025.

Pittard, M. L., Roberts, J. L., Galton-Fenzi, B. K., & Watson, C. S. (2016). Sensitivity of the Lambert-Amery glacial system to geothermal heat flux. *Annals of Glaciology*, *57*(73), 56–68. https://doi.org/10.1017/aog.2016.26

Pittard, M. L., Whitehouse, P. L., Bentley, M. J., & Small, D. (2022). An ensemble of Antarctic deglacial simulations constrained by geological observations. *Quaternary Science Reviews*, *298*, 107800. https://doi.org/10.1016/j.quascirev.2022.107800

Polar Research Board, Ocean Studies Board, Division on Earth and Life Studies, & National Academies of Sciences, Engineering, and Medicine. (2017). *Antarctic Sea Ice Variability in the Southern Ocean-Climate System: Proceedings of a Workshop*. (A. Macalady & K. Thomas, Eds.) (p. 24696). Washington, D.C.: National Academies Press. https://doi.org/10.17226/24696

Pollard, D., DeConto, R. M., & Alley, R. B. (2015). Potential Antarctic Ice Sheet retreat driven by hydrofracturing and ice cliff failure. *Earth and Planetary Science Letters*, *412*, 112–121. https://doi.org/10.1016/j.epsl.2014.12.035

Pollard, D., Gomez, N., & Deconto, R. M. (2017). Variations of the Antarctic Ice Sheet in a Coupled Ice Sheet-Earth-Sea Level Model: Sensitivity to Viscoelastic Earth Properties. *Journal of Geophysical Research: Earth Surface*, *122*(11), 2124–2138. https://doi.org/10.1002/2017JF004371

Porter, D. F., S. R. Springer, L. Padman, H. A. Fricker, K. J. Tinto, S. C. Riser, R. E. Bell, and the ROSETTA-Ice Team (2019), Evolution of the seasonal surface mixed layer of the Ross Sea, Antarctica, observed with autonomous profiling floats, *J. Geophys. Res. Oceans*, 124, 4934–4953, https://doi.org/10.1029/2018JC014683.

Porter, D. F., Springer, S. R., Padman, L., Fricker, H. A., Tinto, K. J., Riser, S. C., et al. (2019). Evolution of the Seasonal Surface Mixed Layer of the Ross Sea, Antarctica, Observed With Autonomous Profiling Floats. *Journal of Geophysical Research: Oceans*, *124*(7), 4934–4953. https://doi.org/10.1029/2018JC014683

Potter, J. R., & Paren, J. G. (1985). Interaction between ice shelf and ocean in George VI Sound, Antarctica. In S. Jacobs (Ed.), *Antarctic Research Series* (Vol. 43, pp. 35–58). Washington, D. C.: American Geophysical Union. https://doi.org/10.1029/AR043p0035

Powers, J. G., Manning, K. W., Bromwich, D. H., Cassano, J. J., & Cayette, A. M. (2012). A Decade of Antarctic Science Support Through Amps. *Bulletin of the American Meteorological Society*, *93*(11), 1699–1712. https://doi.org/10.1175/BAMS-D-11-00186.1

Prager, S., Sexstone, G., McGrath, D., Fulton, J., & Moghaddam, M. (2022). Snow Depth Retrieval With an Autonomous UAV-Mounted Software-Defined Radar. *IEEE Transactions on Geoscience and Remote Sensing*, *60*, 1–16. https://doi.org/10.1109/TGRS.2021.3117509

Pratap, B., Dey, R., Matsuoka, K., Moholdt, G., Lindbäck, K., Goel, V., et al. (2022). Three-decade spatial patterns in surface mass balance of the Nivlisen Ice Shelf, central Dronning Maud Land, East Antarctica. *Journal of Glaciology*, *68*(267), 174–186. https://doi.org/10.1017/jog.2021.93

Pritchard, H. D., Arthern, R. J., Vaughan, D. G., & Edwards, L. A. (2009). Extensive dynamic thinning on the margins of the Greenland and Antarctic ice sheets. *Nature*, *461*(7266), 971–975. https://doi.org/10.1038/nature08471

Pritchard, H. D., Ligtenberg, S. R. M., Fricker, H. A., Vaughan, D. G., van den Broeke, M. R., & Padman, L. (2012). Antarctic ice-sheet loss driven by basal melting of ice shelves. *Nature*, *484*(7395), 502–505. https://doi.org/10.1038/nature10968

Pritchard, H.D., Fretwell, P.T., Fremand, A.C. et al. (2025) Bedmap3 updated ice bed, surface and thickness gridded datasets for Antarctica. *Sci Data* 12, 414. https://doi.org/10.1038/s41597-025-04672-y

Ranalli, G., & Fischer, B. (1984). Diffusion creep, dislocation creep, and mantle rheology. *Physics of the Earth and Planetary Interiors*, *34*(1), 77–84. https://doi.org/10.1016/0031-9201(84)90086-4

Ranganathan, M., Minchew, B., Meyer, C. R., & Gudmundsson, G. H. (2021). A new approach to inferring basal drag and ice rheology in ice streams, with applications to

West Antarctic Ice Streams. *Journal of Glaciology*, *67*(262), 229–242. https://doi.org/10.1017/jog.2020.95

Rathmann, N. M., & Lilien, D. A. (2022). Inferred basal friction and mass flux affected by crystal-orientation fabrics. *Journal of Glaciology*, *68*(268), 236–252. https://doi.org/10.1017/jog.2021.88

Ray, R. D. (1985). Correction of systematic error in magnetic surveys: An application of ridge regression and sparse matrix theory. *Geophysics, 50*(11), 1721–1731. https://doi.org/10.1190/1.1441862

Raymond, C. F. (1983). Deformation in the Vicinity of Ice Divides. *Journal of Glaciology*, *29*(103), 357–373. https://doi.org/10.3189/S0022143000030288

Reading, A. M., Stål, T., Halpin, J. A., Lösing, M., Ebbing, J., Shen, W., et al. (2022). Antarctic geothermal heat flow and its implications for tectonics and ice sheets. *Nature Reviews Earth & Environment*, *3*(12), 814–831. https://doi.org/10.1038/s43017-022-00348-y

Reese, R., Gudmundsson, G. H., Levermann, A., & Winkelmann, R. (2018). The far reach of ice-shelf thinning in Antarctica. *Nature Climate Change*, *8*(1), 53–57. https://doi.org/10.1038/s41558-017-0020-x

Reese, R., Levermann, A., Albrecht, T., Seroussi, H., & Winkelmann, R. (2020). The role of history and strength of the oceanic forcing in sea level projections from Antarctica with the Parallel Ice Sheet Model. *The Cryosphere*, *14*(9), 3097–3110. https://doi.org/10.5194/tc-14-3097-2020

Reese, Ronja, Garbe, J., Hill, E. A., Urruty, B., Naughten, K. A., Gagliardini, O., et al. (2022). The stability of present-day Antarctic grounding lines – Part 2: Onset of irreversible retreat of Amundsen Sea glaciers under current climate on centennial timescales cannot be excluded. *The Cryosphere*, 17(9), 3761-3783, https://doi.org/10.5194/tc-17-3761-2023

Retzlaff, R., & Bentley, C. R. (1993). Timing of stagnation of Ice Stream C, West Antarctica, from short-pulse radar studies of buried surface crevasses. *Journal of Glaciology*, *39*(133), 553–561. https://doi.org/10.3189/S0022143000016440

Reuters. (2019, December 22). Chilean air force chief says cause of Antarctic plane crash may never be known. *The Guardian*. Retrieved from https://www.theguardian.com/world/2019/dec/22/chilean-air-force-chief-says-cause-of-antarctic-plane-crash-may-never-be-known

Richard Peltier, W., Argus, D. F., & Drummond, R. (2018). Comment on “An Assessment of the ICE-6G_C (VM5a) Glacial Isostatic Adjustment Model” by Purcell et al. *Journal of Geophysical Research: Solid Earth*, *123*(2), 2019–2028. https://doi.org/10.1002/2016JB013844

Richardson, C., Aarholt, E., Hamran, S.-E., Holmlund, P., & Isaksson, E. (1997). Spatial distribution of snow in western Dronning Maud Land, East Antarctica, mapped by a ground-based snow radar. *Journal of Geophysical Research: Solid Earth*, *102*(B9), 20343–20353. https://doi.org/10.1029/97JB01441

Richter, O., Gwyther, D. E., Galton-Fenzi, B. K., & Naughten, K. A. (2022). The Whole Antarctic Ocean Model (WAOM v1.0): development and evaluation. *Geoscientific Model Development*, *15*(2), 617–647. https://doi.org/10.5194/gmd-15-617-2022

Riedel, S., Jokat, W., & Steinhage, D. (2012). Mapping tectonic provinces with airborne gravity and radar data in Dronning Maud Land, East Antarctica: Mapping tectonic provinces in East Antarctica. *Geophysical Journal International*, *189*(1), 414–427. https://doi.org/10.1111/j.1365-246X.2012.05363.x

Rignot, E. (1998). Hinge-line migration of Petermann Gletscher, north Greenland, detected using satellite-radar interferometry. *Journal of Glaciology*, *44*(148), 469–476. https://doi.org/10.3189/S0022143000001994

Rignot, E., & Thomas, R. H. (2002). Mass Balance of Polar Ice Sheets. *Science*, *297*(5586), 1502–1506. https://doi.org/10.1126/science.1073888

Rignot, E., Casassa, G., Gogineni, P., Krabill, W., Rivera, A., & Thomas, R. (2004). Accelerated ice discharge from the Antarctic Peninsula following the collapse of Larsen B ice shelf. *Geophysical Research Letters*, *31*(18). https://doi.org/10.1029/2004GL020697

Rignot, E., Mouginot, J., & Scheuchl, B. (2011a). Antarctic grounding line mapping from differential satellite radar interferometry. *Geophysical Research Letters*, *38*(10). https://doi.org/10.1029/2011GL047109

Rignot, E., Mouginot, J., & Scheuchl, B. (2011b). Ice Flow of the Antarctic Ice Sheet. *Science*, *333*(6048), 1427–1430. https://doi.org/10.1126/science.1208336

Rignot, E., Jacobs, S., Mouginot, J., & Scheuchl, B. (2013). Ice-Shelf Melting Around Antarctica. *Science*, *341*(6143), 266–270. https://doi.org/10.1126/science.1235798

Rignot, E., Mouginot, J., Morlighem, M., Seroussi, H., & Scheuchl, B. (2014). Widespread, rapid grounding line retreat of Pine Island, Thwaites, Smith, and Kohler glaciers, West Antarctica, from 1992 to 2011. *Geophysical Research Letters*, *41*(10), 3502–3509. https://doi.org/10.1002/2014GL060140

Rignot, E., Mouginot, J. & Scheuchl, B. (2016). MEaSUREs Antarctic Grounding Line from Differential Satellite Radar Interferometry. (NSIDC-0498, Version 2). [Data Set]. Boulder, Colorado USA. NASA National Snow and Ice Data Center Distributed Active Archive Center. https://doi.org/10.5067/IKBWW4RYHF1Q.

Rignot, E., Mouginot, J. & Scheuchl, B. (2017). MEaSUREs InSAR-Based Antarctica Ice Velocity Map. (NSIDC-0484, Version 2). [Data Set]. Boulder, Colorado USA. NASA National Snow and Ice Data Center Distributed Active Archive Center. https://doi.org/10.5067/D7GK8F5J8M8R.

Rignot, E., Mouginot, J., Scheuchl, B., van den Broeke, M., van Wessem, M. J., & Morlighem, M. (2019). Four decades of Antarctic Ice Sheet mass balance from 1979–2017. *Proceedings of the National Academy of Sciences*, *116*(4), 1095–1103. https://doi.org/10.1073/pnas.1812883116

Rignot, Eric, & Jacobs, S. S. (2002). Rapid Bottom Melting Widespread near Antarctic Ice Sheet Grounding Lines. *Science*, *296*(5575), 2020–2023. https://doi.org/10.1126/science.1070942

Rignot, Eric, Bamber, J. L., Van Den Broeke, M. R., Davis, C., Li, Y., Van De Berg, W. J., & Van Meijgaard, E. (2008). Recent Antarctic ice mass loss from radar interferometry and regional climate modelling. *Nature Geoscience*, *1*(2), 106–110. https://doi.org/10.1038/ngeo102

Rignot, Eric, Mouginot, J., Scheuchl, B., & Jeong, S. (2022). Changes in Antarctic Ice Sheet Motion Derived From Satellite Radar Interferometry Between 1995 and 2022. *Geophysical Research Letters*, *49*(23), e2022GL100141. https://doi.org/10.1029/2022GL100141

Rintoul, S. R. (2018). The global influence of localized dynamics in the Southern Ocean. *Nature*, *558*(7709), 209–218. https://doi.org/10.1038/s41586-018-0182-3

Rintoul, S. R., Silvano, A., Pena-Molino, B., van Wijk, E., Rosenberg, M., Greenbaum, J. S., & Blankenship, D. D. (2016). Ocean heat drives rapid basal melt of the Totten Ice Shelf. *Science Advances*, *2*(12), e1601610. https://doi.org/10.1126/sciadv.1601610

Riser, S. C., Swift, D., & Drucker, R. (2018). Profiling Floats in SOCCOM: Technical Capabilities for Studying the Southern Ocean. *Journal of Geophysical Research: Oceans*, *123*(6), 4055–4073. https://doi.org/10.1002/2017JC013419

Ritz, C., Edwards, T. L., Durand, G., Payne, A. J., Peyaud, V., & Hindmarsh, R. C. A. (2015). Potential sea-level rise from Antarctic ice-sheet instability constrained by observations. *Nature*, *528*(7580), 115–118. https://doi.org/10.1038/nature16147

Roach, L. A., Dörr, J., Holmes, C. R., Massonnet, F., Blockley, E. W., Notz, D., et al. (2020). Antarctic Sea Ice Area in CMIP6. *Geophysical Research Letters*, *47*(9). https://doi.org/10.1029/2019GL086729

Roach, L. A., Eisenman, I., Wagner, T. J. W., Blanchard-Wrigglesworth, E., & Bitz, C. M. (2022). Asymmetry in the seasonal cycle of Antarctic sea ice driven by insolation. *Nature Geoscience*, *15*(4), 277–281. https://doi.org/10.1038/s41561-022-00913-6

Robel, A. A., Sim, S. J., Meyer, C., Siegfried, M. R., & Gustafson, C. D. (2023). Contemporary ice sheet thinning drives subglacial groundwater exfiltration with potential feedbacks on glacier flow. *Science Advances*, 9(33), https://doi.org/10.1126/sciadv.adh3693

Robel, A. A., Seroussi, H., & Roe, G. H. (2019). Marine ice sheet instability amplifies and skews uncertainty in projections of future sea-level rise. *Proceedings of the National Academy of Sciences*, *116*(30), 14887–14892. https://doi.org/10.1073/pnas.1904822116

Robin, G. D. Q. (1953). Measurements of Ice thickness in Dronning Maud Land, Antarctica. *Nature*, *171*(4341), 55–58. https://doi.org/10.1038/171055a0

Rodriguez-Morales, F., Byers, K., Crowe, R., Player, K., Hale, R. D., Arnold, E. J., Smith, L., Gifford, C. M., Braaten, D., Panton, C., Gogineni, S., Leuschen, C. J., Paden, J. D., Li, J., Lewis, C. C., Panzer, B., Alvestegui, D. G.-G., and Patel, A.: Advanced Multifrequency Radar Instrumentation for Polar Research, IEEE Transactions on Geoscience and Remote Sensing, 52, 2824–2842, https://doi.org/10.1109/tgrs.2013.2266415, 2013.

Rose, K. C., Ferraccioli, F., Jamieson, S. S. R., Bell, R. E., Corr, H., Creyts, T. T., et al. (2013). Early East Antarctic Ice Sheet growth recorded in the landscape of the Gamburtsev Subglacial Mountains. *Earth and Planetary Science Letters*, *375*, 1–12. https://doi.org/10.1016/j.epsl.2013.03.053

Rosenblum, E., & Eisenman, I. (2017). Sea Ice Trends in Climate Models Only Accurate in Runs with Biased Global Warming. *Journal of Climate*, *30*(16), 6265–6278. https://doi.org/10.1175/JCLI-D-16-0455.1

Rosevear, M. G., Gayen, B., & Galton-Fenzi, B. K. (2021). The role of double-diffusive convection in basal melting of Antarctic ice shelves. *Proceedings of the National Academy of Sciences*, *118*(6), e2007541118. https://doi.org/10.1073/pnas.2007541118

Rosier, S. H. R., Hofstede, C., Brisbourne, A. M., Hattermann, T., Nicholls, K. W., Davis, P. E. D., et al. (2018). A New Bathymetry for the Southeastern Filchner-Ronne Ice Shelf: Implications for Modern Oceanographic Processes and Glacial History. *Journal of Geophysical Research: Oceans*, *123*(7), 4610–4623. https://doi.org/10.1029/2018JC013982

Rosier, Sebastian H. R., Reese, R., Donges, J. F., De Rydt, J., Gudmundsson, G. H., & Winkelmann, R. (2021). The tipping points and early warning indicators for Pine Island Glacier, West Antarctica. *The Cryosphere*, *15*(3), 1501–1516. https://doi.org/10.5194/tc-15-1501-2021

Rott, H., Floricioiu, D., Wuite, J., Scheiblauer, S., Nagler, T., & Kern, M. (2014). Mass changes of outlet glaciers along the Nordensjköld Coast, northern Antarctic Peninsula, based on TanDEM-X satellite measurements: TanDEM-X Antarctic Peninsula glaciers. *Geophysical Research Letters*, *41*(22), 8123–8129. https://doi.org/10.1002/2014GL061613

Rott, H., Abdel Jaber, W., Wuite, J., Scheiblauer, S., Floricioiu, D., Van Wessem, J. M., et al. (2018). Changing pattern of ice flow and mass balance for glaciers discharging into the Larsen A and B embayments, Antarctic Peninsula, 2011 to 2016. *The Cryosphere*, *12*(4), 1273–1291. https://doi.org/10.5194/tc-12-1273-2018

Rott, H., Wuite, J., De Rydt, J., Gudmundsson, G. H., Floricioiu, D., & Rack, W. (2020). Impact of marine processes on flow dynamics of northern Antarctic Peninsula outlet glaciers. *Nature Communications*, *11*(1), 2969. https://doi.org/10.1038/s41467-020-16658-y

Rudnick, D., Costa, D., Johnson, K., Lee, C., & Timmermans, M.-L. (2017). *ALPS II – Autonomous Lagrangian Platforms and Sensors* (A Report of the ALPS II Workshop) (p. 66 pp.). La Jolla, CA.

Saeedan, M., & Eldawy, A. (2022a). Spatial Parquet: A Column File Format for Geospatial Data Lakes [Extended Version]. In *Proceedings of the 30th International Conference on Advances in Geographic Information Systems* (pp. 1–4). https://doi.org/10.1145/3557915.3561038

Saeedan, M., & Eldawy, A. (2022b). Spatial Parquet: A Column File Format for Geospatial Data Lakes [Extended Version] (Version 1). https://doi.org/10.48550/ARXIV.2209.02158

Sanchez, G., Halpin, J. A., Gard, M., Hasterok, D., Stål, T., Raimondo, T., et al. (2021). PetroChron Antarctica: A Geological Database for Interdisciplinary Use. *Geochemistry, Geophysics, Geosystems*, *22*(12), e2021GC010154. https://doi.org/10.1029/2021GC010154

Sansiviero, M., Morales Maqueda, M. Á., Fusco, G., Aulicino, G., Flocco, D., & Budillon, G. (2017). Modelling sea ice formation in the Terra Nova Bay polynya. *Journal of Marine Systems*, *166*, 4–25. https://doi.org/10.1016/j.jmarsys.2016.06.013

Sasgen, I., Konrad, H., Helm, V., & Grosfeld, K. (2019). High-Resolution Mass Trends of the Antarctic Ice Sheet through a Spectral Combination of Satellite Gravimetry and Radar

Altimetry Observations. *Remote Sensing*, *11*(2), 144. https://doi.org/10.3390/rs11020144

Sauermilch, I., Whittaker, J. M., Klocker, A., Munday, D. R., Hochmuth, K., Bijl, P. K., & LaCasce, J. H. (2021). Gateway-driven weakening of ocean gyres leads to Southern Ocean cooling. *Nature Communications*, *12*(1), 6465. https://doi.org/10.1038/s41467-021-26658-1

Save, H., Bettadpur, S., & Tapley, B. D. (2016). High-resolution CSR GRACE RL05 mascons. *Journal of Geophysical Research: Solid Earth*, *121*(10), 7547–7569. https://doi.org/10.1002/2016JB013007

Scambos, T. A. (2004). Glacier acceleration and thinning after ice shelf collapse in the Larsen B embayment, Antarctica. *Geophysical Research Letters*, *31*(18), L18402. https://doi.org/10.1029/2004GL020670

Scambos, T. A., Haran, T. M., Fahnestock, M. A., Painter, T. H., & Bohlander, J. (2007). MODIS-based Mosaic of Antarctica (MOA) data sets: Continent-wide surface morphology and snow grain size. *Remote Sensing of Environment*, *111*(2–3), 242–257. https://doi.org/10.1016/j.rse.2006.12.020

Schannwell, C., Drews, R., Ehlers, T. A., Eisen, O., Mayer, C., Malinen, M., et al. (2020). Quantifying the effect of ocean bed properties on ice sheet geometry over 40 000 years with a full-Stokes model. *The Cryosphere*, *14*(11), 3917–3934. https://doi.org/10.5194/tc-14-3917-2020

Scheinert, M., Ferraccioli, F., Schwabe, J., Bell, R., Studinger, M., Damaske, D., et al. (2016). New Antarctic gravity anomaly grid for enhanced geodetic and geophysical studies in Antarctica. *Geophysical Research Letters*, *43*(2), 600–610. https://doi.org/10.1002/2015GL067439

Scheinert, M., Zingerle, P., Schaller, T., and Pail, R. (2024), Antarctic gravity anomaly and height anomaly grids (AntGG2021), PANGAEA, https://doi.org/10.1594/PANGAEA.971238.

Schemm, S. (2018). Regional Trends in Weather Systems Help Explain Antarctic Sea Ice Trends. *Geophysical Research Letters*, *45*(14), 7165–7175. https://doi.org/10.1029/2018GL079109

Scher, H. D., Whittaker, J. M., Williams, S. E., Latimer, J. C., Kordesch, W. E. C., & Delaney, M. L. (2015). Onset of Antarctic Circumpolar Current 30 million years ago as Tasmanian Gateway aligned with westerlies. *Nature*, *523*(7562), 580–583. https://doi.org/10.1038/nature14598

Schlegel, N.-J., Seroussi, H., Schodlok, M. P., Larour, E. Y., Boening, C., Limonadi, D., et al. (2018). Exploration of Antarctic Ice Sheet 100-Year Contribution to Sea Level Rise and Associated Model Uncertainties Using the ISSM Framework. *The Cryosphere*, *12*(11), 3511–3534.

Schlegel, R., Murray, T., Smith, A. M., Brisbourne, A. M., Booth, A. D., King, E. C., & Clark, R. A. (2022). Radar Derived Subglacial Properties and Landforms Beneath Rutford Ice Stream, West Antarctica. *Journal of Geophysical Research: Earth Surface*, *127*(1), e2021JF006349. https://doi.org/10.1029/2021JF006349

Schmidt, L.S., Schuler, T.V., Thomas, E.E. and Westermann, S., 2023. Meltwater runoff and glacier mass balance in the high Arctic: 1991–2022 simulations for Svalbard. *The Cryosphere*, 17(7), 2941-2963, https://doi.org/10.5194/tc-17-2941-2023.

Schmidtko, S., Heywood, K. J., Thompson, A. F., & Aoki, S. (2014). Multidecadal warming of Antarctic waters. *Science*, *346*(6214), 1227–1231. https://doi.org/10.1126/science.1256117

Schoof, C. (2007). Marine ice-sheet dynamics. Part 1. The case of rapid sliding. *J. Fluid Mech.*, *573*, 27–55. https://doi.org/10.1017/S0022112006003570

Schoof, C. (2010). Coulomb friction and other sliding laws in a higher-order glacier flow model. *Mathematical Models and Methods in Applied Sciences*, *20*(01), 157–189. https://doi.org/10.1142/S0218202510004180

Schoof, C., & Mantelli, E. (2021). The role of sliding in ice stream formation. *Proceedings of the Royal Society A: Mathematical, Physical and Engineering Sciences*, *477*(2248), 20200870. https://doi.org/10.1098/rspa.2020.0870

Schröder, L., Horwath, M., Dietrich, R., Helm, V., van den Broeke, M. R., & Ligtenberg, S. R. M. (2019). Four decades of Antarctic surface elevation changes from multi-mission satellite altimetry. *The Cryosphere*, *13*(2), 427–449. https://doi.org/10.5194/tc-13-427-2019

Schroeder, D. M., Blankenship, D. D., & Young, D. A. (2013). Evidence for a Water System Transition beneath Thwaites Glacier, West Antarctica. *Proceedings of the National Academy of Sciences*, *110*(30), 12225–12228. https://doi.org/10.1073/pnas.1302828110

Schroeder, D. M., Blankenship, D. D., Young, D. A., & Quartini, E. (2014). Evidence for elevated and spatially variable geothermal flux beneath the West Antarctic Ice Sheet. *Proceedings of the National Academy of Sciences*, *111*(25), 9070–9072. https://doi.org/10.1073/pnas.1405184111

Schroeder, D. M., Bingham, R. G., Blankenship, D. D., Christianson, K., Eisen, O., Flowers, G. E., et al. (2020). Five decades of radioglaciology. *Annals of Glaciology*, *61*(81), 1–13. https://doi.org/10.1017/aog.2020.11

Schroeder, Dustin M., Blankenship, D. D., & Young, D. A. (2013). Evidence for a water system transition beneath Thwaites Glacier, West Antarctica. *Proceedings of the National Academy of Sciences*, *110*(30), 12225–12228. https://doi.org/10.1073/pnas.1302828110

Schroeder, Dustin M., Dowdeswell, J. A., Siegert, M. J., Bingham, R. G., Chu, W., MacKie, E. J., et al. (2019). Multidecadal observations of the Antarctic ice sheet from restored analog radar records. *Proceedings of the National Academy of Sciences*, *116*(38), 18867–18873. https://doi.org/10.1073/pnas.1821646116

Seager, R., Naik, N., & Vecchi, G. A. (2010). Thermodynamic and Dynamic Mechanisms for Large-Scale Changes in the Hydrological Cycle in Response to Global Warming*. *Journal of Climate*, *23*(17), 4651–4668. https://doi.org/10.1175/2010JCLI3655.1

Seehaus, T., Marinsek, S., Helm, V., Skvarca, P., & Braun, M. (2015). Changes in ice dynamics, elevation and mass discharge of Dinsmoor–Bombardier–Edgeworth glacier system, Antarctic Peninsula. *Earth and Planetary Science Letters*, *427*, 125–135. https://doi.org/10.1016/j.epsl.2015.06.047

Seehaus, T., Cook, A. J., Silva, A. B., & Braun, M. (2018). Changes in glacier dynamics in the northern Antarctic Peninsula since 1985. *The Cryosphere*, *12*(2), 577–594. https://doi.org/10.5194/tc-12-577-2018

Seehaus, T. C., Sommer, C., Dethinne, T., & Malz, P. (2023). Mass changes of the northern Antarctic Peninsula Ice Sheet derived from repeat bi-static SAR acquisitions for the period 2013-2017. *The Cryosphere*, 17(11), 4629-4644 https://doi.org/10.5194/tc-2022-251

Sellevold, R., Van Kampenhout, L., Lenaerts, J. T. M., Noël, B., Lipscomb, W. H., & Vizcaino, M. (2019). Surface mass balance downscaling through elevation classes in an Earth system model: application to the Greenland ice sheet. *The Cryosphere*, *13*(12), 3193–3208. https://doi.org/10.5194/tc-13-3193-2019

Selley, H. L., Hogg, A. E., Cornford, S., Dutrieux, P., Shepherd, A., Wuite, J., et al. (2021). Widespread increase in dynamic imbalance in the Getz region of Antarctica from 1994 to 2018. *Nature Communications*, *12*(1), 1133. https://doi.org/10.1038/s41467-021-21321-1

Sergienko, O. V. (2022). No general stability conditions for marine ice-sheet grounding lines in the presence of feedbacks. *Nature Communications*, *13*(1), 2265. https://doi.org/10.1038/s41467-022-29892-3

Sergienko, O. V., & Wingham, D. J. (2022). Bed Topography and Marine Ice-Sheet Stability. *Journal of Glaciology*, *68*(267), 124–138. https://doi.org/10.1017/jog.2021.79

Seroussi, H., Morlighem, M., Rignot, E., Larour, E., Aubry, D., Ben Dhia, H., & Kristensen, S. S. (2011). Ice flux divergence anomalies on 79north Glacier, Greenland. *Geophysical Research Letters*, *38*(9), 2011GL047338. https://doi.org/10.1029/2011GL047338

Seroussi, H., Nakayama, Y., Larour, E., Menemenlis, D., Morlighem, M., Rignot, E., & Khazendar, A. (2017). Continued retreat of Thwaites Glacier, West Antarctica, controlled by bed topography and ocean circulation. *Geophysical Research Letters*, *44*(12), 6191–6199. https://doi.org/10.1002/2017GL072910

Seroussi, H., Ivins, E. R., Wiens, D. A., & Bondzio, J. (2017). Influence of a West Antarctic mantle plume on ice sheet basal conditions. *Journal of Geophysical Research: Solid Earth*, *122*(9), 7127–7155. https://doi.org/10.1002/2017JB014423

Seroussi, H., Nowicki, S., Payne, A. J., Goelzer, H., Lipscomb, W. H., Abe-Ouchi, A., et al. (2020). ISMIP6 Antarctica: a multi-model ensemble of the Antarctic ice sheet evolution over the 21st century. *The Cryosphere*, *14*(9), 3033–3070. https://doi.org/10.5194/tc-14-3033-2020

Seroussi, H., Pelle, T., Lipscomb, W.H., Abe‐Ouchi, A., Albrecht, T., Alvarez‐Solas, J., Asay‐Davis, X., Barre, J.B., Berends, C.J., Bernales, J. and Blasco, J. (2024) Evolution of the Antarctic Ice Sheet over the next three centuries from an ISMIP6 model ensemble. Earth's Future, 12(9), p.e2024EF004561. https://doi.org/10.1029/2024EF004561

Shackleton, C., Matsuoka, K., Moholdt, G., Van Liefferinge, B. and Paden, J. (2023) Stochastic simulations of bed topography constrain geothermal heat flow and subglacial drainage near Dome Fuji, East Antarctica. *Journal of Geophysical Research: Earth Surface*, 128(11), p.e2023JF007269, https://doi.org/10.1029/2023JF007269

Shahateet, K., Seehaus, T., Navarro, F., Sommer, C., & Braun, M. (2021). Geodetic Mass Balance of the South Shetland Islands Ice Caps, Antarctica, from Differencing

TanDEM-X DEMs. *Remote Sensing*, *13*(17), 3408. https://doi.org/10.3390/rs13173408

Shen, Q., Wang, H., Shum, C. K., Jiang, L., Hsu, H. T., & Dong, J. (2018). Recent high-resolution Antarctic ice velocity maps reveal increased mass loss in Wilkes Land, East Antarctica. *Scientific Reports*, *8*(1), 4477. https://doi.org/10.1038/s41598-018-22765-0

Shen, W., Wiens, D. A., Lloyd, A. J., & Nyblade, A. A. (2020). A Geothermal Heat Flux Map of Antarctica Empirically Constrained by Seismic Structure. *Geophysical Research Letters*, *47*(14). https://doi.org/10.1029/2020GL086955

Shepherd, A., & Nowicki, S. (2017). Improvements in ice-sheet sea-level projections. *Nature Climate Change*, *7*(10), 672–674. https://doi.org/10.1038/nclimate3400

Shepherd, A., Ivins, E. R., A, G., Barletta, V. R., Bentley, M. J., Bettadpur, S., et al. (2012). A Reconciled Estimate of Ice-Sheet Mass Balance. *Science*, *338*(6111), 1183–1189. https://doi.org/10.1126/science.1228102

Shepherd, A., Gilbert, L., Muir, A. S., Konrad, H., McMillan, M., Slater, T., et al. (2019). Trends in Antarctic Ice Sheet Elevation and Mass. *Geophysical Research Letters*, *46*(14), 8174–8183. https://doi.org/10.1029/2019GL082182

Sidorenko, D. et al. (2019). Evaluation of FESOM2.0 coupled to ECHAM6.3: preindustrial and HighResMIP simulations. *J. Adv. Model. Earth Syst.* 11, 3794–3815. https://doi.org/10.1029/2019MS001696.

Siegert, M. J., Ross, N., & Le Brocq, A. M. (2016). Recent advances in understanding Antarctic subglacial lakes and hydrology. *Philosophical Transactions of the Royal Society A: Mathematical, Physical and Engineering Sciences*, *374*(2059), 20140306. https://doi.org/10.1098/rsta.2014.0306

Siegert, M. J., Kulessa, B., Bougamont, M., Christoffersen, P., Key, K., Andersen, K. R., et al. (2018). Antarctic subglacial groundwater: a concept paper on its measurement and potential influence on ice flow. *Geological Society, London, Special Publications*, *461*(1), 197–213. https://doi.org/10.1144/SP461.8

Siegfried, M. R., B. Medley, K. M. Larson, H. A. Fricker, and S. Tulaczyk (2017), Snow accumulation variability on a West Antarctic ice stream observed with GPS reflectometry, 2007–2017, Geophys. Res. Lett., 44, 7808–7816, doi:10.1002/2017GL074039.

Silvano, A., Rintoul, S. R., & Herraiz-Borreguero, L. (2016) Ocean-Ice Shelf Interaction in East Antarctica. *Oceanography*, *29*(4), 130–143, https://www.jstor.org/stable/24862288

Silvano, A., Rintoul, S. R., Peña-Molino, B., & Williams, G. D. (2017). Distribution of water masses and meltwater on the continental shelf near the Totten and Moscow University ice shelves,*Journal of Geophysical Research: Oceans*, *122*(3), 2050–2068. https://doi.org/10.1002/2016JC012115

Silvano, A., Rintoul, S. R., Peña-Molino, B., Hobbs, W. R., van Wijk, E., Aoki, S., et al. (2018). Freshening by glacial meltwater enhances melting of ice shelves and reduces formation of Antarctic Bottom Water. *Science Advances*, *4*(4), eaap9467. https://doi.org/10.1126/sciadv.aap9467

Silvano, A., Rintoul, S. R., Kusahara, K., Peña-Molino, B., van Wijk, E., Gwyther, D. E., & Williams, G. D. (2019). Seasonality of Warm Water Intrusions Onto the Continental Shelf Near the Totten Glacier. *Journal of Geophysical Research: Oceans*, *124*(6), 4272–4289. https://doi.org/10.1029/2018JC014634

Silvano, A., Foppert, A., Rintoul, S. R., Holland, P. R., Tamura, T., Kimura, N., et al. (2020). Recent recovery of Antarctic Bottom Water formation in the Ross Sea driven by climate anomalies. *Nature Geoscience*, *13*(12), 780–786. https://doi.org/10.1038/s41561-020-00655-3

Silvano, A., Holland, P. R., Naughten, K. A., Dragomir, O., Dutrieux, P., Jenkins, A., et al. (2022). Baroclinic Ocean Response to Climate Forcing Regulates Decadal Variability of Ice-Shelf Melting in the Amundsen Sea. *Geophysical Research Letters*, *49*(24). https://doi.org/10.1029/2022GL100646

Simav, M., Becker, D., Yildiz, H., & Hoss, M. (2020). Impact of temperature stabilization on the strapdown airborne gravimetry: a case study in Central Turkey. *Journal of Geodesy*, *94*(4), 41. https://doi.org/10.1007/s00190-020-01369-5

Simms, A.R., Whitehouse, P.L., Simkins, L.M., Nield, G., DeWitt, R. and Bentley, M.J., 2018. Late Holocene relative sea levels near Palmer Station, northern Antarctic Peninsula, strongly controlled by late Holocene ice-mass changes. *Quaternary Science Reviews*, 199, 49-59.

Slater, T., Hogg, A. E., & Mottram, R. (2020). Ice-sheet losses track high-end sea-level rise projections. *Nature Climate Change*, *10*(10), 879–881. https://doi.org/10.1038/s41558-020-0893-y

Smith, A. M., Murray, T., Nicholls, K. W., Makinson, K., Aðalgeirsdóttir, G., Behar, A. E., & Vaughan, D. G. (2007). Rapid erosion, drumlin formation, and changing hydrology beneath an Antarctic ice stream. *Geology*, *35*(2), 127. https://doi.org/10.1130/G23036A.1

Smith, A. M., Bentley, C. R., Bingham, R. G., & Jordan, T. A. (2012). Rapid subglacial erosion beneath Pine Island Glacier, West Antarctica,*Geophysical Research Letters*, *39*(12),https://doi.org/10.1029/2012GL051651

Smith, Andrew M., Jordan, T. A., Ferraccioli, F., & Bingham, R. G. (2013). Influence of subglacial conditions on ice stream dynamics: Seismic and potential field data from Pine Island Glacier, West Antarctica. *Journal of Geophysical Research: Solid Earth*, *118*(4), 1471–1482. https://doi.org/10.1029/2012JB009582

Smith, B. E., Fricker, H. A., Joughin, I. R., & Tulaczyk, S. (2009). An inventory of active subglacial lakes in Antarctica detected by ICESat (2003-2008). *J. Glaciol.*, *55*(192), 573–595.

Smith, B., Fricker, H.A., Holschuh, N., Gardner, A.S., Adusumilli, S., Brunt, K.M., Csatho, B., Harbeck, K., Huth, A., Neumann, T. and Nilsson, J., 2019. Land ice height-retrieval algorithm for NASA's ICESat-2 photon-counting laser altimeter. *Remote Sensing of Environment*, 233, p.111352, https://doi.org/10.1016/j.rse.2019.111352

Smith, B. E., Fricker, H. A., Gardner, A. S., Medley, B., Nilsson, J., Paolo, F. S., et al. (2020). Pervasive ice sheet mass loss reflects competing ocean and atmosphere processes. *Science*, *368*(6496), 1239–1242. https://doi.org/10.1126/science.aaz5845

Smith, B., H. A. Fricker, A. Gardner, M. R. Siegfried, S. Adusumilli, B. M. Csath, et al. (2021a). ATLAS/ICESat-2 L3A Land Ice Height, version 5 [Data set]. NASA

National Snow and Ice Data Center DAAC. https://doi.org/10.5067/ATLAS/ATL06.005

Smith, B, Dickinson, Suzanne, Harbeck, Kaitlin, Neumann, Tom, Hancock, David, Lee, Jeffery, & Jelly, Benjamin. (2021b). Ice, Cloud, and Land Elevation Satellite (ICESat-2) Project Algorithm Theoretical Basis Document (ATBD) for Land-Ice Along-Track Products, version 4. https://doi.org/10.5067/3QVXH1HX6VUB

Smith, B., Adusumilli, S., Csathó, B. M., Felikson, D., Fricker, H. A., Gardner, A. S., Holschuh, N., Lee, J., Nilsson, J., Paolo, F., Siegfried, M. R., Sutterley, T. & the ICESat-2 Science Team. (2023a). ATLAS/ICESat-2 L3A Land Ice Height. (ATL06, Version 6). [Data Set]. Boulder, Colorado USA. NASA National Snow and Ice Data Center Distributed Active Archive Center. https://doi.org/10.5067/ATLAS/ATL06.006. Date Accessed 06-16-2025.

Smith, B.E., Medley, B., Fettweis, X., Sutterley, T., Alexander, P., Porter, D. and Tedesco, M., (2023b) Evaluating Greenland surface-mass-balance and firn-densification data using ICESat-2 altimetry. *The Cryosphere*, 17(2), 789-808, https://doi.org/10.5194/tc-17-789-2023

Smith, B., Sutterley, T., Dickinson, S., Jelley, B. P., Felikson, D., Neumann, T. A., Fricker, H. A., Gardner, A. S., Padman, L., Markus, T., Kurtz, N., Bhardwaj, S., Hancock, D. & Lee, J. (2024a). ATLAS/ICESat-2 L3B Gridded Antarctic and Arctic Land Ice Height. (ATL14, Version 4). [Data Set]. Boulder, Colorado USA. NASA National Snow and Ice Data Center Distributed Active Archive Center. https://doi.org/10.5067/ATLAS/ATL14.004.

Smith, B., Sutterley, T., Dickinson, S., Jelley, B. P., Felikson, D., Neumann, T. A., Fricker, H. A., Gardner, A. S., Padman, L., Markus, T., Kurtz, N., Bhardwaj, S., Hancock, D. & Lee, J. (2024b). ATLAS/ICESat-2 L3B Gridded Antarctic and Arctic Land Ice Height Change. (ATL15, Version 4). [Data Set]. Boulder, Colorado USA. NASA National Snow and Ice Data Center Distributed Active Archive Center. https://doi.org/10.5067/ATLAS/ATL15.004.

Smith, B. E., Studinger, M., Sutterley, T., Fair, Z., & Neumann, T. (2025). Understanding biases in ICESat-2 data due to subsurface scattering using Airborne Topographic Mapper waveform data. *The Cryosphere*, 19(3), 975–995. https://doi.org/10.5194/tc-19-975-2025

Smith, E. C., Smith, A. M., White, R. S., Brisbourne, A. M., & Pritchard, H. D. (2015). Mapping the ice-bed interface characteristics of Rutford Ice Stream, West Antarctica, using microseismicity. *Journal of Geophysical Research: Earth Surface*, *120*(9), 1881–1894. https://doi.org/10.1002/2015JF003587

Smith, Emma C., Hattermann, T., Kuhn, G., Gaedicke, C., Berger, S., Drews, R., et al. (2020). Detailed Seismic Bathymetry Beneath Ekström Ice Shelf, Antarctica: Implications for Glacial History and Ice-Ocean Interaction. *Geophysical Research Letters*, *47*(10). https://doi.org/10.1029/2019GL086187

Smith, J. A., Graham, A. G. C., Post, A. L., Hillenbrand, C.-D., Bart, P. J., & Powell, R. D. (2019). The marine geological imprint of Antarctic ice shelves. *Nature Communications*, *10*(1), 5635. https://doi.org/10.1038/s41467-019-13496-5

Smith, R. S., Mathiot, P., Siahaan, A., Lee, V., Cornford, S. L., Gregory, J. M., et al. (2021). Coupling the U.K. Earth System Model to Dynamic Models of the Greenland and

Antarctic Ice Sheets. *Journal of Advances in Modeling Earth Systems*, *13*(10), e2021MS002520. https://doi.org/10.1029/2021MS002520

Smith, W. O., Jr., and Y. Zhong (2024), Under-ice mixed layers and the regulation of early spring phytoplankton growth in the Southern Ocean, *Geophys. Res. Lett.*, 51, e2023GL106796, https://doi.org/10.1029/2023GL106796.

Smith-Johnsen, S., Schlegel, N.-J., de Fleurian, B., & Nisancioglu, K. H. (2020). Sensitivity of the Northeast Greenland Ice Stream to Geothermal Heat. *Journal of Geophysical Research: Earth Surface*, *125*(1). https://doi.org/10.1029/2019JF005252

Snow, K., Goldberg, D. N., Holland, P. R., Jordan, J. R., Arthern, R. J., & Jenkins, A. (2017). The Response of Ice Sheets to Climate Variability. *Geophysical Research Letters*, *44*(23), 11,878-11,885. https://doi.org/10.1002/2017GL075745

Sokolov, S., & Rintoul, S. R. (2009). Circumpolar structure and distribution of the Antarctic Circumpolar Current fronts: 2. Variability and relationship to sea surface height. *Journal of Geophysical Research*, *114*(C11), C11019. https://doi.org/10.1029/2008JC005248

Sommers, A., Rajaram, H., & Morlighem, M. (2018). SHAKTI: Subglacial Hydrology and Kinetic, Transient Interactions v1.0. *Geoscientific Model Development*, *11*(7), 2955–2974. https://doi.org/10.5194/gmd-11-2955-2018

Sørensen, L. S., Simonsen, S. B., Nielsen, K., Lucas-Picher, P., Spada, G., Adalgeirsdottir, G., et al. (2011). Mass balance of the Greenland ice sheet (2003–2008) from ICESat data – the impact of interpolation, sampling and firn density. *The Cryosphere*, *5*(1), 173–186. https://doi.org/10.5194/tc-5-173-2011

Song, P., Scholz, P., Knorr, G. et al. (2025). Regional conditions determine thresholds of accelerated Antarctic basal melt in climate projection. *Nat. Clim. Chang.* 15, 521–527. https://doi.org/10.1038/s41558-025-02306-0

Souney, J. M., Twickler, M. S., Aydin, M., Steig, E. J., Fudge, T. J., Street, L. V., et al. (2021). Core handling, transportation and processing for the South Pole ice core (SPICEcore) project. *Annals of Glaciology*, *62*(84), 118–130. https://doi.org/10.1017/aog.2020.80

Souverijns, N., Gossart, A., Demuzere, M., Lenaerts, J. T. M., Medley, B., Gorodetskaya, I. V., et al. (2019). A New Regional Climate Model for POLAR-CORDEX: Evaluation of a 30-Year Hindcast with COSMO-CLM ^{2} Over Antarctica. *Journal of Geophysical Research: Atmospheres*, *124*(3), 1405–1427. https://doi.org/10.1029/2018JD028862

Spikes, V. B., Hamilton, G. S., Arcone, S. A., Kaspari, S., & Mayewski, P. A. (2004). Variability in accumulation rates from GPR profiling on the West Antarctic plateau. *Annals of Glaciology*, *39*, 238–244. https://doi.org/10.3189/172756404781814393

Sproson, A. D., Yokoyama, Y., Miyairi, Y., Aze, T., & Totten, R. L. (2022). Holocene melting of the West Antarctic Ice Sheet driven by tropical Pacific warming. *Nature Communications*, *13*(1), 2434. https://doi.org/10.1038/s41467-022-30076-2

Stål, T., Halpin, J. A., Goodge, J. W., & Reading, A. M. (2024). Geology matters for Antarctic geothermal heat. *Geophysical Research Letters*, 51(13), e2024GL110098, https://doi.org/10.1029/2024GL110098

Stål, T., Reading, A. M., Halpin, J. A., & Whittaker, J. M. (2021). Antarctic Geothermal Heat Flow Model: Aq1. *Geochemistry, Geophysics, Geosystems*, *22*(2). https://doi.org/10.1029/2020GC009428

Stål, T., Reading, A. M., Halpin, J. A., Phipps, S. J., & Whittaker, J. M. (2020). The Antarctic crust and upper mantle: A flexible 3D model and software framework for interdisciplinary research. *Frontiers in Earth Science*, 8, 577502, https://doi.org/10.3389/feart.2020.577502

Stanton, T. P., Shaw, W. J., Truffer, M., Corr, H. F. J., Peters, L. E., Riverman, K. L., et al. (2013). Channelized Ice Melting in the Ocean Boundary Layer Beneath Pine Island Glacier, Antarctica. *Science*, *341*(6151), 1236–1239. https://doi.org/10.1126/science.1239373

Stearns, L. A., Smith, B. E., & Hamilton, G. S. (2008). Increased flow speed on a large East Antarctic outlet glacier caused by subglacial floods. *Nat. Geosci.*, *1*(12), 827–831. https://doi.org/10.1038/ngeo356

Steig, E. J., Schneider, D. P., Rutherford, S. D., Mann, M. E., Comiso, J. C., & Shindell, D. T. (2009). Warming of the Antarctic ice-sheet surface since the 1957 International Geophysical Year. *Nature*, *457*(7228), 459–462. https://doi.org/10.1038/nature07669

Stern, A. A., Dinniman, M. S., Zagorodnov, V., Tyler, S. W., & Holland, D. M. (2013). Intrusion of warm surface water beneath the McMurdo Ice Shelf, Antarctica. *Journal of Geophysical Research: Oceans*, *118*(12), 7036–7048. https://doi.org/10.1002/2013JC008842

Stevens, C. M., Verjans, V., Lundin, J. M. D., Kahle, E. C., Horlings, A. N., Horlings, B. I., & Waddington, E. D. (2020). The Community Firn Model (CFM) v1.0. *Geoscientific Model Development*, *13*(9), 4355–4377. https://doi.org/10.5194/gmd-13-4355-2020

Stewart, A. L., & Thompson, A. F. (2015). Eddy-mediated transport of warm Circumpolar Deep Water across the Antarctic Shelf Break. *Geophysical Research Letters*, *42*(2), 432–440. https://doi.org/10.1002/2014GL062281

Stewart, C. L., Christoffersen, P., Nicholls, K. W., Williams, M. J. M., & Dowdeswell, J. A. (2019). Basal melting of Ross Ice Shelf from solar heat absorption in an ice-front polynya. *Nature Geoscience*, *12*(6), 435–440. https://doi.org/10.1038/s41561-019-0356-0

Stokes, C. R., Sanderson, J. E., Miles, B. W. J., Jamieson, S. S. R., & Leeson, A. A. (2019). Widespread distribution of supraglacial lakes around the margin of the East Antarctic Ice Sheet. *Scientific Reports*, *9*(1), 13823. https://doi.org/10.1038/s41598-019-50343-5

Studinger, M., Bell, R. E., Blankenship, D. D., Finn, C. A., Arko, R. A., Morse, D. L., & Joughin, I. (2001). Subglacial sediments: A regional geological template for ice flow in West Antarctica. *Geophysical Research Letters*, *28*(18), 3493–3496. https://doi.org/10.1029/2000GL011788

Studinger, M., Bell, R., & Frearson, N. (2008). Comparison of AIRGrav and GT-1A airborne gravimeters for research applications. *Geophysics*, *73*(6), I51–I61. https://doi.org/10.1190/1.2969664

Studinger, M., Manizade, S. S., Linkswiler, M. A., & Yungel, J. K. (2022). High-resolution imaging of supraglacial hydrological features on the Greenland Ice Sheet with

NASA's Airborne Topographic Mapper (ATM) instrument suite. *The Cryosphere*, *16*(9), 3649–3668. https://doi.org/10.5194/tc-16-3649-2022

Studinger, M., Smith, B. E., Kurtz, N., Petty, A., Sutterley, T., & Tilling, R. (2024). Estimating differential penetration of green (532 nm) laser light over sea ice with NASA's Airborne Topographic Mapper: Observations and models. *The Cryosphere*, 18(5), 2625–2652. https://doi.org/10.5194/tc-18-2625-2024

Suganuma, Y., Kaneda, H., Mas E Braga, M., Ishiwa, T., Koyama, T., Newall, J. C., et al. (2022). Regional sea-level highstand triggered Holocene ice sheet thinning across coastal Dronning Maud Land, East Antarctica. *Communications Earth & Environment*, *3*(1), 273. https://doi.org/10.1038/s43247-022-00599-z

Sun, S., Pattyn, F., Simon, E. G., Albrecht, T., Cornford, S., Calov, R., et al. (2020). Antarctic ice sheet response to sudden and sustained ice-shelf collapse (ABUMIP). *Journal of Glaciology*, *66*(260), 891–904. https://doi.org/10.1017/jog.2020.67

Talley, L. D., Pikard, G.L., Emery, W.J., Swift, J.H. (2011). *Descriptive Physical Oceanography: An Introduction*. Academic Press. ISBN:978-0-7506-4552-2.

Tamura, T., Ohshima, K. I., & Nihashi, S. (2008). Mapping of sea ice production for Antarctic coastal polynyas.*Geophysical Research Letters*, *35*(7), https://doi.org/10.1029/2007GL032903

Tan, A. E.-C., McCulloch, J., Rack, W., Platt, I., & Woodhead, I. (2021). Radar Measurements of Snow Depth Over Sea Ice on an Unmanned Aerial Vehicle. *IEEE Transactions on Geoscience and Remote Sensing*, *59*(3), 1868–1875. https://doi.org/10.1109/TGRS.2020.3006182

Tankersley, M. D., Horgan, H. J., Siddoway, C. S., Caratori Tontini, F., & Tinto, K. J. (2022). Basement Topography and Sediment Thickness Beneath Antarctica's Ross Ice Shelf. *Geophysical Research Letters*, *49*(10). https://doi.org/10.1029/2021GL097371

Tapley, B. D., Bettadpur, S., Watkins, M., & Reigber, C. (2004). The gravity recovery and climate experiment: Mission overview and early results. *Geophysical Research Letters*, *31*(9), n/a-n/a. https://doi.org/10.1029/2004GL019920

Testor, P., B. de Young, D. L. Rudnick, J. R. Ledwell, J. D. Sherman, J. C. Bane, L. Centurioni, J. C. Gascard, J. Gould, C. Guihou, C. E. Lee, J. L. Pelegrí, J. A. Smith, and colleagues (2019), Ocean gliders: A component of the integrated global ocean observing system, *Front. Mar. Sci.*, 6, 422, https://doi.org/10.3389/fmars.2019.00422.

The IMBIE team. (2018). Mass balance of the Antarctic Ice Sheet from 1992 to 2017. *Nature*, *558*(7709), 219–222. https://doi.org/10.1038/s41586-018-0179-y

The Scientific Committee on Antarctic Research (SCAR), 2022, *SCAR Data Policy* (SCAR Rep. 42), Zenodo, https://doi.org/10.5281/zenodo.7825314.

The Secretariat of the Antarctic Treaty. (2004). *Guidelines for the Operation of Aircraft near concentrations of birds*. Retrieved from https://documents.ats.aq/recatt/att224_e.pdf

Thoma, M., Jenkins, A., Holland, D., & Jacobs, S. (2008). Modelling Circumpolar Deep Water intrusions on the Amundsen Sea continental shelf, Antarctica. *Geophysical Research Letters*, *35*(18), L18602. https://doi.org/10.1029/2008GL034939

Thomas, R. (2007). Tide-induced perturbations of glacier velocities. *Global and Planetary Change*, *59*(1), 217–224. https://doi.org/10.1016/j.gloplacha.2006.11.017

Thomas, R., & Bentley, C. R. (1978). A Model for Holocene Retreat of the West Antarctic Ice Sheet. *Quaternary Research*, *10*(2), 150–170. https://doi.org/10.1016/0033-5894(78)90098-4

Thomas, R., Rignot, E., Kanagaratnam, P., Krabill, W., & Casassa, G. (2004). Force-perturbation analysis of Pine Island Glacier, Antarctica, suggests cause for recent acceleration. *Ann. Glaciol.*, *39*(1), 133–138, https://doi.org/10.3189/172756404781814429

Thompson, A. F., Stewart, A. L., Spence, P., & Heywood, K. J. (2018). The Antarctic Slope Current in a Changing Climate. *Reviews of Geophysics*, *56*(4), 741–770. https://doi.org/10.1029/2018RG000624

Thompson, S. S., Kulessa, B., Luckman, A., Halpin, J. A., Greenbaum, J. S., Pelle, T., et al. (2023). Glaciological history and structural evolution of the Shackleton Ice Shelf system, East Antarctica, over the past 60 years. *The Cryosphere*, *17*(1), 157–174. https://doi.org/10.5194/tc-17-157-2023

Thomson, S. N., Reiners, P. W., Hemming, S. R., & Gehrels, G. E. (2013). The contribution of glacial erosion to shaping the hidden landscape of East Antarctica. *Nature Geoscience*, *6*(3), 203–207. https://doi.org/10.1038/ngeo1722

Timmermann, R., & Goeller, S. (2017). Response to Filchner–Ronne Ice Shelf cavity warming in a coupled ocean–ice sheet model – Part 1: The ocean perspective. *Ocean Science*, *13*(5), 765–776. https://doi.org/10.5194/os-13-765-2017

Tinto, K. J., & Bell, R. E. (2011). Progressive unpinning of Thwaites Glacier from newly identified offshore ridge: Constraints from aerogravity. *Geophysical Research Letters*, *38*(20), n/a-n/a. https://doi.org/10.1029/2011GL049026

Tinto, K. J., Padman, L., Siddoway, C. S., Springer, S. R., Fricker, H. A., Das, I., et al. (2019). Ross Ice Shelf response to climate driven by the tectonic imprint on seafloor bathymetry. *Nature Geoscience*, *12*(6), 441–449. https://doi.org/10.1038/s41561-019-0370-2

Trani, M., Falco, P., Zambianchi, E., & Sallée, J. B. (2014). Aspects of the Antarctic Circumpolar Current dynamics investigated with drifter data. *Progress in Oceanography*, *125*, 1–15. https://doi.org/10.1016/j.pocean.2014.05.001

Trusel, L. D., Frey, K. E., Das, S. B., Munneke, P. K., & van den Broeke, M. R. (2013). Satellite-based estimates of Antarctic surface meltwater fluxes. *Geophysical Research Letters*, *40*(23), 6148–6153. https://doi.org/10.1002/2013GL058138

Trusel, L. D., Frey, K. E., Das, S. B., Karnauskas, K. B., Kuipers Munneke, P., van Meijgaard, E., & van den Broeke, M. R. (2015). Divergent trajectories of Antarctic surface melt under two twenty-first-century climate scenarios. *Nature Geoscience*, *8*(12), 927–932. https://doi.org/10.1038/ngeo2563

Turner, J., & Comiso, J. (2017). Solve Antarctica’s sea-ice puzzle. *Nature*, *547*(7663), 275–277. https://doi.org/10.1038/547275a

Turner, J., & Pendlebury, S. (2004). *The international Antarctic weather forecasting handbook*. British Antarctic Survey.

Turner, J., Bracegirdle, T. J., Phillips, T., Marshall, G. J., & Hosking, J. S. (2013). An Initial Assessment of Antarctic Sea Ice Extent in the CMIP5 Models. *Journal of Climate*, *26*(5), 1473–1484. https://doi.org/10.1175/JCLI-D-12-00068.1

Turner, J., Orr, A., Gudmundsson, G. H., Jenkins, A., Bingham, R. G., Hillenbrand, C.-D., & Bracegirdle, T. J. (2017). Atmosphere-ocean-ice interactions in the Amundsen Sea Embayment, West Antarctica. *Reviews of Geophysics*, *55*(1), 235–276. https://doi.org/10.1002/2016RG000532

Turner, J., Phillips, T., Marshall, G. J., Hosking, J. S., Pope, J. O., Bracegirdle, T. J., & Deb, P. (2017). Unprecedented springtime retreat of Antarctic sea ice in 2016. *Geophysical Research Letters*, *44*(13), 6868–6875. https://doi.org/10.1002/2017GL073656

Turner, J., Phillips, T., Thamban, M., Rahaman, W., Marshall, G. J., Wille, J. D., et al. (2019). The Dominant Role of Extreme Precipitation Events in Antarctic Snowfall Variability. *Geophysical Research Letters*, *46*(6), 3502–3511. https://doi.org/10.1029/2018GL081517

Turner, J., Holmes, C., Caton Harrison, T., Phillips, T., Jena, B., Reeves-Francois, T., et al. (2022). Record Low Antarctic Sea Ice Cover in February 2022. *Geophysical Research Letters*, *49*(12), e2022GL098904. https://doi.org/10.1029/2022GL098904

Turton, J. V., Kirchgaessner, A., Ross, A. N., King, J. C., & Kuipers Munneke, P. (2020). The influence of föhn winds on annual and seasonal surface melt on the Larsen C Ice Shelf, Antarctica. *The Cryosphere*, *14*(11), 4165–4180. https://doi.org/10.5194/tc-14-4165-2020

University Of Texas Institute For Geophysics (UTIG). (2015). IceBridge HiCARS 1 L1B Time-Tagged Echo Strength Profiles, Version 1 [Data set]. NASA National Snow and Ice Data Center Distributed Active Archive Center. https://doi.org/10.5067/W2KXX0MYNJ9G

Urruty, B., Hill, E. A., Reese, R., Garbe, J., Gagliardini, O., Durand, G., et al. (2022). The stability of present-day Antarctic grounding lines – Part A: No indication of marine ice sheet instability in the current geometry. *The Cryosphere*, 17(9), 3739-3759 https://doi.org/10.5194/tc-2022-104

Van Achter, G., Fichefet, T., Goosse, H., & Moreno-Chamarro, E. (2022). Influence of fast ice on future ice shelf melting in the Totten Glacier area, East Antarctica. *The Cryosphere*, *16*(11), 4745–4761. https://doi.org/10.5194/tc-16-4745-2022

van Calcar, C. J., van de Wal, R. S. W., Blank, B., de Boer, B., & van der Wal, W. (2022). *Simulation of a fully coupled 3D GIA – ice-sheet model for the Antarctic Ice Sheet over a glacial cycle* (preprint). Solid Earth. https://doi.org/10.5194/egusphere-2022-1328

Van De Wal, R. S. W., Nicholls, R. J., Behar, D., McInnes, K., Stammer, D., Lowe, J. A., et al. (2022). A High-End Estimate of Sea Level Rise for Practitioners. *Earth's Future*, *10*(11), e2022EF002751. https://doi.org/10.1029/2022EF002751

Van Der Veen, C. J., Leftwich, T., Von Frese, R., Csatho, B. M., & Li, J. (2007). Subglacial topography and geothermal heat flux: Potential interactions with drainage of the Greenland ice sheet. *Geophysical Research Letters*, *34*(12), L12501. https://doi.org/10.1029/2007GL030046

Van Der Wal, W., Barletta, V., Nield, G., & Van Calcar, C. (2023). Glacial isostatic adjustment and post-seismic deformation in Antarctica. *Geological Society, London, Memoirs*, *56*(1), 315–341. https://doi.org/10.1144/M56-2022-13

Van Liefferinge, B., & Pattyn, F. (2013). Using Ice-Flow Models to Evaluate Potential Sites of Million Year-Old Ice in Antarctica. *Climate of the Past*, *9*(5), 2335–2345. https://doi.org/10.5194/cp-9-2335-2013

Van Liefferinge, Brice, Taylor, D., Tsutaki, S., Fujita, S., Gogineni, P., Kawamura, K., et al. (2021). Surface Mass Balance Controlled by Local Surface Slope in Inland Antarctica: Implications for Ice-Sheet Mass Balance and Oldest Ice Delineation in Dome Fuji. *Geophysical Research Letters*, *48*(24). https://doi.org/10.1029/2021GL094966

van Wessem, J. M., van de Berg, W. J., Noël, B. P. Y., van Meijgaard, E., Amory, C., Birnbaum, G., et al. (2018). Modelling the climate and surface mass balance of polar ice sheets using RACMO2 – Part 2: Antarctica (1979–2016). *The Cryosphere*, *12*(4), 1479–1498. https://doi.org/10.5194/tc-12-1479-2018

van Wessem, J. M., van den Broeke, M. R., Wouters, B., & Lhermitte, S. (2023). Variable temperature thresholds of melt pond formation on Antarctic ice shelves. *Nature Climate Change*. https://doi.org/10.1038/s41558-022-01577-1

Vance, T. R., Roberts, J. L., Moy, A. D., Curran, M. A. J., Tozer, C. R., Gallant, A. J. E., et al. (2016). Optimal site selection for a high-resolution ice core record in East Antarctica. *Climate of the Past*, *12*(3), 595–610. https://doi.org/10.5194/cp-12-595-2016

Vaňková, I., & Nicholls, K. W. (2022). Ocean Variability Beneath the Filchner-Ronne Ice Shelf Inferred From Basal Melt Rate Time Series. *Journal of Geophysical Research: Oceans*, *127*(10). https://doi.org/10.1029/2022JC018879

Vaňková, I., Cook, S., Winberry, J. P., Nicholls, K. W., & Galton-Fenzi, B. K. (2021). Deriving Melt Rates at a Complex Ice Shelf Base Using In Situ Radar: Application to Totten Ice Shelf. *Geophysical Research Letters*, *48*(7), e2021GL092692. https://doi.org/10.1029/2021GL092692

Vaughan, D. G. (1995). Tidal flexure at ice shelf margins. *Journal of Geophysical Research: Solid Earth*, *100*(B4), 6213–6224. https://doi.org/10.1029/94JB02467

Vaughan, D. G., Corr, H. F. J., Doake, C. S. M., & Waddington, Ed. D. (1999). Distortion of isochronous layers in ice revealed by ground-penetrating radar. *Nature*, *398*(6725), 323–326. https://doi.org/10.1038/18653

Veldhuijsen, S. B. M., van de Berg, W. J., Brils, M., Kuipers Munneke, P., & van den Broeke, M. R. (2023). Characteristics of the 1979–2020 Antarctic firn layer simulated with IMAU-FDM v1.2A. *The Cryosphere*, *17*(4), 1675–1696. https://doi.org/10.5194/tc-17-1675-2023

Velicogna, I., & Wahr, J. (2006). Measurements of Time-Variable Gravity Show Mass Loss in Antarctica. *Science*, *311*(5768), 1754–1756. https://doi.org/10.1126/science.1123785

Velicogna, I., & Wahr, J. (2013). Time-variable gravity observations of ice sheet mass balance: Precision and limitations of the GRACE satellite data. *Geophysical Research Letters*, *40*(12), 3055–3063. https://doi.org/10.1002/grl.50527

Velicogna, I., Mohajerani, Y., A, G., Landerer, F., Mouginot, J., Noel, B., et al. (2020). Continuity of Ice Sheet Mass Loss in Greenland and Antarctica From the GRACE and GRACE Follow-On Missions. *Geophysical Research Letters*, *47*(8). https://doi.org/10.1029/2020GL087291

Verdun, J., Bayer, R., Klingelé, E. E., Cocard, M., Geiger, A., & Halliday, M. E. (2002). Airborne gravity measurements over mountainous areas by using a LaCoste & Romberg air-sea gravity meter. *Geophysics*, *67*(3), 807–816. https://doi.org/10.1190/1.1484525

Verfaillie, D., Pelletier, C., Goosse, H., Jourdain, N. C., Bull, C. Y. S., Dalaiden, Q., et al. (2022). The circum-Antarctic ice-shelves respond to a more positive Southern Annular Mode with regionally varied melting. *Communications Earth & Environment*, *3*(1), 139. https://doi.org/10.1038/s43247-022-00458-x

Vergnano, A., Franco, D., & Godio, A. (2022). Drone-Borne Ground-Penetrating Radar for Snow Cover Mapping. *Remote Sensing*, *14*(7), 1763. https://doi.org/10.3390/rs14071763

Verjans, V., Leeson, A. A., McMillan, M., Stevens, C. M., Van Wessem, J. M., Van De Berg, W. J., et al. (2021). Uncertainty in East Antarctic Firn Thickness Constrained Using a Model Ensemble Approach. *Geophysical Research Letters*, *48*(7). https://doi.org/10.1029/2020GL092060

Vieli, A., & Payne, A. J. (2005). Assessing the ability of numerical ice sheet models to simulate grounding line migration. *Journal of Geophysical Research: Earth Surface*, *110*(F1). https://doi.org/10.1029/2004JF000202

Vionnet, V., Brun, E., Morin, S., Boone, A., Faroux, S., Le Moigne, P., et al. (2012). The detailed snowpack scheme Crocus and its implementation in SURFEX v7.2. *Geoscientific Model Development*, *5*(3), 773–791. https://doi.org/10.5194/gmd-5-773-2012

Vizcaino, M. (2014). Ice sheets as interactive components of Earth System Models: progress and challenges. *WIREs Climate Change*, *5*(4), 557–568. https://doi.org/10.1002/wcc.285

Vreugdenhil, C. A., & Taylor, J. R. (2019). Stratification Effects in the Turbulent Boundary Layer beneath a Melting Ice Shelf: Insights from Resolved Large-Eddy Simulations. *Journal of Physical Oceanography*, *49*(7), 1905–1925. https://doi.org/10.1175/JPO-D-18-0252.1

Waddington, E. D., Neumann, T. A., Koutnik, M. R., Marshall, H.-P., & Morse, D. L. (2007). Inference of accumulation-rate patterns from deep layers in glaciers and ice sheets. *Journal of Glaciology*, *53*(183), 694–712. https://doi.org/10.3189/002214307784409351

van der Wal, W., Whitehouse, P. L., & Schrama, E. J. O. (2015). Effect of GIA models with 3D composite mantle viscosity on GRACE mass balance estimates for Antarctica. *Earth and Planetary Science Letters*, *414*, 134–143. https://doi.org/10.1016/j.epsl.2015.01.001

Walker, R. T., Parizek, B. R., Alley, R. B., Anandakrishnan, S., Riverman, K. L., & Christianson, K. (2013). Ice-shelf tidal flexure and subglacial pressure variations. *Earth and Planetary Science Letters*, *361*, 422–428. https://doi.org/10.1016/j.epsl.2012.11.008

Wallace, L. O., E. M. van Wijk, S. R. Rintoul, and B. Hally (2020), Bathymetry-constrained navigation of Argo floats under sea ice on the Antarctic continental shelf, *Geophys. Res. Lett.*, 47, e2020GL087019, https://doi.org/10.1029/2020GL087019.

Wallis, B. J., Hogg, A. E., Van Wessem, J. M., Davison, B. J., & Van Den Broeke, M. R. (2023). Widespread seasonal speed-up of west Antarctic Peninsula glaciers from 2014 to 2021. *Nature Geoscience*, *16*(3), 231–237. https://doi.org/10.1038/s41561-023-01131-4

Walters, D., Boutle, I., Brooks, M., Melvin, T., Stratton, R., Vosper, S., et al. (2017). The Met Office Unified Model Global Atmosphere 6.0/6.1 and JULES Global Land 6.0/6.1 configurations. *Geoscientific Model Development*, *10*(4), 1487–1520. https://doi.org/10.5194/gmd-10-1487-2017

Wan, J. X. W., Gomez, N., Latychev, K., & Han, H. K. (2022). Resolving glacial isostatic adjustment (GIA) in response to modern and future ice loss at marine grounding lines in West Antarctica. *The Cryosphere*, *16*(6), 2203–2223. https://doi.org/10.5194/tc-16-2203-2022

Wang, G., Hendon, H. H., Arblaster, J. M., Lim, E.-P., Abhik, S., & van Rensch, P. (2019). Compounding tropical and stratospheric forcing of the record low Antarctic sea-ice in 2016. *Nature Communications*, *10*(1), 13. https://doi.org/10.1038/s41467-018-07689-7

Wang, J., Luo, H., Yang, Q., Liu, J., Yu, L., Shi, Q., & Han, B. (2022). An Unprecedented Record Low Antarctic Sea-ice Extent during Austral Summer 2022. *Advances in Atmospheric Sciences*, *39*(10), 1591–1597. https://doi.org/10.1007/s00376-022-2087-1

Wang, S., Liu, H., Jezek, K., Alley, R. B., Wang, L., Alexander, P., & Huang, Y. (2022). Controls on Larsen C Ice Shelf Retreat From a 60-Year Satellite Data Record. *Journal of Geophysical Research: Earth Surface*, *127*(3), e2021JF006346. https://doi.org/10.1029/2021JF006346

Wang, Yang, Zhou, D., Bunde, A., & Havlin, S. (2016). Testing reanalysis data sets in Antarctica: Trends, persistence properties, and trend significance. *Journal of Geophysical Research: Atmospheres*, *121*(21), 12,839-12,855. https://doi.org/10.1002/2016JD024864

Wang, Yetang, Ding, M., Reijmer, C. H., Smeets, P. C. J. P., Hou, S., & Xiao, C. (2021). The AntSMB dataset: a comprehensive compilation of surface mass balance field observations over the Antarctic Ice Sheet. *Earth System Science Data*, *13*(6), 3057–3074. https://doi.org/10.5194/essd-13-3057-2021

Wang, Yetang, Zhang, X., Ning, W., Lazzara, M. A., Ding, M., Reijmer, C. H., et al. (2023). The AntAWS dataset: a compilation of Antarctic automatic weather station observations. *Earth System Science Data*, *15*(1), 411–429. https://doi.org/10.5194/essd-15-411-2023

Wannamaker, P., Hill, G., Stodt, J., Maris, V., Ogawa, Y., Selway, K., et al. (2017). Uplift of the central transantarctic mountains. *Nature Communications*, *8*(1), 1588. https://doi.org/10.1038/s41467-017-01577-2

Warburton, K. L. P., Hewitt, D. R., & Neufeld, J. A. (2020). Tidal Grounding-Line Migration Modulated by Subglacial Hydrology. *Geophysical Research Letters*, *47*(17), e2020GL089088. https://doi.org/10.1029/2020GL089088

Warner, T. T. (2010). *Numerical Weather and Climate Prediction* (1st ed.). Cambridge University Press. https://doi.org/10.1017/CBO9780511763243

Watkins, M. M., Wiese, D. N., Yuan, D.-N., Boening, C., & Landerer, F. W. (2015). Improved methods for observing Earth's time variable mass distribution with GRACE using spherical cap mascons: Improved Gravity Observations from GRACE. *Journal of Geophysical Research: Solid Earth*, *120*(4), 2648–2671. https://doi.org/10.1002/2014JB011547

Watts, A. C., Ambrosia, V. G., & Hinkley, E. A. (2012). Unmanned Aircraft Systems in Remote Sensing and Scientific Research: Classification and Considerations of Use. *Remote Sensing*, *4*(6), 1671–1692. https://doi.org/10.3390/rs4061671

Wauthy, S., Tison, J.-L., Inoue, M., El Amri, S., Sun, S., Fripiat, F., Claeys, P., & Pattyn, F. (2024). Spatial and temporal variability of environmental proxies from the top 120 m of two ice cores in Dronning Maud Land (East Antarctica). *Earth System Science Data*, 16, 35–58. https://doi.org/10.5194/essd-16-35-2024

Wåhlin, A.K., Steiger, N., Darelius, E., Assmann, K.M., Glessmer, M.S., Ha, H.K., Herraiz-Borreguero, L., Heuzé, C., Jenkins, A., Kim, T.W. and Mazur, A.K. (2020). Ice front blocking of ocean heat transport to an Antarctic ice shelf. Nature, 578(7796), 568-571, https://doi.org/10.1038/s41586-020-2014-5

WCRP Global Sea Level Budget Group. (2018). Global sea-level budget 1993–present. *Earth System Science Data*, *10*(3), 1551–1590. https://doi.org/10.5194/essd-10-1551-2018

Wearing, M. G., Kingslake, J., & Worster, M. G. (2020). Can unconfined ice shelves provide buttressing via hoop stresses? *Journal of Glaciology*, *66*(257), 349–361. https://doi.org/10.1017/jog.2019.101

Webber, B. G. M., Heywood, K. J., Stevens, D. P., Dutrieux, P., Abrahamsen, E. P., Jenkins, A., et al. (2017). Mechanisms driving variability in the ocean forcing of Pine Island Glacier. *Nature Communications*, *8*(1), 14507. https://doi.org/10.1038/ncomms14507

Weertman, J. (1957). On the sliding of glaciers. *J. Glaciol.*, *3*, 33–38.

Weertman, J. (1974). Stability of the Junction of an Ice Sheet and an Ice Shelf. *Journal of Glaciology*, *13*(67), 3–11. https://doi.org/10.3189/S0022143000023327

Wei, W., Blankenship, D. D., Greenbaum, J. S., Gourmelen, N., Dow, C. F., Richter, T. G., et al. (2020). Getz Ice Shelf melt enhanced by freshwater discharge from beneath the West Antarctic Ice Sheet. *The Cryosphere*, *14*(4), 1399–1408. https://doi.org/10.5194/tc-14-1399-2020

Werder, M. A., Hewitt, I. J., Schoof, C. G., & Flowers, G. E. (2013). Modeling channelized and distributed subglacial drainage in two dimensions. *J. Geophys. Res.*, *118*, 1–19. https://doi.org/doi:10.1002/jgrf.20146,

Wernecke, A., Edwards, T. L., Nias, I. J., Holden, P. B., & Edwards, N. R. (2020). Spatial probabilistic calibration of a high-resolution Amundsen Sea Embayment ice sheet model with satellite altimeter data. *The Cryosphere*, *14*(5), 1459–1474. https://doi.org/10.5194/tc-14-1459-2020

Wessel, B., Huber, M., Wohlfart, C., Bertram, A., Osterkamp, N., Marschalk, U., et al. (2021). TanDEM-X PolarDEM 90 m of Antarctica: generation and error characterization. *The Cryosphere*, *15*(11), 5241–5260. https://doi.org/10.5194/tc-15-5241-2021

Wild, C. T., Drews, R., Neckel, N., Lee, J., Kim, S., Han, H., et al. (2025). Monitoring shear-zone weakening in East Antarctic outlet glaciers through differential InSAR measurements. *The Cryosphere,* 19(10), 4533–4554. https://doi.org/10.5194/tc-19-4533-2025

Winberry, J. P., S. Anandakrishnan, and R. B. Alley (2009), Seismic observations of transient subglacial water-flow beneath MacAyeal Ice Stream, West Antarctica, *Geophys. Res. Lett.*, 36, L11502, https://doi.org/10.1029/2009GL037730

Whitehouse, P. L. (2018). Glacial isostatic adjustment modelling: historical perspectives, recent advances, and future directions. *Earth Surface Dynamics*, *6*(2), 401–429. https://doi.org/10.5194/esurf-6-401-2018

Whitehouse, P. L., Bentley, M. J., Milne, G. A., King, M. A., & Thomas, I. D. (2012). A new glacial isostatic adjustment model for Antarctica: calibrated and tested using observations of relative sea-level change and present-day uplift rates: A new GIA model for Antarctica. *Geophysical Journal International*, *190*(3), 1464–1482. https://doi.org/10.1111/j.1365-246X.2012.05557.x

Whitehouse, P. L., Gomez, N., King, M. A., & Wiens, D. A. (2019). Solid Earth change and the evolution of the Antarctic Ice Sheet. *Nature Communications*, *10*(1), 503. https://doi.org/10.1038/s41467-018-08068-y

Whitworth III, T., Orsi, A. H., Kim, S.-J., Nowlin Jr., W. D., & Locarnini, R. A. (1985). Water Masses and Mixing Near the Antarctic Slope Front. In *Ocean, Ice, and Atmosphere: Interactions at the Antarctic Continental Margin* (pp. 1–27). American Geophysical Union (AGU). https://doi.org/10.1029/AR075p0001

van Wijk, E. M., Rintoul, S. R., Wallace, L. O., Ribeiro, N., & Herraiz-Borreguero, L. (2022). Vulnerability of Denman Glacier to Ocean Heat Flux Revealed by Profiling Float Observations. *Geophysical Research Letters*, *49*(18). https://doi.org/10.1029/2022GL100460

Wild, C. T., Alley, K. E., Muto, A., Truffer, M., Scambos, T. A., & Pettit, E. C. (2022). Weakening of the pinning point buttressing Thwaites Glacier, West Antarctica. *The Cryosphere*, *16*(2), 397–417. https://doi.org/10.5194/tc-16-397-2022

Wilkinson, M. D., Dumontier, M., Aalbersberg, Ij. J., Appleton, G., Axton, M., Baak, A., et al. (2016). The FAIR Guiding Principles for scientific data management and stewardship. *Scientific Data, 3*(1), 160018. https://doi.org/10.1038/sdata.2016.18

Willcocks, S., Hasterok, D., & Jennings, S. (2021). Thermal refraction: implications for subglacial heat flux. *Journal of Glaciology*, *67*(265), 875–884. https://doi.org/10.1017/jog.2021.38

Wille, J. D., Favier, V., Dufour, A., Gorodetskaya, I. V., Turner, J., Agosta, C., & Codron, F. (2019). West Antarctic surface melt triggered by atmospheric rivers. *Nature Geoscience*, *12*(11), 911–916. https://doi.org/10.1038/s41561-019-0460-1

Wille, J. D., Favier, V., Gorodetskaya, I. V., Agosta, C., Kittel, C., Beeman, J. C., et al. (2021). Antarctic Atmospheric River Climatology and Precipitation Impacts. *Journal of Geophysical Research: Atmospheres*, *126*(8). https://doi.org/10.1029/2020JD033788

Wille, J. D., Favier, V., Jourdain, N. C., Kittel, C., Turton, J. V., Agosta, C., et al. (2022). Intense atmospheric rivers can weaken ice shelf stability at the Antarctic Peninsula.

Communications Earth & Environment, *3*(1), 90. https://doi.org/10.1038/s43247-022-00422-9

Wilson, D. S., & Luyendyk, B. P. (2009). West Antarctic paleotopography estimated at the Eocene-Oligocene climate transition. *Geophysical Research Letters*, *36*(16), L16302. https://doi.org/10.1029/2009GL039297

Wilson, S.F., Hogg, A.E., Rigby, R., Gourmelen, N., Nias, I. and Slater, T. (2025). Detection of 85 new active subglacial lakes in Antarctica from a decade of CryoSat-2 data. *Nature Communications*, 16(1), 8311, https://doi.org/10.1038/s41467-025-63773-9

Wingham, D.J., Francis, C. R., Baker, S., Bouzinac, C., Brockley, D., Cullen, R., et al. (2006). CryoSat: A mission to determine the fluctuations in Earth's land and marine ice fields. *Advances in Space Research*, *37*(4), 841–871. https://doi.org/10.1016/j.asr.2005.07.027

Wingham, Duncan J., Ridout, A. J., Scharroo, R., Arthern, R. J., & Shum, C. K. (1998). Antarctic Elevation Change from 1992 to 1996. *Science*, *282*(5388), 456–458. https://doi.org/10.1126/science.282.5388.456

Wingham, Duncan J., Siegert, M. J., Shepherd, A., & Muir, A. S. (2006). Rapid discharge connects Antarctic subglacial lakes. *Nature*, *440*(7087), 1033–1036. https://doi.org/10.1038/nature04660

Winstrup, M., Vallelonga, P., Kjær, H. A., Fudge, T. J., Lee, J. E., Riis, M. H., et al. (2019). A 2700-year annual timescale and accumulation history for an ice core from Roosevelt Island, West Antarctica. *Climate of the Past*, *15*(2), 751–779. https://doi.org/10.5194/cp-15-751-2019

Wise, M. G., Dowdeswell, J. A., Jakobsson, M., & Larter, R. D. (2017). Evidence of Marine Ice-Cliff Instability in Pine Island Bay from Iceberg-Keel Plough Marks. *Nature*, *550*(7677), 506–510. https://doi.org/10.1038/nature24458

Wolovick, M. J., Creyts, T. T., Buck, W. R., & Bell, R. E. (2014). Traveling slippery patches produce thickness-scale folds in ice sheets. *Geophysical Research Letters*, *41*(24), 8895–8901. https://doi.org/10.1002/2014GL062248

Wong, A. P. S., & Riser, S. C. (2011). Profiling Float Observations of the Upper Ocean under Sea Ice off the Wilkes Land Coast of Antarctica. *Journal of Physical Oceanography*, *41*(6), 1102–1115. https://doi.org/10.1175/2011JPO4516.1

Wright, A. P., Young, D. A., Roberts, J. L., Schroeder, D. M., Bamber, J. L., Dowdeswell, J. A., et al. (2012). Evidence of a hydrological connection between the ice divide and ice sheet margin in the Aurora Subglacial Basin, East Antarctica. *Journal of Geophysical Research, 117, F01033,* 1–15. https://doi.org/10.1029/2011JF002066

Xu, Y., Rignot, E., Fenty, I., Menemenlis, D., & Flexas, M. M. (2013). Subaqueous melting of Store Glacier, west Greenland from three-dimensional, high-resolution numerical modeling and ocean observations. *Geophys. Res. Lett.*, *40*(17), 4648–4653. https://doi.org/10.1002/grl.50825

Yamazaki, K., Aoki, S., Katsumata, K., Hirano, D., & Nakayama, Y. (2021). Multidecadal poleward shift of the southern boundary of the Antarctic Circumpolar Current off East Antarctica. *Science Advances*, *7*(24), eabf8755. https://doi.org/10.1126/sciadv.abf8755

Yan, L., Wang, Z., Liu, C., Wu, Y., Qin, Q., Sun, C., et al. (2023). The Salinity Budget of the Ross Sea Continental Shelf, Antarctica. *Journal of Geophysical Research: Oceans*, *128*(3), e2022JC018979. https://doi.org/10.1029/2022JC018979

Yang, J., Guo, J., Greenbaum, J.S., Cui, X., Tu, L., Li, L., Jong, L.M., Tang, X., Li, B., Blankenship, D.D. and Roberts, J.L. (2021). Bathymetry beneath the Amery Ice Shelf, East Antarctica, revealed by airborne gravity. *Geophysical Research Letters*, 48(24), p.e2021GL096215, https://doi.org/10.1029/2021GL096215

Yang, J., Luo, Z., & Tu, L. (2020). Ocean Access to Zachariæ Isstrøm Glacier, Northeast Greenland, Revealed by OMG Airborne Gravity. *Journal of Geophysical Research: Solid Earth*, *125*(11). https://doi.org/10.1029/2020JB020281

Yi, D., Harbeck, J. P., Manizade, S. S., Kurtz, N. T., Studinger, M., & Hofton, M. (2015). Arctic Sea Ice Freeboard Retrieval With Waveform Characteristics for NASA's Airborne Topographic Mapper (ATM) and Land, Vegetation, and Ice Sensor (LVIS). *IEEE Transactions on Geoscience and Remote Sensing*, *53*(3), 1403–1410. https://doi.org/10.1109/TGRS.2014.2339737

Yoon, S.-T., Lee, W. S., Stevens, C., Jendersie, S., Nam, S., Yun, S., et al. (2020). Variability in high-salinity shelf water production in the Terra Nova Bay polynya, Antarctica. *Ocean Science*, *16*(2), 373–388. https://doi.org/10.5194/os-16-373-2020

Young, D. A., Schroeder, D. M., Blankenship, D. D., Kempf, S. D., & Quartini, E. (2016). The distribution of basal water between Antarctic subglacial lakes from radar sounding. *Philosophical Transactions of the Royal Society A: Mathematical, Physical and Engineering Sciences*, *374*(2059), 20140297. https://doi.org/10.1098/rsta.2014.0297

Young, D., Roberts, J.L., Blankenship, D.D., Van Ommen, T., Ritz, C., Cavitte, M.G. and Frezzotti, M. (2021) ICECAP radargrams in support of the international old ice search at Dome C-2016. [Data set]. Australian Antarctic Data Centre. https://doi.org/10.26179/5WKF-7361

Young, T. J., Schroeder, D. M., Jordan, T. M., Christoffersen, P., Tulaczyk, S. M., Culberg, R., & Bienert, N. L. (2021). Inferring Ice Fabric From Birefringence Loss in Airborne Radargrams: Application to the Eastern Shear Margin of Thwaites Glacier, West Antarctica. *Journal of Geophysical Research: Earth Surface*, *126*(5). https://doi.org/10.1029/2020JF006023

Zachos, J., Pagani, M., Sloan, L., Thomas, E., & Billups, K. (2001). Trends, Rhythms, and Aberrations in Global Climate 65 Ma to Present. *Science*, *292*(5517), 686–693. https://doi.org/10.1126/science.1059412

Zeitz, M., Levermann, A., & Winkelmann, R. (2020). Sensitivity of ice loss to uncertainty in flow law parameters in an idealized one-dimensional geometry. *The Cryosphere*, *14*(10), 3537–3550. https://doi.org/10.5194/tc-14-3537-2020

Zhan, Z., Tsai, V. C., Jackson, J. M., & Helmberger, D. (2014). Ambient noise correlation on the Amery Ice Shelf, East Antarctica. *Geophysical Journal International*, *196*(3), 1796–1802. https://doi.org/10.1093/gji/ggt488

Zhang, Z., Nakata, N., Karplus, M., Kaip, G., & Yi, J. (2022). Shallow Ice-Sheet Composite Structure Revealed by Seismic Imaging Near the West Antarctic Ice Sheet (WAIS) Divide Camp. *Journal of Geophysical Research: Earth Surface*, *127*(12), e2022JF006777. https://doi.org/10.1029/2022JF006777

Zhao, C., Gladstone, R., Galton-Fenzi, B. K., Gwyther, D., & Hattermann, T. (2022). Evaluation of an emergent feature of sub-shelf melt oscillations from an idealized coupled ice sheet–ocean model using FISOC (v1.1) – ROMSIceShelf (v1.0) – Elmer/Ice (v9.0). *Geoscientific Model Development*, *15*(13), 5421–5439. https://doi.org/10.5194/gmd-15-5421-2022

Zhao, C., Gladstone, R., Zwinger, T., Gillet-Chaulet, F., Wang, Y., Caillet, J., et al. (2025). Subglacial water amplifies Antarctic contributions to sea-level rise. *Nature Communications*, 16(1), 3187. https://doi.org/10.1038/s41467-025-58375-4

Zhou, Q., & Hattermann, T. (2020). Modeling ice shelf cavities in the unstructured-grid, Finite Volume Community Ocean Model: Implementation and effects of resolving small-scale topography. *Ocean Modelling*, *146*, 101536. https://doi.org/10.1016/j.ocemod.2019.101536

Zhou, Y., Franke, S., Kleiner, T., Drews, R., Humbert, A., Jansen, D., Steinhage, D. and Eisen, O., 2025. Reactivation of a subglacial channel around the grounding zone of Roi Baudouin Ice Shelf, Antarctica. *Geophysical Research Letters*, 52(2), p.e2024GL112476.

Zilberman, N. V. (2017). Deep Argo: sampling the total ocean volume in state of the climate in 2016. *Bull. Am. Meteorol. Soc*, *98*, S73–S74.

Zoet, L. K., & Iverson, N. R. (2020). A slip law for glaciers on deformable beds. *Science*, *368*(6486), 76–78. https://doi.org/10.1126/science.aaz1183

Zou, X., Bromwich, D. H., Montenegro, A., Wang, S., & Bai, L. (2021a). Major surface melting over the Ross Ice Shelf part I: Foehn effect. *Quarterly Journal of the Royal Meteorological Society*, *147*(738), 2874–2894. https://doi.org/10.1002/qj.4104

Zou, X., Bromwich, D. H., Montenegro, A., Wang, S., & Bai, L. (2021b). Major surface melting over the Ross Ice Shelf part II : Surface energy balance. *Quarterly Journal of the Royal Meteorological Society*, *147*(738), 2895–2916. https://doi.org/10.1002/qj.4105

Zurbuchen, J. and Simms, A.R., 2019. Late Holocene ice-mass changes recorded in a relative sea-level record from Joinville Island, Antarctica. *Geology*, 47(11), 1064-1068.

Zwally, H. J., Abdalati, W., Herring, T., Larson, K., Saba, J., & Steffen, K. (2002). Surface Melt-Induced Acceleration of Greenland Ice-Sheet Flow. *Science*, *297*(5579), 218–222. https://doi.org/10.1126/science.1072708

Zwally, H. J., Giovinetto, M. B., Beckley, M., & Saba, J. (2012). Antarctic and Greenland Drainage Systems [Data set]. 610 Web Dev. Retrieved from GSFC Cryospheric Sciences Laboratory, at http://icesat4.gsfc.nasa.gov/cryo_data/ant_grn_drainage_systems.php